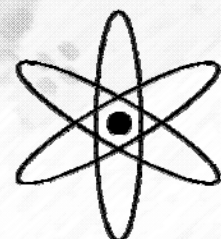


Design, development and verification of the eROSITA thermal control system

Dissertation von
Maria Fürmetz



TECHNISCHE UNIVERSITÄT MÜNCHEN
MAX-PLANCK-INSTITUT FÜR EXTRATERRESTRISCHE PHYSIK

Design, development and verification
of the eROSITA
thermal control system

Maria Regina Fürmetz

Vollständiger Abdruck der von der Fakultät für Physik der Technischen Universität
München zur Erlangung des akademischen Grades eines

Doktors der Naturwissenschaften (Dr. rer. nat.)

genehmigten Dissertation.

Vorsitzender:

Univ.-Prof. Dr. H. Friedrich

Prüfer der Dissertation:

1. Hon.-Prof. Dr. G. Hasinger
2. Univ.-Prof. Dr. L. Oberauer

Die Dissertation wurde am 31.07.2012 bei der Technischen Universität München eingereicht
und durch die Fakultät für Physik am 12.09.2012 angenommen.

Abstract

In the course of this work an innovative thermal control system for the X-ray telescope eROSITA (**e**xtended **R**Oentgen **S**urvey with an **I**maging **T**elescope **A**rray) has been developed, manufactured and tested. eROSITA is the core instrument on the Spektrum-Röntgen-Gamma mission that will be launched in 2014.

Special attention is paid to the cooling system for the seven CCD cameras, always considering the interaction with the complete telescope. The complex assembly with the sevenfold symmetry of the eROSITA telescope requires an innovative design. Large distances in combination with a very low operating temperature between 173 K and 183 K demand a great deal to the cooling chain. Extreme temperatures with the Sun on the one side and the cold space on the other present a real challenge to the cooling system.

In total, three different low-temperature ethane heat pipes are used to transport the heat from the cameras to two radiators outside the telescope structure. The heat pipes were developed and optimised in the course of this work. Small camera heat pipes are connected to each CCD module. Ring heat pipes are collecting the heat of all seven cameras and are conducting it to two exchange points. Each of these points is connected to one camera radiator with special variable conductance heat pipes (sVCHPs). To avoid condensation of outgassed material on the detectors, they will not be cooled within the first weeks after launch. So the sVCHPs can be switched on during the mission with the help of an electric solenoid latching valve. Furthermore these heat pipes provide a sensitive means of temperature control by adjusting the active condenser length – and therefore the cooling power – by means of a movable diffusion barrier. Besides the working fluid, the heat pipes contains nitrogen as non-condensable gas. Its volume can be easily changed with a small heating power.

Extensive measurements of liquid velocity, maximum heat transport capabilities and heat transfer coefficients were made and correlated with the underlying theory. All relevant limitations were examined and evaluated. A drop tower campaign proved the heat pipes' functionality under zero gravity. Thermal vacuum tests were made

to analyse and optimise the heat pipe performance. The determination of the ideal amount of working fluid and non-condensable gas inside the variable conductance heat pipes required several revision cycles.

A thermal model of the complete telescope was used to predict the thermal behaviour of the subsystems. Step by step this model was improved by various test results. The most complex test to date verified the camera cooling system. Former assumptions of heat transfer coefficients and optical properties were confirmed and improved respectively.

Furthermore, the mission scenario's impact not only on the telescope operation but also on the science was examined. Since the orbit around L2 has a duration of approximately 180 days, an undesired superposition with the Earth's revolution around the Sun had to be eliminated. The influences of spacecraft movements within and perpendicular to the ecliptic were separated and classified as uncritical. Exposure maps of different possible orbit scenarios were generated. They show the distribution of the telescope exposure for the whole mission over the complete sky. They are an important means for the mission planning and vice versa, since the scan procedure may be – to some degree – adjusted to the scientific requirements. Last but not least the exposure maps serve as basis for different simulations.

The next steps include the production and completion, respectively, of all flight heat pipes. Further tests and long-term measurements have to be made. A solar simulation test with the complete telescope and a flight-like thermal control system will eliminate the remaining uncertainties and allow for a precise prediction of the thermal behaviour during the mission.

Zusammenfassung

In dieser Arbeit wird die Entwicklung, Umsetzung und Verifizierung eines innovativen Thermalsystems für das Röntgenteleskop eROSITA (extended **RO**entgen **S**urvey with an **I**magin**g** **T**elescope **A**rray) vorgestellt. Das Teleskop ist das Hauptinstrument der Spektrum-Röntgen-Gamma-Mission, die ab 2014 den Röntgenhimmel durchmustern soll.

Das Hauptaugenmerk dieser Arbeit liegt auf dem Kühlsystem der sieben CCD-Kameras, gleichzeitig wird aber der Thermalhaushalt des gesamten Teleskops analysiert. Das komplexe Design mit der siebenfachen Symmetrie erfordert ein völlig neuartiges Kühlkonzept. Große Distanzen, die überbrückt werden müssen, gepaart mit einer tiefen Solltemperatur zwischen 173 K und 183 K, stellen hohe Anforderungen an die Kühlung. Zusätzlich bieten extreme Umweltbedingungen mit der Sonne auf der einen Seite und dem kalten Weltraum auf der anderen eine besondere Herausforderung.

Insgesamt leitet eine Kette von drei verschiedenen Arten von Tieftemperatur-Heatpipes die Wärme der Kameras zu zwei Radiatoren an der Außenseite der Teleskopstruktur. Alle Heatpipes wurden im Zuge dieser Arbeit entwickelt, getestet und optimiert. Jeder Detektor ist über eine kleine Kamera-Heatpipe mit zwei Ring-Heatpipes verbunden, welche die Wärme von allen sieben Kameras sammeln und zu jeweils einem Übergabepunkt führen. Diese sind wiederum mit jeweils zwei schaltbaren Variable Conductance Heatpipes (sVCHP) mit den Radiatoren verbunden. Diese sVCHPs werden nach einer bestimmten Zeit per Telekommando eingeschaltet. Zuvor verhindert das Unterbinden der Kühlung, dass aus der Struktur austretende Substanzen auf dem Detektor auskondensieren. Außerdem stellen sVCHPs eine effektive Methode zur Temperaturregelung dar, indem der aktive Kondensorbereich (und damit die Kühlleistung) variiert werden kann. Dies geschieht über eine verschiebbare Gasfront. Zusätzlich zum Arbeitsmedium Ethan ist eine geringe Menge Stickstoff enthalten. Dessen Volumen kann durch eine geringe Heizleistung entsprechend verringert oder erhöht werden.

Detaillierte Messungen der Transportgeschwindigkeiten innerhalb der Heatpipes, des

maximalen Leistungstransports und diverser Wärmeübergangskoeffizienten wurden mit der zugrunde liegenden Theorie verglichen. Des Weiteren wurden alle Faktoren untersucht und bewertet, die das Transportverhalten der Heatpipes potentiell beeinträchtigen könnten. Eine Fallturm-Kampagne bestätigte die Funktionalität der Heatpipes in der Schwerelosigkeit. Zusätzlich wurden zahlreiche Thermal-Vakuum-Tests durchgeführt, um die Transporteigenschaften der Heatpipes zu analysieren und zu optimieren. Insbesondere um die idealen Füllmengen von Arbeitsmedium und Gas zum Regeln der Temperatur für die sVCHPs zu bestimmen, waren mehrere Durchläufe vonnöten.

Von Beginn an wurde ein Thermalmodell des gesamten Teleskops verwendet, um das thermische Verhalten der einzelnen Subsysteme vorherzusagen. Dieses Modell wurde im Laufe der Zeit mit Hilfe der Testresultate verbessert und verfeinert. Der bisher umfangreichste Testaufbau beinhaltete einen Teil des Kamera-Kühlsystems. Alle betroffenen thermischen Übergangswerte und Modellparameter konnten bestätigt bzw. durch genauere Werte ersetzt werden.

Weiterhin wurden verschiedene Aspekte des operationellen Betriebs untersucht – zum einen dessen unmittelbare Konsequenzen für das Instrument, zum anderen aber auch die Auswirkungen auf die Wissenschaft. Durch den Betrieb am Lagrangepunkt 2 ergeben sich bestimmte Randbedingungen für die Orientierung des Satelliten. Aufgrund der Umlaufdauer von 180 Tagen war eine Überlagerung mit dem Umlauf der Erde um die Sonne nicht auszuschließen. Daher wurden Bewegungen sowohl in der Ekliptik als auch senkrecht dazu separat untersucht, wobei sich herausstellte, dass keine unerwünschten Effekte bezüglich der räumlichen Verteilung der Exposure – der Beobachtungszeit – auftreten. Entsprechende Verteilungen für mögliche Orbits wurden berechnet und dienen als Grundlage für die Missionsplanung, denn bis zu einem gewissen Grad kann die Scan-Prozedur an die wissenschaftlichen Anforderungen angepasst werden. Nicht zuletzt dient die Exposure-Verteilung auch als Basis für verschiedene Simulationen.

In den kommenden Monaten wird die Produktion der Flughardware vorangetrieben. Weitere Tests und Langzeitmessungen sind notwendig, um die Heatpipes zu qualifizieren. Ein Thermal-Vakuum-Test mit Sonnensimulation des gesamten Teleskops inklusive des repräsentativen Thermalsystems wird letzte Unsicherheiten in den Modellparametern beseitigen. So kann das thermischen Verhaltens von eROSITA während der Mission präzise vorhergesagt werden.

Acknowledgements

Now I'm coming to the best and at the same time the most difficult part of my thesis – doing those people justice who helped me through the last few years.

First of all, I want to express my gratitude to Günther Hasinger. You made this thesis possible. And even from the other end of the world, you are still supporting me and giving me the chance to finish it.

Special thanks goes to my boss and supervisor Peter Predehl. Peter, you are holding this team together. Thank you for your support through all these years in every way and for believing in me even if I didn't. You brought me back on track when I got lost – especially after my first thesis draft.

Thank you also to the HEG group and our director Kirpal Nandra, for providing a great working atmosphere and lively discussions.

Elmar Pfeffermann, you were my mentor from the beginning on. All the stuff about vacuum, leakage, safety, cleaning, I know from you. You showed me the importance of a diligent and well-organized performance, and of questioning everything. Thank you for being such a patient teacher and for countless tips and ideas for improvement.

Thank you to our system engineer Josef Eder who showed me how to manage a project and to deal with subcontractors and schedules. Also thank you to the other construction engineers Lars Tiedemann, Reiner Schreib and Heinz Huber for realizing our ideas and dealing with my regular change requests.

Sometimes there's too much work for one person and sometimes there's also work you don't want to do by yourself – thank you Andrea Kim, Alexander Buron and Steffen Sedlak for being great subordinates :) – it was a pleasure working with you. Alex, the Lord of Labview, I still wouldn't find my test data if it weren't for you. Steffen, I'd still have to write my test reports from last year and Andrea, besides all your fantastic ideas and improvements, you made me more than once crying from all the laughing and it is really hard to letting you go.

One of the most important data in my work was produced in the PANTER facility in Neuried. For several weeks I was a permanent resident and despite of long shifts and hard work, I really enjoyed it there. No problem which couldn't be solved. Vadim Burwitz, who always cares about me and has a smile in his face, even if he hasn't slept for days. Bernd Budau, my personal master of making long holes and any kind of adapter if a screw just doesn't want to fit in. Gisela Hartner and Wolfgang Burkert, who always have an open ear, not only for programming issues. Thank you for a great time!

Thank you to the IMPRS students and supervisors, especially Werner Becker, for broadening my horizon during a lot of courses, lectures and seminars.

A big thank you to the best colleagues in the world. Thanks for all the day-saving discussions – from rather serious and physical topics (which more than once led to the solution of a problem) to really hilarious ones. Thank you all, apart from the ones already mentioned above: Heinrich Bräuninger, also for being a great room mate, I learned a lot about cleanliness, contamination and test facilities. Peter Friedrich, thank you for attending my thesis committee, for giving me always valuable hints, not only in IDL issues and for making some great photographs of my heat pipes. Thank you to Anita Winter, Monika Vongehr (we miss you!), Walter Kink, Reinhard Lederer, Fritz Schrey and Siegfried Müller, for helping me out whenever I have a problem with wires and electrons. I really appreciate having such great colleagues!

Instruments have to be built before producing great data. And therefore you need people with great experience and helpfulness – our workshop specialists. I know I stepped in more than once five minutes before closing time. Or with a sketch and only a rough idea that "I want to have something that can do something". And you never let me down. Special thanks to Stefan Czempel, Franz Huber, Armin Goldbrunner, Hans Eibl and all the other members of the machine shop, Johann Gahl, Walter Schunn, Peter Reiss, Thomas Rupprecht, Franz Oberauer, Martin Deuter, Patricia Langer, Franz Soller, Johannes Hartwig, Robert Bayer, the IPP-team (especially Norbert Dekorsy and Robert Gieb), Dragan Winter from LPT, the ZARM Drop Tower team and all the others whom I may have driven to despair with my "physical" point of view.

A big thank you to my friend Mike, my uncle Walter and my former colleague Martin Mühlegger for very helpful comments and proof reading. Sometimes I really couldn't believe that I wrote such nonsense.

I also want to thank my family and friends. I really appreciate your support and I'm

truly sorry that I wasn't present for a very long time. Thank you for your understanding and your love.

Last but not least I want to thank my partner Niki. Not only for proof reading, but mainly for your never-ending patience, your incredible support and always giving me a shoulder to lean on. Without you, I wouldn't have made it through the last few months. I know that this wasn't always easy and I don't take that for granted. You made me realise what is really important in life. I love you!

Contents

List of Figures	xi
List of Tables	xv
Acronyms	xvii
1 eROSITA on Spektrum-Röntgen-Gamma	1
1.1 Science drivers	2
1.2 Instrument description	4
1.3 Boundary conditions for the thermal control system	6
2 The eROSITA camera thermal control	9
2.1 Requirements	9
2.2 Thermal environment	11
2.3 Design	12
3 Heat pipes	21
3.1 Underlying physical concepts	22
3.1.1 Functional principle	22
3.1.2 Heat transfer coefficients at evaporator and condenser	24
3.1.3 Capillary limit and heat transport factor	28
3.1.4 Further heat pipe limitations	37
3.1.5 Variable conductance heat pipes	42
3.2 Technical solution	48
3.2.1 Camera and ring heat pipes	50
3.2.2 Switchable variable conductance heat pipes	54
3.3 Heat pipe performance test under microgravity	58
3.3.1 Test set-up	58
3.3.2 Test campaign	63
3.3.3 Results	65

3.4	Camera and ring heat pipe equilibrium performance	74
3.4.1	Camera heat pipe	74
3.4.2	Ring heat pipe	82
3.5	Optimisation of the switchable variable conductance heat pipes	84
3.5.1	Test set-up	85
3.5.2	Test results	85
4	Thermal design and analysis of the camera cooling system	95
4.1	Camera assembly thermal model	96
4.2	Heat pipe thermal model	103
4.3	Camera cooling thermal balance test	105
4.3.1	Test set-up	106
4.3.2	Test campaign	110
4.3.3	Thermal model	110
4.3.4	Test results	113
4.3.5	Adaption of the thermal model	117
5	eROSITA thermal control system	123
5.1	Multilayer Insulation	124
5.2	Mirror assembly	134
5.3	Camera electronics	139
5.4	Predictions for the eROSITA thermal control system performance	142
6	Orbit scenarios	149
6.1	The Lagrange point 2	149
6.2	Spacecraft pointing	150
6.3	Exposure	152
6.4	The Low Earth Orbit	155
7	Summary and outlook	157
A	Heat transport	161
A.1	From Fourier's law to the heat equation – conductive heat transport	161
A.2	Convection	165
A.3	Radiative heat exchange	165
B	Computational methods for solving differential equations	177
C	Thermal software	181

List of Figures

1.1	Number of galaxy clusters as a function of redshift	3
1.2	The Spektrum-Röntgen-Gamma mission	5
1.3	Telescope overview	6
1.4	CCD design	7
1.5	Camera assembly	7
2.1	Temperature dependence of the CCD dark current	10
2.2	Temperature dependence of the CCD energy resolution	11
2.3	Radiator temperature in dependence of radiator area	13
2.4	Design of the camera cooling	14
2.5	Camera heat pipe	15
2.6	Ring heat pipe	15
2.7	Switchable variable conductance heat pipe	16
2.8	Working principle of a VCHP	18
2.9	Camera module configuration	19
3.1	Heat pipe scheme	21
3.2	Heat pipe resistances	23
3.3	Conductive heat transfer at evaporator and condenser	27
3.4	Schematic of the capillary force inside a small tube	30
3.5	Heat pipe pressures	31
3.6	Effective pore radii for different wick geometries	33
3.7	Derivation of HP boiling limit	41
3.8	General temperature dependence of heat pipes limits	43
3.9	Temperature dependence of eROSITA camera heat pipe limits	43
3.10	Wetting angle of ethane	50
3.11	Test of the heat pipe crimping procedure	53
3.12	Crimping of the camera heat pipe	54
3.13	Welded joint of the camera heat pipe	54
3.14	Spiral spring inside the sVCHP	55

LIST OF FIGURES

3.15	Stainless steel mesh for the sVCHP	55
3.16	sVCHP mesh pulling device	55
3.17	Manufacturing of the sVCHP valve complex	57
3.18	Manufacturing of the complete sVCHP	57
3.19	Latent cold storage for zero-g test	59
3.20	Melting curve of the latent cold storage	60
3.21	Set-up for zero-g test	60
3.22	Heat pipes for zero-g test	61
3.23	Zero-g test scheme of heat pipe attachment	62
3.24	Read-out electronics	64
3.25	ZARM Drop Tower	64
3.26	Temperature curves of straight and bent camera heat pipes with different ethane levels	67
3.27	Temperature curves of straight and bent ring-type heat pipes	69
3.28	Optimum ethane level at different condenser temperatures	70
3.29	Determination of the sensor response time	71
3.30	Capillary velocities for the liquid phase	73
3.31	Camera heat pipe in vacuum chamber	75
3.32	HTC at camera heat pipe evaporator, $T = 175$ K	75
3.33	Heat transport factor and maximum heat load of camera heat pipes	76
3.34	Low temperature dry-out of camera heat pipes	77
3.35	Reduced heat transport factor at camera heat pipe evaporator	78
3.36	Oscillations in camera heat pipes	79
3.37	Heat transport factor and maximum heat load of excess ethane camera heat pipes	81
3.38	Global heat transfer coefficients for camera heat pipes	81
3.39	Cooling curve of the ring heat pipe	82
3.40	Performance of the ring heat pipe	83
3.41	Global heat transfer coefficient for ring heat pipes	83
3.42	Test set-up for VCHP optimisation	85
3.43	sVCHP temperature profile	88
3.44	Dry-out curve of straight sVCHP with 26.7 g ethane	90
3.45	Heat transport factor and maximum heat load of sVCHPs	91
3.46	Global and local heat transfer coefficients for sVCHP	92
3.47	Weber number and entrainment limit for eROSITA heat pipes	93
3.48	Boiling limit for eROSITA heat pipes	93
3.49	Mach number and sonic limit for eROSITA heat pipes	94
3.50	Viscous limit for eROSITA heat pipes	94

4.1	Thermal model of the camera module	97
4.2	Thermal model of the camera electronics	98
4.3	Thermal connectors of the camera assembly	102
4.4	Heat pipe thermal modelling	104
4.5	Replacement heaters	106
4.6	CAD model of the test set-up	107
4.7	Test set-up on platform upside down	108
4.8	Mounting of VCHPs and radiator	109
4.9	Final test set-up	109
4.10	Geometric thermal model of the camera assembly thermal balance test	111
4.11	Thermal couplings of the camera assembly thermal balance test	112
4.12	Cold case results	113
4.13	Control of CCD temperature	115
4.14	Overworked thermal couplings	120
4.15	Thermal budget for the nominal operation	121
5.1	Submodel principle for the thermal model	124
5.2	Multi-layer insulation	125
5.3	Influence of MLI layers	128
5.4	Effective emissivity as a function of number of layers	129
5.5	Fitting of measured MLI heat transfer coefficients	130
5.6	Effective emissivity as a function of average temperature	130
5.7	ESTEC MLI measurements of lay-ups comparable to eROSITA MLI. . .	132
5.8	Effective emissivity of the XMM-Newton MLI	133
5.9	Design of the mirror assembly	135
5.10	Heaters at the mirror module spider	135
5.11	Geometric thermal model of the mirror assembly	136
5.12	Thermal connectors of the mirror assembly	138
5.13	Mirror module temperature profile	138
5.14	Design of the electronics cooling	139
5.15	Camera electronics casing with embedded water heat pipes	140
5.16	Heat pipe interfaces of the electronics	140
5.17	Influence of the thermal baffle temperature on the mirror assembly . .	141
5.18	Loop Heat Pipe concept for electronics cooling	143
5.19	Telescope cooling curve after launch	144
5.20	Surface temperatures in nominal operation	145
6.1	Lagrange points of the Earth-Sun system	150

LIST OF FIGURES

6.2	Exposure maps for one and 50 days	151
6.3	Influence of orbital movements on the exposure	153
6.4	Complete exposure maps	154
6.5	Radiator temperatures in the Low Earth Orbit	155
7.1	Assembly of the qualification model	160
A.1	Spectral radiant exitance	169
A.2	Specular and diffuse reflectivity	171
A.3	Directional spectral emissivities of dielectrics	173
A.4	Directional spectral emissivity of metals	173
A.5	View factor calculation	175
B.1	Node scheme for the Crank-Nicolson method	179
C.1	ESATAN-TMS workbench	182
C.2	Example of an ESATAN model	184
C.3	Grid with thermal nodes of various distances	185

List of Tables

1.1	Subsystem temperature requirements	8
3.1	Properties of common heat pipe wick structures	36
3.2	Examples for active feedback control VCHP applications	48
3.3	eROSITA heat pipe properties	51
3.4	Ethane filling levels for zero-g test	63
3.5	Drop configurations for zero-g test	65
3.6	Performance of different ethane levels of bent sVCHPs	87
3.7	Performance of different nitrogen levels of sVCHPs	90
4.1	Parts and materials of the camera assembly	100
4.2	Conductive couplings of camera module and camera electronics	101
4.3	Heat pipe heat transfer coefficients for eROSITA heat pipes	104
4.4	Different load cases for the thermal balance test	110
4.5	Temperatures of different load cases	114
4.6	Controlling of nitrogen levels in VCHPs	115
4.7	VCHP global heat transfer coefficients	118
4.8	Prediction and data for the nominal operational case	119
5.1	eROSITA MLI lay-ups	126
5.2	Effective emissivity and conductance values for the eROSITA MLI thermal model	132
5.3	Parts and materials of the mirror assembly	137
5.4	Performance prediction for eROSITA	146
5.5	MLI sensitivity analysis	147
A.1	Definition of different emissivities	170

Acronyms

CA	Camera Assembly
CAMEX	CMOS Amplifier and MultipLEXer
CCD	Charged-Coupled Device
CE	Camera Electronics
CFRP	Carbon Fibre Reinforced Plastics
eROSITA	extended Roentgen Survey with an Imaging Telescope Array
GFRP	Glass Fibre Reinforced Plastics
gN ₂	gaseous Nitrogen
HP	Heat Pipe
HTC	Heat Transfer Coefficient
HTF	Heat Transport Factor
ITC	InTerface Controller
LEO	Low Earth Orbit
LHP	Loop Heat Pipe
MA	Mirror Assembly
MLI	Multi-Layer Insulation
MM	Mirror Module
MPE	Max-Planck-Institut für extraterrestrische Physik
NCG	Non-Condensable Gas
PCB	Printed Circuit Board
SRG	Spektrum-Röntgen-Gamma
STM	Structural Thermal Model
(s)VCHP	(switchable) Variable Conductance Heat Pipe
TB	Thermal Baffle
TEQ	Thermal EQUilibrium
μg	microgravity

1 eROSITA on Spektrum-Röntgen-Gamma

The X-ray telescope eROSITA (extended **R**Oentgen **S**urvey with an **I**maging **T**elescope **A**rray) is the core instrument on the Russian Spektrum-Roentgen-Gamma mission which will be launched in 2014 from Baikonur in Kazakhstan to an orbit around the Lagrange point 2 (L2) point of the Earth-Sun-system. Its design and manufacturing is led by the Max-Planck-Institut für extraterrestrische Physik (MPE). A mission overview as well as a rough instrument description is given in this chapter (section 1.2) and in Predehl et al. (2010).

This work focuses on the thermal control system of the instrument with particular attention paid to the camera cooling. An unprecedented configuration of seven cameras in total needs to be cooled to the optimum working temperature of about 180 K. The easiest solution (with the shortest paths) of a heat rejection system at the bottom of the telescope is not possible because the instrument is directly mounted on the spacecraft. Apart from that, a complete thermal decoupling is required by the spacecraft manufacturers. Despite the large number and the difficult accessibility of the cameras, which are mounted at the bottom of the telescope, a certain level of redundancy has to be provided. This results in a complex set-up of the thermal control system.

All this has to be realized at very low temperatures with an excellent temperature stability. A chain of three different heat pipe types – all designed, built and tested in the course of this work – connect the detectors to the radiators. Two of them are constant conductance heat pipes, the third is a special kind of switchable variable conductance heat pipe, which has been developed for an optimum performance of the camera cooling system. Extensive tests were performed to verify the functionality – not only of the heat pipes but of the complete thermal control system. The requirements and the resulting design are presented in chapter 2, while chapter 3 concentrates on the theory, manufacturing and testing of the heat pipes.

Simultaneously the design has to be verified by thermal calculations. Not only the

camera cooling performance has to be predicted and verified as done in chapter 4, but the complete telescope thermal control system has to be modelled. This includes the camera cooling as well as the mirror modules, the electronics and the mechanical structure (chapter 5).

An important factor influencing the design and performance of the instrument in general and the thermal control in particular is the orbit of the spacecraft. The exact orbit scenario changed during the development phase of the project and still depends on various technical constraints. In chapter 6 different orbits are compared and consequences for the mission are discussed. The last chapter provides an outlook into the future of the project and the next steps that have to be taken before launch.

1.1 Science drivers

eROSITA will perform the first all-sky-survey with an imaging telescope in the energy range between 0.3–10 keV and also will carry out pointed observations. The main objective of this mission is the detection of 100 000 clusters of galaxies up to a redshift¹ of ≈ 1.3 in order to constrain cosmological parameters, amongst others the density and evolution of Dark Energy.

Galaxy clusters are the largest gravitationally bound entities in our Universe and their evolution is governed by the underlying cosmology. The cluster mass function $n(M)$, which describes the distribution of clusters with a certain mass, strongly depends on the matter density Ω_m and the amplitude of the primordial power spectrum σ_8 , i.e. a description of density fluctuations in the early Universe. The evolution of $n(M)$ with time on its part depends on the evolution of the large scale structure (Springel et al. 2005), dominated by Dark Matter (DM) and Dark Energy (DE). Galaxy clusters emerge from a gravitational collapse, caused by the irregularities of the large-scale structure. Gas is gravitational caught in the potential barrier, accelerated and heated up to X-ray temperatures by shocks and compression. This is the reason why galaxy clusters shine bright in the X-ray energy band and most notably can be identified clearly as an entity.

An X-ray survey with a flux limit of 2.3×10^{-14} erg/cm²/s in the 0.3–2 keV band and a sky coverage of about 20 000 deg² will detect all collapsed objects within these limits. Figure 1.1 motivates the mission goal of 100 000 galaxy clusters up to a redshift of $z \leq 2$,

¹measure for the galaxy cluster distance, $z = \frac{\lambda_{\text{observed}} - \lambda_0}{\lambda_0}$

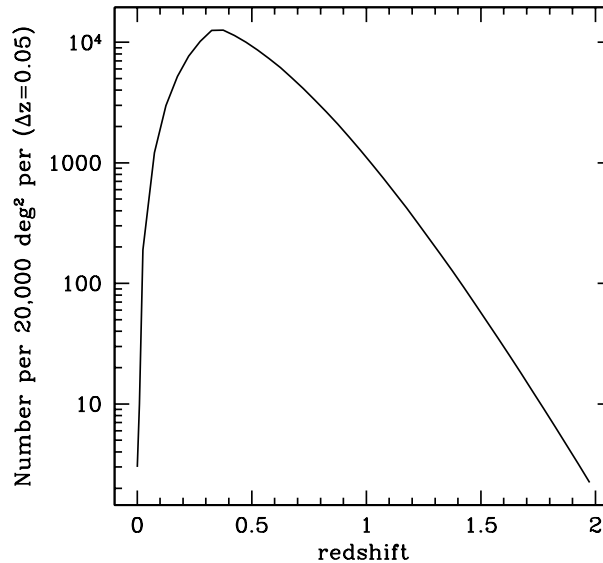


Figure 1.1: Number of galaxy clusters as a function of redshift in a survey with a flux limit of 2.3×10^{-14} erg/cm²/s (image credit to Haiman et al. (2005))

the full range where these objects are expected (Haiman et al. 2005). This number allows reliable constraints on the DE equation of state, since the X-ray luminosity of a galaxy cluster is tightly related to its mass (Reiprich et al. 2002). Therefore, observing a large amount of galaxy clusters at different redshifts provides a method to trace the evolution of the DE density with time.

Apart from this, one may learn about many other structures in the universe; for example active galactic nuclei (AGN), neutron stars, cataclysmic variables, black holes, supersoft sources, classical novae and gamma-ray bursts. In this respect eROSITA can be regarded as a multi-purpose instrument with a high discovery potential.

In comparison to previous and present missions, eROSITA has a higher spatial resolution and a higher grasp² and is therefore predestined for these tasks. A high angular resolution of 15 arcsec and a large grasp are required to detect galaxy clusters and to distinguish them from point sources. This puts high demands on the telescope design as described in the following section. Simulations done by Muehleger (2010) showed the feasibility of detecting the required amount of galaxy clusters with eROSITA.

²effective area times field of view

1.2 Instrument description

The origins of eROSITA can be found shortly after the failure of the ABRIXAS mission in 1999 (Predehl 1999). ABRIXAS was designed for scanning the X-ray sky in the range between 0.3 keV and 12 keV and therefore to expand the successful ROSAT mission to higher X-ray energies. Still convinced of the scientific benefits from an X-ray all-sky survey, the ROSITA mission was planned to be operated on the International Space Station (Predehl et al. 2003). Unfortunately contamination pre-tests showed the infeasibility of an X-ray mission within this environment (Friedrich et al. 2005). After another failed attempt to fly a copy of ROSITA on a NASA satellite, called DUO, negotiations of the DLR³ and Roscosmos, the German and Russian space agencies, were successful and the Spektrum-Röntgen-Gamma mission was reborn⁴. To gain more sensitivity in the low energy range where the strongest cluster emission occurs, the former mirror systems were expanded (this explains the "e" for "extended" in eROSITA). With originally four different instruments on board, now only eROSITA and the Russian Astronomical Röntgen Telescope (ART) are left on the Navigator platform (see figure 1.2).

The seven separate telescopes of eROSITA are arranged hexagonally within an optical bench made of CFRP⁵. Other components made of CFRP are the sun shield and the telescope cover. While the former screens incoming sunlight, the latter protects the sensitive optics and detectors during launch. A hexapod structure with three mounting points makes the complete instrument independent of spacecraft distortions, see figure 1.3.

Each of the seven telescopes consists of a mirror module with a focal length of 1.6 m and a CCD camera in its focus. Since X-ray photons can only be focused in grazing incidence, a special mirror geometry is required, namely a Wolter-I (named after its inventor Hans Wolter) with 54 nested paraboloid/hyperboloid electro-formed nickel shells. The reflecting area has a gold coating because the maximum angle for total reflection depends on the atomic number of the material.

Two different kinds of baffles, an X-ray baffle and an optical baffle, in front of each mirror system suppress certain X-ray photons and stray light (Friedrich et al. 2008). Optical light is undesirable in any case, and so are X-ray photons which are reflected

³Deutsches Zentrum für Luft- und Raumfahrt

⁴A first attempt to initiate a similar Russian-German collaboration was made in the nineties.

⁵Carbon fibre reinforced plastics

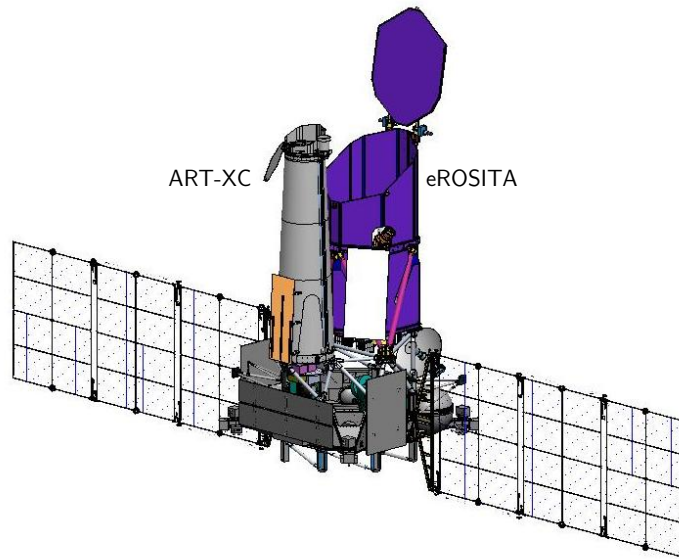


Figure 1.2: The Spektrum-Röntgen-Gamma mission (image credit to Lavochkin Association)

only once on the hyperbola. The photons finally are focused onto the detectors which are composed of a CCD plus read-out electronics.

The CCD size was increased from 256×256 pixels to 384×384 pixels in 2007 which also enlarged the field of view to $61.8'$ in diameter. Each CCD is equipped with a framestore area which acts as an image buffer and therefore allows for simultaneous photon collection and read-out. After illumination of the image area of the CCD, the charge is transferred within $120 \mu\text{s}$ into a framestore area. This reduces the probability for out-of-time events significantly. The read-out of the analogue CCD signals is done by three CAMEX⁶ chips per module, the data pre-processing happens outside the focal plane in the camera electronics box (for details refer to Meidinger et al. (2008)). Two telescope interface controllers (one nominal, one redundant) are regulating the thermal system and further control electronics.

The detectors are embedded in an aluminium casing and protected from proton radiation, which degrades the silicon CCD sensor, with a massive copper shielding. The electronics boxes are mounted directly on these proton shieldings (refer to figure 1.5). On the other side of the cameras a filter wheel allows for different filters to be rotated

⁶CMOS Amplifier and MultipLEXer

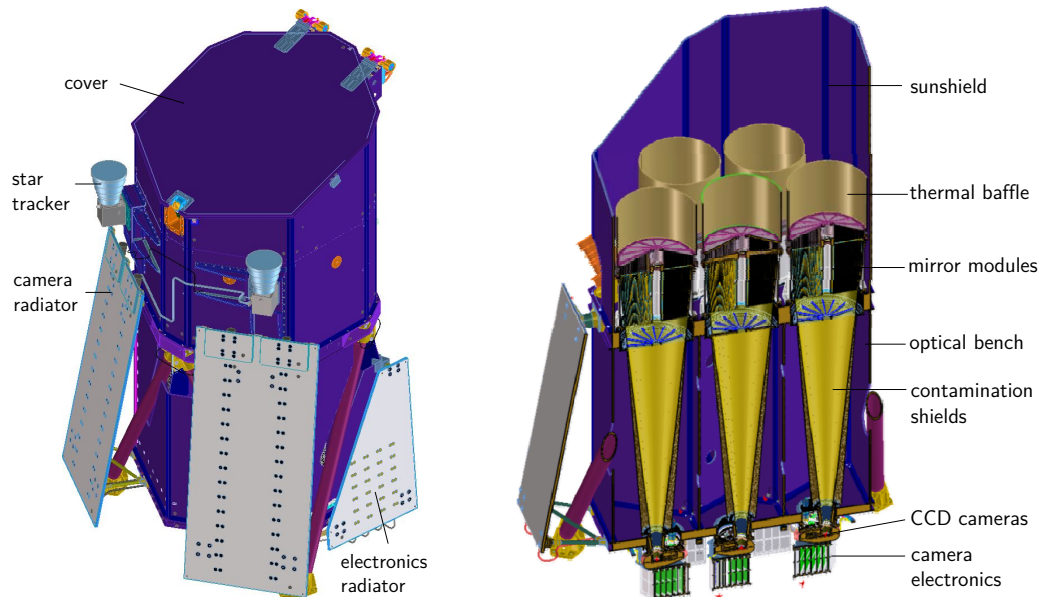


Figure 1.3: Overview over the eROSITA telescope

in front of the CCD, providing also a closed position for launch and calibration. The complete set-up, the so-called camera assembly, is mounted onto the lower platform of the optical bench. Four radiators in total remove the waste heat from the cameras and electronics, radiating it into space. These are connected by a system of heat pipes, which is discussed in chapter 3.

1.3 Boundary conditions for the thermal control system

Suitable boundary conditions are essential for optimal operation of the different subsystems. The telescope thermal control has to ensure that the temperatures of the components of the telescope structure and subsystems remain within the required limits.

The telescope structure with all components will be assembled inside a clean room at stable conditions of 293 K. Deviations from this temperature are known to cause a change in the focal length due to expansion or shrinking of the material. This

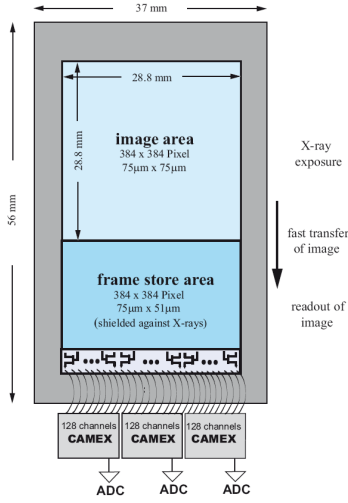


Figure 1.4: Scheme of the eROSITA CCD design, image taken from Meidinger et al. (2008)

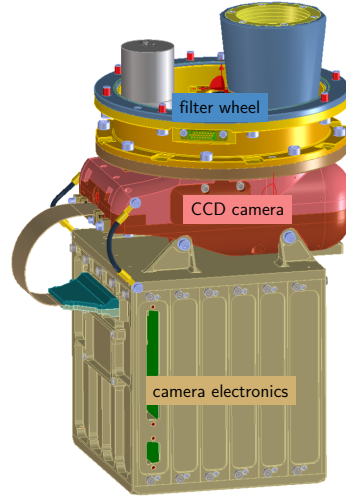


Figure 1.5: Camera assembly with the filter wheel, the CCD camera and the camera electronics

change must be smaller than 0.2 mm to stay within the error budget (Friedrich 2009). Otherwise the focus of the mirror modules would not be coincident with the plane of the CCD detectors. This results in a maximum allowed temperature gradient of about 77 K⁷. This condition will be fulfilled, because the design temperature for the complete telescope⁸ lies between 253 K and 313 K. This range has to be maintained because the thermal stress due to temperature gradients is much more critical than the change in the focal length. In addition, the interfaces of the different materials have to be considered; especially the spiders of the X-ray baffle and the mirror module, the complete camera cooling system, and the telescope cover mechanism.

Certain temperature limits have to be kept not only to guarantee mechanical stability but also to ensure a correct performance. A deviation of only few degrees causes a deformation of the mirror shells due to the different expansion coefficients of the shells and their support structure. These deformations would reduce the performance of the mirror system. Furthermore, temperature variations at the detector would require temperature dependent calibration efforts. The requirements of the most stringent subsystems are listed in table 1.1.

⁷ $\Delta T \leq \frac{\Delta l}{CTE \cdot l} = \frac{0.0002m}{1.98 \cdot 10^{-6} K^{-1} \cdot 1.3m} = 77 K$; with 1.3m length of the optical bench, and CTE the coefficient of thermal expansion of carbon fibre

⁸with exception of the cooling system

These requirements have to be guaranteed for all possible scenarios. The following main load cases are distinguished:

- Launch phase: cover closed, no power
- Commissioning phase: step-by-step startup of the instrument
- Survival phase: guaranteeing minimum requirements
- Operational phase: guaranteeing optimum working conditions

The main scope of this work is to ensure the fulfilment of all thermal requirements simultaneously without losing sight of the overall mission, including the environmental conditions and operating modes as well as the scientific aspects.

All subsystems are connected more or less by thermal conduction and/or radiation, and changes at one end of the telescope may influence components at the other end. Therefore, small models for quick estimations are useful, but the interaction among the various parts should not be underestimated. Especially radiation can have major unexpected effects. Reason for that is the fourth power of the Stefan-Boltzmann law. This is why the complete thermal model was used for all important decisions in the design phase of the project.

As a consequence, always complete thermal models have been used for calculating the performance of test set-ups and especially for the determination of the thermal behaviour of the complete telescope. This is also valid for future applications. In the end the main motivation is a successful mission. Special attention is paid to the thermal conditions, to guarantee the best possible boundary conditions for excellent data.

Table 1.1: Subsystem temperature requirements

subsystem	nominal operation [K]	survival case [K]
telescope structure	$253 \leq T \leq 313$	$243 \leq T \leq 343$
radiators	$143 \leq T \leq 163$	$143 \leq T \leq 323$
mirror shells	$291 \leq T \leq 295$	$273 \leq T \leq 313$
CCDs	$173 \leq T \leq 183$	$153 \leq T \leq 323$
camera electronics	$163 \leq T \leq 313$	$243 \leq T \leq 323$

2 The eROSITA camera thermal control

The subsystem with the most stringent thermal requirements is the camera thermal control system. Without sufficient and stable cooling of the eROSITA CCD cameras the whole mission is put at risk. While other subsystems as the telescope structure or the mirror systems at least partially can draw upon the experience of other missions, the cameras present a completely new challenge. The large number and configuration of the seven camera modules in combination with the low optimum working temperature is unique and requires new, special developments.

2.1 Requirements

The optimum operating temperature of the pn-CCD is between 183 K and 193 K with respect to radiation damage. Furthermore, the operational temperature variations must not be greater than 0.5 K.

At these temperatures, the effects of lattice defects are minimal. They are generated by high energy protons, mainly from the Sun but also cosmic rays. One aspect is the temperature dependent increase of dark current $DC(T)$ by thermal generation of electron-hole-pairs. These additional charge carriers cause a noise contribution $\sqrt{DC(T)}$, which decreases the energy resolution of the detector.

This dark current can be calculated with the Shockley-Read-Hall recombination-generation theory (Sze 2007) under the assumption of reasonable simplifications:

$$DC(T) \propto T^2 \cdot e^{\frac{-E_g}{2kT}} \quad (2.1)$$

with E_g the band gap of the semiconductor, k the Boltzmann constant and T the temperature. Results for different proton fluences are shown in figure 2.1. For the

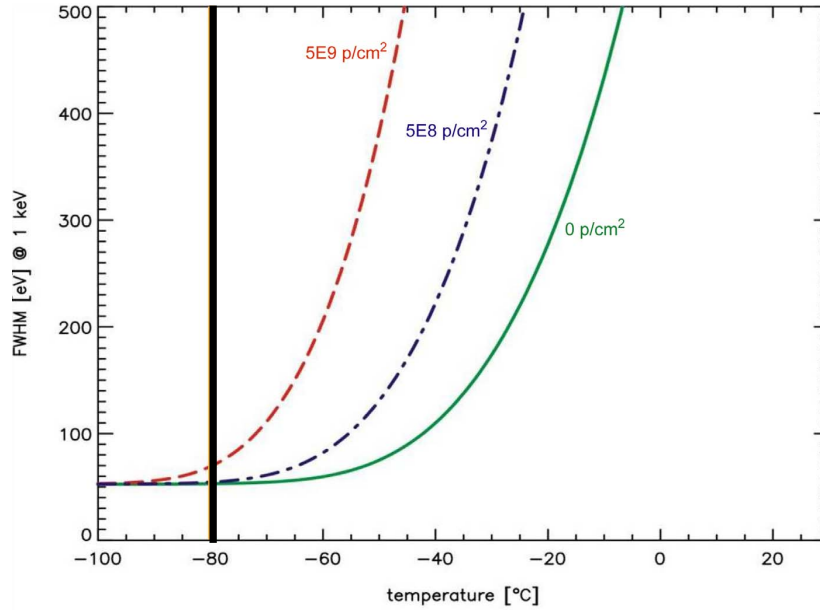


Figure 2.1: Temperature dependence of the CCD energy resolution at a photon energy of 1 keV, due to thermally generated dark current for different 10-MeV proton fluences. Calculated for a pixel size of 75 μm and a frame rate of 20 Hz. Taken from Meidinger (2009).

calculation of the relevant range an expedient shielding of the CCD modules made of 30 mm copper (or equivalent) has been assumed. It lowers the incoming proton fluence and therefore mitigates the consequences of the radiation damage.

Moreover, these high energy protons induce a degradation of the charge transfer efficiency. Electrons, generated by X-ray photons, may be trapped in lattice defects and decrease the energy resolution of the detector. In an (energy dependent) optimum temperature range the released electrons interfere least with the other charge carriers. But due to the superposition of the influence of different lattice defects, measurements are indispensable and cannot be replaced by corresponding calculations. In figure 2.2 the test results for two different energies and proton fluences are shown.

While the dark current already is sufficiently suppressed below 193 K, the lowest charge transfer efficiency degradation for simultaneously low and high energies is between 183 K and 173 K. So the latter constrains the optimum working temperature for the CCDs.

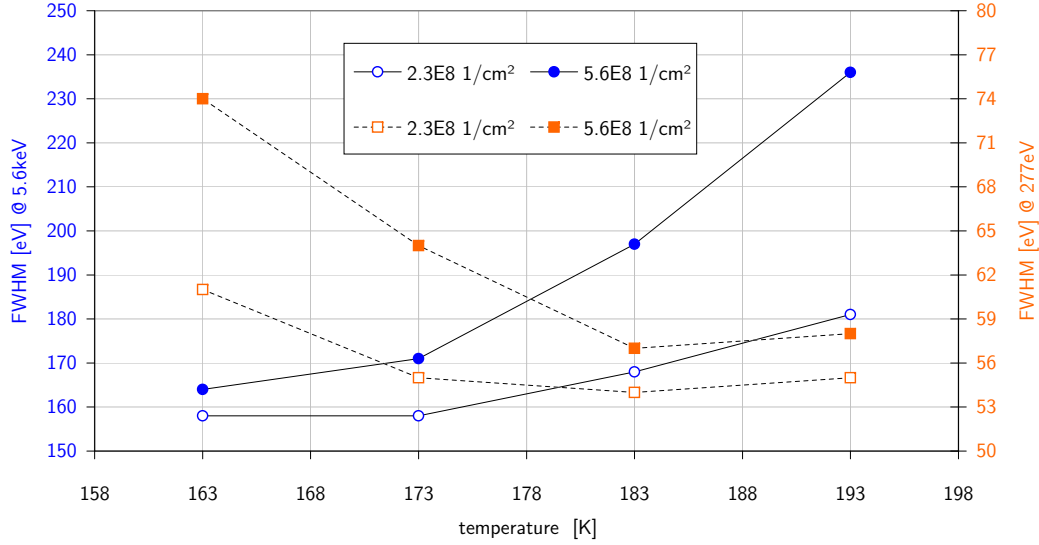


Figure 2.2: Temperature dependence of the CCD energy resolution due to electron trapping after a proton irradiation of $2.3 \times 10^8 \text{ cm}^{-2}$ (which corresponds to the equivalent eROSITA proton fluence of $2.5 \times 10^8 \text{ cm}^{-2}$ after 7 years of mission), and $5.6 \times 10^8 \text{ cm}^{-2}$ for comparison. Values from Meidinger et al. (2010).

2.2 Thermal environment

Spektrum-Röntgen-Gamma will be operated at the Lagrange point 2 which is 1.5 Mio. km away from the Earth, in anti-Sun direction. A detailed description of the mission scenario can be found in chapter 6. This place guarantees stable thermal conditions without mentionable influence due to thermal radiation of the Earth or albedo radiation. The only relevant parameters are the space temperature¹ of 2.7 K and the solar irradiance with a value of

$$E_{s,L_2} = 1367 \text{ W m}^{-2} \cdot \frac{(150 \times 10^6 \text{ km})^2}{((150+1.5) \times 10^6 \text{ km})^2} = 1340 \text{ W m}^{-2} \quad (2.2)$$

using the solar constant of 1367 W m^{-2} and the Sun-Earth-distance of $150 \times 10^6 \text{ km}$. These boundary conditions the satellite will be exposed to are stable but extreme. And since always the same side of the telescope will point towards the Sun in the nominal

¹Temperature of the cosmic microwave background black body spectrum (Fixsen 2009)

operation mode, the temperature gradients between the Sun side and the deep space side require an elaborated thermal control system of the complete telescope which is presented in chapter 5. For cooling purposes, however, this is a big advantage because the cooling capacity is constant during the mission.

2.3 Design

The CCD detectors are cooled passively with a system of different heat pipes and two radiators. Means of active cooling would contain the risk of movable parts, high wasted heat or mission limiting consumables, depending on the specific design.

Radiator area

Passive cooling in this temperature range on the other hand is difficult with the thermal emission being very low because of the T^4 -dependence of the Stefan Boltzmann law (appendix A.21). This is the reason why for a constant payload power it is rather easy to cool about 100 K from room temperature with a radiator with only 0.6 m^2 . But even without considering parasitics, twice the area only causes a further temperature drop of about 25 K (figure 2.3).

The lower the temperature, the greater is the influence of parasitic heat loads since parasitics go linear with temperature. Possible sources of parasitics are radiation and conduction through the back side insulation, radiation on the front side and conduction through the mounting brackets. None of them may be avoided completely but they have to be reduced as far as possible. Assuming only radiation onto the radiator backside, attenuated by multi-layer insulation (refer to section 5.1), already increases the saturation temperature significantly.

Only the instrument's side opposite of the Sun is suitable for the radiator attachment. Otherwise solar radiation and parasitics from the solar panels would increase the temperature. A tilt of the radiator panels minimizes the influence of the spacecraft. Due to mechanical reasons it is not possible to put both radiators completely into the telescope's shadow, so at least some parts of the back side are illuminated by the Sun anyway.

The real power consumption of the eROSITA detectors is only 0.75 W per detector and therefore almost negligible. The main part of the heat load onto the radiator are

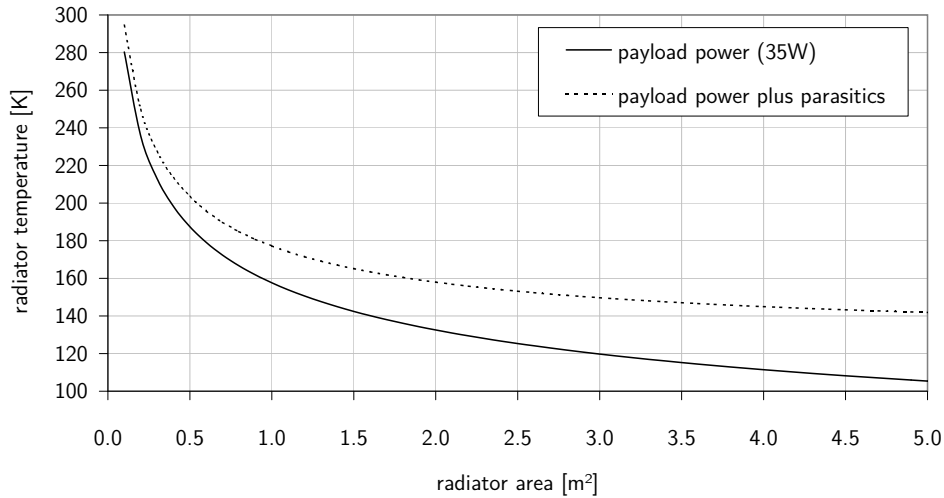


Figure 2.3: Radiator temperature against radiator area with $\epsilon = 0.82$ and a power input of $P=35$ W. This corresponds to the total predicted thermal load of the cooling system. Parasitics on the radiator are, respectively, ignored and assumed to result from radiation through multi-layer insulation on the radiator rear side with an outer layer temperature of 293 K and $\epsilon_{eff} = 0.03$. Refer to section 5.1 for details.

parasitics such as conduction through attachments and radiative loads. To fulfil the eROSITA CCD temperature requirements, we need a radiator temperature of about 160 K and therefore about 2 m² of radiator area.

Due to mechanical reasons, eROSITA has two radiators with 1.2 m² each. They consist of a 20 mm aluminium honeycomb structure with two face sheets of 1 mm thickness. On the backside additional honeycomb elements guarantee extra stability. They are thermally decoupled from the telescope with GFRP²-struts. The surface facing deep space is coated with a high emissivity white paint³. Black paint would also work for the normal operation mode because the front side of the radiators point in an anti-Sun direction. But the white paint with a low solar absorptivity guarantees a moderate temperature of the camera cooling system even in worst-case scenarios with direct Sun irradiation whereas a black radiator then easily could reach more than 370 K. This would exceed the acceptable temperature range of the cooling chain components (table 1.1).

²Glass fibre reinforced plastics, very low thermal conductivity

³MAP SG 121FD

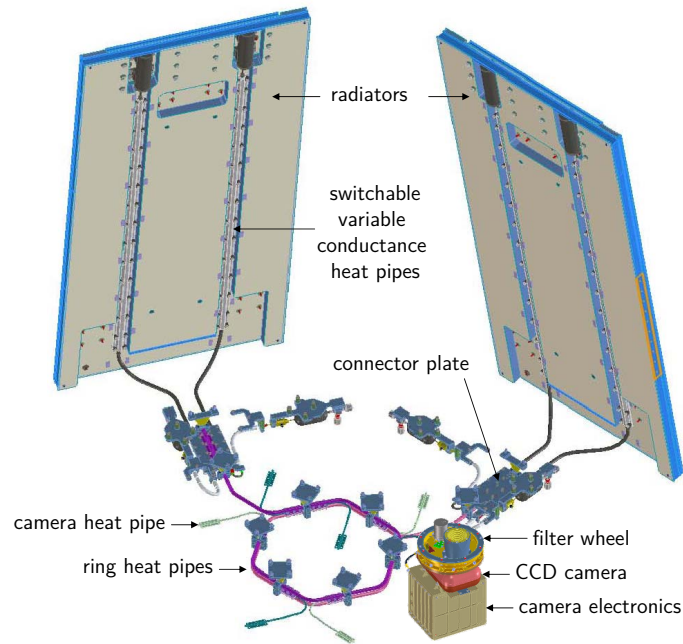


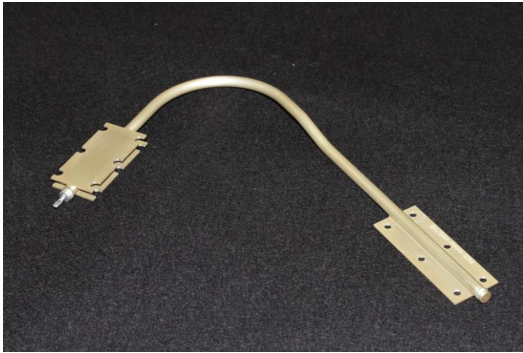
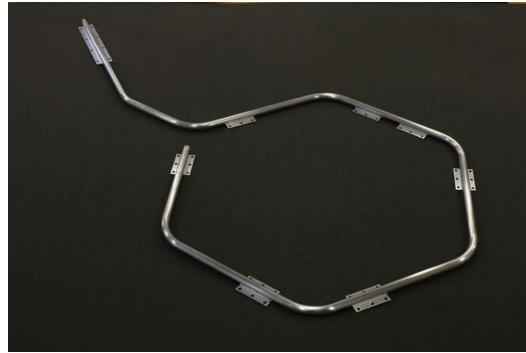
Figure 2.4: Design of the camera cooling

Camera module configuration

The rather high parasitics have their origin not only in the large required radiator area but also in the configuration of the camera modules. Every telescope has its own camera, so all in all seven CCDs have to be cooled (see figure 2.4). Due to their location at the bottom of the telescope, the most obvious cooling strategy with the shortest pathways would include a radiator nearby all cameras simultaneously. But because of the mounting of the instrument, this radiator would point towards the spacecraft. Firstly, this would violate the requirement of thermal decoupling and secondly, this would not provide enough cooling power.

The necessity of a long cooling chain because of seven independent cameras inside the telescope is a big disadvantage compared to other passive cooled projects with short distances and therefore minimum parasitics, for example XMM-Newton (Stramaccioni et al. 2000).

An ideal means of heat transport are heat pipes. Heat pipes are a very effective way for carrying heat loads over large distances with a small temperature gradient. They consist of tubes, containing a working fluid, and make use of the latent heat of

**Figure 2.5:** Camera HP**Figure 2.6:** Ring HP

vaporization. An explanation of the working principle of heat pipes, the underlying physics as well as a description of the eROSITA heat pipes including test results can be found in chapter 3.

Heat pipe chain

Since the detectors are embedded inside a massive proton shielding (see figure 2.9), it is not possible to have a single heat pipe between a CCD and the radiator due to handling and integration purposes. The cooling interface of each camera module has to be compact and easily accessible, so a small heat pipe is attached to each detector during assembly of the camera module (figure 2.5).

Two ring-shaped heat pipes or "ring heat pipes" (one for each radiator, figure 2.6) collect the heat of all cameras. Each camera heat pipe is directly attached to both of them by a sandwich construction for redundancy reasons. A second interconnection between these ring heat pipes and the radiators is necessary, again because of handling and integration.

The ring heat pipes are mounted onto two different connector plates, each connected with one radiator by means of two switchable variable conductance heat pipes (sVCHP), which provide a controllable connection between these plates and the radiators. Tests have shown that additional thermal fillers such as indium or thermal grease are obsolete at such low heat flows (section 4.3).

Both the camera and ring heat pipes consist of an extruded aluminium profile, filled with ethane. For details of the heat pipe design and manufacturing refer to chapter 3.

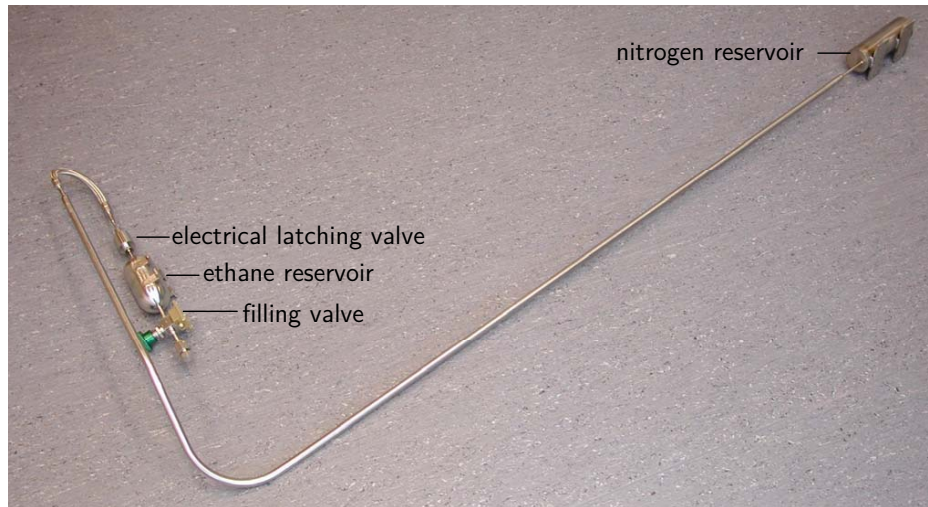


Figure 2.7: Switchable variable conductance heat pipe (sVCHP)

The sVCHPs (figure 2.7) are made of stainless steel tubes and are also filled with ethane, using a stainless steel mesh for capillarity. Another heat pipe concept has to be used because of two different reasons:

- Within the first weeks of the mission the heat pipes shall transport no power to the radiators to keep the CCDs warm. This should prevent condensation or icing of materials on the CCDs, outgassed by different telescope components in the beginning.
- During the whole mission the CCD temperatures have to be kept very stable with variations ≤ 0.5 K, despite partially different illuminated radiators and other irregularities.

To solve the first problem, the ring heat pipes have to be disconnected from the radiator temporarily. Survival heaters are not an option because of the large radiator area. As every watt affects the radiator temperature at low temperatures, about 500 W in total would be necessary to keep them above 273 K. Because this amount of power is not available, especially not in the early phase of the mission, a switchable connection to the radiator is required. The only way to completely prevent a heat pipe from working under zero gravity, is to remove or freeze the working fluid. Freezing is not possible – among other things – because of the ethane melting point of 90 K. Therefore we added an ethane reservoir at the camera-end with an electrical latching valve in

between (refer to figure 2.7 and figure 2.8). The ethane is enclosed until cooling power is required.

In order to guarantee the temperature stability, we decided to keep the sVCHPs we developed for the operation in a Low Earth Orbit (Fürmetz et al. 2008) rather than just regulate the temperature with heaters. For an effective control, heaters have to be placed close to the CCDs, best at the aluminium casing. But because of the very limited space, the input leads could cause a thermal coupling between the warm proton shield and the cold casing. This happened during the first thermal balance test with the camera head due to a pinched temperature sensor. And even if attaching them to the connector plate between ring HPs and sVCHPs, we still would have to use the highest occurring temperature (plus margin) as the control temperature.

Changing the conductivity of the HP to the radiator with a minimum heat load provides an effective method to regulate the CCD temperature without increasing the radiator temperature. Besides ethane as working fluid the sVCHPs also contain gaseous nitrogen (gN_2) which cannot condense⁴ in the relevant temperature range ($T \geq 140$ K). Depending on the location of the gN_2 , some parts of the sVCHP are blocked and prevent the ethane from evaporation or condensation, see figure 2.8.

At the radiator end of the sVCHPs is a nonwicked reservoir for gN_2 (see section 3.1.5). In normal operation the nitrogen is inside this reservoir and does not participate in the heat pipe functionality. Therefore the amount of nitrogen precisely has to be adjusted to the working temperature as described in section 3.1.5.

As soon as the reservoir is heated by means of attached foil heaters, the partial pressure of the nitrogen rises and the pressure equilibrium is shifted towards a higher nitrogen volume. As a consequence parts of the condenser are blocked. For an effective temperature change of the reservoir without interfering in the radiator heat balance, thermally decoupled reservoir radiators are required. This is realized by thermally decoupled but mechanically embedded parts of the radiator to which the reservoirs are attached. Only a very small heater power (1–2 W) is required to control for example the connector plate temperatures, which provides stable conditions for all seven cameras.

Before the ethane is ejected into the heat pipe, the nitrogen fills out the tube completely. After opening of the valve, the nitrogen and the ethane get mixed, which takes about 15–30 minutes for both to segregate. The circulation of the ethane forces

⁴triple point at $T = 126$ K and $p = 33$ bar

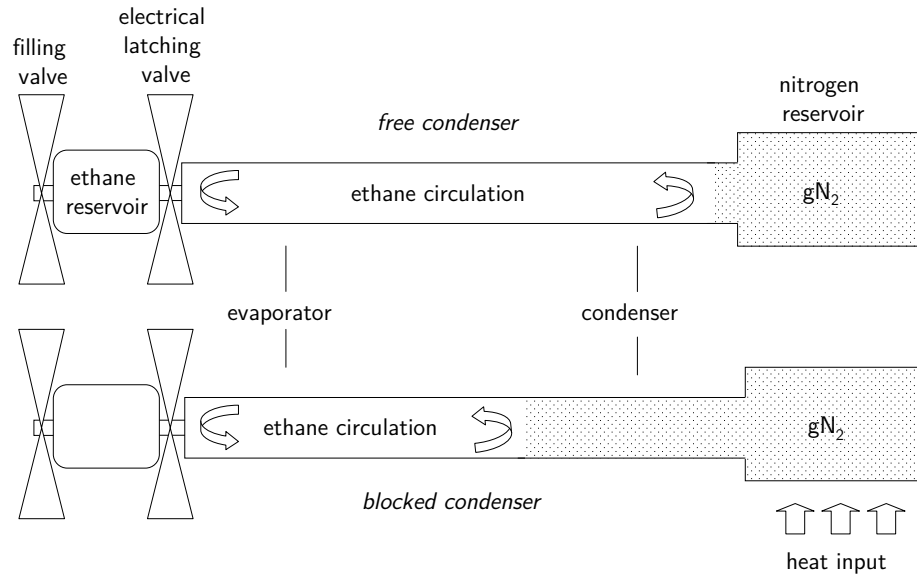


Figure 2.8: Working principle of a VCHP. The upper sketch shows the nominal operation with almost the complete nitrogen inside the reservoir. The lower sketch shows the effect of a heated reservoir when the nitrogen blocks the condenser.

the nitrogen into the reservoir during HP operation. By controlling the reservoir temperature with heaters we can control the heat transfer coefficient and so the CCD temperature very accurately (see section 4.3).

Ethane heat pipes with both aluminium and stainless steel containers are space proofed under long-term conditions (McIntosh et al. 1993) and common for low temperature applications.

Camera module design

A critical part of the camera head thermal design is the attachment of the cold detector casing. Since the proton shielding consists of more than 10 kg of copper – which is necessary to reduce the proton fluence to an acceptable level – it is not possible to decouple it thermally. Therefore cooling of this massive shielding on the one hand would require way too much cooling power and on the other hand would cool down large parts of the telescope. So the aim is keeping the cold part as small and lightweight as possible for an easier decoupling. This is realized by the aluminium detector casing

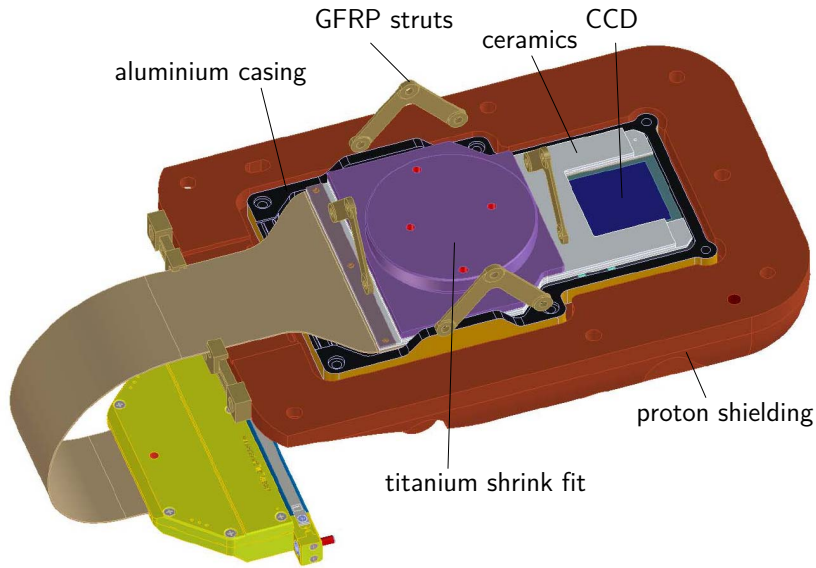


Figure 2.9: Configuration of the camera module with the proton shielding and the thermally decoupled aluminium detector casing

being attached to the proton shielding by means of GFRP-struts (see figure 2.9). Between the aluminium casing and the detector module (ceramics, read-out electronics and CCD) a titanium shrink fit provides the thermal connection.

Radiative couplings can be influenced only by suitable surface properties which we realised by gold coating of the proton shield and the outer surface of the aluminium casing, the most effective method to get a low emissivity. Because of contamination issues a multilayer insulation cannot be considered. The inner side of the aluminium casing is black (Kepla coat) for preventing stray light reaching the CCD. The active heat load of about 0.75 W is produced by the CAMEX, the part of the read-out electronics that performs the amplification and shaping of the CCD signals.

3 Heat pipes

Heat pipes are one of the most effective ways of heat transport, especially in the absence of conductivity. Using the latent heat of evaporation, heat pipes can transport large amounts of excess heat over considerable distances with simultaneously small temperature differences. Space-saving, completely passive and maintenance free, they are ideal for space applications and belong meanwhile to the basic equipment of a satellite's thermal control system. First patented by Gaugler of General Motors in 1944, it took two decades until the principle was discovered independently by Grover et al. (1964) from the Los Alamos Scientific Laboratory and before this idea was finally appreciated.

Consisting of metal tubes with diameters of typically a few mm and an interior capillary wick (figure 3.1), they contain a working fluid sealed at saturation conditions. This means the pressure of the liquid and vapour phase of the working fluid are in equilibrium. This resulting inside pressure is temperature dependent and determined by the fluid's vapour pressure curve. The coexistence of the liquid and vapour phase is indispensable for heat pipe functionality and limits the working temperature.

However, more advanced versions of heat pipes contain a control mechanism (for example electrical heaters) to adjust the heat transfer capability. Those features make

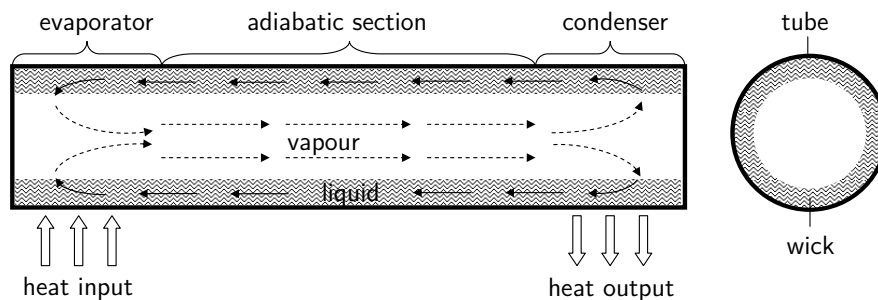


Figure 3.1: Working principle of a heat pipe

them a powerful means for very effective heat transport and temperature control, exceeding the capability of conventional conduction or convection methods.

3.1 Underlying physical concepts

Basic characteristics of a heat pipe are the power transport capability and the resulting temperature gradients. The mathematical model of a heat pipe contains several different approaches. Heat input and output depend on the conductivity of the tube as well as the wick. Fluid dynamics describe the heat transport from the evaporator to the condenser, driven by capillary force. In the next sections expressions for the relevant phenomena are motivated and derived.

3.1.1 Functional principle

Heat application on one end, referred in the following as the *evaporator*, vaporizes the working fluid which causes a rise in the vapour pressure p_v . That drives the vapour to the cooler end where it condenses into the wick structure. Thus this region where the heat is released is called the *condenser*. The liquid loss at the evaporator in turn forms highly curved menisci which leads to a capillary pressure that forces the condensate back and the process starts again. Being almost negligible at the condenser, the menisci radii and capillary force change over the heat pipe. This change in capillarity is the driving force within a heat pipe. The area between evaporator and condenser is referred to as the *adiabatic (transport) section*. Depending on the heat pipe configuration, this division may be altered by having for example several heat sources and therefore several evaporators or also several condensers.

The transport process takes place as long as the capillary pressure inside the wick is sufficient to drive enough condensate back to keep the evaporator saturated. Besides the intrinsic wick geometry, gravity can be one of the reasons for the heat pipe reaching capillary limit (section 3.1.3). Too much heat input or inappropriate temperatures will disrupt the functionality of the heat pipe by reaching the sonic, boiling or entrainment limit (see section 3.1.4). A comprehensive collection of heat transfer limitations can be found in chapter 4 of Faghri (1995). Since in space gravity is not an issue, the cooling system guarantees appropriate temperature ranges and we have low or moderate heat inputs and flow rates, we will mainly focus on the maximum heat input in terms of

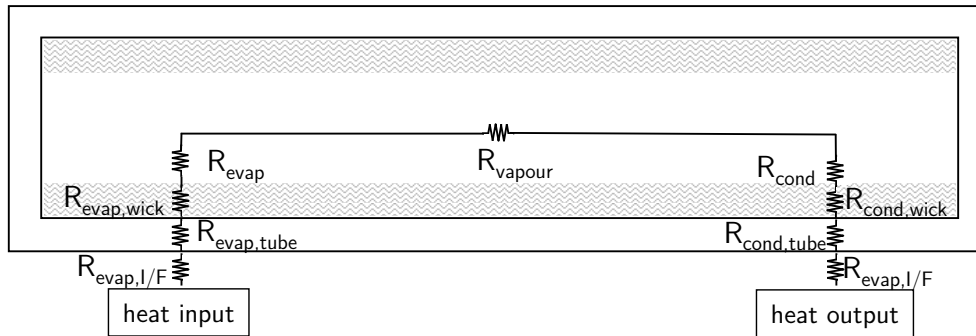


Figure 3.2: Different resistances inside a heat pipe that determine the overall heat transfer coefficient. Axial resistances of wick and tube are neglected since they are several orders of magnitude larger than the radial ones.

the capillary limit. Nevertheless we will derive corresponding formulas for the other possibly relevant limits and consider them for the eROSITA heat pipe design.

The overall heat transfer coefficient of a heat pipe consists of the source-evaporator interface resistance, the transition between the evaporator wall and the vapour, the heat transfer between the evaporator and condenser, condenser and condenser wall and finally the resistance to the heat sink, see figure 3.2. Interface values of the source and the sink are dependent on the attachment. A reasonable assumption for the heat transfer coefficient¹ of screwed connections is about 1500 W m^{-2} , see Hermann et al. (1976). Thermal fillers can be used to increase this value, especially for rather high heat fluxes. For metal tubes and non-metal working fluids, the tube resistance can be neglected in most cases as stated in Hermann et al. (1976), while the effective conductivity of the saturated wick determines the local temperature gradients of evaporator and condenser.

For the global temperature gradient mainly these transitions are responsible. Depending on the exact wick geometry and the working fluid properties, sometimes the resistance of the liquid layer may limit the evaporation process. But this mainly affects very low temperature heat pipes (Faghri (1995, pp. 82–87)). The vapour itself is assumed to have a more or less constant temperature throughout the pipe.

Therefore a simplified heat pipe thermal model consists of only two or three nodes:

¹reciprocal thermal resistance

the evaporator, (the vapour) and the condenser, refer to section 4.2. For the design it is critical that a continuous vapour and liquid flow is guaranteed and the evaporation and condensation processes are not constrained. For the overall thermal performance, however, the final temperature gradient is also of importance. In the following sections formulas for all relevant transitions are derived before the concrete technical implementation and tests of the eROSITA heat pipes are discussed.

3.1.2 Heat transfer coefficients at evaporator and condenser

The radial heat transfer Q , $[Q] = W$, at a cylindrical evaporator and condenser with length L , outer tube diameter D_a and inner diameter D_i can be calculated with (compare to equation (A.4))

$$\frac{\partial T}{\partial r} = \frac{Q}{-k_{eff}A(r)} = \frac{Q}{-k_{eff}2\pi rL} \quad (3.1)$$

after integration over r :

$$T(r) = T_v - \frac{Q}{-k_{eff}2\pi L} \cdot \ln \frac{r}{D_i} \quad (3.2)$$

$$T(D_a) = T_w = T_v - \frac{Q}{-k_{eff}2\pi L} \cdot \ln \frac{D_a}{D_i} \quad (3.3)$$

solving for Q then yields:

$$Q = HTC \cdot \Delta T \quad (3.4)$$

with

$$HTC = k_{eff} \cdot \frac{2\pi L}{\ln(D_a/D_i)} \quad (3.5)$$

where T_v is the temperature of the vapour at the liquid-vapour interface, T_w the wall temperature and k_{eff} the total effective conductivity of the wick structure, including tube wall, wick and liquid within the wick. As stated above, we often can neglect the contribution of the wall and concentrate on the effective wick conductivity k_{eff} ,

$D_a - D_i$ being only the wick thickness. In either case the wall conductivity has to be compared to the wick conductivity before being neglected. If required, we have a serial connection of wall and wick conductivity. $HTC = \frac{Q}{\Delta T}$ is the resulting local heat transfer coefficient.

Heat transport within the wick

In conventional heat pipes a wick at the inner side of the tube wall is responsible for the capillary force. The most common wick types are grooves, metal meshes or sinter materials. These wicks contribute to the radial thermal resistance between the heat source and the liquid-vapour interface where evaporation occurs. The *effective radial conductivity* of the wick is important for the design, for example it dictates the maximum wick thickness. It depends on the corresponding values for the wick k_w and the working fluid k_l and is their volume-weighted arithmetic mean, assuming the upper limit of k_{eff} with a pure parallel connection:

$$k_{eff} = \varphi k_l + (1 - \varphi)k_w \quad (3.6)$$

where φ is the *porosity*, defined as the ratio between the pore volume and the total volume of the wick. Values for the porosity of certain wick structures can be found in table 3.1.

If we have to consider a serial connection, we get for k_{eff} with the volume-weighted harmonic mean:

$$k_{eff} = \frac{1}{\frac{\varphi}{k_l} + \frac{1-\varphi}{k_w}} = \frac{k_l k_w}{\varphi k_w + (1 - \varphi)k_l} \quad (3.7)$$

In reality the effective conductivity often contains contributions of both parallel and serial connections, depending on the wick geometry. The porosity determination for common heat pipe wick structures can be found in table 3.1.

Grooved heat pipes Grooved heat pipes have different values for the conductivity of the evaporator and condenser region. At the evaporator mostly the transition between fins and liquid contributes to the conductivity (because of very concave menisci), whereas at the condenser the complete surface is available (refer to figure 3.3).

For the latter a pure parallel connection of grooves and liquid as in equation (3.6) is a reasonable approximation. We need (1) the path through the liquid in the channels and (2) the path through the fins. Thus we get for the effective heat transfer coefficient at the condenser (refer to equation (3.6)):

$$k_{eff,cond} = \varphi k_1 + (1 - \varphi)k_2 = \varphi k_l + (1 - \varphi)k_w \quad (3.8)$$

At the evaporator the path of the heat flux is more complex and besides the (1) path through the liquid in the channels, we (2) have to take into account not only the heat transfer through the fins but also through a thin liquid film with thickness δ at the transition region. For rectangular grooves with a width W , distance S and depth D ($\delta \ll D$), this leads to the following expression for the effective conductivity (which also can be used for trapezoidal and circular grooves as a first approximation (Faghri 1995)):

$$\begin{aligned} k_{eff,evap} &= \varphi k_1 + (1 - \varphi)k_2 \\ &= \varphi k_l + (1 - \varphi) \left(\frac{k_w k_l D}{0.185 k_w (S - W) + k_l D} \right) \end{aligned} \quad (3.9)$$

k_2 consists of a serial connection of the fin contribution as well as the contribution of the liquid film $k_2 = \frac{k_l D}{0.185(S-W)}$, where the factor of 0.185 accounts for the complex path through the fin and the liquid (from Chi 1976).

Mesh wicks An approach for the effective conductivity of metal mesh wicks was first done by Rayleigh (1892) and this formula is still common usage for heat pipe mesh calculations:

$$k_{eff} = \frac{k_l [(k_l + k_w) - (1 - \varphi)(k_l - k_w)]}{(k_l + k_w) + (1 - \varphi)(k_l - k_w)} \quad (3.10)$$

Corresponding values for the porosity again may be found in table 3.1.

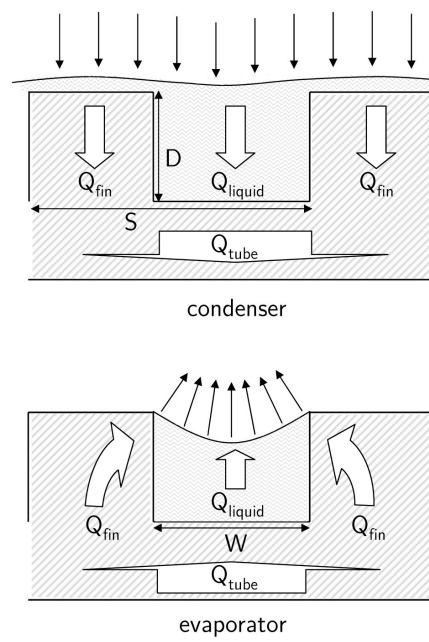


Figure 3.3: Conductive heat transfer at evaporator and condenser for rectangular grooved heat pipes

3.1.3 Capillary limit and heat transport factor

Several phenomena can be responsible for limiting the heat transport capability of heat pipes, depending on the temperature range and heat load. Most commonly encountered at rather low temperatures is the capillary limit which will be described hereafter. Other phenomena are discussed in section 3.1.4.

Surface tension and capillary force

Surface tension² and capillary force appear in boundary layers between a liquid and another medium due to a force imbalance at the interface. Besides the popular examples of water drops in air or gas bubbles in water, this other medium also can be the liquid's own vapour.

According to Batchelor (2000), a boundary between two media in equilibrium is the seat of a special form of energy. Its amount is proportional to the interface area. The surface dependent expression makes a contribution of σA to the free energy³ of the system. Work δW done on the system directly increases the amount of total free energy and – if temperature, volume and density are held constant – can be described by σdA . This means, only the surface A of the system is changed and σ can be interpreted as a surface free energy or – specific for liquids – surface tension which is caused by intermolecular cohesive forces:

$$\sigma = \left(\frac{\partial F}{\partial A} \right)_{V,T,N} \quad (3.11)$$

Assuming a liquid surrounded by vapour, the force exerted by the surface tension directs into the liquid (provided that the liquid density exceeds the vapour density). Trying to minimize its surface, we obtain a liquid sphere and in equilibrium we can equalise the energy required to displace the surface and the work to generate the necessary pressure difference to get the relation between the curvature, the surface tension and the pressure difference Δp at the boundary:

²If no liquid is involved, the correct terminology is surface energy, otherwise both expressions are synonymous.

³ $F = H - TS$, $dF = -pdV - SdT + \mu dN + \sigma dA$ is minimal for a canonical system with $V, T, N = const$

$$\begin{aligned}
 dF &= \delta W & (3.12) \\
 \sigma dA &= \Delta p dV \\
 \sigma \cdot 8\pi r dr &= \Delta p \cdot 4\pi r^2 dr \\
 2\sigma &= \Delta p \cdot r \\
 p_{cap} = \Delta p &= \frac{2\sigma}{r} & (3.13)
 \end{aligned}$$

For a more general curved interface with r_1 and r_2 as the principal radii of curvature, the resulting pressure difference across the fluid interface can be derived as shown in Faghri (1995, pp. 66–67):

$$p_{cap} = \Delta p = \sigma \left(\frac{1}{r_1} + \frac{1}{r_2} \right) \quad (3.14)$$

This equation is known as the *Young-Laplace equation* and was discovered independently by Thomas Young and Pierre-Simon Laplace in 1805. It is the fundamental equation for capillary pressure.

In sufficiently narrow capillaries with radius r it is $r_1 = r_2 = d = \frac{r}{\cos\theta}$ and the capillary pressure yields to (refer to figure 3.4):

$$p_{cap} = \Delta p = p_v - p_l = \sigma \cdot \frac{2}{r} = \frac{2\sigma}{d} \cdot \cos\theta \quad (3.15)$$

with $\Delta p = p_v - p_l$ the pressure difference of the vapour and liquid phase and θ the contact or wetting angle. θ is only determined by the physical properties of the capillary tube, the liquid and its vapour – in general the three contacting media solid (s), liquid (l) and vapour (v). This gives us three surface tension forces which act tangentially along the contact surfaces (figure 3.4). The contact angle always is measured through the liquid. In equilibrium, all three forces have to be balanced (Young’s equation):

$$\sigma_{s,v} = \sigma_{s,l} + \sigma_{l,v} \cos\theta \quad (3.16)$$

If using the height a liquid rises inside a capillary, we directly can determine θ by equalizing the capillary and hydrostatic pressure:

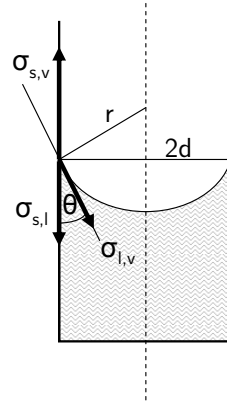


Figure 3.4: Schematic of the capillary force inside a small tube

$$\begin{aligned}
 p_{cap} &= p_{hydr} \\
 \frac{2\sigma}{d} \cdot \cos\theta &= (\rho_l - \rho_v)gh \\
 \cos\theta &= \frac{hd(\rho_l - \rho_v)g}{2\sigma}
 \end{aligned} \tag{3.17}$$

Besides the fluid properties (surface tension and density) and the capillary radius itself, the wetting angle plays an important role in the final value for the capillary pressure. Only wetting fluids with $\theta \leq 90^\circ$ are suitable for use in heat pipes.

Pressure gradients and capillary pressure

The capillary limit manifests itself in a dry-out of the wick structure at the evaporator when more liquid is vaporized than supplied by the wick structure. This happens when the necessary interface pressure exceeds the available capillary pressure that can be provided by the wick-fluid-system.

If the pressure difference $p_v - p_l$ at the evaporator and condenser interface is only balanced by the surface tension, the condition for the capillary limit is

$$p_{cap,max} = \Delta p_{max} = (p_v - p_l)_{max} \tag{3.18}$$

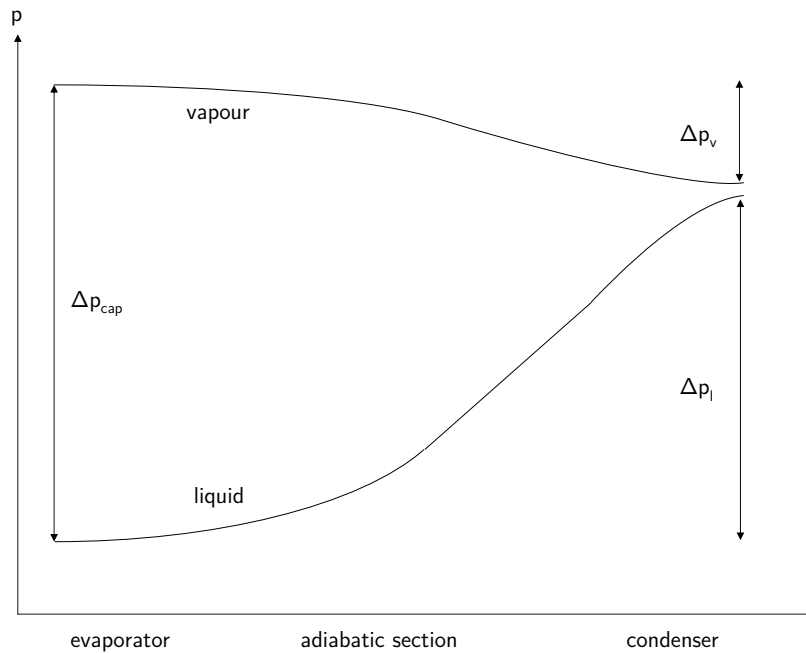


Figure 3.5: Partial pressures inside a heat pipe

Generally, the pressure loss due to phase transition, gravity and other forces has to be taken into account in addition, depending on the specific geometry and boundary conditions. However, equation (3.18) provides an upper limit for the pressure difference or a minimum value for the required capillarity, respectively.

During the evaporation process the increase in vapour pressure p_v makes the liquid recede into the wick structure. Concave menisci occur (or increase) and induce the capillary pressure $p_{cap,evap} = p_{cap,max}$ as derived in equation (3.14), which acts against the surface tension forces and points towards the vapour. A change in the curvatures along the heat pipe causes a pressure difference between evaporator and condenser. This acts as driving force for working fluid circulation. The vapour is driven towards the condenser where the pressure difference approaches zero at the capillary limit. Therefore we have $\Delta p_{cap,cond} = 0$ which implies flat menisci. Just enough liquid is returned to the wick structure and driven towards the evaporator to keep it saturated.

The liquid pressure p_l increases from the evaporator to the condenser whereas the vapour pressure p_v drops as shown in figure 3.5. Reasons for this change are mostly friction for the liquid; for the vapour, inertia, blowing and suction effects make a

contribution in addition (Faghri 1995, p. 4). As a consequence, the maximum local pressure difference occurs in the evaporator region. For the capillary limit, this pressure needs to be equal to the sum of the vapour and liquid pressure drops along the heat pipe. Figure 3.5 shows the decreasing vapour pressure and the increasing liquid pressure. So both contributions have a different sign. To denote the evaporator end with $x = 0$ and the condenser end with $x = L$, L being the total length of the heat pipe, we can find the integrated version for the capillary pressure:

$$p_{cap,max} = - \int_0^L \frac{dp}{dx} dx = - \int_0^L \left(\frac{dp_v}{dx} - \frac{dp_l}{dx} \right) dx \quad (3.19)$$

To replace the left side of equation (3.19), we have to rewrite the Young-Laplace equation (3.14). Ideally a heat pipe has a relatively small pore radius at the liquid-vapour interface for a high capillary pressure and larger curvatures within the wick for a preferably unrestricted liquid flow. For that reason, heat pipes with special requirements can have composite wicks for a high capillary limit *and* large heat transfer values.

Common wick geometries are circular, rectangular or trapezoidal grooves, or mesh wicks. More specific wick types are sintered materials or composites. The maximum capillary pressure in grooves depends on the wetting angle as shown above. Mesh screens in contrast belong to a class of wick structures where the maximum capillary pressure rather corresponds to the coalescence of adjacent menisci. The Young-Laplace equation therefore gives:

$$p_{cap,max} = \frac{2\sigma}{r_{eff}} \cdot \cos\theta \quad (3.20)$$

with the r_{eff} being the wick's effective pore radius (refer to figure 3.6).

Replacing the right hand side of equation (3.19) necessitates finding an expression for the pressure gradient. With the *Darcy-Weisbach equation*, which relates the friction-based pressure loss in a pipe to the kinetic energy, we may write the vapour pressure gradient as a function of the fluid velocity (if we considered the influence of gravity with a tilt angle θ , we would have to add the term $\rho_v g \cdot \sin\theta$ to the right hand side):

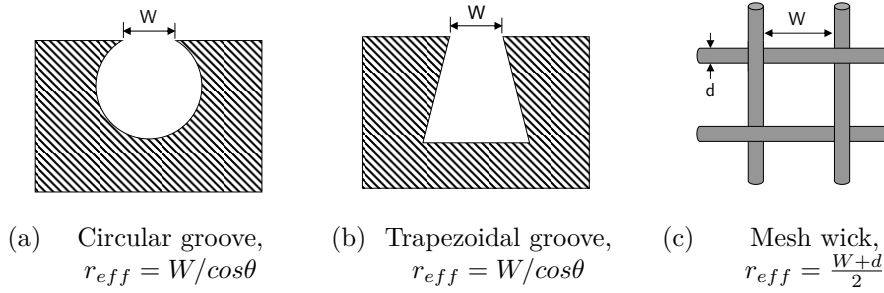


Figure 3.6: Effective pore radii for different wick geometries (formulas taken from table 3.1 in Faghri (1995)), θ is the wetting angle of the working fluid

$$\begin{aligned} \frac{\partial p_v}{\partial x} &= -\frac{f}{D_{h,v}} \cdot \frac{1}{2} \rho_v u_v(x)^2 \\ &\stackrel{(3.23)}{=} -\frac{\eta_v (f \cdot Re)_v}{2D_{h,v}^2} u_v(x) \end{aligned} \quad (3.21)$$

where f is the *Darcy friction factor*⁴, and $\rho_v, u_v, D_{h,v}, \eta_v$, respectively, the density, velocity, *hydraulic diameter* and viscosity of the vapour. The hydraulic diameter is a reasonable approximation for fluid flow in non-circular tubes and is defined by Kays et al. (1993):

$$D_h = 4 \cdot \frac{\text{cross-sectional area}}{\text{wetted perimeter}} \quad (3.22)$$

For circular tubes, $D_h = D$ is simply the tube diameter.

The dimensionless *Reynolds number*

$$Re = \frac{\rho D_h u}{\eta} \quad (3.23)$$

describes the ratio of inertial to viscous forces in fluid mechanics. For laminar flow ($Re \lesssim 2000$) of a Newtonian fluid (shear stress $\tau \propto u$) in a circular tube – which is a

⁴or also Moody friction factor, not to be confused with the Fanning friction factor, also denoted as f but only a fourth of the value

good approximation for most heat pipes – we can write $f = \frac{64}{Re}$ for the Darcy friction factor by equalizing the *Hagen-Poiseuille*⁵ and Darcy-Weisbach equation (3.21). More complex geometries can be derived from the Navier-Stokes Equations. A comprehensive collection of fRe -values for different common wick structures can be found in Faghri (1995, pp. 124–126). For rectangular grooves also refer to figure 6.13 in Karam (1998).

Using the conservation of mass and energy, one can assume that a local heat input $q(x)$, $[q] = \text{W m}^{-1}$, is completely converted into phase change. The resulting mass flow can be expressed by a velocity gradient:

$$\begin{aligned} q(x)\Delta x &= H_v(\dot{m}_{x+\Delta x} - \dot{m}_x) \\ &= H_v(\rho A_v u_{v,x+\Delta x} - \rho A_v u_{v,x}) \\ &= H_v \rho_v A_v \left(\frac{du_v(x)}{dx} \right) \Delta x \end{aligned} \quad (3.24)$$

$$\frac{du_v}{dx} = \frac{q(x)}{H_v \rho_v A_v} \quad (3.25)$$

with $m = \rho \cdot V = \rho \cdot A \cdot l$ and therefore $\dot{m} = \frac{dm}{dt} = \rho \cdot A \frac{dl}{dt} = \rho \cdot A \cdot v$. After integration this can be inserted into equation (3.21) as done in Karam (1998):

$$u_v(x) = \frac{1}{H_v \rho_v A_v} \int_0^x q(x) dx = \frac{1}{H_v \rho_v A_v} Q(x) \quad (3.26)$$

and therefore

$$\frac{dp_v}{dx} = -\frac{(f \cdot Re)_v \eta_v}{2D_{h,v}^2 H_v \rho_v A_v} Q(x) = -F_v \cdot Q(x) \quad (3.27)$$

with the latent heat of vaporization H_v , the vapour flow area A_v and the resulting vapour friction coefficient F_v .

⁵Pressure drop of a laminar, viscous and incompressible flow of a fluid with volume V in a tube, $\frac{dV}{dt} = -\frac{r^4 \pi}{8\eta} \frac{dp}{dx}$, $r = \frac{D}{2}$.

For the liquid pressure drop also the permeability φ of the wick has to be taken into account. *Darcy's law*, a specific solution of the Navier-Stokes equations⁶, is a reasonable simplification of the liquid flow in a porous medium, such as wick structures:

$$\frac{dp_l}{dx} = -\frac{\eta_l}{K}u_l(x) \quad (3.28)$$

with the liquid viscosity η_l , the axial velocity $u_l(x)$ and the permeability K of the wick. Since the velocity vector points towards the evaporator, a minus is required.

The conservation of mass, expressed by $\dot{m}_l = u_l(x)A_w\rho_l$, A_w being the wick cross-sectional area, leads to the liquid pressure gradient:

$$\frac{dp_l}{dx} = -\frac{\eta_l}{K} \frac{\dot{m}_l}{\rho_l A_w} = \frac{\eta_l}{\rho_l A_w K} \frac{Q(x)}{H_v} = F_l \cdot Q(x) \quad (3.29)$$

Using again the Darcy-Weisbach equation (3.21), this time for the liquid flow in the wick, to substitute the left hand side of equation (3.28) leads to an expression for the permeability K :

$$\frac{\eta_l(f \cdot Re)_l}{2D_{h,l}^2}u_{l,w} = \frac{\eta_l}{K}u_l \quad (3.30)$$

$$K = \frac{2D_{h,l}^2}{(fRe)_l} \frac{u_l}{u_{l,w}} = \frac{2D_{h,l}^2\varphi}{(fRe)_l} \quad (3.31)$$

In the last step the Dupuit-Forchheimer relationship for the wick porosity was used:

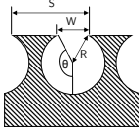
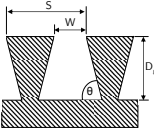
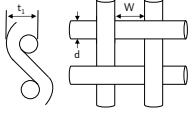
$$\varphi = \frac{u_l}{u_{l,w}} \quad (3.32)$$

which relates the volume-averaged velocity u_l and the pore velocity $u_{l,w}$.

D_h and φ depend on the particular heat pipe and wick geometry. For simple geometries their values may be determined analytically; complex wicks as single or multi-layer mesh screens require partly experimental results as collected for example in Marcus (1972). Predictions for the permeability of multi-layer meshes are especially difficult. A

⁶Conservation of mass, momentum and energy for a liquid flow

Table 3.1: Properties of common heat pipe wick structures (Faghri 1995; Marcus 1972): Hydraulic diameter $D_{h,l}$, porosity φ , friction factor times Reynold's number fRe and permeability K

Wick geometry	$D_{h,l}$	φ	fRe	K
	$2R - \frac{W}{\theta} \cos(\theta)$	$\frac{R\theta - \frac{W}{2} \cos(\theta)}{S(1 - \cos\theta)}$	61 – 64	$\frac{2D_{h,l}^2\varphi}{(fRe)_l}$
	$4 \left[\frac{D_g(W + D_g/\tan\theta)}{W + 2D_g(1/\tan\theta + 1/\sin\theta)} \right]$	$\frac{W + D_g/\tan\theta}{S}$	52 – 96	$\frac{2D_{h,l}^2\varphi}{(fRe)_l}$
	$\frac{d\varphi}{1 - \varphi}$	$\varphi_1 = 1 - \frac{1.05\pi d}{4(d+W)}$ $\varphi_N = 1 - \frac{Nt_1(1 - \varphi_1)}{t_n}$	122	$\frac{d^2\varphi^3}{122(1 - \varphi)^2}$

conservative estimation is the assumption of tightly wrapped layers. Refer to table 3.1 for common heat pipe wick geometries.

The total pressure gradient then yields

$$\frac{dp}{dx} = \frac{dp_v}{dx} - \frac{dp_l}{dx} = -(F_v + F_l) \cdot Q(x) \quad (3.33)$$

where the minus on the right hand side accounts for the direction of the pressure drop.

Heat transport factor (HTF)

Inserting equation (3.20) and (3.33) in equation (3.19) and assuming constant fluid properties as well as consistent geometry, we get a correlation between the geometry of a heat pipe tube and the maximum HTF:

$$\frac{2\sigma}{r_{eff}} = - \int_0^L \frac{dp}{dx} dx = (F_l + F_v) \int_0^L Q(x) dx = (F_l + F_v) \cdot HTF \quad (3.34)$$

and hence an expression for the heat transport factor with $[HTF] = W\ m$:

$$\boxed{HTF = \frac{2\sigma}{r_{eff} \cdot (F_v + F_l)}} \quad (3.35)$$

with F_v and F_l from equation (3.27) and (3.29), respectively. Assuming the maximum (uniform, $q(x) = const$) heat input Q_{max} at only one evaporator, we can integrate $Q(x)$ over the complete heat pipe length ($0 \leq x \leq L$) which gives us the chance to calculate the HTF with the maximum transported heat load:

$$HTF = \int_0^L Q(x)dx = \quad (3.36)$$

$$= \int_0^{L_e} \frac{Q_{max}}{L_e} dx + \int_{L_e}^{L_e+L_a} Q_{max} dx + \int_{L_e+L_a}^L \frac{Q_{max}}{L_e} (L-x) dx = \quad (3.37)$$

$$= (0.5L_e + L_a + 0.5L_c) \cdot Q_{max} \quad (3.38)$$

With a known HTF this allows solving for Q_{max} , $[Q] = W$:

$$\boxed{Q_{max,1\ evap} = \frac{HTF}{0.5L_e + L_a + 0.5L_c}} \quad (3.39)$$

For n evaporators of same length L_e and distance L_d we get a similar result:

$$HTF = ((n - 0.5)L_e + (n - 1)L_d + L_a + 0.5L_c) Q_{max} \quad (3.40)$$

$$Q_{max} = \frac{HTF}{(n - 0.5)L_e + (n - 1)L_d + L_a + 0.5L_c} \quad (3.41)$$

The result of equation (3.35) being inserted in equation (3.39) gives the maximum heat load a heat pipe can transport in capillary limit.

3.1.4 Further heat pipe limitations

Several other phenomena can occur in heat pipes to prevent them from performing at their capillary limit. When designing a heat pipe, one has to estimate the respective risk. In the following section a short overview over common limitations is given as well as the corresponding formula for the calculations.

Sonic limit

Under certain circumstances as in the application of a large heat load, the vapour velocity at the evaporator exit may reach or even exceed the speed of sound u_s . A measure is the dimensionless Mach number:

$$Ma = \frac{u_v}{u_s} = \frac{Q}{H_v \rho_v A_v} \left(\frac{c_p RT_v}{c_v M} \right)^{-\frac{1}{2}} \quad (3.42)$$

with the vapour velocity u_v , $u_s = \left(\frac{c_p RT_v}{c_v M} \right)^{\frac{1}{2}}$ the speed of sound of the vapour phase, Q the transported power, H_v the latent heat of vaporisation, ρ_v the vapour density, A_v the vapour flow area, c_p and c_v the vapour specific heats, M the molecular mass, and finally R the gas constant (compare to equation (3.26)). From fluid dynamics we get that as long as $Ma < 0.3$, vapour flow can be considered as incompressible. For larger Mach numbers this effects the maximum heat transfer capability up to the Mach number of 1 at the sonic limit for $u_v = u_s$. The first closed-form relation of the sonic limit was made by Levy (1968). Taking into account also friction effects at the heat pipe wall, this requires the application of the Navier-Stokes equations and may lead to deviations of the maximum heat load up to 20% as shown in Faghri (1995) (chapter 4.4).

A heat pipe in sonic limit does not show catastrophic failure as for example in the capillary limit. It still transports heat but at the expense of larger gradients between evaporator and condenser because the sonic limit increases with evaporator temperature. This mainly occurs at large heat loads, low densities and high vapour velocities. As seen from equation (3.42), the maximum heat load is proportional to the square root of the vapour temperature.

Viscous limit

The viscous limit is the opposite of the sonic limit, regarding viscous and inertia forces on the vapour flow. In both cases the vapour is assumed to be a perfect gas (Faghri 1995). It appears if the vapour pressure reaches 0 at the condenser end of the heat pipe. Then the pressure difference between evaporator and condenser is not large enough to overcome viscous forces. Taking the equation of state of an ideal gas, the

conservation of mass and the Darcy-Weißbach-equation 3.21, Busse (1967) derived the following expression for the maximum heat flux:

$$Q_{max,VL} = \frac{D_{h,v}^2 H_v \rho_v p_{v,evap}}{64\eta L_{eff}} \quad (3.43)$$

$$L_{eff} = \frac{1}{2}(L_{evap} + L_{cond}) + L_{adiab}$$

with definitions as above and L_{eff} the effective length of the heat pipe. It is supposed to be only relevant for very low temperatures.

Entrainment limit

If the vapour velocity⁷ is too high, entrainment limit may occur. In this case the vapour tears off droplets of the liquid surface and therefore reduces the amount of liquid being available at the condenser. Entrainment can be measured by means of the Weber number We . It relates the shearing force of the vapour (proportional to the dynamic pressure and the exposed liquid area A_l) to the capillary force restraining the liquid (dependent of the surface tension and the wetted perimeter P_l):

$$We = C \cdot \frac{\rho_v u_v^2}{\sigma} \quad (3.44)$$

C depends on the geometry of the wick structure and is $2W$ for axial grooves and W for screens (Kemme 1967; Wright 1970; Faghri 1995). With equation (3.26), the corresponding maximum heat flow rate for $We = 1$ – which is believed to be the onset of entrainment – is:

$$Q_{max,EL} = H_v \rho_v A_v u_v = H_v A_v \sqrt{\frac{\sigma \rho_v}{C}} \quad (3.45)$$

First detected by Kemme (1967), Kemme himself showed a few years later that probably other vapour flow effects limited the experiments (Kemme 1976) and up to now this phenomenon only has been demonstrated without a doubt for gravity-assisted

⁷Generally the vapour velocity is supposed to be several orders of magnitude larger than that of the liquid (Faghri 1995).

heat pipes. As stated by Faghri (1995) (p. 255), the capillaries most likely retard the growth of surface waves.

However, if the vapour velocity is high, the liquid in the uncovered channels of a grooved heat pipe may be exposed to a shearing force due to the vapour counterflow. In this case, the corresponding liquid loss must be taken into account in the liquid pressure equation (3.29) as derived by Hufschmidt et al. (1975).

Further experimentally not verified equations were stated by Tien and Chung (1978) and Rice and Fulford (1978).

For the eROSITA heat pipes entrainment is not expected to be an issue during nominal operation. In figure 3.47 the Weber number as well as the resulting maximum heat flux are shown for the eROSITA heat pipes.

Boiling limit

If the heat input gets too large, nucleate boiling in the wick of the evaporator causes vapour bubbles that may prevent wetting of the wick. If the wick is dried out (stable vapour film between evaporator wall and liquid), the boiling limit is reached. This limit is a radial heat flux limitation in contrast to the axial heat flux limitations discussed so far. Under low heat loads, stable boiling is possible without causing dry-out as stated in Faghri (1995, p. 33). This may cause oscillations as discussed in section 3.4.

The vapour inside the heat pipe is saturated. Because of the direction of heat input, the temperature decreases from the wall to the vapour. As a consequence, the saturation pressure p_l at the wall is higher than the saturation pressure p_v of the system at temperature T . This provides a superheating $T_{sat} - T$ of the liquid and vapour bubbles can form. Furthermore the saturation pressure of the vapour in the bubble exceeds the liquid pressure by the surface tension. As soon as the bubble radius reaches a certain critical value, the bubbles are stable, can grow and therefore act as an additional resistance to heat transfer.

Contamination of the wick, non-condensable gas and surface irregularities can initiate and assist nuclear boiling processes. Those unpredictable factors make it difficult to anticipate the actual heat pipe performance (Karam 1998). So the only reliable estimation is the formation of vapour bubbles due to balance of forces, caused by temperature difference.

In figure 3.7 the relevant pressures and temperatures are defined, r_b is the critical radius of the bubble.

If the force caused by pressure difference equals the surface tension (equation (3.13)), we have a stable bubble with radius r_b . A derivation was done by Karam (1998) and Faghri (1995):

$$4\pi r_b^2(p_b - p_l) = \frac{2\sigma}{r_b} \cdot 4\pi r_b^2$$

using $p_l = p_v - p_{cap}$ with $p_{cap} = \frac{2\sigma}{w}$, w the wick size, leads to

$$p_b - p_v = \Delta p = \frac{2\sigma}{r_b} - p_{cap} = \frac{2\sigma}{r_b} - \frac{2\sigma}{w} \approx \frac{2\sigma}{r_b}$$

and with the Clausius-Clapeyron relation $\frac{\Delta p}{\Delta T} = \frac{H_v}{T\Delta v} \simeq \frac{H_v\rho_v}{T_v}$:

$$\Delta T_{crit} = \frac{T_v}{H_v\rho_v} \frac{2\sigma}{r_b}$$

and with equation (3.5) we finally get an expression for the maximum heat input:

$$Q_{max,BL} = \frac{4\sigma\pi L_e k_{eff, evap} T_v}{r_b H_v \rho_v \ln(D_a/D_i)} \quad (3.46)$$

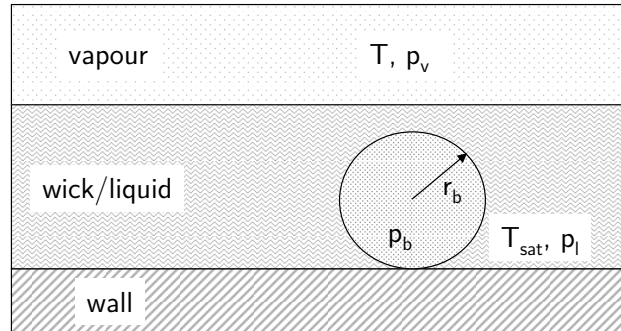


Figure 3.7: Derivation of HP boiling limit

Thus it is obvious that the maximum heat load strongly depends on the maximum bubble size. The larger bubbles can grow, the more likely the heat pipe is limited by the nuclear boiling. Various sources (Chi 1976; Faghri 1995; Marcus 1972) place this value within the range of 10^{-5} m to 10^{-8} m. This large range of possible radii and their unpredictability as mentioned above make it impossible to exactly determine the boiling limit. The best approach to avoid it in either case is to limit the heat load to about 1 W cm^{-2} as stated by Karam (1998).

As noted in the literature, for example in Ivanovsky et al. (1982, p. 146), Faghri (1995) or Karam (1998), limits like entrainment or boiling limit are not likely to occur in low temperature heat pipes with small heat loads. A lot of former missions have proven that this is a reasonable approach if tube and working fluid are free of contamination and heat loads stay below 5 W cm^{-2} .

Nevertheless the exact course of the mentioned heat pipe limits always depends on the HP geometry and on the working fluid, so this cannot be generalised. A typical plot as often found in the literature is shown in figure 3.8. Figure 3.9 is the corresponding plot for the eROSITA camera heat pipes, for comparison. For the boiling limit a critical radius of 1×10^{-8} m was assumed. As we will see in section 3.4 and section 3.5, the heat transport capability for high temperatures – where the boiling limit may become significant – is even higher as the capillary limit. This indicates a small critical radius since the heat pipes are not limited by nuclear boiling.

Besides these intrinsic limitations, there are also external circumstances that can limit the performance of a heat pipe. For example an effective heat removal has to be guaranteed and the heat pipe temperature has to stay within the designated working temperature to prevent condenser limitation and frozen start-up limit.

3.1.5 Variable conductance heat pipes

Conventional heat pipes as described so far are not capable of temperature control. In fact, the overall conductivity stays more or less constant, until one of the limitations described above is reached. For some applications it is desired to change the heat pipe performance, for example if a power dissipating device with varying heat load should be kept at constant temperature or the cold sink temperature is not stable.

Several methods are used to vary the conductance of a heat pipe (Marcus 1972), for example the excess-liquid heat pipe, where an excess amount of working fluid blocks

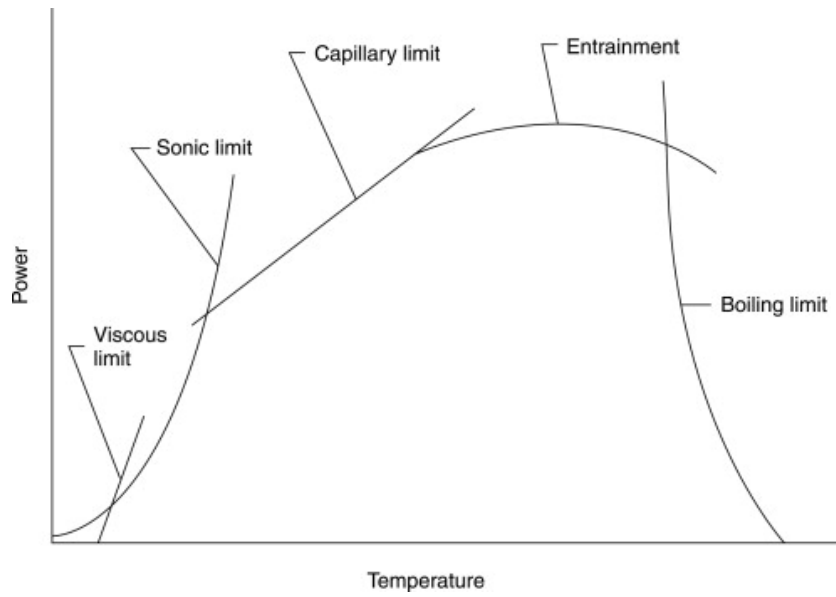


Figure 3.8: General temperature dependence of heat pipes limits (taken from Suman (2009))

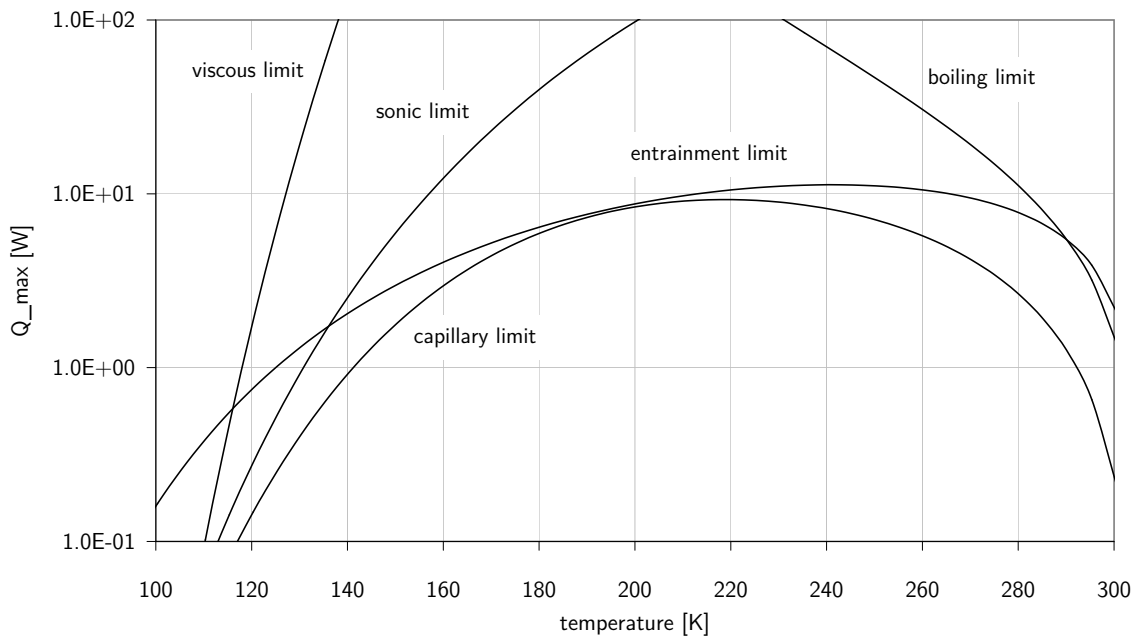


Figure 3.9: Temperature dependence of eROSITA camera HP limits

part of the condenser, or the vapour-flow modulated heat pipe with a heat-input-dependent vapour flow. Both heat pipes contain a bellows that reacts on changing heat input. The most popular kind of variable conductance heat pipe (VCHP) is the *gas-loaded heat pipe*. All kinds of gas-loaded VCHPs (which simply will be referred to as VCHPs in this work) do have in common that they are filled with a certain amount of non-condensable gas (NCG) in addition to the working fluid. This gas acts as a diffusion barrier for the working fluid, blocks parts of the condenser and therefore reduces the active surface region S [m], which leads to a decreased heat transfer coefficient h [$\text{W m}^{-1} \text{K}^{-1}$] and therefore to a decreased power throughput Q [W]:

$$Q = hS(T_{w,cond} - T_{sink}) \quad (3.47)$$

Depending on the exact type and operating conditions of the VCHP, the condenser end of the heat pipe does have only an extended tube or a gas reservoir, wicked or non-wicked. The larger the condenser, the more gas is required to block it and an additional reservoir is necessary where the gas may enter in full operation mode. Whether the reservoir needs to contain a wick depends on the boundary conditions and the scope of the set-up. With a wick inside the reservoir, liquid always will be present and therefore the gas pressure will equal the liquid saturation pressure (Kosson et al., 1973). This design is critical for large variations of the sink temperature; an enhanced condenser temperature will on the one hand increase the intrinsic working temperature of the heat pipe, on the other hand the heat transfer is reduced due to a larger blocked condenser area (see figure 2.8). This will result in further increase of the hardware temperature. Moreover, if the reservoir temperature is below the heat pipe working temperature, working fluid condenses in the reservoir and is no longer available for heat transport.

To some extent, a VCHP containing NCG has an intrinsic temperature control. The higher the applied power, the higher gets the vapour pressure of the working fluid, increasing the condenser region. Passive feedback for a gas-loaded VCHP can be used to improve the temperature stability of a device with varying heat load. This can be realized by a gas reservoir volume that depends on the applied source power, for example regulated by a bellows (Bienert et al. 1971). The more power is applied, the larger becomes the reservoir and the more condenser region becomes active due to receding NCG. However, this is not suitable for significant changes in the sink temperature, since this rather would enhance temperature variations.

Without a wick in the condenser the reservoir temperature (and therefore the gas pressure) is rather independent of the heat pipe working temperature (Rogovin and Swerdling, 1971), which can be used for active feedback control. The first study for evaluation of the feasibility of feedback controlled VCHPs was made by Brennan (1970). A few years later, Bienert et al. (1971) built the first active feedback control HP by heating the non-condensable gas reservoir of a water heat pipe with argon for the NCG. With this method the VCHP can react on environmental influences, for example changing sink temperatures. Moreover, this allows for a very accurate evaporator temperature control of $\Delta T < 0.5$ K, see section 4.3. A low conductivity of the container material enhances the available temperature range since higher reservoir temperature deviations can be achieved. Examples for active feedback controlled VCHPs – including space applications – are listed in table 3.2.

Theoretical model of the diffusion barrier

Several attempts were made during the last 40 years to describe the location and shape of the vapour-gas interface mathematically. The most simplified approach is the so-called *one-dimensional flat-front model* with the interface being sharp by neglecting mass diffusion as well as any kind of radial and axial conductance.

The NCG can be treated as an ideal gas with

$$p \cdot V = nRT \quad (3.48)$$

with p , V and T the pressure, volume and temperature, n the amount of substance and R the gas constant. The saturation pressure curve of the working fluid $p_{sat}(T)$ follows the Clausius-Clapeyron relation

$$\frac{dp_{sat}}{dT} = \frac{H_v}{\Delta v T} \approx \frac{p_{sat} H_v}{RT^2} \quad (3.49)$$

with the latent heat of vaporization H_v , the molar volume change of the phase transition v , the saturation temperature T and the gas constant R . In the last step the ideal gas law was used. Integration gives an exponential relationship, so the partial pressure of the working fluid in general has a larger percentage change than the linear correlation of the NCG. Even small changes in heat load will cause a significant change of the vapour pressure and therefore a fast response of the VCHP.

Inserting the working fluid vapour pressure (determined by the temperature of the adiabatic section) and the reservoir temperature in equation (3.48) gives us the effective NCG volume which allows for a reasonable estimation of the interface location as demonstrated in section 3.5.

The first publication for the steady-state case was from Marcus et al. (1970). Transient solutions were for example examined by Faghri et al. (1994). Including axial mass diffusion on the vapour-gas interface, implemented by Fick's law, led to the *one-dimensional diffuse models*. Steady-state solutions were made by Edwards et al. (1972), Shukla (1972) and Bobco (1987). Improvements were made by Delil et al. (1981) by adding inertia effects of the vapour. Shukla (1972) developed the most popular transient model, taking into account quasi-steady vapour-gas diffusion with incompressible vapour flow, and axial conductivity in the condenser section. Harley (1993) made further improvements by introducing overall axial conductance (including the vapour) and accounting for friction effects.

The last level of refinement are *two-dimensional diffusion models*, additionally containing radial mass diffusion. The necessity is given due to the fact that NCG may accumulate at the liquid-vapour interface (Faghri 1995). Harley et al. (1972) used the differential equations for mass, momentum and energy to develop their comprehensive transient description of gas-loaded VCHPs.

If an accurate temperature profile is not required, but only the position of the diffusion barrier, the one-dimensional model is sufficient. However, one should keep in mind that this is not a sharp boundary but rather a smooth transition area between the working fluid and the NCG.

The proper amount of non-condensable gas (NCG)

The ideal amount of NCG depends on the condenser length, the working temperature range and the expected heat loads. A passive VCHP, that must keep the temperature of a device with varying heat load, has to be designed extra carefully because intervention is not possible afterwards.

For active feedback VCHPs, the diffusion barrier can be controlled by the reservoir temperature. The achievable temperature difference determines the VCHP's operating range. The larger the temperature can be varied, the less NCG (and therefore reservoir volume) is necessary.

In the hot case, if the maximum heat load is applied (which means maximum vapour pressure of the working fluid), the condenser region should be completely active to maximize the heat pipe efficiency. This is supported by a low reservoir temperature – and therefore no power applied onto the reservoir – to reduce the volume of the NCG (refer to equation (3.48)). In the cold case, with the minimum source power, the condenser should be blocked as far as possible. In contrast to a passive feedback VCHP, the active feedback allows for heating the reservoir to the maximum temperature.

The volume ratio of the reservoir and the condenser $\frac{V_{res}}{V_c}$ depends on the hot and cold case conditions as well as on the corresponding vapour pressures of the working fluid.

Underlying principle for the calculation of this ratio is the conservation of mass. We neglect diffusion and assume a simple 1-D flat-front model. Using equation (3.48) and $n = \frac{m_{NCG}}{M_{NCG}}$ with M_{NCG} being the molar mass of the NCG, we can write for the required NCG mass in the hot and cold case:

$$m_{NCG,h} = \frac{M_{NCG} \cdot p_{v,max} \cdot V_{res}}{R \cdot T_{res,min}} \quad (3.50)$$

$$m_{NCG,c} = \frac{M_{NCG} \cdot p_{v,min} \cdot (V_{res} + V_c)}{R \cdot T_{res,max}} \quad (3.51)$$

with the maximum and minimum reservoir temperature T_{res} as well as the maximum and minimum saturation pressure of the working fluid p_v . If we equal both expressions and solve for the desired volume ratio, we get:

$$\frac{V_{res}}{V_c} = \left(\frac{p_{v,max} T_{max}}{p_{v,min} T_{min}} - 1 \right)^{-1} \quad (3.52)$$

Gas-loaded start-up

Before heat is applied to the evaporator, the mixture of working fluid and NCG is distributed uniformly over the heat pipe tube. After heat is applied to the evaporator, the working fluid and the NCG segregate step by step, the working fluid vapour forces the NCG back to the condenser and – if applicable – into the designated reservoir. This start-up takes between a few minutes up to almost half an hour, depending on heat pipe length and specific boundary conditions.

Table 3.2: Examples for active feedback control VCHP applications

Project reference	tube material	working fluid	NCG	working temperature [K]
Bienert et al. (1971)	stainless steel + mesh	water	Ar	273 – 373
B&K Engineering (1979)*	SS + mesh	methanol	He	273 – 323
Wanous et al. (1975)*	SS	methanol	He	221 – 293
Cleveland et al. (2003)*	–	ammonia	N ₂	268 – 275
Peeples et al. (1977)	SS + mesh, Al + grooves	Freon-21, ammonia	He	172 – 295

*in-orbit operation

As long as the gas partially blocks the condenser region, a steep temperature drop occurs at the diffusion barrier. The higher the heat load (and so the vapour pressure) the larger is the free condenser region which provides a passive control of the evaporator temperature.

3.2 Technical solution

In general heat pipes are a standard product nowadays. Besides space applications, they are commonly used in computers, solar thermal water heaters, pipeline and railway systems or air conditioning systems. Mostly water or ammonia are used as working fluids, suitable for room temperature and – with ammonia – down to about 210 K.

Below that temperatures suitable working fluids are rare. For very low temperatures the noble gases can be used. But in the range between 150 K and 190 K, which is important for the eROSITA mission, only very few substances are applicable (Faghri 1995).

Apart from an appropriate melting point and critical point, the compatibility with the container material (aluminium, stainless steel) is also important. Moreover, the vapour pressure limit may be approached at pressures below 0.1 bar. Considering also

storage, transport and handling, the pressure at room temperature must not exceed the mechanical limits of the heat pipe tube, including fluid containers and valves for complex heat pipe systems.

Methan for example melts at 91 K but has its critical point already at 190 K. Above this temperature condensation is no longer possible. Close the critical point, the surface tension and so the heat transport capability decreases. Other fluids as propane, propylene or several chlorofluorocarbons as tetrafluoromethane (with the trade name R14) or Monochlorotrifluoromethane (R22, Freon-22) have a suitable temperature range but have not been extensively tested for space applications or are even halted due to environmental issues. Ethane as a promising candidate has been tested extensively as heat pipe working fluid, especially in long-term experiments in space (McIntosh et al. 1993).

Due to all these facts ethane was chosen for the eROSITA project. Disadvantages of this fluid are a low surface tension⁸, high viscosity and low heat of vaporization, and therefore a resulting low heat transfer coefficient in comparison to other working fluids. Important for the heat pipe performance, amongst others, is the wetting capability of the fluid. This value determines the capillary force as shown in section 3.1.3.

In contrast to other heat pipe working fluids such as ammonia or Freon-22, the wetting angle of ethane decreases for lower temperatures, namely from 44° at 273 K to 23° at 158 K (see figure 3.10). This fact benefits the low temperature ethane heat pipes. Nevertheless the capillary force of ethane is low, which makes it difficult to test on ground, because even small deviations from the horizontal position can cause severe decrease of the heat transport capability. One of the ethane heat pipe tubes of the SWIFT XRT cooling system for example happened to have a very small bump. This had severe consequences on the performance during the first performance tests. After removing the bump the heat pipe worked as expected (Kobel et al. 2003).

As described in section 2.3, three different types of heat pipes are needed for the eROSITA camera cooling system, which will be described in the following sections.

⁸Only $\approx 1/4$ the value of water

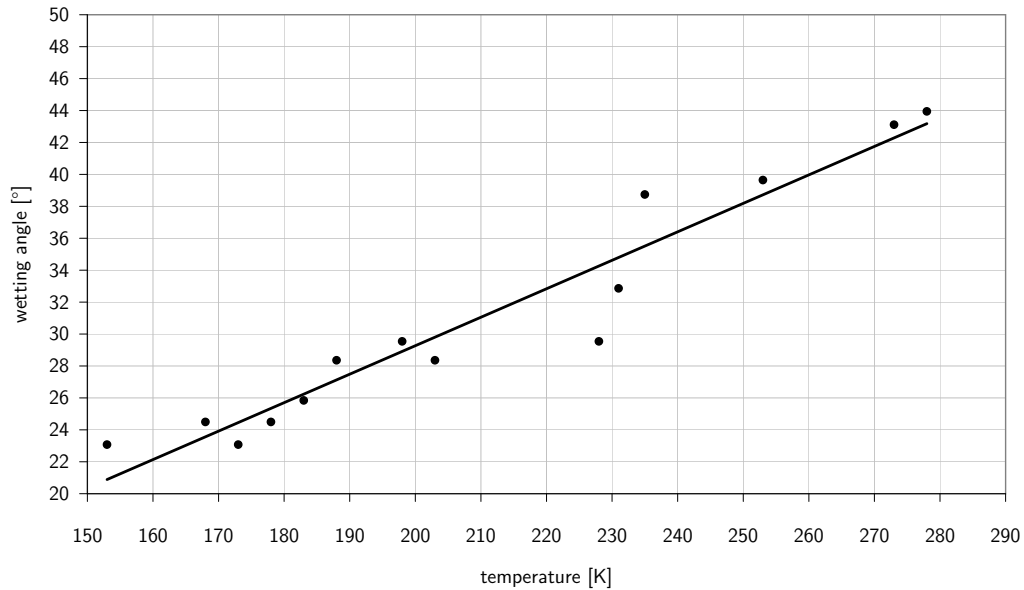


Figure 3.10: Wetting angle of ethane, data taken from Rybkin et al. (1979)

3.2.1 Camera and ring heat pipes

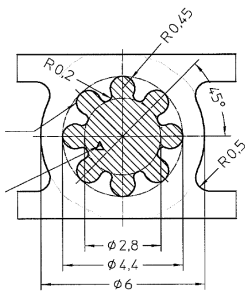
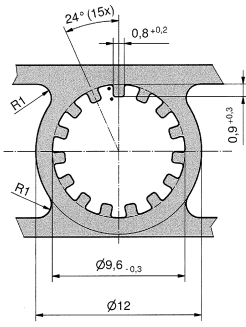
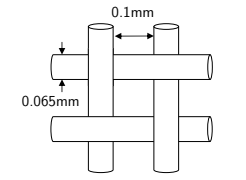
Due to reasons of easy manufacturing, extruded axial grooved aluminium⁹ tubes are used as heat pipe container where possible. This works for the camera heat pipes as well as for the ring heat pipes since a common constant conductance design is sufficient.

The grooves were manufactured as small and accurately as possible to enhance capillary action. An overview of the specific geometric heat pipe profile parameters is summarized in table 3.3. During the qualification tests some values deviate from the theoretical values, for example the porosity of the ring HP and VCHP has to be higher than assumed to reproduce the data. Otherwise the measured heat transport capability would be much larger than the theoretical capillary limit. This also leads to a higher permeability. Details are described in section 3.4 for camera and ring HPs and in section 3.5 for VCHPs.

Since the camera HPs are attached radially to the ring HP, it may happen that some of them are not arranged completely horizontally during tests with the complete heat

⁹Al6060

Table 3.3: eROSITA HP properties for camera HPs, ring HPs and VCHPs. Theoretical values in brackets, if in deviation from the experimental determined values (refer to section 3.4 and section 3.5). A_l/A_v are the liquid and vapour cross sections, $D_{h,l}/D_{h,v}$ the hydraulic diameters, φ the porosity, fRe the friction factor times the Reynold's number and K_l the permeability.

Wick geometry	A_l/A_v [mm ²]	$D_{h,l}/D_{h,v}$ [mm]	φ	$(fRe)_l/$ $(fRe)_v$	K_l [10 ⁻¹⁰ m ²]
	4.2 (5.1)/ 3.1 (6.2)	1.1/ 2.0 (2.8)	0.72	63/64	295
	16 (14)/ 48	1.3/ 7.8	0.70 (0.64)	58/64	321
	46 (15)/ 32 (64)	0.40 (0.19)/ 6.4 (9.0)	$\varphi_1 = 0.82$ (0.68) $\varphi_3 = 0.86$ (0.75)	122/64	11.2 (2.2)

pipe chain. Therefore a bending in the second dimension was added to guarantee that the evaporator always is above the condenser, see figure 2.5. Otherwise the HPs would have to work against gravity which would mean a severe performance drop.

For both HP types special bending tools were manufactured, with cavities of the final HP shape. After bending, the HPs were cut to length and the screw holes were made into the saddles. This ensures the correct position of the different interfaces.

Afterwards an accurate cleaning of the tube interior in an ultrasonic bath and purging with acetone guarantees removal of contaminants. Particles or oily films can destroy liquid and vapour flow and chemical reactions can generate non-condensable gas which would block the condenser. The next step is the welding of a cap to the one end and a capillary with a Swagelok-connector for filling purposes to the other end, before the tube surface is passivated with yellow chromating. A hand valve is attached for the evacuation and filling procedure.

To determine the amount of ethane afterwards, the heat pipe has to be weighed very accurately when evacuated (to avoid the contribution of enclosed air). Heating up and purging several times with ethane during the evacuation process supports the removal of potential persistent contaminant remains, water and air.

The ideal volume of working fluid fills the capillaries exactly. Too less would cause a dry-out at high heat loads and low temperatures, too much of it would accumulate at the coldest part and therefore block the condenser region. The absolute mass depends on the operating temperature range since density increases with decreasing temperature. The ideal theoretical amount at 178 K is 0.90 g ethane for the eROSITA camera heat pipes and 15 g for the ring heat pipes. The latter is not as critical because of the larger volume and therefore a larger condenser area. But various tests with filled camera HPs showed a slightly smaller optimum mass of about 0.85 g. Otherwise the radial conductivity is too small and oscillation effects occur as shown in section 3.4.1.

After a brief performance check the capillary is crimped and welded, using a special handling device (see figure 3.12). A lot of pre-tests were conducted to find out the right approach to the crimping (figure 3.11) and the optimum parameters for the welding machine to guarantee the leak tightness, since welding of aluminium has its pitfalls.

The segregated valve, which contains a small amount of ethane, is welded as well for an exact mass balance.

Immediately afterwards a first leakage test is made by dipping the capillary into alcohol. This is sufficient to find major leaks and would give the chance to repeat the

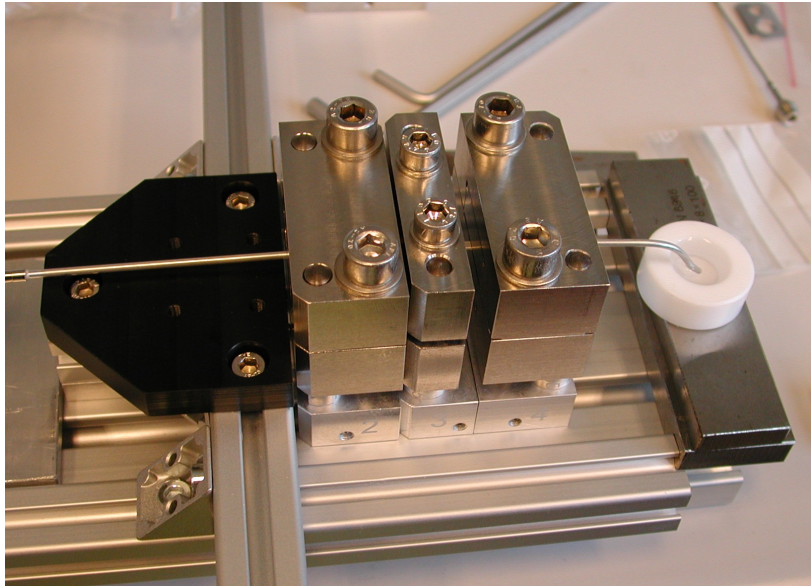


Figure 3.11: Test of the eROSITA heat pipe crimping procedure. The capillary was put under a pressure of 60 bar helium and crimped until leakage vanished. This gave us the optimum final thickness of the capillary for the welding process.

welding if necessary. Subsequently weighing the heat pipe and the valve (with and without the enclosed ethane) gives the final amount of working fluid.

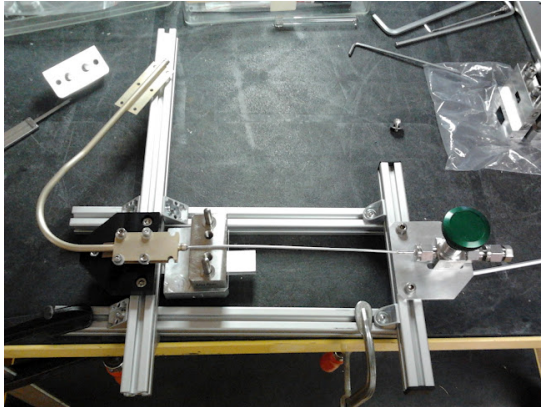


Figure 3.12: Crimping and welding device for the camera HP

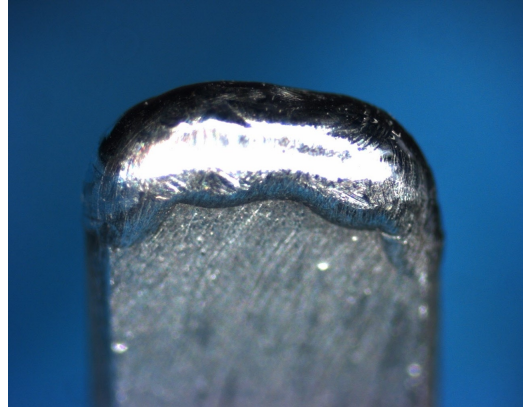


Figure 3.13: Welded joint of the heat pipe capillary

3.2.2 Switchable variable conductance heat pipes (sVCHPs)

The complexity of the sVCHPs with two reservoirs and two valves as well as the high thermal conductivity of aluminium make it necessary to use another container material. Stainless steel is easy to weld and has a low conductivity, moreover it is compatible with ethane. However, it has a larger density and, even more important, it has another thermal expansion coefficient than the aluminium radiator. This complicates the HP attachment due to thermal stress.

Stainless steel cannot be extruded as simply as aluminium, therefore we use three layers of stainless steel mesh for capillary action instead. Exact parameters are listed in table 3.3. The mesh as well as the tube are cleaned in acetone, an ultrasonic bath and purged with nitrogen, the mesh is dried in a vacuum oven in addition.

To have a smooth, uniform distribution of the mesh inside the tube, we built a device which allows us to pull the mesh into the tube. Since the bending happens afterwards, it has to be ensured that the mesh does not get any kinks in the bend, which would hinder the flow of the working fluid. Therefore a stainless steel spiral spring was added in the bending area (see figure 3.14).

Endoscopic measurements for bent tubes with and without the spring showed the effectivity of this method. So we avoided to eliminate the wick from the bent areas and use arteries as done for example by Peeples et al. (1977).

The appropriate size of the NCG reservoir was calculated with equation (3.52), as-



Figure 3.14: Spiral spring to keep the sVCHP mesh in place



Figure 3.15: Stainless steel mesh for the sVCHP after cleaning

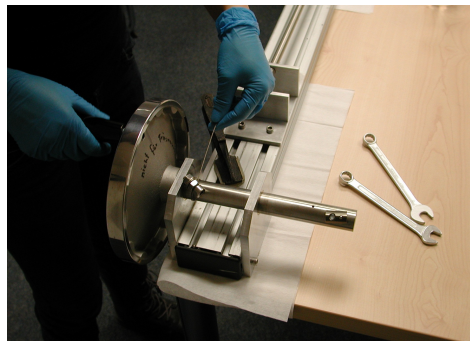


Figure 3.16: Pulling device for the VCHP mesh

suming a desired maximum range of the NCG front of 1 m, a reservoir temperature between 150 K and 190 K and an average ethane vapour pressure of 0.23 bar which corresponds to an adiabatic temperature of 165 K. Since the heat load does not change in the operational case, the ethane vapour pressure also stays constant:

$$V_{res} = V_c \cdot \left(\frac{p_{v,max} T_{max}}{p_{v,min} T_{min}} - 1 \right)^{-1} \quad (3.53)$$

$$= (0.5 \text{ cm})^2 \pi \cdot 100 \text{ cm} \left(1 \cdot \frac{190 \text{ K}}{150 \text{ K}} - 1 \right)^{-1} \quad (3.54)$$

$$= 300 \text{ cm}^3 \quad (3.55)$$

The HP tube, the nitrogen and ethane reservoirs and the two valves are welded together, with a leakage test after each welded joint. The optimum filling levels of ethane and nitrogen were found in a separate experiment, described in section 3.5. It is 27 g of ethane and 0.16 g of nitrogen. The volume of the ethane reservoir is designed in a way that the pressure inside does not to exceed 60 bar at 313 K, which is the maximum storage temperature. The limiting component in the valve complex is the hand valve, it is only leak proof up to 70 bar. Between the ethane reservoir and the tube, the electrical solenoid latching valve acts as filling valve (refer to figure 3.17).

With the help of a radiator simulator the final orientation of the tube and the valve complex can be determined. A flexible hose allows for a certain level of mechanical decoupling (refer to figure 3.18).

For determining the desired parameters such as maximum heat transport capability and heat transfer coefficients a lot of tests were necessary. Those conducted only with the heat pipes are described in the next section, whereas a test of the complete camera assembly cooling system can be found in chapter 4.

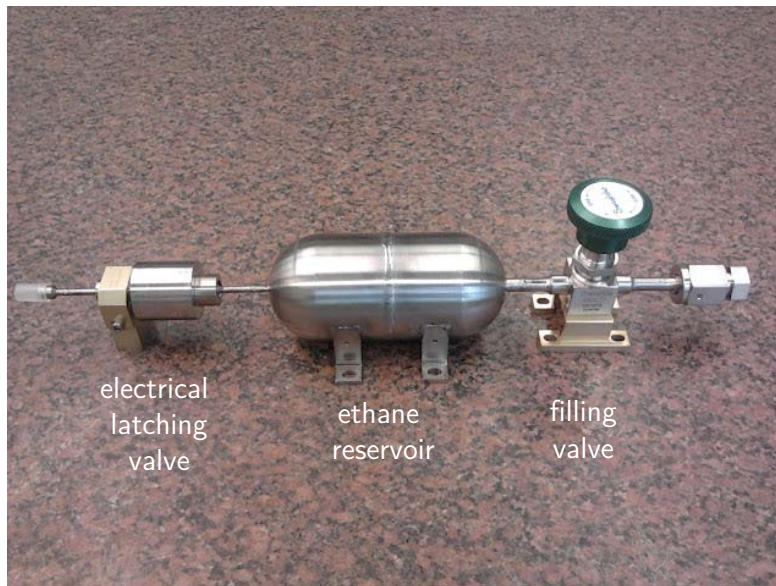


Figure 3.17: Manufacturing of the sVCHP valve complex. Leakage test after each welded joint.

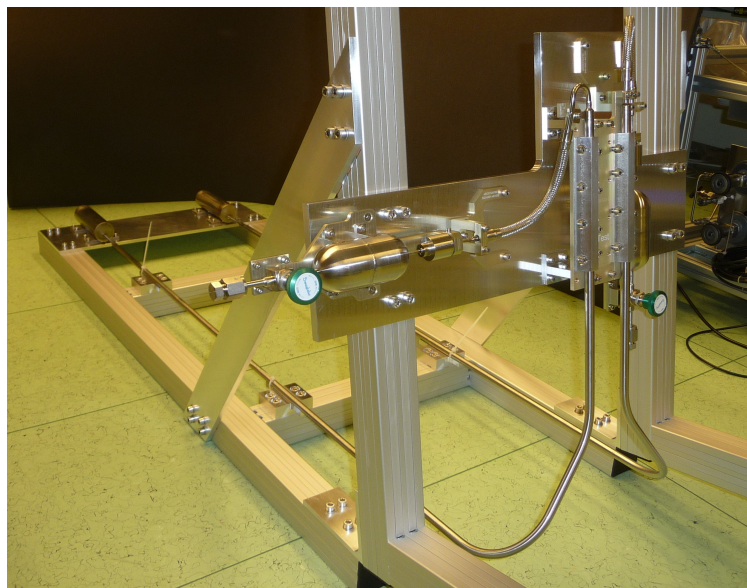


Figure 3.18: Manufacturing of the complete sVCHP with help of a radiator simulator.

3.3 Heat pipe performance test under microgravity

The scope of the campaign at the ZARM Drop Tower in Bremen was the examination of the heat pipe functionality under zero gravity. Calculations predicted and laboratory tests showed that low temperature heat pipes filled with ethane are very sensitive to tilt. The material constants of ethane like surface tension and viscosity of ethane result in a much lower capillary force than e.g. water. Due to ambiguous test results it was not definitely clear if sufficient capillary forces were present at all.

Under zero gravity conditions in the Drop Tower the existence of capillary force in both camera-type and ring-type heat pipe tubes could be proved. Different parameters (temperature, heating power, influence of ethane level) were examined as well. The ring-type HPs (12 mm diameter) surprisingly had a higher capillary velocity than the camera-type HPs (6 mm diameter). According to expectations, the optimum filling level during this test corresponded to the amount of ethane that fits into the capillaries.

3.3.1 Test set-up

Several boundary conditions had to be taken into account when designing the experimental set-up. The evacuation time of the drop tower is 2 hours, so the operational temperature of about 160 K to 170 K had to be guaranteed after this time. The maximum allowable weight of the experiment was 160 kg. Outer dimensions of the available space were about 600 mm in diameter and about 800 mm in height to fit into the capsule. For clear evidence of the existence of capillary forces the heat pipes had to work against gravity in the microgravity (μg) phase, that means the evaporator had to be above the condenser all the time. Otherwise we would have run the risk to get temporally delayed effects from the time before and after the drop. To decide whether the heat pipes are working, we had to foresee the measurement of the ethane level in the tube.

Temperature control happened via a "latent cold storage unit"¹⁰. It consisted of an aluminium block with a cavity in the centre (figure 3.19).

Liquid nitrogen was supposed to be filled in to cool the complete set-up down far beyond the required 173 K. The total heat capacity of the container had to be large

¹⁰Despite the fact that actually heat is stored, this phrase was coined during an earlier phase of the project to point out the low temperature.

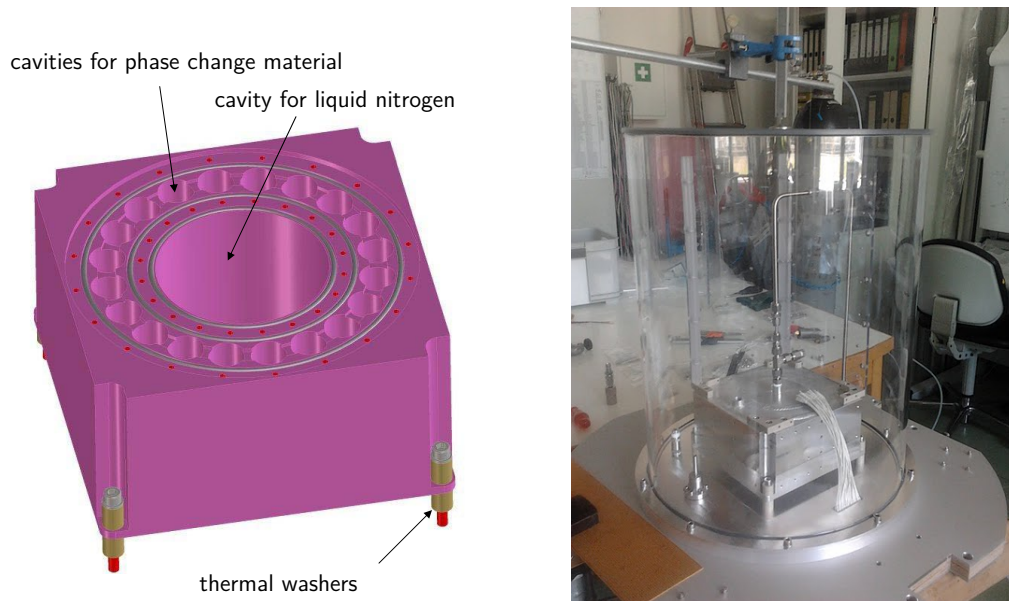


Figure 3.19: Design and manufacturing of the latent cold storage

enough to endure the tower evacuation time and delay the temperature drifting. To expand the time the required temperature was available, cavities filled with propanal as phase change material were added. Propanal's melting point is at 171 K and therefore induced a plateau in the melting curve, see figure 3.20. The container was thermally decoupled from the experiment platform by thermal insulators to reduce parasitics.

The phase change material was not able to cause a complete flat temperature plateau because the ratio between propanal and aluminium was rather disadvantageous. Further improvements with styrofoam and other insulation material had to be made in order to double the melting time by reducing the convection to a minimum. The whole set-up was covered with a cylinder of acrylic glass which could be purged with gaseous nitrogen to prevent ice.

Heat pipes

Two main types of heat pipes were tested – camera-type heat pipes with an outer diameter of 6 mm and ring-type heat pipes with an outer diameter of 12 mm, each in bent and straight shape, see figure 3.22.

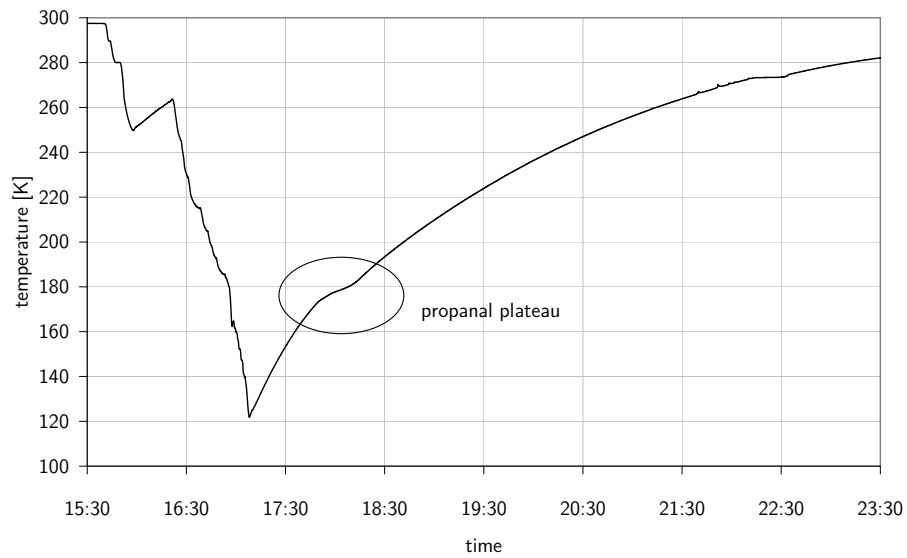


Figure 3.20: Melting curve of the latent cold storage

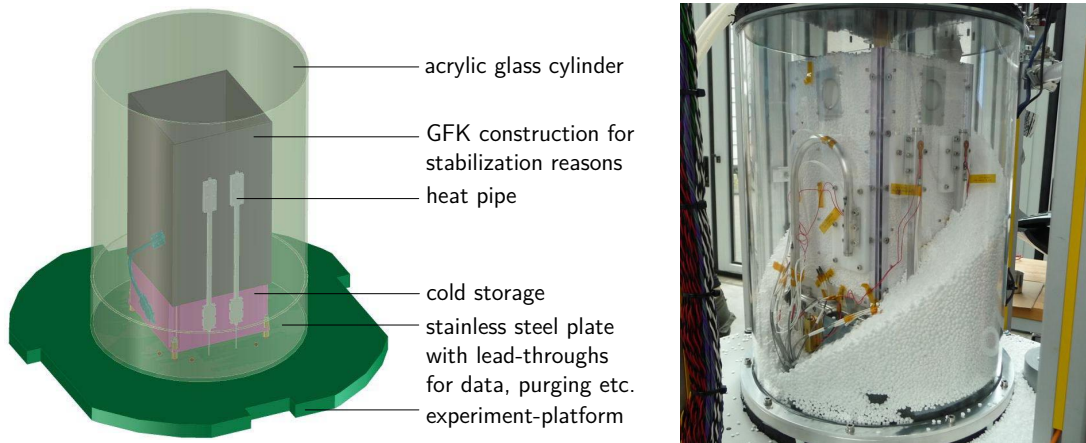


Figure 3.21: Test set-up

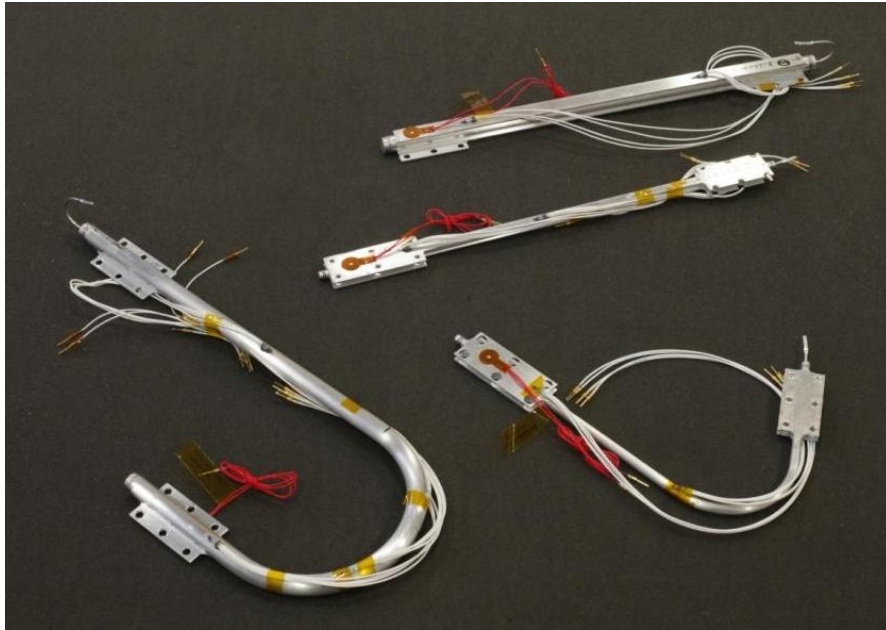


Figure 3.22: Different heat pipe types with temperature sensors and heaters: bent and straight camera-type HPs (small diameter) and ring-type HPs (large diameter)

All HPs were screwed onto the cold storage. It represented the cold sink for the heat pipes. So the HP flange at the cold storage acted as condenser. The other end, the evaporator, pointed upwards and was attached thermally isolated. This guaranteed that the evaporator was always above the condenser and therefore the HPs were always in a mode where they had to work against gravity; the liquid phase at the bottom was supposed to reach the evaporator at the top only due to capillary action.

Each HP was equipped with one foil heater and two or three temperature sensors. One sensor was on top at the evaporator and one was approximately 3 cm above the ethane level. Some of the heat pipes also had a sensor in between. Additionally temperature sensors were on the cold storage, representing the condenser temperature. See figure 3.23 for the schematic heat pipe attachment.

During the evacuation time a thermal equilibrium was reached where the evaporator temperature was much higher than the condenser temperature. The exact gradient depended on the insulation – the better the convection was suppressed, the colder was the evaporator. Though always a residual difference of at least 10 K remained. Therefore a potential temperature drop over the heat pipe during zero g was proven

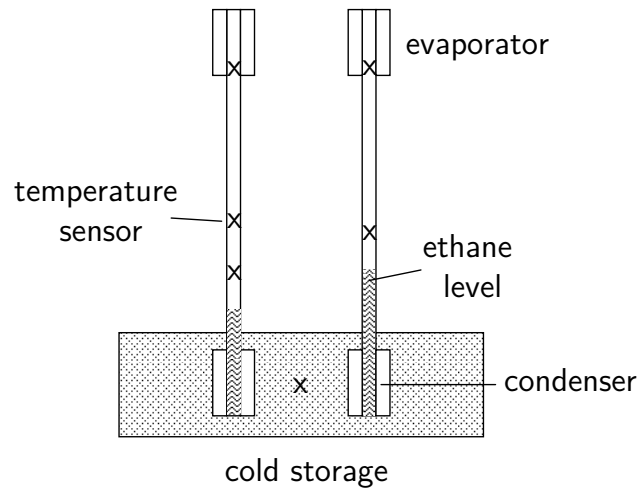


Figure 3.23: Scheme of the heat pipe attachment. Each HP condenser is attached to the cold storage while the evaporator is thermally isolated. Two or three sensors monitor the temperature.

for the existence of capillary forces. Moreover, the heat input onto the evaporator could be calculated with the equilibrium temperatures. Surprisingly used, compressed styrofoam had a much better isolation capability (150 K after two hours) than the new, globular one (170 K after two hours).

This experiment did not intend to find the maximum heat transport capability or the resulting temperature difference. This was done in the camera cooling thermal balance test in section 4.3 since the zero g time of about 9.2s was too short to reach thermal equilibrium. The main goal of this test was the evidence for capillary forces inside the heat pipe tubes under microgravity.

Each heat pipe was filled with a different amount of ethane in order to examine its influence and to find the optimum level. Baseline was the amount that fits exactly into the capillaries at 173 K (bold). Additionally more and less ethane was tested, refer to table 3.4.

Electronics

The electronics set-up of the experiment consisted of two main parts: heating power and temperature measurement. The heat sources were the already mentioned foil

Table 3.4: Ethane filling levels. Theoretically determined optimum levels in bold letters.

camera-type			ring-type	
HP 5	0.81 g	straight	HP 1	2.95 g
HP 6	0.44 g		HP 2	2.47 g
HP 7	0.88 g		HP 3	2.04 g
HP Sp*	0.79 g		HP 4	2.41 g
HP A	0.70 g	bent	HP C	3.97 g
HP B	0.86 g		HP D	4.54 g

*contained a spiral spring

heaters with 8 W maximum heating power, one at the evaporator of each heat pipe. 16 JUMO dTRANS T02 LCD (type 707022) smart transmitters were responsible for the temperature sensor read-out. Each transmitter belonged to one PT 100 temperature sensor and the output was the temperature in Kelvin.

Data were directly transferred from the capsule computer to the ground station, during flight via WIFI.

3.3.2 Test campaign

The drop tower in Bremen is 146 m high, with an actual drop distance of 110 m (figure 3.25). Hereby the drop tube is free-standing due to reasons of wind-induced vibrations. In the catapult mode about 9.2 seconds of microgravity can be achieved. In contrast to the normal dropping procedure a catapult accelerates the capsule up to $50 \frac{m}{s}$ in less than 300 ms. The quality of microgravity is excellent, it is between 10^{-5} and $10^{-6} g_0$ (FABmbH 2011).

About one hour before handover of the experiment the liquid nitrogen cooling has been started. As soon as a temperature of 100 K was reached, the capsule was closed and brought into the drop tower. After about two hours of evacuation time the pressure in the tower was below 0.1 hPa and the launch sequence could be started.

Altogether 12 drops instead of 10 were performed. Due to technical problems with the capsule communication, the data storage did not work twice. After replacing the wireless transmitter the drops could be repeated successfully.

Different flight configurations with different boundary conditions were carried out.

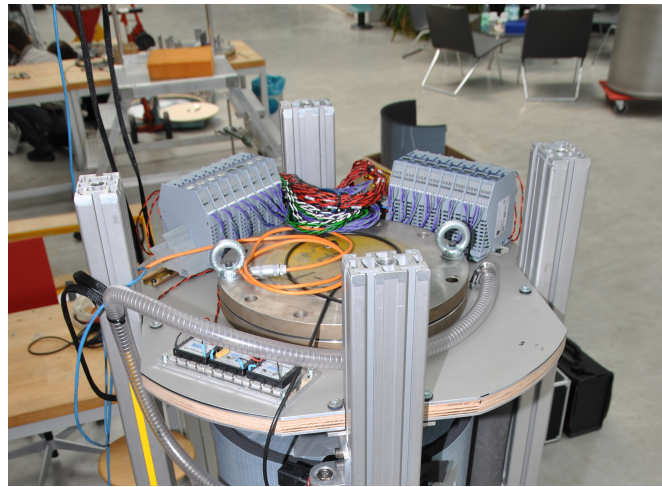


Figure 3.24: Read-out electronics

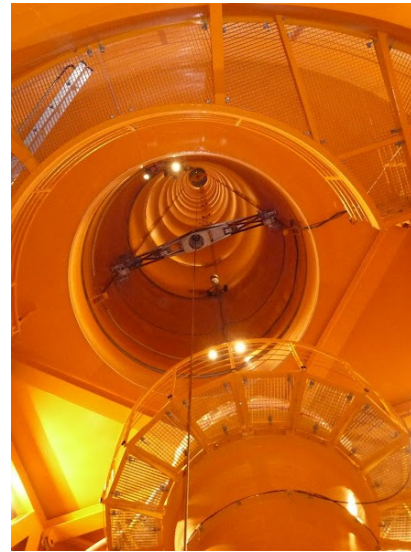


Figure 3.25: The ZARM Drop Tower

The condenser and evaporator temperatures varied, depending on thermal insulation and heating power, see table 3.5.

Table 3.5: Drop configurations, "c" for camera-type HPs and "r" for ring-type HPs

Drop number	HP type	Cold storage temperature [K]	Heating power [W]
1	c	178	–
2	c	174.5	–
3	no data		
4	no data		
5	c	179.5	2.56
6	r	182.5	–
7	r	159	–
8	r	173	–
9	c r	174.5	2.56
10	c r	158.5	–
11	c r	173	–
12	c r	174	varying

3.3.3 Results

In a first approach the influence of the different ethane levels in both HP types was examined. The result is the same as stated in the literature, for example in Marcus (1972) (p.73–74): The HP is most effective if the capillaries are filled with ethane completely because a deficiency can cause a dry-out. Excess working fluid on the other hand also should be avoided. Firstly, it may form a liquid plug blocking parts of the condenser region, secondly, it could interfere with the vapour flow inside the heat pipe.

Influence of ethane level

Different heat pipe types and different shapes were compared. In figure 3.26 the temperature behaviour of different amounts of ethane in straight and bent camera-type heat pipes is shown (exemplarily for one condenser temperature). The upper lines represent the evaporator temperatures, the bottom lines the temperatures in the adiabatic region. The vertical green line marks the begin, the red line the end of the microgravity phase.

A measure for the capillary pressure was the slope of the temperature drop. The steeper the curve, the faster the heat pipe reacted and the higher the driving force.

It was conspicuous that the temperature sensor nearest to the ethane surface of the heat pipe with the 0.88 g was rising instead of dropping (sensor 1b in the upper plot of figure 3.26). This could be explained by the fact that the corresponding sensor was at or even below the liquid surface, depending on the exact temperature. A rise of the liquid level due to capillary forces in zero gravity therefore was supposedly not able to cause a temperature drop. On the other hand, this part of the heat pipe was now exposed for vapour condensation which initiated the increase in temperature. To confirm the presence of capillary force, an additional sensor (1a) was attached above the said one. During the next drop this sensor proved the full functionality of the heat pipe.

Unsurprisingly, the heat pipe with half the ethane amount had the weakest temperature decline. So for further tests this one was skipped. The same applied for the heat pipe with the spiral spring inside which did not work properly at all. The spiral seemed to inhibit the capillary forces rather than to increase it. Summing up, in all cases only the lower temperature sensors showed significant temperature drops. The velocity of the liquid ethane inside the capillaries was barely fast enough to reach the evaporator. Only a very decent reaction could be detected.

The bent camera-type HPs showed a very similar behaviour. This indicates that the bending does not influence the quality of the capillaries significantly. The slope of the two heat pipes is almost identical (figure 3.26) which means that the HP functionality is not too sensitive to the amount of ethane as long as the capillaries are filled. For further tests only HP B with 0.86 g ethane was used.

The ring-type HPs in general showed a faster progression of the liquid front, which was expressed by a quicker response of the temperature sensors. The sensors at the evaporator all showed a major temperature decline, while the bottom sensors measured

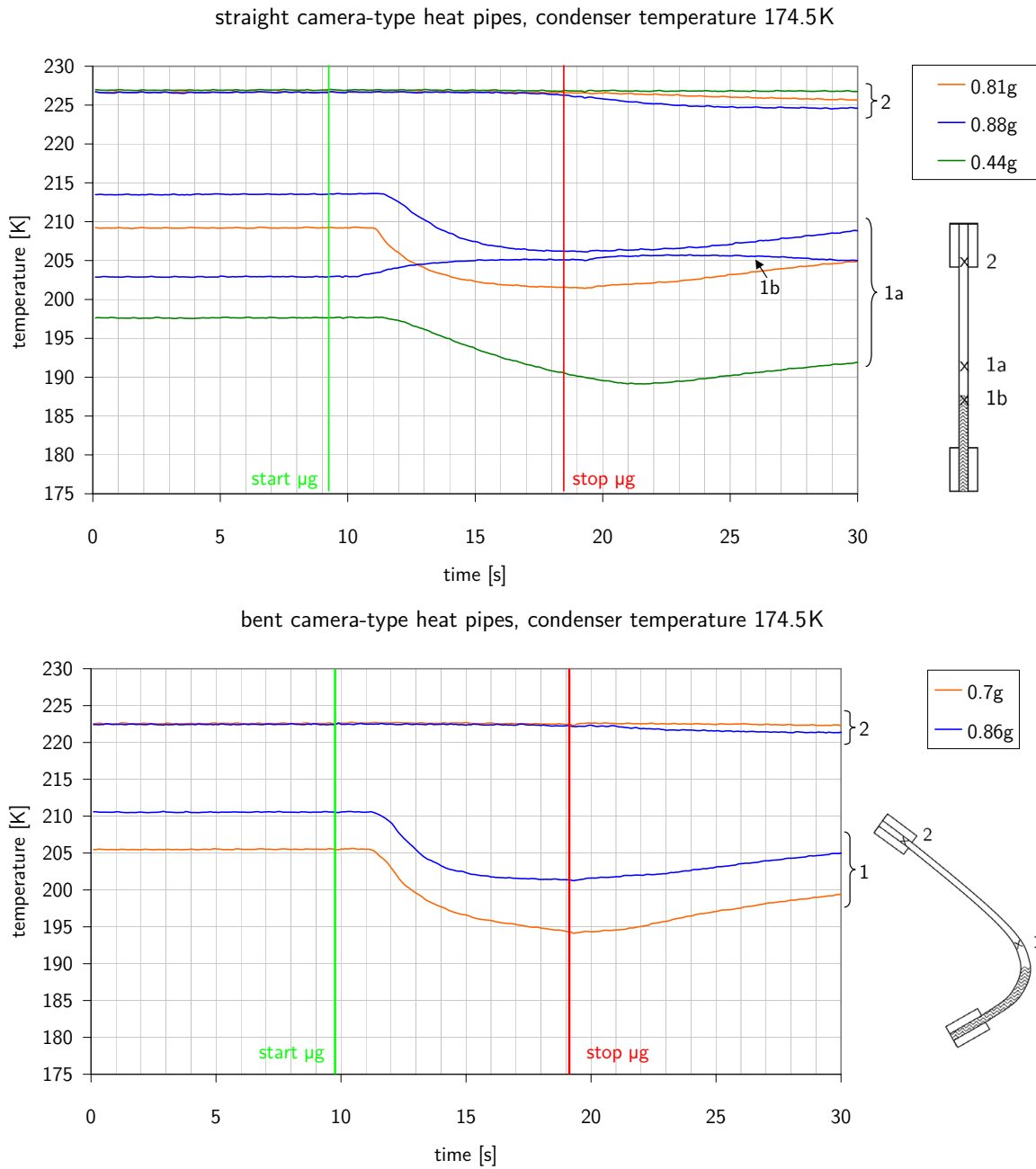


Figure 3.26: Temperature curves of straight (top) and bent (bottom) camera heat pipes with different ethane levels

an increase in temperature, see figure 3.27. This effect was similarly in all the ring-type HPs, but unlike to the camera-type HP – as described above – a short temperature drop was detected in the beginning. The only exception was the sensor of the HP with the largest ethane mass. Again the sensors were attached close to the liquid level but this time above. So they were first passed by the rising liquid before the vapour condensation – followed by the temperature rise – began.

At the working temperature of 173 K both HPs with 2.41 g and 2.47 g showed the steepest slope. This amount corresponds to full capillaries but no excess ethane. For a higher condenser temperature less ethane was more effective, for a lower condenser temperature the heat pipe with 2.97 g showed the steepest cooling curve. The lower the temperature, the higher the density and the more ethane is required. As before, the delayed onset of the temperature drop was a consequence of different ethane levels.

After the first drop the bent ring-type HPs turned out to be too long, so the ethane was not able to make it to the evaporator within the μg -phase (figure 3.28). In the 4.54 g-heat pipe the ethane level seemed to scratch around the curvature. During impact of the capsule, a small amount of ethane was forced to the evaporator which caused a sudden temperature drop (refer to note in figure 3.27).

In order to prove that assumption, additional sensors were attached to each of the bent HPs – with a maximum distance to the ethane level that could be covered during the drop. The ethane should have been able to reach the sensor but should also have passed the curvature. Baseline for this position was the first rough estimation of the capillary force velocity of about 3 cm s^{-1} (calculated with data of the straight heat pipes). The temperature decline (orange curve in figure 3.27) proved that capillary forces also work in bent ring-type geometries.

Influence of condenser and evaporator temperatures

Now that we found the optimum filling level at the nominal working temperature, we examine the behaviour of one constellation over a certain temperature range. The results are shown exemplary in figure 3.28 for both straight HP versions. Even if the temperature drop was smoother for lower temperatures, the HPs did not stop working and they contained still enough ethane to reach the evaporator. Another result was the temperature dependence of the capillary velocity. The higher the condenser temperature, the faster the ethane progressed. This observation is examined more closely in the next section.

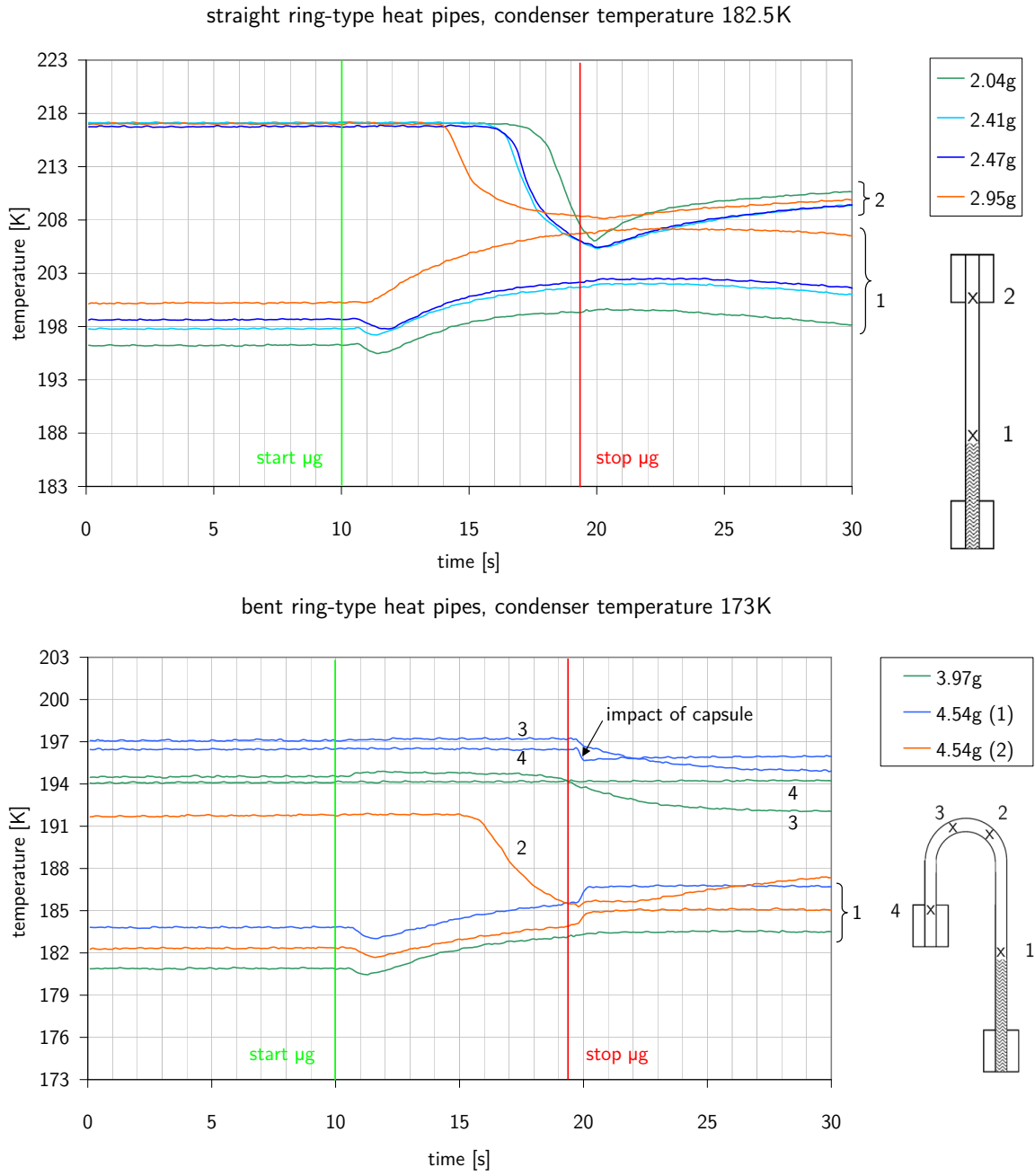


Figure 3.27: Temperature curves of straight (top) and bent (bottom) ring-type heat pipes with different ethane levels

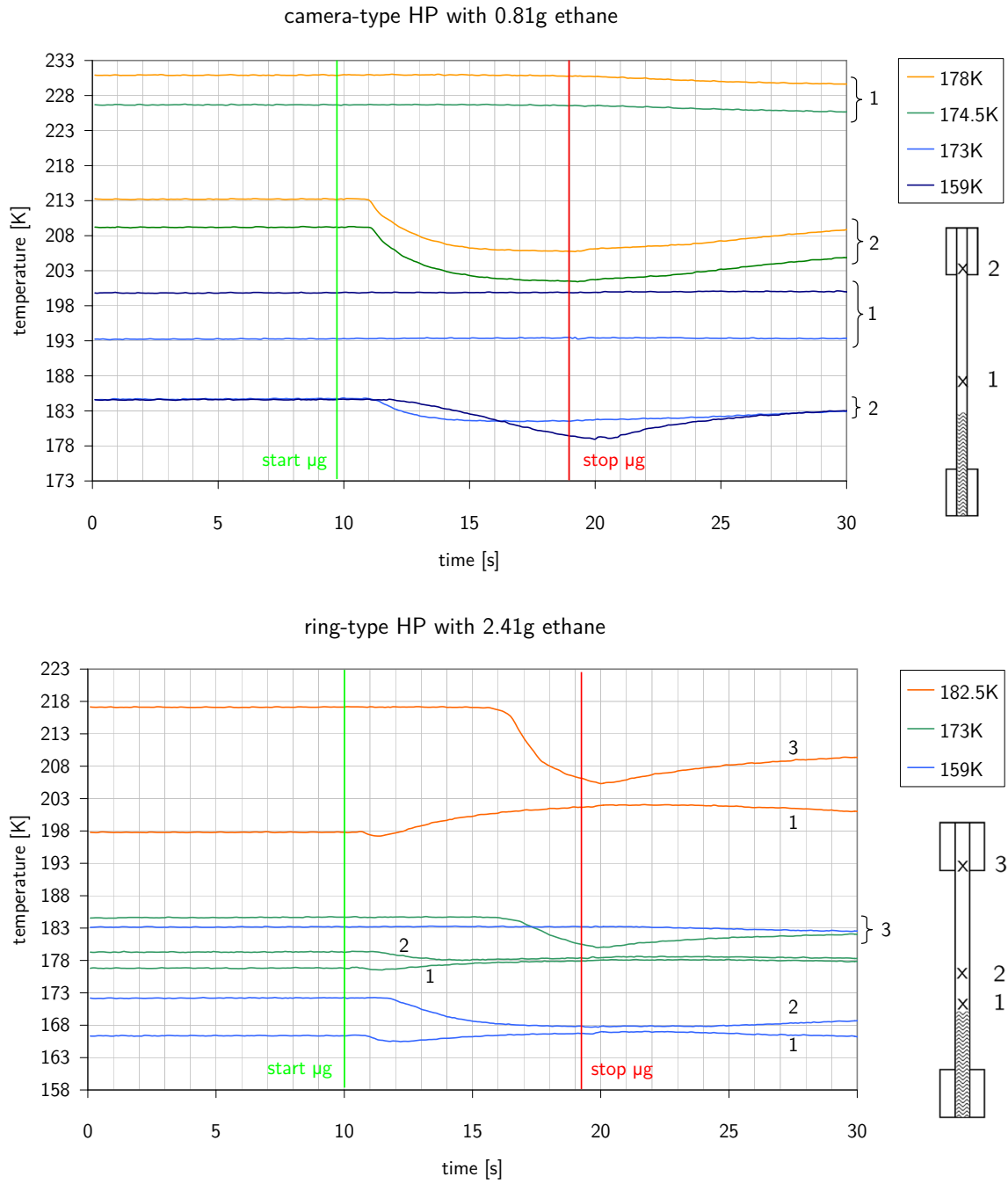


Figure 3.28: Optimum ethane level at different condenser temperatures for camera-type (top) and ring-type (bottom) HPs

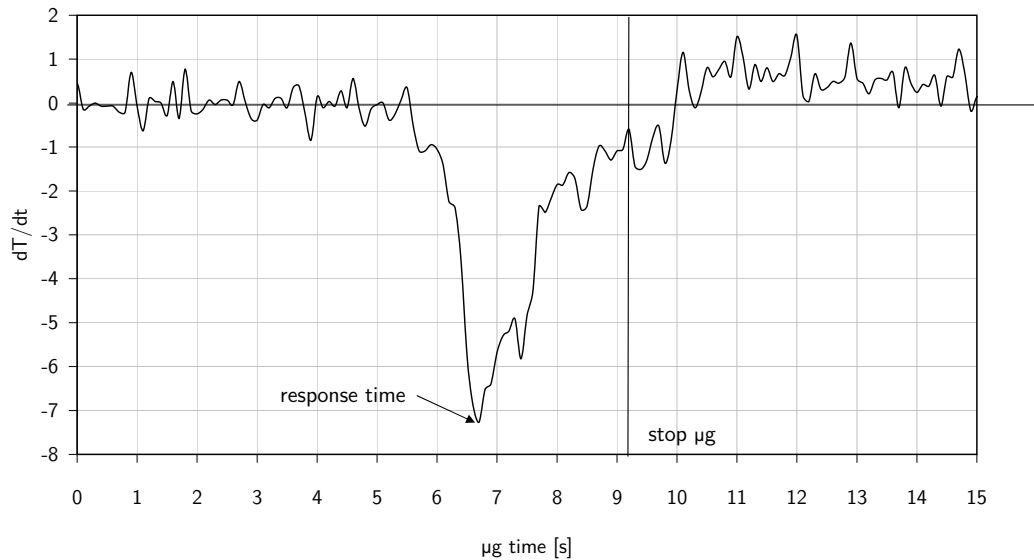


Figure 3.29: Determination of the sensor response time with the first time derivative

Capillary velocity

Besides the qualitative HP performance depending on filling level, we also can make a statement about the liquid phase velocity inside the grooves.

The actual liquid level inside the tube strongly depends on the ethane density (and therefore on the temperature). And due to gradients in the set-up we could not simply equal the ethane temperature with the cold storage temperature. So we mainly used HPs with at least two responding sensors during zero gravity (refer to figure 3.23). The accurate time measurement guarantees a maximum reliability of the (varying) covered distance.

To determine the exact response time, the minimum value of the first derivation of the temperature curve was used. An example is shown in figure 3.29.

Nevertheless, this value is the biggest uncertainty (0.5 s to 1 s) and mainly responsible for the error bar in the ring-type HPs. By reason of smaller liquid velocities in the camera-type HPs, in most cases the sensor at the evaporator did not respond within the zero-g-time. Only in a few cases we could process the data similarly. When using the (uncertain) liquid level before the drop, the second important error contribution is because of the covered distance (uncertainty of 10 mm to 20 mm).

The results, plotted against the estimated ethane temperature, are summarized in figure 3.30. To determine the ethane temperature, the sensors of the cold storage and the lowest sensor on the HP were compared. The closer to the ethane level, the more reliable was the sensor at the HP. In addition, the thermal conductivity through the HP tube and the ethane were taken into account.

A light temperature dependence of the liquid velocity is present, due to the temperature dependence of density and latent heat of vaporisation. Comparing equation (3.28) with equation (3.29) and using equation (3.32), we get the theoretical prediction for the liquid velocity in the capillaries:

$$u_{l,cap} = c \cdot \frac{Q}{H_v \rho_l A_w \varphi} \quad (3.56)$$

with Q the applied power, H_v the latent heat of vaporisation, ρ_l the liquid density, A_w the liquid flow area, i.e. the wick cross section, and φ the wick porosity. To fit the experimental data, we additionally have to introduce a constant of proportionality which accounts for the deviations of the theoretical value and the measurements. While $c = 2.8$ is sufficient for the camera-type heat pipes, we need $c = 25$ for the ring-type HPs, so the line of best fit matches the experimental values. This indicates either wrong assumptions regarding the parasitic heat loads, the latent heat of vaporisation, the density, the capillary cross-sectional area or the porosity. Since H_v and ρ are properties of the working fluid, only wrong temperature assumptions of the liquid contribute to their total error. This fact is responsible for the horizontal error bars.

Q can be estimated from the equilibrium data before the drop. Its error is not supposed to be greater than 20%. Though φ and A_l both may differ, the porosity cannot explain a factor of 2 or more¹¹. Apart from that, we could narrow the geometric properties during the thermal balance tests (table 3.3, section 3.4 and section 3.5). So the only possibility left is a smaller effective liquid cross section as a reason for the higher liquid velocities. This indicates that not the complete capillary cross section is used for the liquid flow. While the camera-type data can be fitted by only minor deviations of the assumed parameters, the high velocities of the ring-type HPs may indicate that only a small amount of the capillaries is wetted during the drops.

For the maximum power transport capability, we had to create a thermal equilibrium. This was done separately, see section 3.4 for camera HPs and ring HPs and section 3.5 for the sVCHPs. Results from this chapter are included in the calculations.

¹¹ $0 \leq \varphi \leq 1$

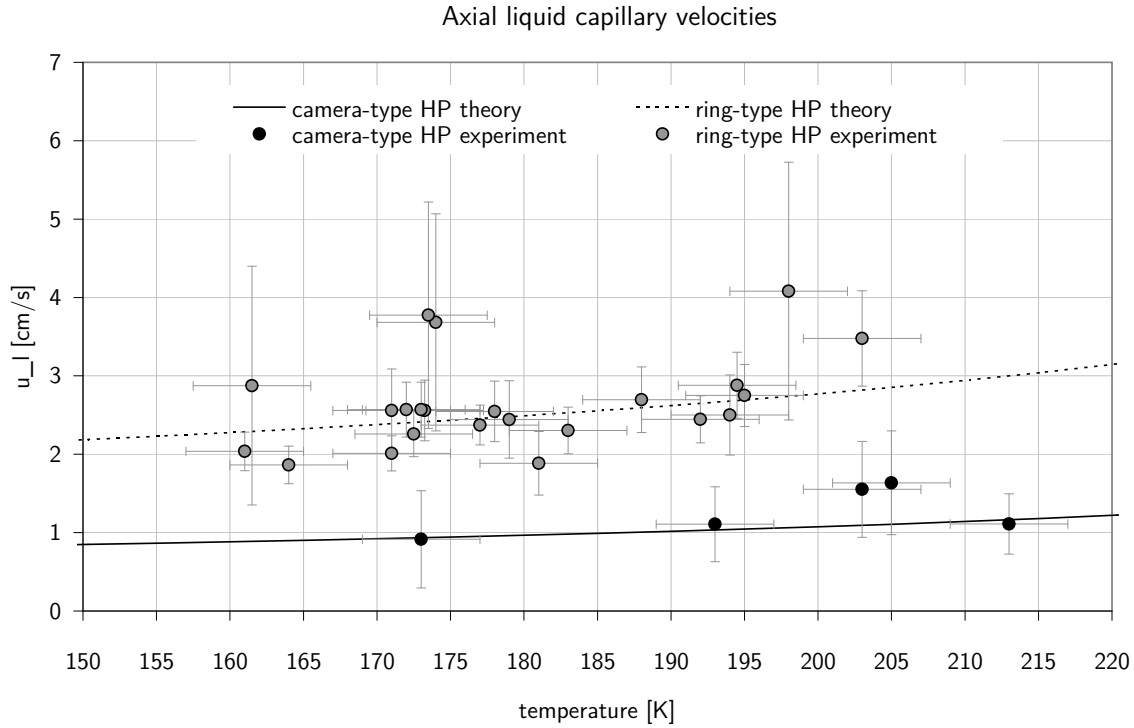


Figure 3.30: Capillary velocities for the liquid phase. For the error mainly the response time uncertainties are contributing, but in some cases also the covered distance. The theoretical curves use equation (3.56) with an additional constant of proportionality c and $Q = 3 \text{ W}$ (derived from thermal equilibrium data before the drops), H_v the latent heat of vaporisation, ρ_l the liquid density (both from Lemmon et al. (2012)), φ the porosity from table 3.3 and, respectively, $A_w = 5.1 \times 10^{-6} \text{ m}^2$ and $A_w = 1.4 \times 10^{-5} \text{ m}^2$ for the wick cross section of camera- and ring-type HPs. The constant of proportionality is $c = 2.8$ for camera-type HPs and $c = 25$ for ring-type HPs (explanation see text).

3.4 Camera and ring heat pipe equilibrium performance

After prove of the general functionality, thermal balance tests were required to define performance parameters such as heat transfer coefficients and maximum power transport capabilities.

3.4.1 Camera heat pipe

Different versions of the camera HP were mounted in the small vacuum chamber LUCHS. One was only bent in one dimension to rule out gravity effects, the other had the flight-like bending in two dimensions (refer to chapter 2). Besides, the ethane masses were slightly different. Figure 3.31 shows the test set-up. A stirling cooler was able to control the cold plate down to 77 K, a foil heater at the HP evaporator could apply heat up to 11 W. A cover blanket of multi-layer insulation suppressed parasitic heat loads due to radiation.

In general the temperature difference between evaporator and condenser was smaller than 1 K for powers up to 2 W. The exact value was temperature dependent. For larger heat loads the heat transfer coefficient of the container produced a proportional temperature gradient. Dry-out occurred when the maximum heat load was exceeded (see figure 3.32).

As soon as the dry-out occurred or the temperature gradient between evaporator and condenser exceeded 10 K, the maximum heat load was reached per definition. In figure 3.33 the theoretical predictions for the capillary limit, got from equation (3.35) and (3.39), are compared with the experimental results. With the original values, the theoretical curve peaks between 180 K and 190 K. To shift the theoretical maximum towards higher temperatures, the effective area for the vapour flow – former the geometric inner radius – has to be reduced about 30%. Discrepancies between geometric and effective values were already observed when determining the liquid velocity (see section 3.3.3).

At high temperatures the performance is much better than predicted by the capillary limit. This effect is evident for all eROSITA ethane heat pipes. Near the critical point at 305 K the heat pipe was still working and was capable of transporting about 3 W. This was already observed by Kobel et al. (2003). Surprisingly even beyond the critical

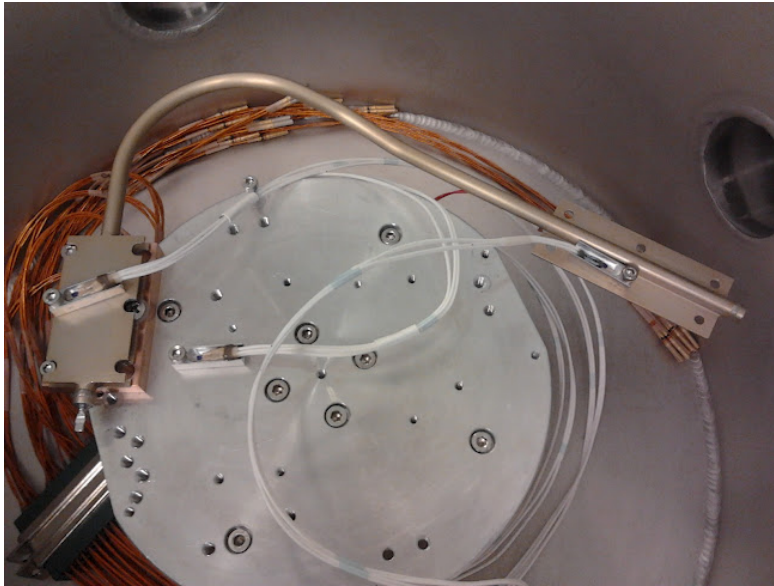


Figure 3.31: Camera heat pipe qualification model in vacuum chamber LUCHS for extensive measurements

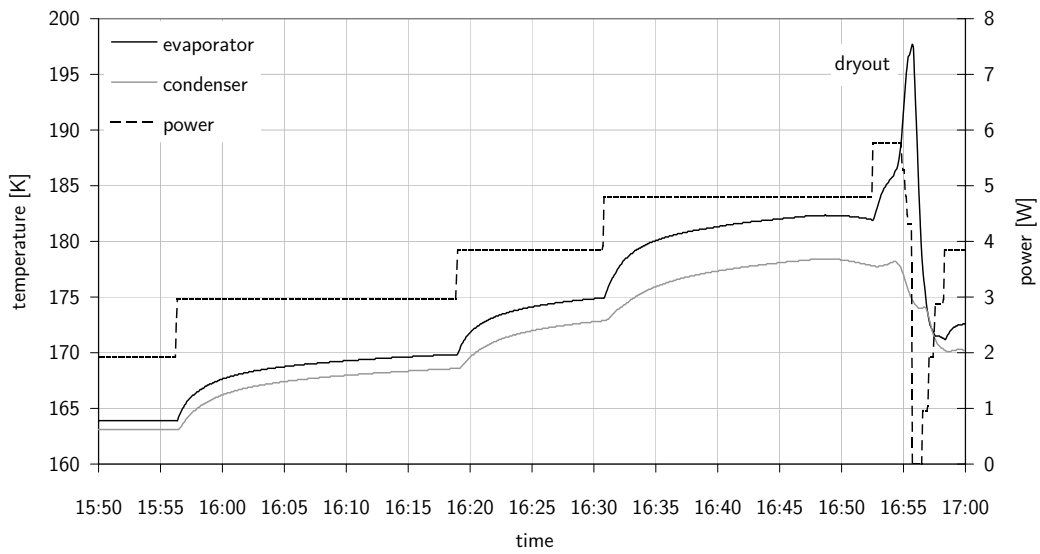


Figure 3.32: Determination of the maximum heat transport capability of the camera heat pipe at a condenser temperature of about $T = 175$ K.

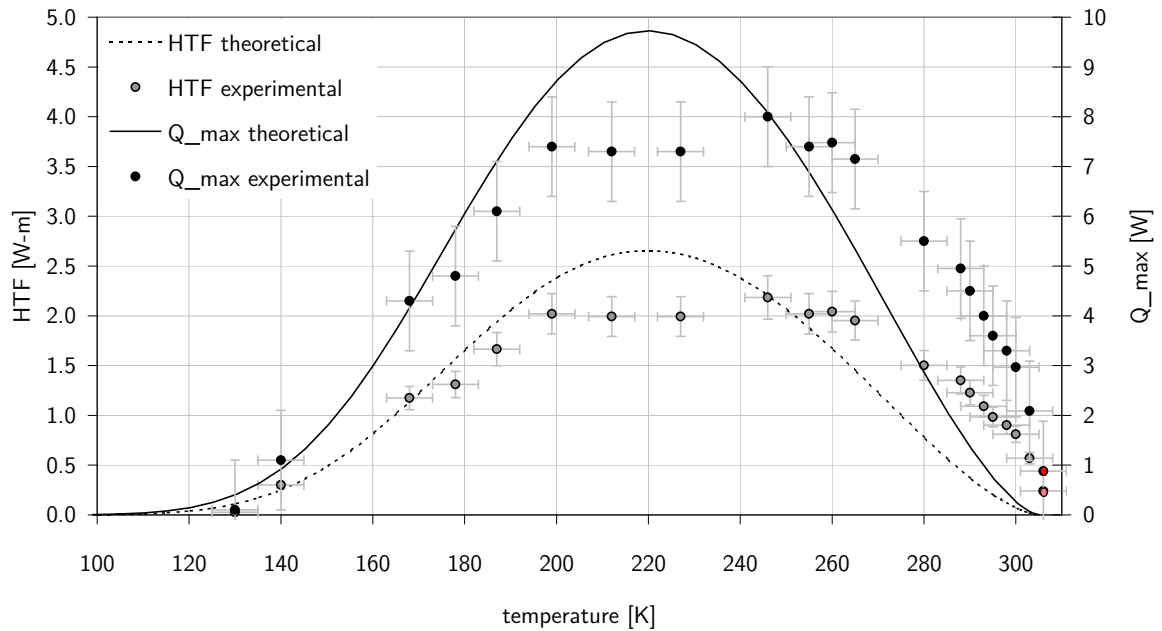


Figure 3.33: HTF and maximum heat load of the camera heat pipes in capillary limit, predictions calculated with equation (3.35) and (3.39). A minor reduction of the theoretical effective vapour radius is necessary to shift the theoretical maximum towards higher temperatures. Also the effective liquid cross section has to be smaller than the theoretical value to explain the data. Since the asymptotic behaviour for higher temperatures is based on the material properties of ethane, it is not possible to fit the data for $T > 260$ K. Even beyond the critical point a small heat transport capability is left. This behaviour cannot be explained by standard heat pipe theory (see text). The slight performance decrease around 200 K may be due to entrainment effects (compare to figure 3.47). The temperature error mainly is based on deviations from the actual ethane temperature, since the condenser temperature is used in the plot. The power error accounts for the uncertainties in the determination of the maximum power.

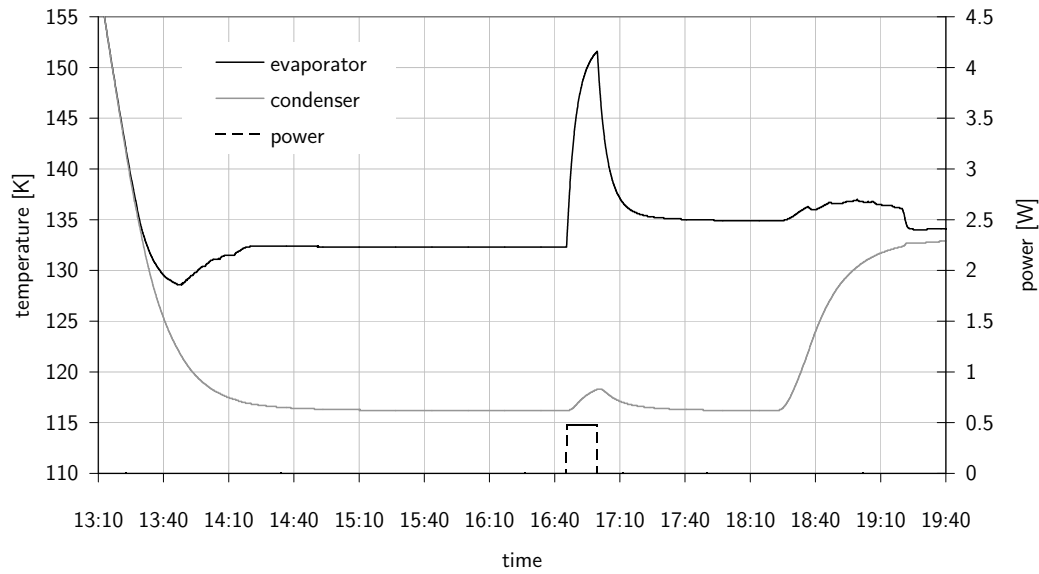


Figure 3.34: Low temperature dry-out. For temperatures below 130 K heat pipe functionality is no longer present. Due to the high density the evaporator is not provided with enough liquid.

point, where condensation is no longer possible, a certain amount of HP performance remained (see red marks in figure 3.33). The heat transport capability was very low, however, and "dry-out" occurred very fast.

This phenomenon of small but effective heat transport in a supercritical fluid may explain the deviations from the theoretical capillary limit. Saturation of the wick with liquid is not necessary, the supercritical fluid phase provides an effective heat transport.

At the lower end of the temperature curve the heat transport capability reaches zero at about 135 K. Since the density increases with lower temperatures while the viscosity increases, the liquid film collapses at some point. As soon as the evaporator is not provided with enough liquid, heat transport is no longer possible. Above a certain temperature HP functionality starts again as can be seen in figure 3.34.

Noticeable was the behaviour between approximately 200 K and 140 K if the amount of ethane was about 10% above the optimum mass that fills the capillaries at working temperature. Without any heat load the temperature gradient over the HP suddenly increased and turned into an oscillatory behaviour when enough heat load was ap-

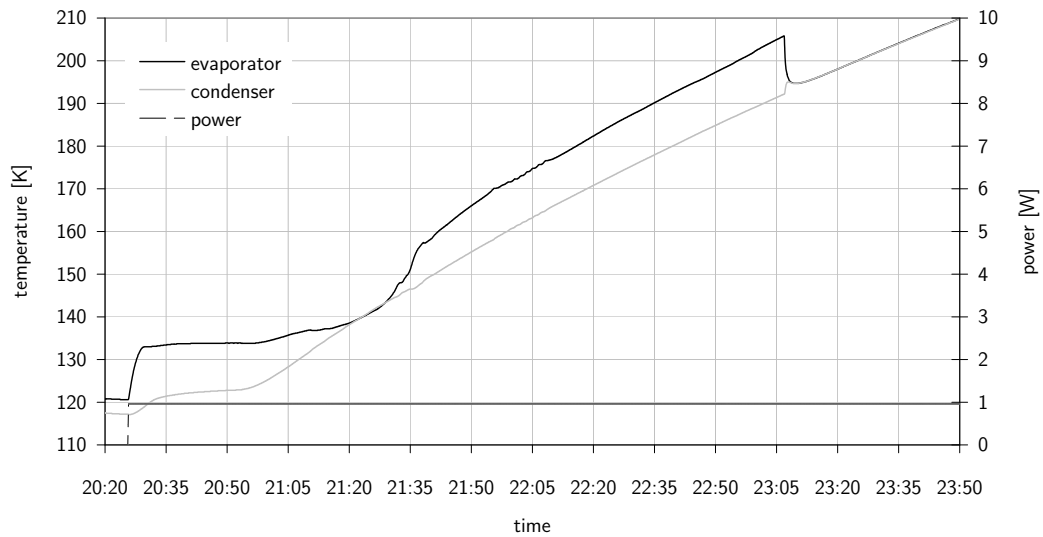


Figure 3.35: Reduced heat transport capability at the camera heat pipe evaporator for 10% excess of ethane mass. The applied power was 1 W which was not enough to cause large oscillations but demonstrated the decreased HP performance.

plied. These oscillations vanished with increasing heat load (the exact value again was temperature dependent), see figure 3.36 and figure 3.35. The transition happened in a temperature range of about 10 K and the power values were slightly dependent on the pre-treatment and the exact cooling or heating procedure. But within these boundaries the behaviour was always the same. Beyond these limits the HP worked perfectly with almost zero temperature gradient.

Oscillations normally are a phenomenon in thermosyphons, that means gravity-assisted HPs in more or less vertical position that do not need capillary forces for liquid transport. Three different origins are known for oscillatory behaviour (Faghri 1995, p. 398 ff.):

- Near dry-out oscillations (unstable liquid rivulet)
- Geyser boiling (liquid superheating at high filling rates)
- Flooding oscillations (entrainment of the liquid by the vapour in the evaporator section)

Due to the fact that oscillations vanished with increasing heat load, dry-out could be

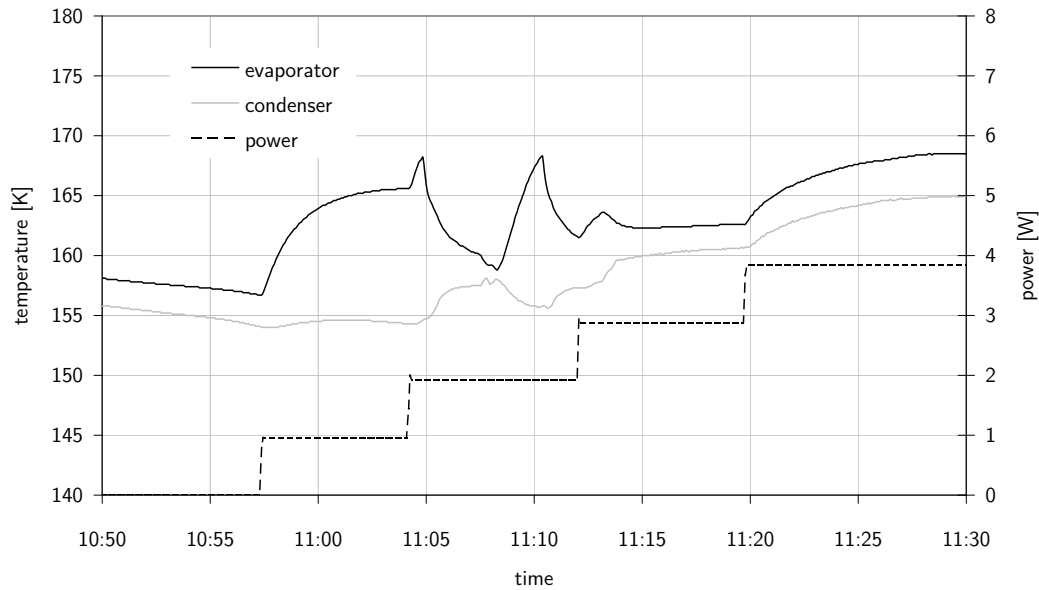


Figure 3.36: Camera heat pipe with 10% excess ethane at $T = 170$ K. With increasing heat load oscillations occur, for higher loads they vanish.

excluded. Since oscillations also vanished with very low temperatures where the shear forces increase, flooding as the reason also could be dropped.

So geyser boiling is the only possibility left. In this case this was not a classical dry-out of the wick but a steady nuclear boiling phenomenon. This may be explained by a low heat transfer coefficient between the evaporator wall and the vapour because of accumulation of liquid at the bottom of the evaporator section.

The heat input was insufficient to cause a steady, smooth vaporization state, so the liquid in the evaporator region became superheated. Vapour bubbles increased in size and caused a surge of liquid, being propelled to the condenser region. Afterwards the liquid fell back to the evaporator where the process started from the beginning.

Without gravity, the liquid will not concentrate at the bottom of the heat pipe but smoothly distribute over the complete evaporator area, which leads to the reasonable assumption that this phenomenon would not occur in space. The heat transport capability is influenced by the boiling limitation as shown in figure 3.37.

Besides the maximum heat transport capability, the second important value is the heat transfer coefficient (HTC) between evaporator and condenser, determined by the radial

heat flux at evaporator and condenser. This number defines the final temperature gradient over the HP and will be included in the thermal modelling.

With the equations (3.8) and (3.9), which were derived in section 3.1.2, and the data from table 3.3, we get the following predictions for the effective conductivity at evaporator and condenser (the effective conductivity of the wall is defined by the conductivity of the tube material, Al-6061):

- k_{eff} of evaporator/condenser wall: 167 W K^{-1}
- k_{eff} of evaporator grooves: $1-2 \text{ W K}^{-1}$
- k_{eff} of condenser grooves: 65 W K^{-1}

The effective conductivity at the evaporator is quite sensitive to the exact value of the ethane conductivity – which is temperature dependent – while the deviations of the condenser value are much smaller. Therefore the heat transfer at the evaporator determines the global conductivity. Inserting the effective conductivities in equation (3.5) gives the corresponding HTCs. The conductivity of the wall does not have a significant influence, since it is several magnitudes higher than the groove values. Connecting the HTCs in series finally gives the total value.

While the theoretical HTCs are constant for a specific temperature, the experimental results show minor deviations figure 3.38. A reason may be the varying ethane level in the capillaries which is assumed to be constant for the theoretical calculations. Furthermore the error is large for low heat loads. Uncertainties in the measurement then have a large effect due to small temperature differences.

The limiting factor is the evaporator conductivity, since it is by far the smallest value. So small variations in the porosity produce significant changes in the global HTC. Determining the capillary velocity in section 3.3.3 already showed a slightly decreased porosity.

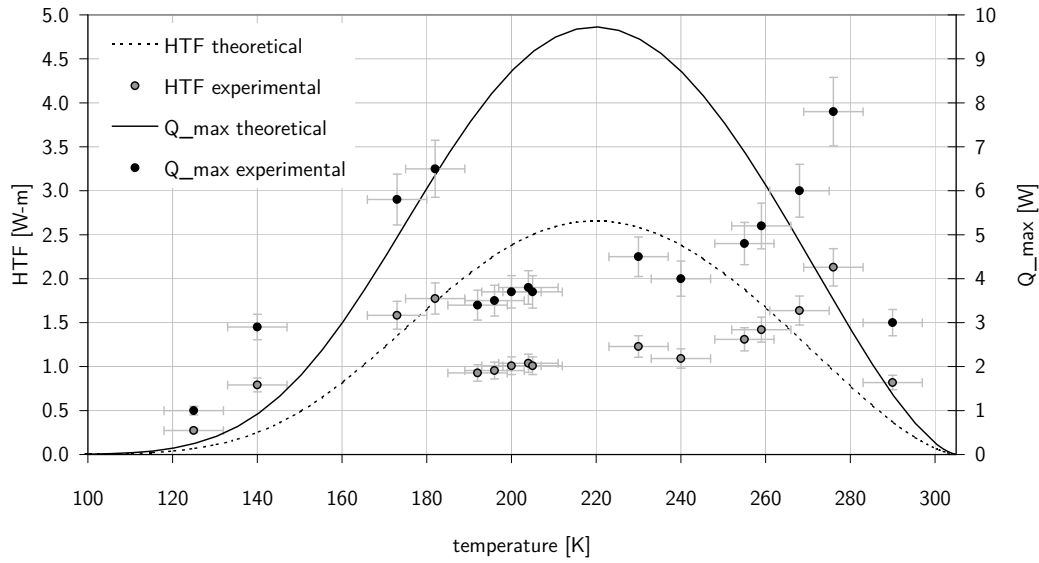


Figure 3.37: HTF and maximum heat load of the camera heat pipes in capillary limit with a 10% excess of ethane, predictions are the same as in figure 3.33. In the region where boiling occurs the heat transport is reduced.

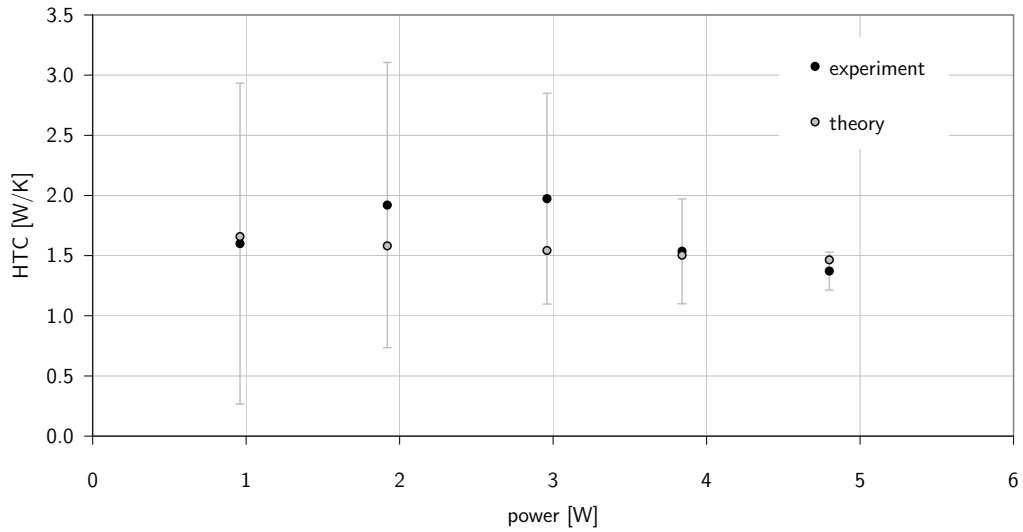


Figure 3.38: Global HTCs for the camera HP at 170 K. Error bars result from uncertainties in the temperature measurement. The higher the heat load is, the higher is the temperature difference and the smaller is the error.

3.4.2 Ring heat pipe

Since the ring heat pipe was too large for the LUCHS vacuum chamber, the thermal balance test took place during the camera assembly thermal balance test in the PANTER facility (see section 4.3). As long as no power was applied, the complete heat pipe was isothermal, see figure 3.39. The only exception was evaporator 2 with about 1 K gradient where the camera heat pipe was attached and therefore brought in a parasitic heat load. The cooling power of the radiator was the limiting factor, so the condenser temperature could not be kept constant during the performance test. Nevertheless, no significant gradients occurred until dry-out at about 35 W at 190 K. In case of failure of one ring HP, the other has to transport about 25 W, including parasitics. Due to the limitations of the test set-up it was not possible to measure the maximum heat transport capability for different temperatures.

The total HTC was calculated similar to the one of the camera HP. All seven evaporators were connected in parallel, while evaporator and condenser were connected in series again. Figure 3.41 shows the experimental results which are consistent with the calculations. Further measurements will be made with the qualification model.

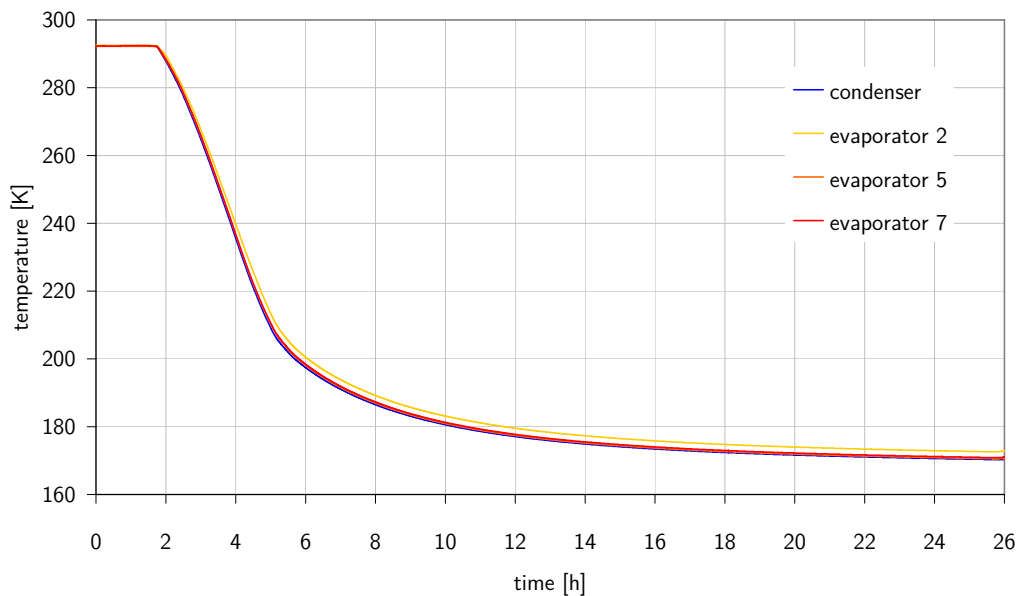


Figure 3.39: Cooling curve of the ring heat pipe

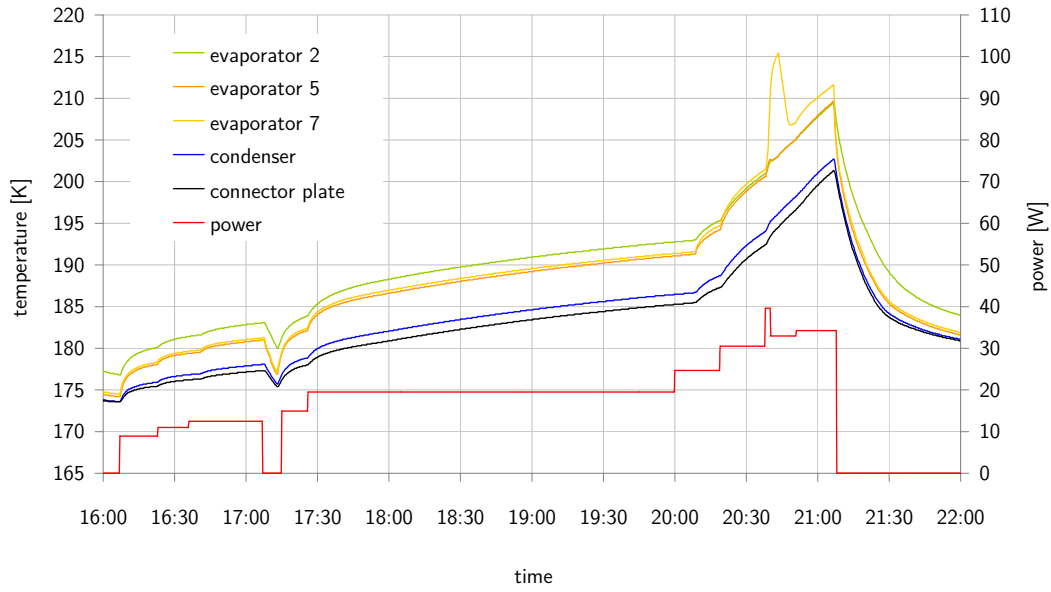


Figure 3.40: Performance of the ring heat pipe

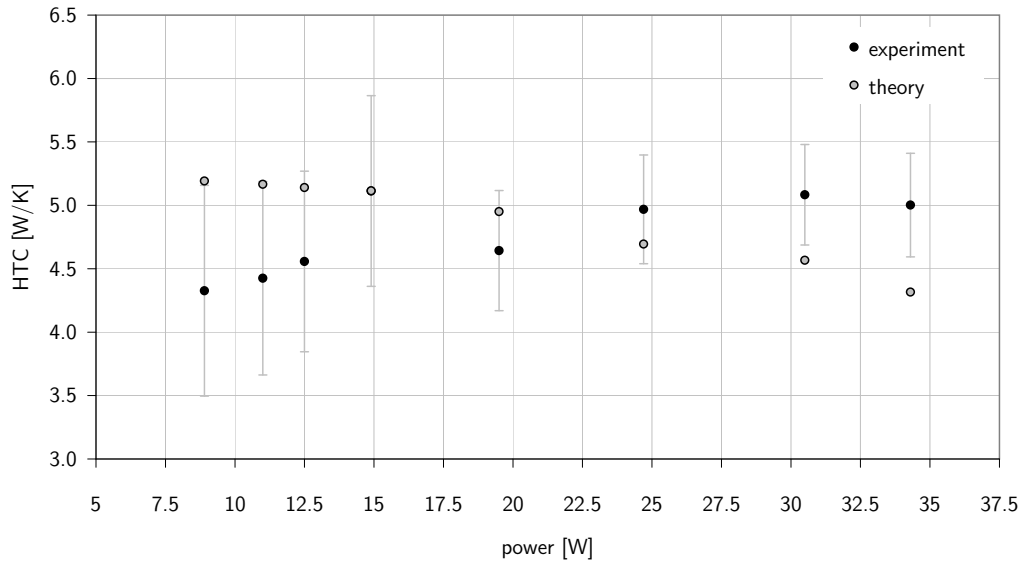


Figure 3.41: Global HTC for the ring HP at about 180 K. Deviations from theory can be explained by a slightly rising temperature during the test (from 175 K to 195 K).

3.5 Optimisation of the switchable variable conductance heat pipes (sVCHP)

During the camera assembly thermal balance test (section 4.3) the switchable variable conductance heat pipes (sVCHPs, refer to section 2.3 for a description) turned out to have a rather large temperature gradient between evaporator and condenser. Besides, one heat pipe showed clearly a better performance than the other one. Therefore improvements at this point may be able to reduce the CCD temperature by a few more degrees.

Thermal modelling showed that about 35 W in total have to be transported to both radiators. This results in up to 10 W per sVCHP in nominal operation. To fulfil the redundancy requirements, each heat pipe has to be capable of transporting at least twice the power in case one heat pipe does not work. The maximum heat transport depends – among the geometry, wick design and ethane properties – on the amount of working fluid. Too less ethane would cause a dry-out of the wick. For grooved heat pipes it is rather easy to calculate the amount of working fluid that is necessary to fill the grooves without generating a fluid excess. The optimum ethane mass for the mesh wick only can be estimated in advance. However, due to the very long condenser even a slight excess of working fluid would not cause harm.

Straight and bent heat pipes were examined. Due to the special bending in two dimensions it was not possible to align the sVCHP in a single plane. Therefore, the final shape could only be tested gravity assisted. To guarantee sufficient capillarity in zero gravity, also a straight heat pipe with identical length was tested.

The second compound inside the heat pipe besides the ethane is the non-condensable gaseous nitrogen. Its purpose is the control of the heat transport efficiency at the condenser. The larger the volume of the nitrogen, the less condenser area is available for the ethane circuit (section 3.1.5). Even if this volume can be calculated more accurately, this value is critical and has to be adjusted very precisely to prevent a condenser blocking in nominal operation. In the first test phase the optimum amount of ethane was determined. Afterwards, the influence of the nitrogen mass was examined.

The nitrogen mass has to be small enough to fit into the reservoir completely if no power is applied. Otherwise, the condenser runs the risk of being blocked permanently. Furthermore, this guarantees an optimum temperature control. By heating up the reservoir, the nitrogen level can be adjusted everywhere at the condenser. Too less

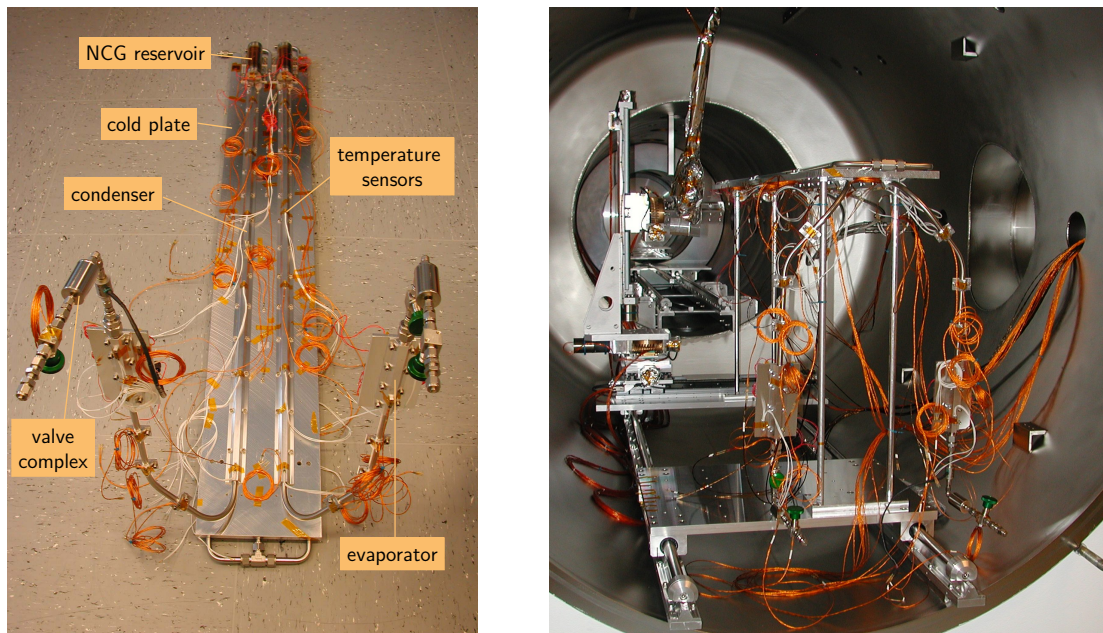


Figure 3.42: Test set-up for VCHP optimisation before (left) and after (right) integration into the vacuum chamber

nitrogen on the other hand would reduce the possible blocking range and in addition ethane may condense in the reservoir.

3.5.1 Test set-up

A set-up was designed for testing of two sVCHPs simultaneously. This ensured a shorter testing duration and better comparability of different filling levels. The cold plate was cooled with liquid nitrogen, heaters allowed for temperature control. Nitrogen reservoirs and evaporators of both heat pipes were equipped with heaters as well, temperature sensors were attached at several positions. The complete test report with a detailed discussion of the results may be found in Kim (2012).

3.5.2 Test results

Different amounts of ethane were tested in the bent heat pipes while the nitrogen amount was kept constant (the same amount as in the well working sVCHP of the

thermal balance test, 323 mbar at 293 K which is equivalent to 0.17 g). This was necessary due to the uncertainty of trapped ethane in the mesh wick. Heat load was applied step by step ($\Delta P = 5 \text{ W}$) at constant condenser temperature until the maximum heat transport capability was reached. This was defined as the power that made the temperature gradient between evaporator and condenser exceed 10 K within the first 10 min after start of heating. The results are summarized in table 3.6. The range of a suitable ethane mass is between 22 g and 33 g, so the exact filling level is not too critical. All heat pipes within that range were able to transport at least 20 W which is a factor 2 larger than the nominal heat load. However, due to the coarse power steps the maximum heat load is not too accurate. This is also reflected in minor deviations at similar test conditions. In those cases always the lowest occurrent heat load was chosen.

To define the optimum mass, the boundary values as well as temperature gradients between evaporator and condenser in the nominal operation mode with a heating power of 10 W were used as decision criterion. Best results were achieved with 27 g with only 1 K gradient. Additionally this value is far away from the lower and upper boundary.

Afterwards, this amount of ethane was paired with different nitrogen levels. The 0.17 g during the former test already seemed to meet the requirement of a free condenser area at maximum heat load paired with a good control functionality. But since a large part of the condenser was blocked in nominal operation, slightly smaller amounts were tested.

However, with an amount of NCG that was able to control the sVCHP at about 165 K, it was not possible to operate the HP at much lower temperatures. Beyond 155 K the ethane vapour pressure decreased so far that the nitrogen pressure was able to push the NCG front over the complete condenser towards the adiabatic section. Therefore the evaporator was thermally decoupled from the condenser and the temperature gradient increased if the condenser temperature was decreased even further.

With the 1D flat-front model (see section 3.1.5) it was possible to verify the location of the NCG very accurately, only limited by the test set-up (measuring of temperatures, position of sensors) itself. In figure 3.43 heat was applied at the reservoir. In the beginning, only a part of the condenser was blocked by nitrogen. In the end the complete condenser was inactive. For each time step the nitrogen-ethane front was derived from the data. In addition results of the flat-front model are added to the data.

Table 3.6: Performance of different ethane levels in sVCHPs

ethane mass [g]	condenser temperature [K]	max. power [W]	comments
14.4	160	10	–
14.4	170	10	–
21.5	160	25	–
21.5	170	25	–
21.8	160	25	–
24.2	160	30	–
24.2	200	30	–
25.8	160	35	–
26.1	180	≥ 25	no dry-out measurement
26.7	155	20	straight HP
26.7	190	22.5	straight HP
27.3	160	30	–
27.5	160	25	–
33.7	160	≥ 25	no dry-out measurement
36.0	175	≥ 25	no dry-out measurement
36.8	155	30	oscillations due to superheating

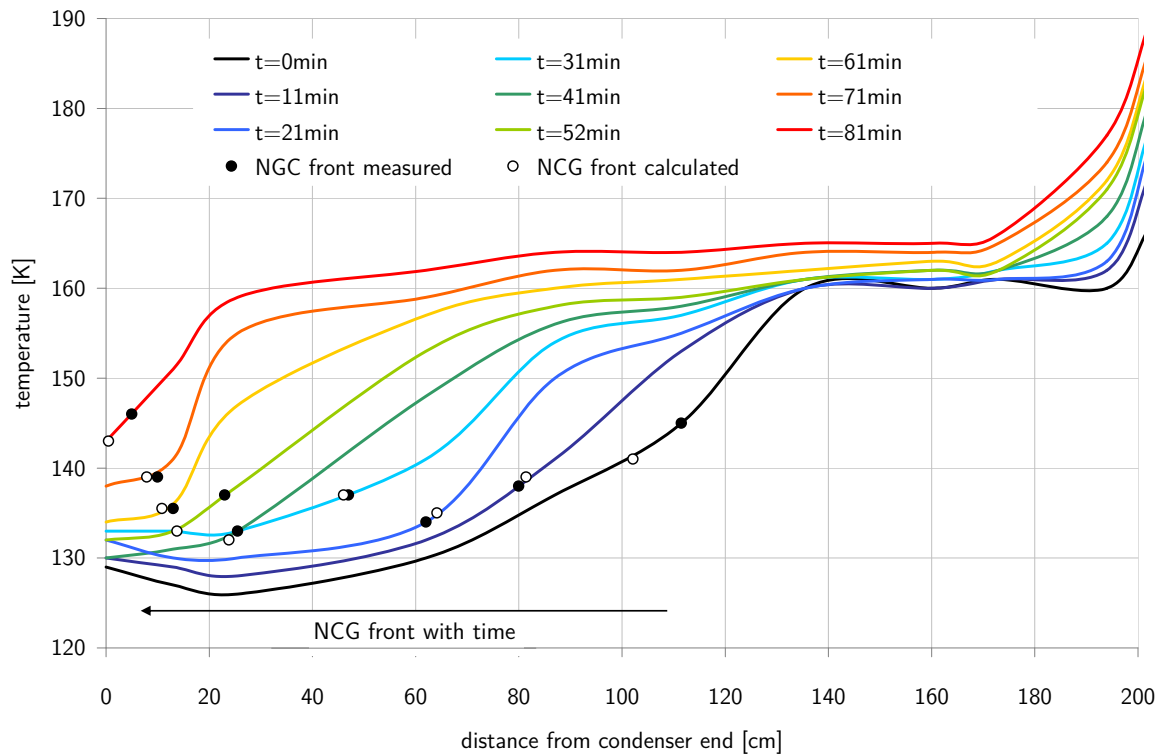


Figure 3.43: Time-dependent temperature profile of the sVCHP. In the beginning almost the complete condenser ($l = 120$ cm) is blocked with nitrogen. As a consequence it is much colder ($T \geq 125$ K, the cold plate was cooled with liquid nitrogen) than the adiabatic region ($T = 160$ K). Step by step, after power was applied onto the evaporator, the NCG front was shifted towards the condenser as indicated by the arrow. The area that was no longer blocked with nitrogen was then part of the active HP section. This caused a temperature rise until the active region was isothermal. In the end almost the complete condenser (from $l = 20$ cm) was thermally coupled to the rest of the HP. The measured NCG front was read off the data plots – a temperature sensor with suddenly increasing temperature indicated the receding NCG front. For the 1D flatfront-model calculations corresponding temperatures of adiabatic section and condenser were used as ethane and nitrogen temperature (taken from Kim (2012)).

Due to the large condenser the exact nitrogen mass is not as critical as in HPs with a short condenser, nevertheless it has to be determined very carefully to guarantee an optimum performance. The final mass has to be reconciled exactly with the working temperature. On the one hand it has to be ensured that enough NCG is present to allow for an effective temperature control. As long as no power is applied, most of the condenser should be filled with NCG. Also it has to block the reservoir when the maximum heat load is applied, so no ethane could condense there. On the other hand the diffusion barrier needs to recede and expose the condenser as soon as power is applied at the evaporator. Even for small heat loads the HP has to work. During nominal operation and without heat applied to the reservoir, most of the condenser should be part of the active HP region.

In table 3.7 the results for different nitrogen masses are summarized. Because of the NCG, it was not possible to reach any low temperature. The ethane vapour pressure has a steeper slope than the nitrogen pressure, so beyond a certain condenser and reservoir temperature the nitrogen always blocked the complete condenser – regardless of the exact mass. As a consequence, the radiator temperature distribution has to be determined very accurately before determining the final filling.

In this test set-up the lowest achievable evaporator temperature was between 158 K and 167 K. With 1D flatfront-model calculations we were able to make exact predictions of the HP behaviour and to constrain the final nitrogen mass, but it cannot be defined finally until the thermal vacuum test with the complete telescope under flight conditions (see chapter 7).

In the end a straight sVCHP with 27 g ethane, but without nitrogen, was tested to verify the maximum heat load capability without gravity assistance. As shown in figure 3.44, 20 W still could be transported at a temperature of 160 K which corresponds to a performance loss of about 25% in comparison to the bent HP. Figure 3.45 compares theoretical predictions and experimental values. The formulas used for the plots were derived in section 3.1.3, fluid properties were taken from Lemmon et al. (2012) and Funke et al. (2002).

The effective conductivity of the mesh was calculated with equation (3.10), but according to the comparison of theory and measurements the real value is slightly higher. Additionally, the effective liquid cross section is also enhanced to explain the high capillary limit. For the total heat transfer coefficient the same approach as of the other heat pipes was used. Results are summarized in figure 3.46(b). In addition the HTFs of evaporator and condenser were examined separately, see figure 3.46(a). While the

Table 3.7: Performance of different nitrogen levels. Nominal operation with $P = 10\text{ W}$ and $T_{cond} \approx 160\text{ K}$

nitrogen mass [g]	blocked condenser length in nominal operation [cm]	min. working temperature [K]	comments
0.188	≈ 100	not measured	data from camera assembly test
0.177	25–62	159	–
0.167	13–26	165	–
0.153	13–26	164	–
0.137	–	158	T_{cond} too low

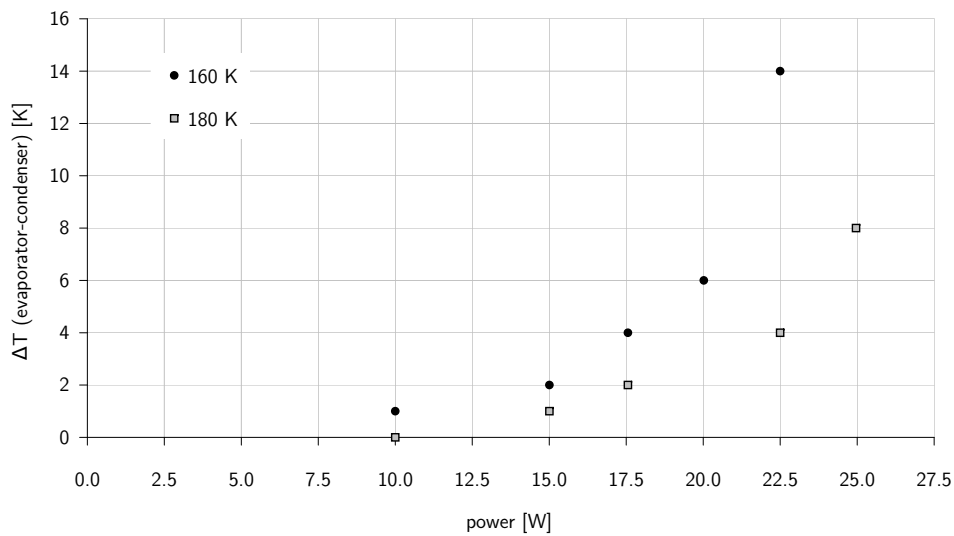


Figure 3.44: Dry-out curve of straight sVCHP with 26.7 g ethane. Temperatures were measured 10 min after power increase.

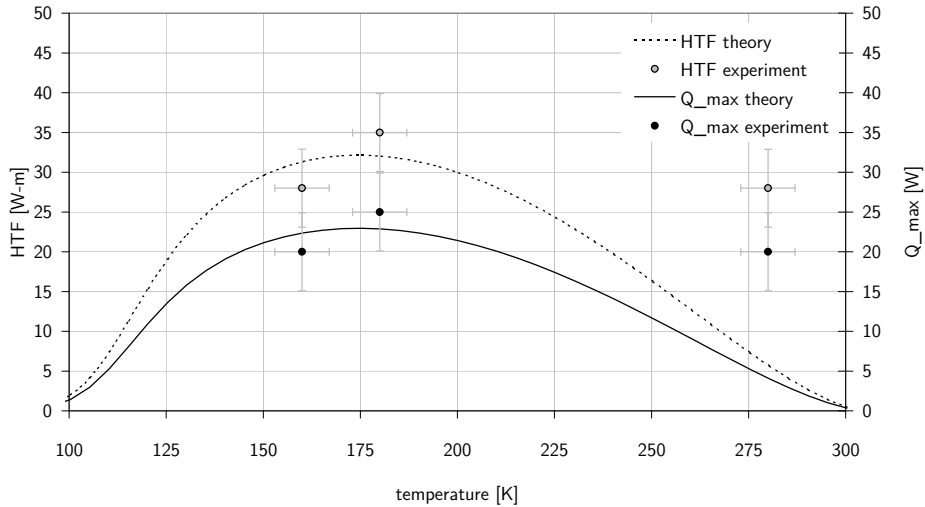
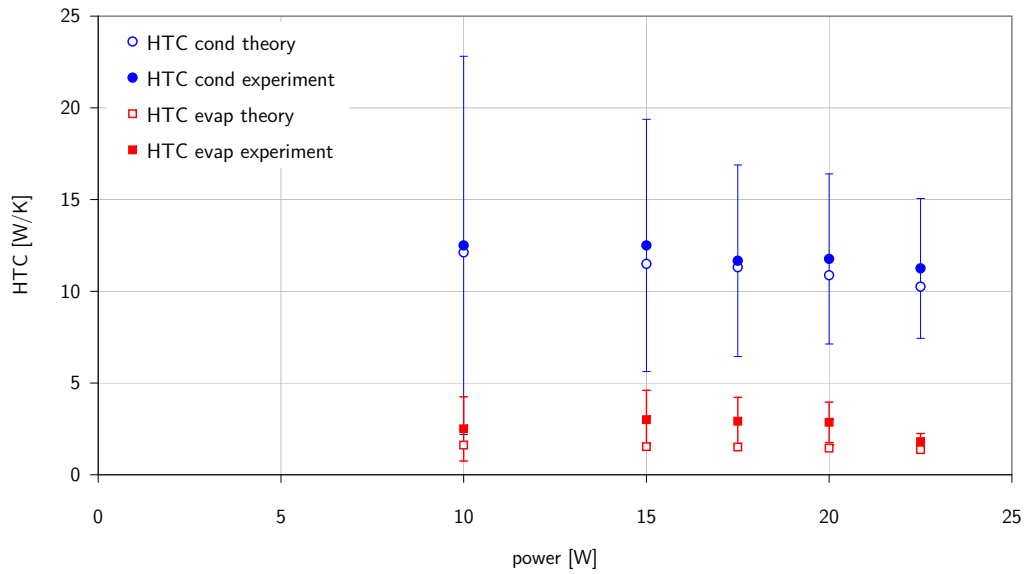


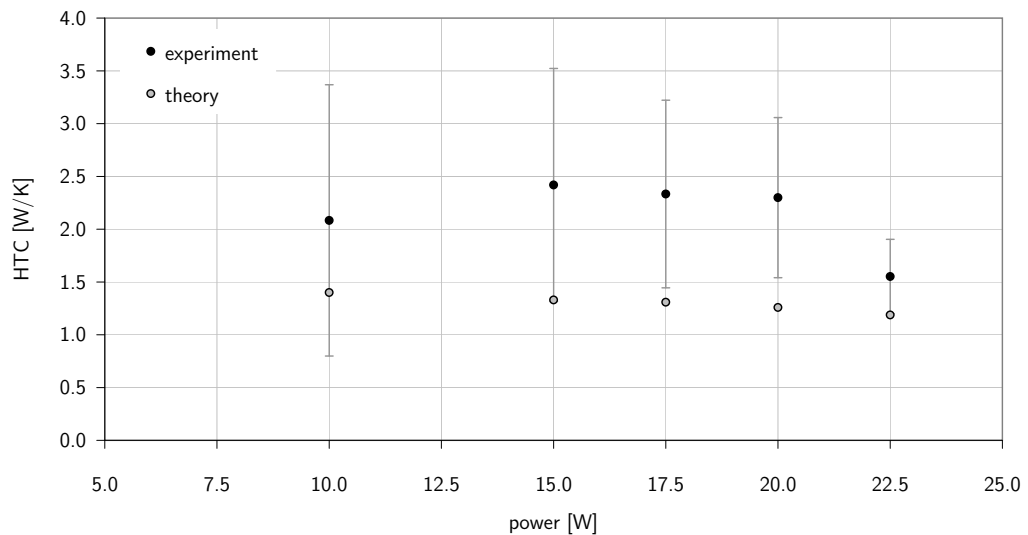
Figure 3.45: Theoretical HTF and maximum heat load of the sVCHP in capillary limit, calculated with equation (3.35) and (3.39). For high temperatures HP performance is much better than assumed.

HTF at the condenser is always at least 10 W K^{-1} , even at dry-out conditions, the HTF at the evaporator is limiting the performance. Its value goes down to 1 W K^{-1} .

The influence of the other HP limitations described in section 3.1.4 are examined for all three heat pipe types. For the given heat loads and temperatures, only entrainment and boiling limit need to be considered. The others are not expected to play an important role. The entrainment limit in the camera heat pipes is only slightly larger than the capillary limit. Reason for that is the very small inner radius which provides a significant resistance for the vapour flow. The results for the Weber number as well as the maximum heat transport capability due to the entrainment limit can be seen in figure 3.47. The boiling limit cannot be calculated exactly since the critical radius of vapour bubbles is unknown (see figure 3.48). But for reasonable values it is only dominant at higher temperatures. The Mach number and the corresponding sonic limit are presented in figure 3.49. It is not relevant for the eROSITA heat pipes. The same holds for the viscous limit (figure 3.50).



(a) Local HTC



(b) Global HTC

Figure 3.46: Global and local HTC for the sVCHP at a condenser temperature of ≈ 160 K. The deviations between theoretical and experimental data can be explained with the uncertainty in the effective wick conductivity (equation (3.10)) and by general uncertainties in determination of the temperature difference. The latter decreases with increasing temperature differences and heat loads respectively.

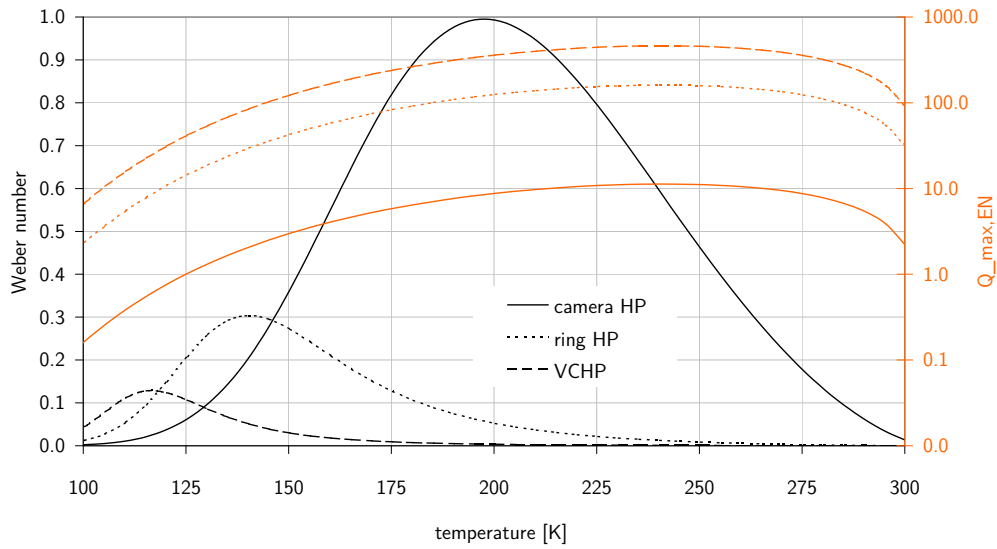


Figure 3.47: Weber number at capillary limit and entrainment limit for eROSITA HPs. We (equation (3.44)) is always smaller than 1. Only the camera HPs may be effected by entrainment for large heat loads, but the maximum heat transport capability for $We = 1$ still slightly exceeds the capillary limit. For nominal operation entrainment is not an issue.

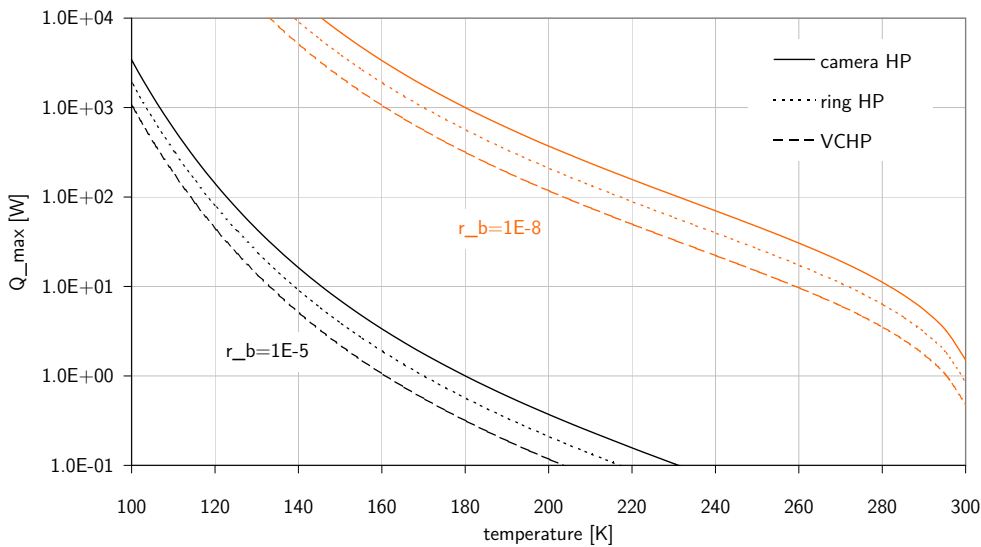


Figure 3.48: Boiling limit for eROSITA HPs. Boiling limit (equation (3.46)) strongly depends on the critical radius r_b .

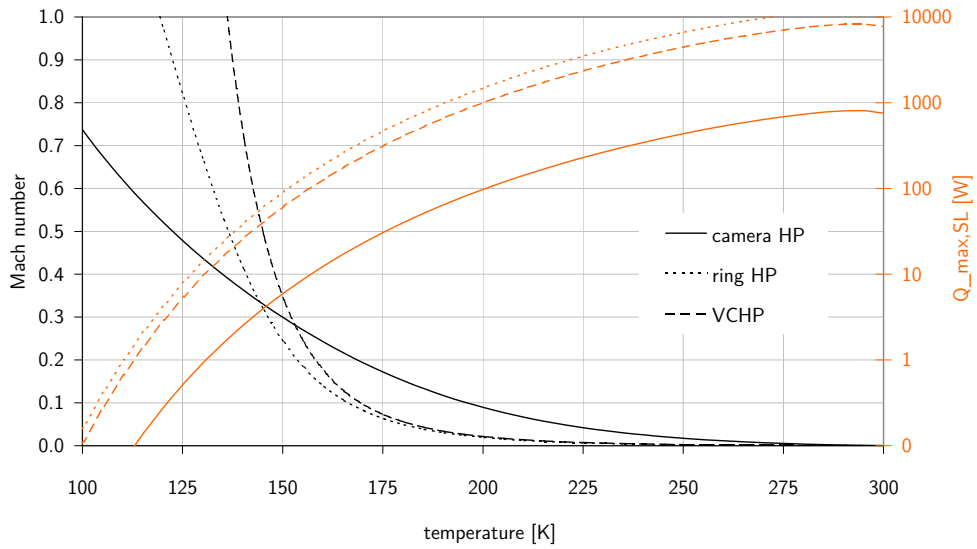


Figure 3.49: Mach number at capillary limit and sonic limit for eROSITA HPs. Since Ma (equation (3.42)) is always smaller than 1, the vapour velocity never exceeds the speed of sound. For calculation of the sonic limit $Ma = 1$ was used as cross check. The results always are above the capillary limit.

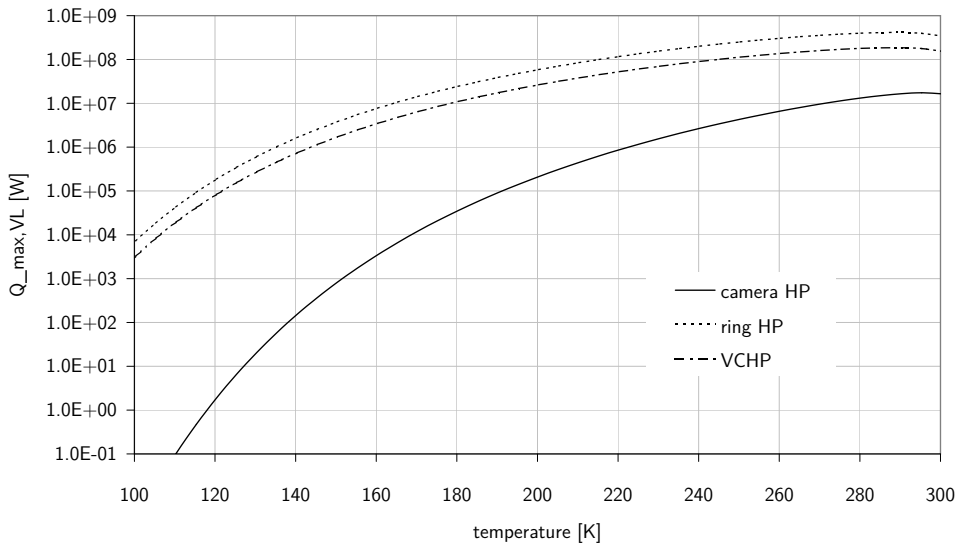


Figure 3.50: Viscous limit for eROSITA HPs. Viscous limit (equation (3.43)) is not relevant for the eROSITA HPs, the maximum heat transport capability always is much higher than the other limits.

4 Thermal design and analysis of the camera cooling system

In chapter 3 we optimized the three different heat pipe types of the eROSITA camera cooling system. Apart from that, the rest of the telescope also has to be modelled, tested and verified. The complete eROSITA thermal control system can be classified into four main parts:

- Telescope structure thermal control
- Mirror thermal control
- Camera thermal control
- Camera electronics thermal control

In this chapter the focus is on the camera thermal control, the other subsystems are discussed in chapter 5.

Due to absence of convection in space, the relevant mechanisms and equations for heat transport within the telescope are conduction and radiation. The basic mechanisms and equations are derived in appendix A. Like for many other physical problems, solving a spacecraft thermal model leads to a system of differential equations. Very common for heat transfer calculations is the lumped parameter method. With this method, a continuous medium is modelled as a discrete network of nodes, representing the heat capacity of the system, and linked by corresponding conductors. The conceptual origin of this method can be found in the begin of the 19th century, when thermal/electric analogies¹ were used to deal with thermal problems.

Mathematically, this approach is a simple but effective means of deriving a first-order finite-difference approximation of the underlying parabolic partial differential equation, the heat equation (appendix A.1). This finally leads to a system of nonlinear

¹temperature $\hat{=}$ voltage, heat flow $\hat{=}$ current

ordinary differential equations. A detailed description how to get the system of differential equations out of the physical equations is given in chapter B. For thermal modelling the ESATAN-software was used which is presented in chapter C.

4.1 Camera assembly thermal model

The camera assembly is composed of the filter wheel, the camera module and the camera electronics (compare figure 1.5 in section 1.2). The camera module, consisting of the CCD, the CCD ceramics, the aluminium casing and the proton shielding, is represented by detailed shells (figure 4.1). This part of the model is crucial because even very low amounts of power due to parasitics cause a significant raise of the CCD temperature, which is the most sensitive part of the telescope with the most stringent temperature requirements. Therefore its thermal model has to be as accurate as possible to not ignore any contribution of the surrounding components. Especially the radiation part is hard to estimate manually.

As described in chapter 2, we made great efforts to decouple the cold from the warm components with GFRP struts. So the conductivity of these struts is an important part of the thermal model, especially because of the large temperature difference. First tests showed that the aluminium casing with the detector inside is almost completely isothermal. Therefore these interfaces and transitions are less critical.

The model of the camera electronics contains several nodes at the aluminium casing as well as the five printed circuit boards (PCBs) to account for heat exchange between the PCBs and the casing as well as between the PCBs among each other (figure 4.2). For heat rejection we again use two radiators which are connected with the electronics via heat pipes. A design description of the complete cooling chain is given in section 5.3.

All thermally important material properties and surface treatments are considered: The casing's surface treatment is yellow chromating while we chose a gold-plated outer surface to minimize the interaction with the telescope. The PCBs do have a thickness of 1.5 mm and are tin-plated. An internal copper layer of 300 μm has been included in the conductive calculations to simulate the enhanced heat transport capability due to the tracks. Heating power is applied uniformly over the four nodes of each PCB.

The main conductive couplings of the electronics are between the PCBs and the casing (clamped with wedge locks) and between casing and heat pipe (both have a heat

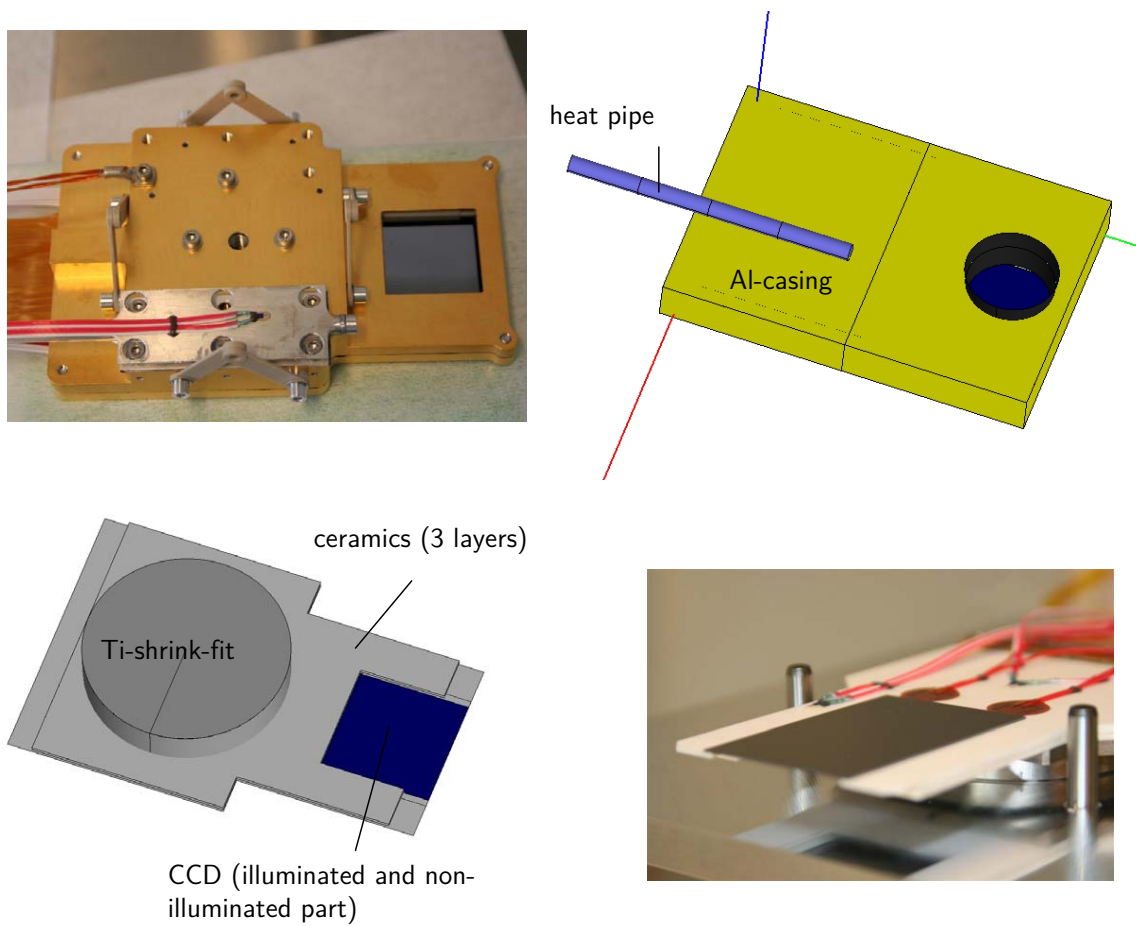


Figure 4.1: Thermal model of the camera module

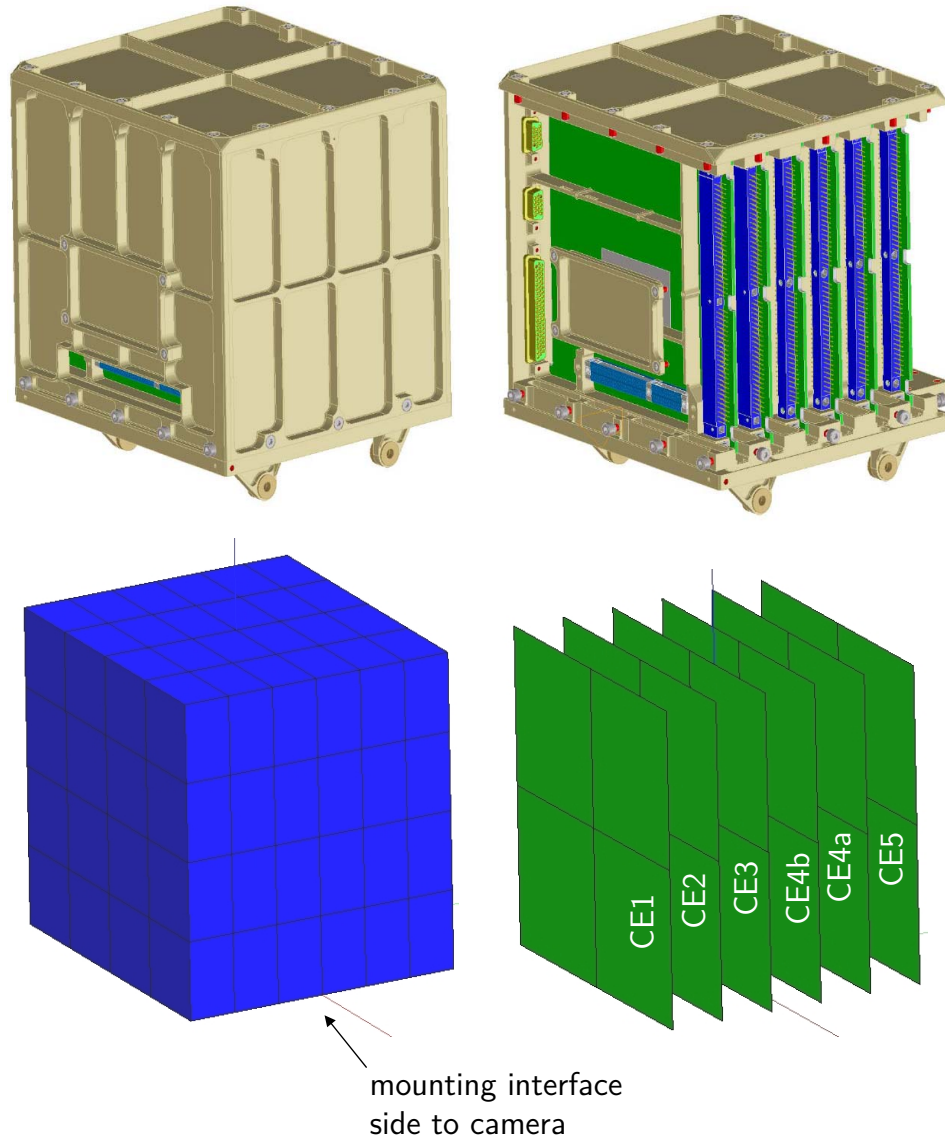


Figure 4.2: CAD model of the camera electronics (above); ESATAN model for radiative calculations (below)

conductivity of about $k = 1000 \text{ W m}^{-2} \text{ K}^{-1}$, but the latter has a much larger interface area). The connections to the camera proton shielding is considered as well.

Dimensions of the components, the used materials and physical properties are listed in table 4.1. Manually inserted conductive couplings, partly adjusted in the separate thermal balance tests of the camera module and the camera electronics, can be found in table 4.2.

The filter wheel is assumed to be mainly an additional capacity without any major impact, so it is only considered as a single node with a corresponding capacity.

The radiative and conductive couplings of the camera assembly are summarized in the thermal model in figure 4.3. Please note that some values differ in comparison to table 4.2 if several connectors are put in series: The conductivity between two thermal nodes normally contains the contribution of both nodes (with the properties of the bulk material) and the interface. Only the latter is listed in table 4.2, while the bulk properties in general are calculated automatically by the ESATAN software.

Table 4.1: Parts and materials of the camera assembly

Part	material	dimensions [mm]	ρ [kg/m ³]	λ [W/mK]	c_p [J/kgK]	ϵ (out/in)
filter wheel	AW-7075	$r = 105, h = 39$	2770	150	890	0.06
proton shield	CW009A Cu-OFE	$160 \times 100 \times 80$ $d = 30$	8900	390	300	0.05/0.05
aluminium casing	AW-6082	$160 \times 100 \times 80$ $d = 2$	2700	170	890	0.05/0.7
struts	GFK	$2 \times 15 \times 4 \times 1$ ($\times 3$)	1800	0.35	1000	–
purging tube	Viton FKM	$r_a = 3.174,$ $r_i = 1.524,$ $l = 13.7$	1850	0.25	1800	–
shrink fit	Titan	$r = 30, d = 7$	4500	20	500	0.15
ceramics	Al ₂ O ₃	$120 \times 80 \times 1$	3960	80	500	0.23
CCD	Si	$37 \times (23 + 33)^*$	2300	125	800	0.7
glue	EPOTEK 920FL	–	–	1.1		–
CE casing	AW-6082	$276 \times 190 \times 200$	2700	170	890	0.05/0.56
PCBs	Hgw2372 Cu	160×160 $d = 0.3$	1800 8900	0.3 390	– 300	0.1 –
screws	A2-70	M3–M5	7900	16	500	–

*non-illuminated+illuminated part

Table 4.2: Conductive couplings of camera module and camera electronics

Affected nodes	Connection	Value [W/K]
filter wheel – proton shield	$2 \times (8 \times \text{M6})$, adapter plate ($r = 10 \text{ cm}$, $d = 1 \text{ cm}$)	0.80
proton shield – Al casing	3×2 GFK struts	3×0.00019
Al casing – Ti	shrink fit	3.4
Ti – ceramics	glue	3.3
ceramics – CCD	glue, 2 mm overlap	1.0
ceramics – CE	flex lead, $A_{Cu} = 1 \text{ mm}^2$, $l = 25 \text{ cm}$	0.0016
proton shield – CE	PEEK spacings	0.02
PCB – casing	wedge lock 1.5 mm Hgw2372 + 0.3 mm Cu	2×0.29 2×0.24
casing – HP interface	2 water heat pipes + 95 mm \times 36 mm \times 4 mm	4
HP interface – HP evaporator	screwed saddle, $A = 30 \text{ mm} \times 95 \text{ mm}$	4.3

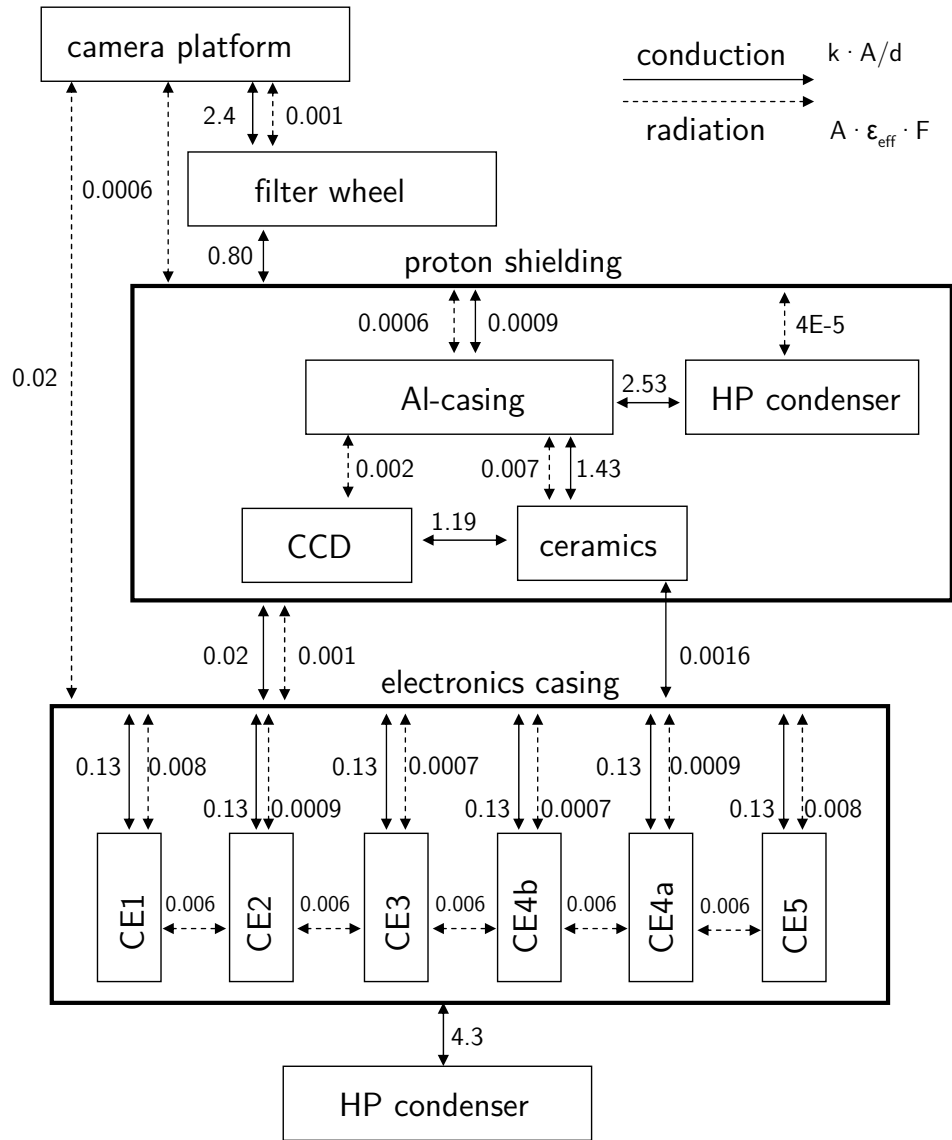


Figure 4.3: Thermal connectors of the camera assembly

4.2 Heat pipe thermal model

Complex theoretical calculations for all kinds of heat pipe phenomena can be found in the literature, for example in Brennan et al. (1979); Faghri (1995); Marcus (1972); Ivanovsky et al. (1982). These kinds of calculations are of particular importance for the design of heat pipes. Once working properly, it is sufficient to use a simplified approach.

Simple heat pipe thermal models only consist of an evaporator and condenser node and sometimes also a vapour node (figure 4.4(a)). The latter is connected to the first two nodes by the respective heat transfer coefficients. This copes with the heat pipe functionality where the evaporating and condensing processes constrain the performance. The evaporator and condenser are also directly connected with a coupling representing the tube. For standard constant conductance heat pipes it may be also sufficient to only use one evaporator node and one condenser node, especially if the separate heat transfer coefficients of evaporator and condenser are not known, but just the overall thermal gradient at a certain heat load.

For each heat pipe type the heat transfer coefficients (HTCs) differ. Reasonable experience values were replaced step by step after the verification tests (chapter 3, section 4.3).

VCHPs have to be treated separately. Simple HTCs are not sufficient to reflect the variable HTC at the condenser, depending on the nitrogen temperature. The condenser needs to be divided into several nodes, and only those parts not being in contact with the nitrogen contribute to the condenser area (figure 4.4(b)). The flat front model can be used to calculate the position of the diffusion barrier between the working fluid and the NCG (refer to section 3.5), inserting the temperatures of the vapour node and the reservoir.

By introducing a variable for the contributing area percentage, a temperature control can be added by heating the nitrogen reservoir.

The derivation and measurement of the corresponding heat transfer coefficients for the different heat pipe types can be found in section 3.4 and 3.5. The experimental values (see section 3.4 and 3.5) are summarized in table 4.3.

To complete the camera cooling system, we have to add the radiators. The honeycomb structure is modelled by several nodes to examine the lateral temperature distribution. Opposing nodes on each of the two aluminium face sheets are connected by the cor-

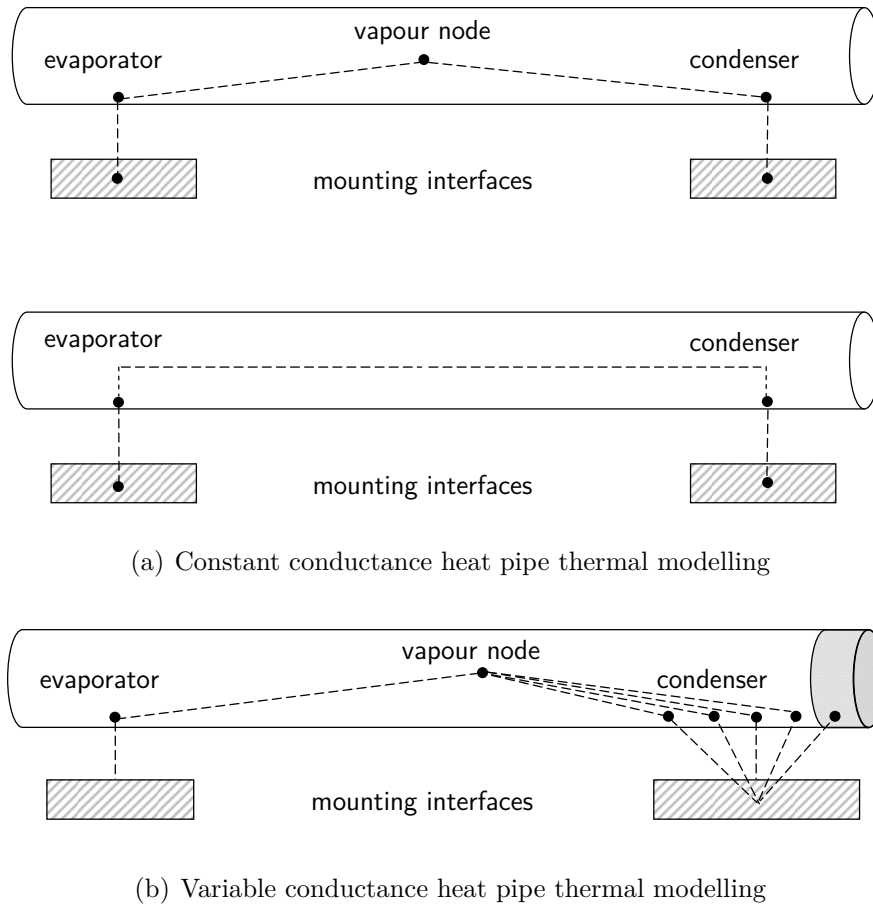


Figure 4.4: Heat pipe thermal modelling

Table 4.3: Heat pipe heat transfer coefficients for 170 K and nominal power (2 W for camera HPs, 20 W for ring HPs and 10 W for VCHPs)

	condenser [W m ⁻¹ K ⁻¹]	evaporator [W m ⁻¹ K ⁻¹]	global [W K ⁻¹]
camera HP	–	–	1.9
ring HP	4.7	1.0	4.6
VCHP	12.5	2.5	2.1

responding conductivity of the aluminium honeycomb. Finally, when all components are modelled adequately, internal heat sources (CCD, PCBs) and boundary conditions (interface temperatures, radiative couplings with the environment) have to be defined. For the main load cases the power of the CCDs and camera electronics is considered to be a constant heat source on the corresponding nodes.

For mission representative results, the camera cooling system has to be embedded into the complete telescope thermal model. After fulfilling the stability criteria, the solving routines produce the equilibrium temperatures of the thermal nodes. With the transient analysis it is possible to determine the cooling after launch or to examine the influence of temperature or power fluctuations. The results are presented in chapter 5.

A verification of the cooling system was done in a thermal balance test (see next section, 4.3). Before that, a structural thermal model of the camera module (with the proton shielding, the aluminium casing and the detector) and of the electronics were tested, verified and improved separately.

An important result of this pre-test was the fact, that temperatures inside the proton shielding have to be measured very carefully and with very thin cables, otherwise the emerging thermal bridge would destroy the thermal decoupling. Parameters for conductivity between ceramics, shrink fit and aluminium casing slightly had to be adjusted.

The conductivity between the PCBs and the housing of the camera electronics was worse than predicted, so additional water heat pipes inside the bottom were added to decrease the temperature gradient. Moreover, different means of a better thermal connection between critical elements and the PCBs are investigated in parallel, to prevent hot spots. For the complete test reports refer to Fürmetz (2011c) and Fürmetz (2011b).

4.3 Camera cooling thermal balance test

The complete cooling loop was approved in the thermal balance test of the camera assembly. For this, the MPE PANTER X-ray test facility was temporarily converted into a thermal vacuum chamber by means of a thermal shroud.

The scope of the thermal balance test was the verification of the thermal concept, especially the cooling concept of the CCD module and the functionality of the heat

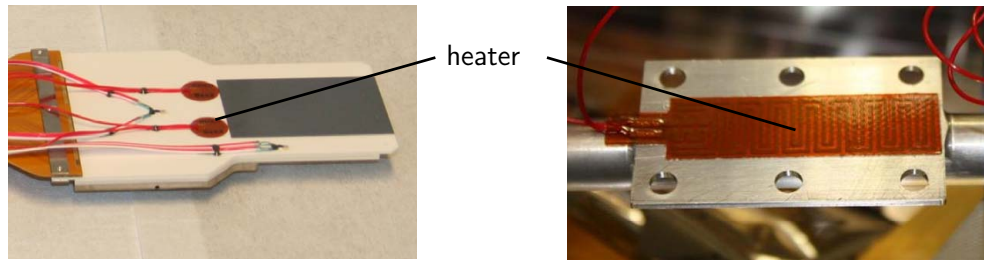


Figure 4.5: Replacement heaters at the CCD ceramics (left) and the ring HP saddles (right)

pipes. Parameters of the thermal model have been adapted to the test results. The required temperature level of the CCD was achieved. The camera and ring heat pipe worked as predicted. Only the VCHPs needed some further optimisation process regarding the heat transfer coefficients. The ethane and nitrogen mass have a major influence on the performance as shown in section 3.5.

4.3.1 Test set-up

The set-up consisted of a dummy camera platform made of aluminium, the structural-thermal model of one camera assembly (filter wheel, camera module and electronic box) and one radiator cooling loop (camera heat pipe, one ring heat pipe, two VCHPs and one camera radiator). Small foil heaters at the ring heat pipe saddles. simulated the active and parasitic heat loads of the outer six cameras. The power consumption of the central camera was represented by a heater on the detector module CCD ceramics of the STM shown in figure 4.5.

The cooling of the electronics box was not representative because the old cooling design with a loop heat pipe was still used (see section 5.3). But this had no effect on the test of the camera cooling, as long as the electronics casing had the right interface temperature (which also could be adjusted with a heater).

Most of the set-up was integrated upside down onto the aluminium platform (figure 4.7). 30 temperature sensors were attached on all important parts and the heat pipes were wrapped into MLI to suppress parasitic heat loads due to radiation.

In the second part of the integration the radiator with the two VCHPs was mounted. Both VCHPs had a flight-like shape, but instead of the valve complex mounted on

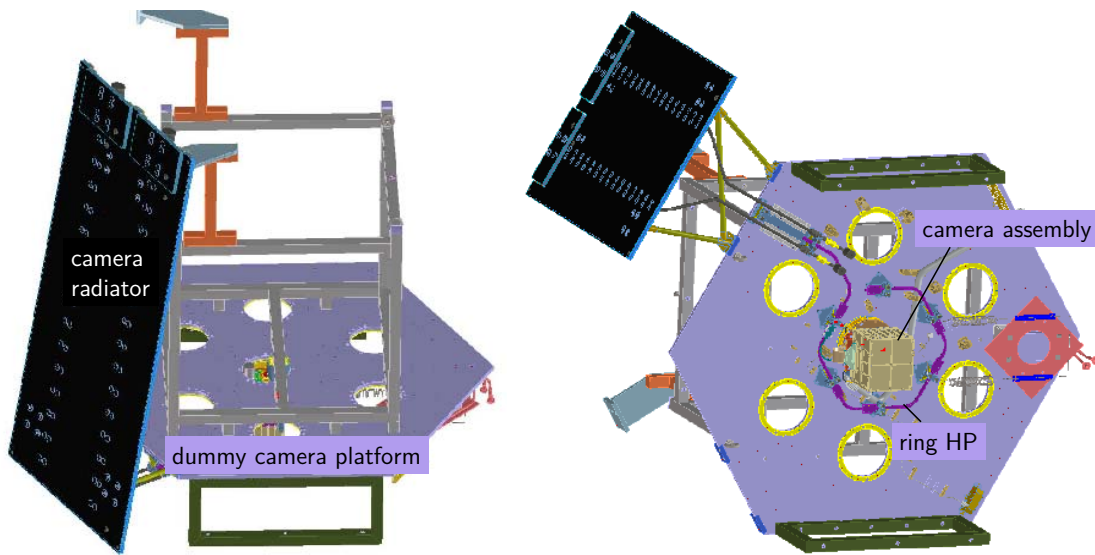


Figure 4.6: CAD model of the test set-up

the camera platform (as described in figure 3.17), whose design was not finished at that time, a simpler, self-supporting construction was used. It consisted of Swagelok-fittings, small ethane reservoirs and filling hand valves at the evaporator side. Additionally, one HP was equipped with an electric latching solenoid valve.

First the heat pipes were attached to the radiator, then the radiator was mounted at the camera platform (figure 4.8). Temperature sensors were stuck on the condenser saddles, the reservoir and the backside of the radiator.

Finally the backside of the radiator was covered with MLI. To simulate the thermal environment, the complete set-up was mounted inside a thermal shroud. This shroud consisted of an aluminium cabin with a black, high-emissivity inner surface, heaters on the outer surface and an additional cold plate opposite to the camera radiator. The latter was cooled with liquid nitrogen down to 77 K². This assembly was placed inside the vacuum chamber of the PANTER facility (see figure 4.9). All inner surfaces are black for a high radiative coupling. The complete shroud was equipped with heaters, additionally a shroud radiator (opposite to the camera radiator) was cooled with liquid nitrogen. The outer surface was completely covered with MLI as well.

²The deviation from the space temperature of 3K has no major effects but is considered in the thermal calculations.

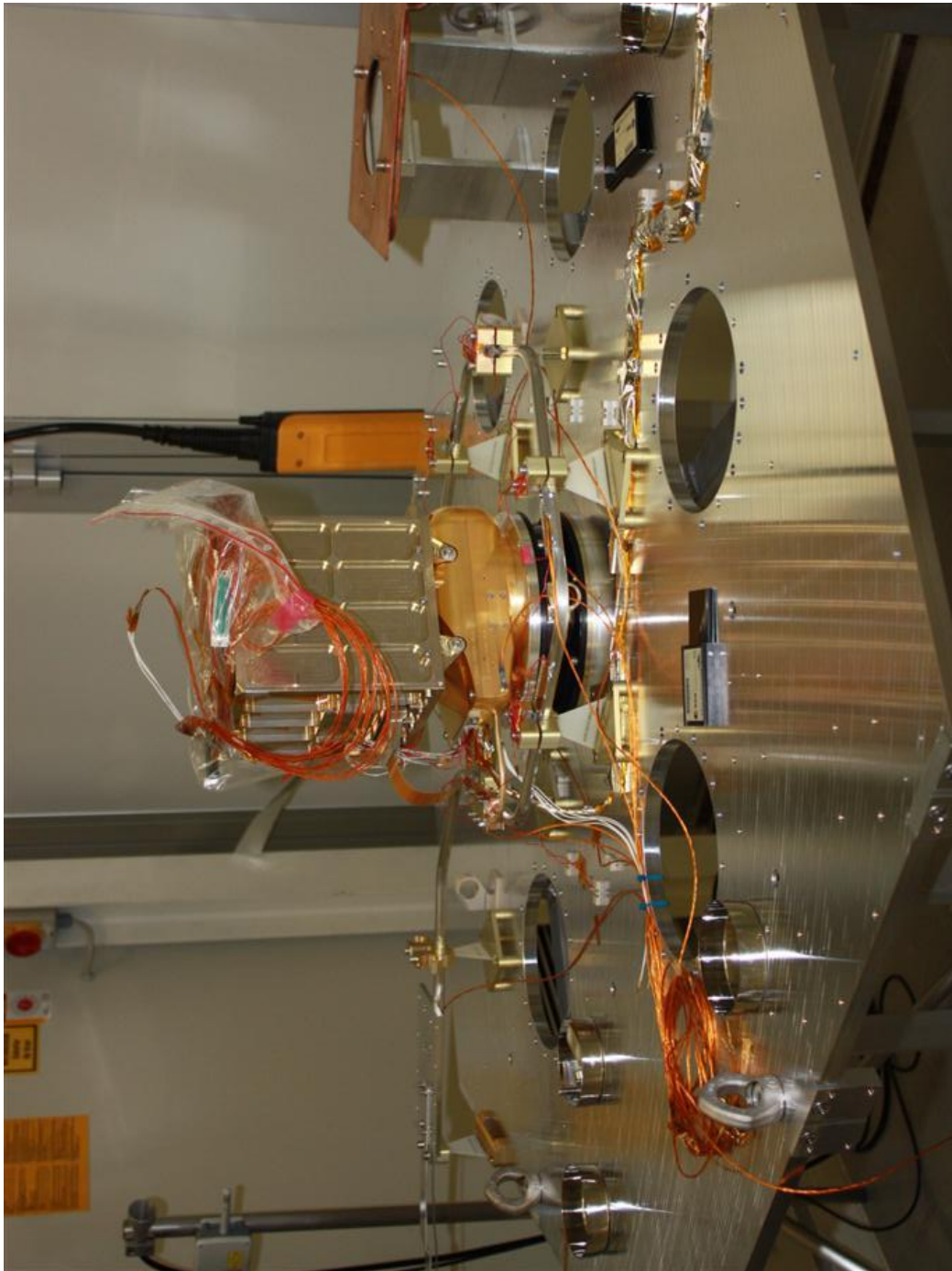


Figure 4.7: Test set-up on platform upside down

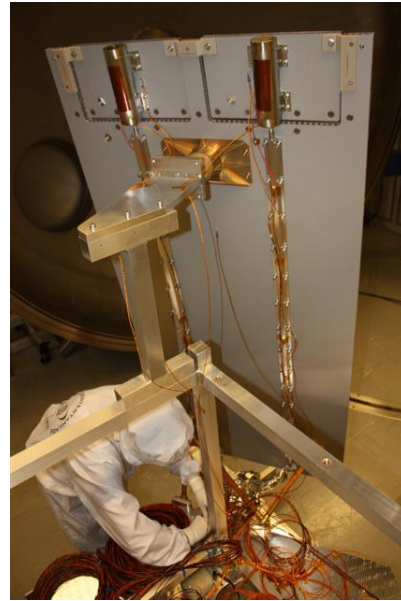
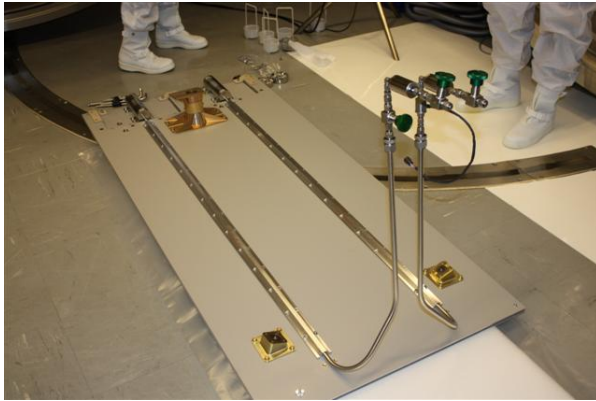


Figure 4.8: Mounting of VCHPs and radiator



Figure 4.9: Final test set-up

Table 4.4: Different load cases for the thermal balance test

load case	CCD power [W]	ring HP power [W]	CE power [W]	shroud [K]
non-operational cold case	0	0	0	273
operational cold case	0.75	9	23	268
non-operational nominal case	0	0	23	288
operational nominal case	0.75	9	23	288
non-operational hot case	0	0	23	296
operational hot case	0.75	9	23	296

4.3.2 Test campaign

The most important test scenarios were the different load cases. The operational cases were simulated by the nominal CAMEX power (0.75 W) on the STM camera ceramics and 9 W onto the ring heat pipe in total. This corresponded to 1.5 W per camera, which was an upper limit according to the pre-test. The camera electronics was powered during the complete test (with exception of the cooling phase). It was ensured that the casing always stayed at 293 K to have stable boundary conditions. This is the temperature that will be provided by the new electronics cooling concept, according to model predictions. In table 4.4 the different load cases are summarized.

The terms of cold and hot case do not correspond to cold and hot cases during the mission. The impact of the black thermal shroud with its very high emissivity was quite different to the impact of the spacecraft, the telescope and of course the Sun. The MLI also was not flight-like at all. So the parasitic heat loads on the cooling system were larger than they are expected to be in space. Nevertheless, three different load cases were examined for a better correlation of the underlying thermal model.

4.3.3 Thermal model

An adapted thermal model was used to calculate the expected temperatures. The test set-up was modelled as close as possible and only the heat pipes were not in-

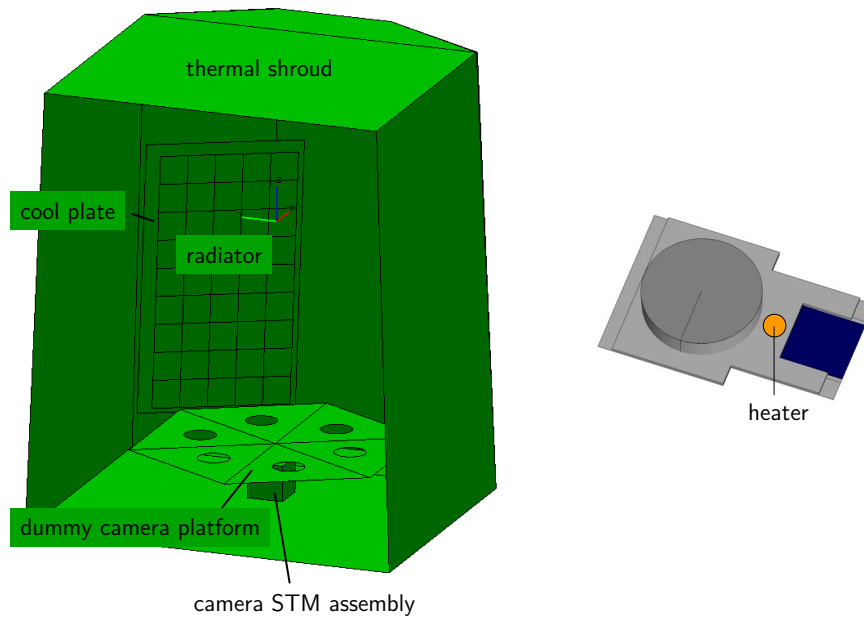


Figure 4.10: Geometric thermal model

cluded in the calculation of the radiation exchange factors (compare to figure 4.11) but modelled as described in 4.2. The modelling of the camera assembly was the same as in section 4.1, with some small adjustments, since the design was not completely flight-like.

For the conductive values results from former tests were adapted where possible. The largest uncertainty were the heat transport capabilities of the heat pipes, where reasonable values from commercial heat pipes have been used so far. A complete overview of all radiative and conductive connectors can be found in the thermal model of the test set-up (shown in figure 4.11).

It has to be noted that a thermal equilibrium was not completely reached during the test, but deviations were not expected to be greater than one or two degrees maximum.

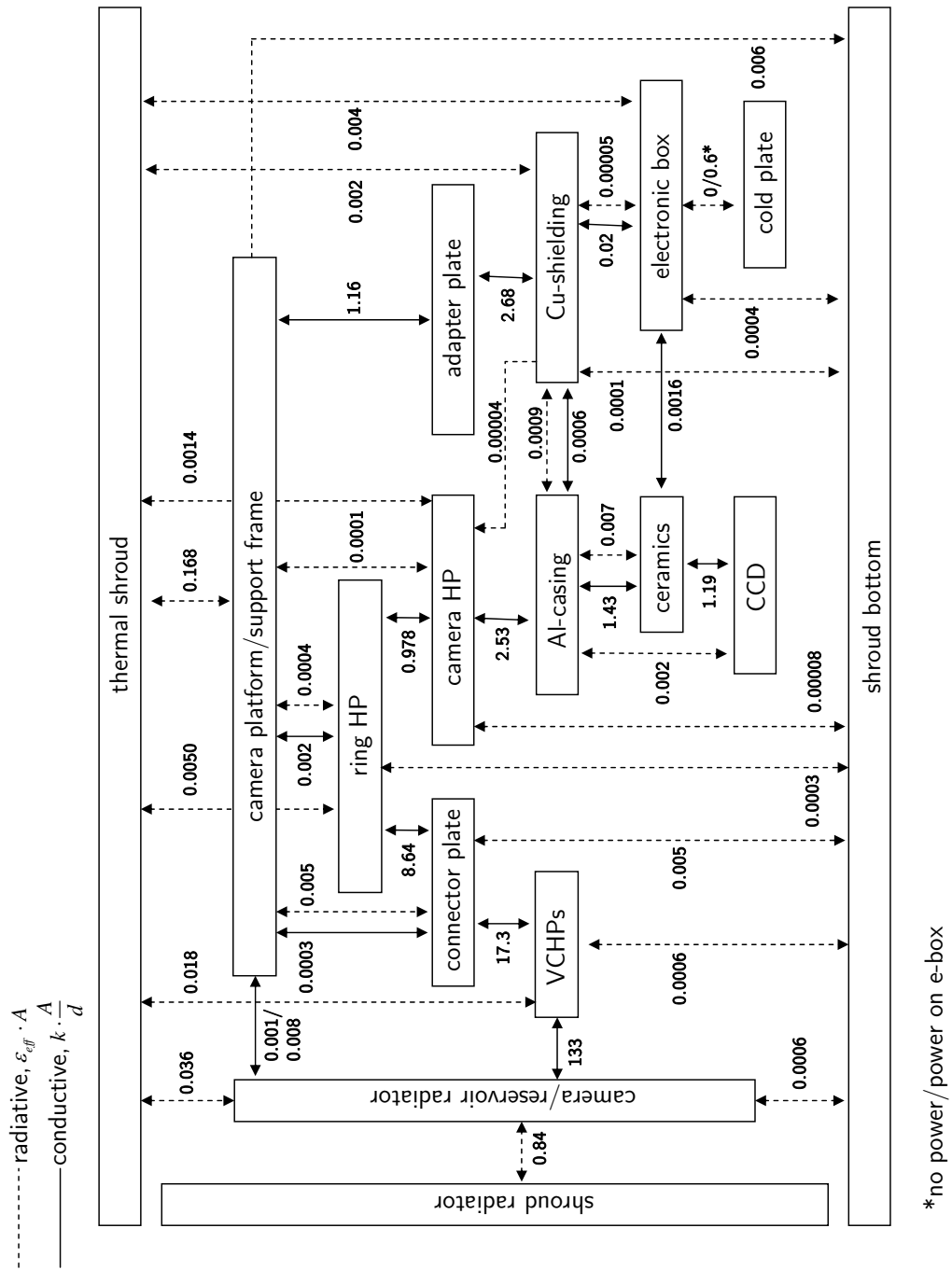


Figure 4.11: Thermal couplings

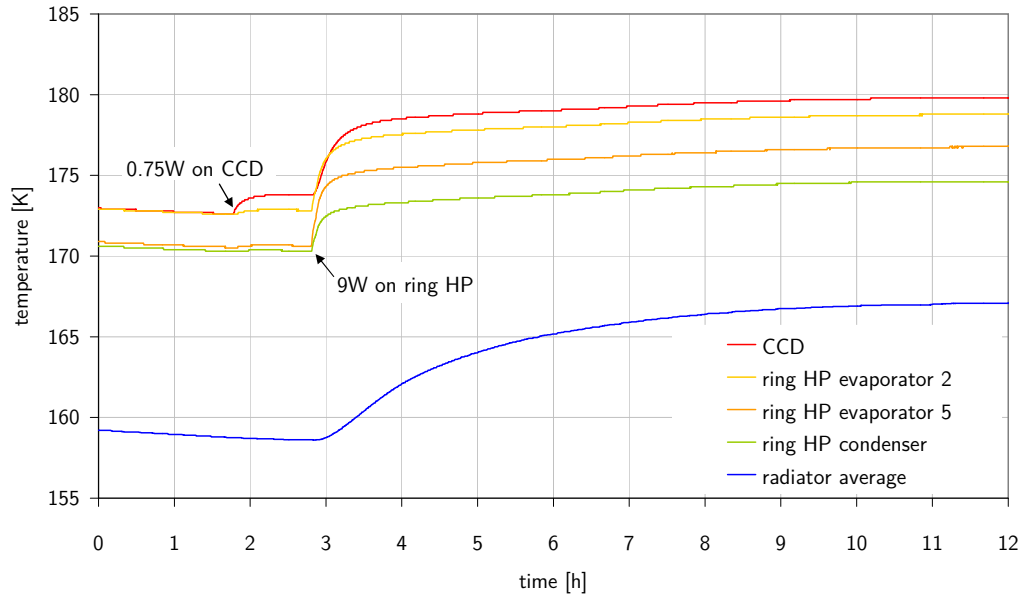


Figure 4.12: Temperature curves for the cold operational case

4.3.4 Test results

Different scenarios with varying heat loads were examined as well as heat pipe performances and limits. All components showed the expected performance; the CCD temperature reached the required temperature range.

In figure 4.12 the temperature plot for the cold operational case is shown, where heat was applied first on the STM ceramics and then on the ring heat pipe to simulate the other cameras.

As expected, the cooling system reacted very sensitive on small heat loads. Even less than one watt caused the ring heat pipe and one of the VCHPs to show an increase in temperature. Additional 10 W resulted in an about 8 K higher radiator and CCD temperature. The key results of the different load cases are listed in table 4.5.

After examination of the steady state cases some further tests were made, especially with the VCHPs and the possibility to change their heat transport capability by heating up the nitrogen reservoirs.

First of all, the temperature control was tested with the automatic PID control function of the read-out device. The heaters on the reservoirs and the connector plate tem-

Table 4.5: Temperatures of different load cases

	cold non-op.	cold op.	nominal non-op.	nominal op.	hot non-op.	hot op.
shroud [K]	268	268	288	288	296	296
radiator (average) [K]	159	162	161	172	166	174
CCD [K]	172	178	174	185	179	188

perature were the control parameters. For more than six hours a CCD temperature stability of 0.1 K was achieved (figure 4.13), despite varying environmental conditions.

The radiator and shroud temperature were decreasing over more than seven hours. To keep the CCD temperature constant, the heat conductivity to the radiator had to be reduced by increasing the heating power on the VCHP reservoirs. At the beginning of the control phase the average heating power at the reservoir was 0.5 W. After six hours the average radiator temperature decreased about 4 K and the shroud temperature about 18 K. The heating power was 0.6 W at that time and the reservoir temperature about 1 K higher than in the beginning.

Temperatures at VCHP 2 were higher at the top condenser range than those of VCHP 1 (see table 4.6, *condenser top* and *condenser middle*-sensors). That means the blocked condenser range was larger in VCHP 1. This can be explained by a higher nitrogen mass than in VCHP 2 (0.188 g vs. 0.177 g). Nevertheless both heat pipes could be controlled and the CCD temperature stayed perfectly constant.

For design reasons of the telescope interface controller, it was tested if the heaters of the reservoirs could be operated pulsed instead of powered continuously. With intervals of 30 seconds twice the nominal power was switched on and off. The CCD temperature was completely stable during this test.

Another important value is the maximum heat transport capability of the different heat pipes. Especially the ring heat pipes and sVCHPs have to be capable of transporting at least twice the nominal heat load. Otherwise the redundancy concept cannot be validated. High demands are made on the ring heat pipes in particular. In case of failure of one ring heat pipe the other one has to ensure a proper cooling of all seven cameras alone.

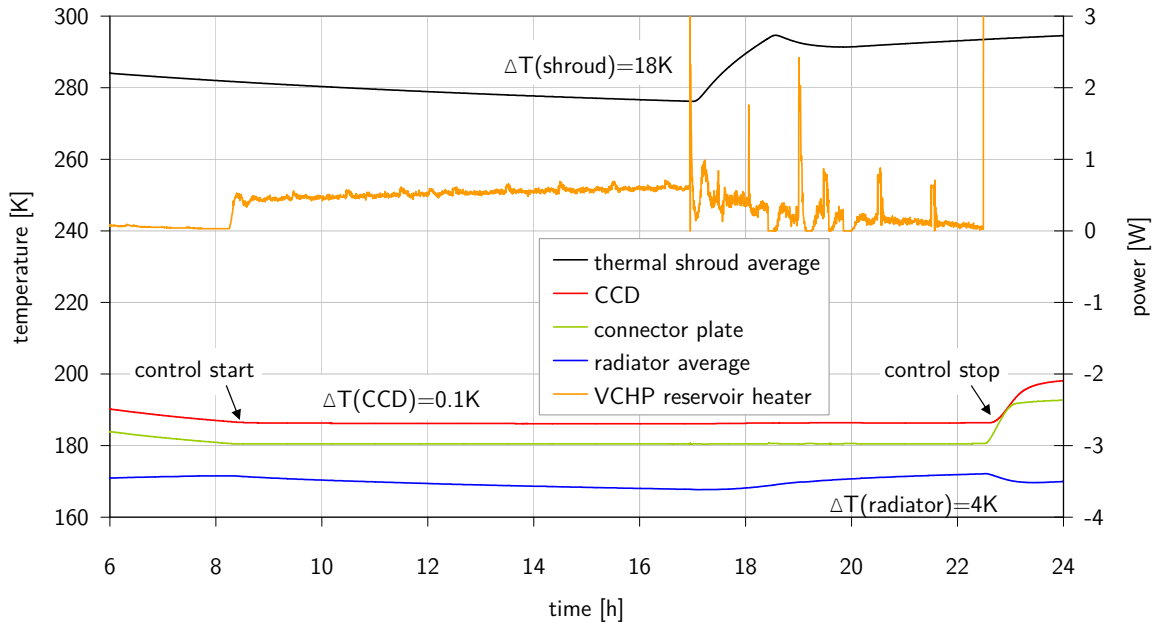


Figure 4.13: Control of CCD temperature

Table 4.6: Controlling the nitrogen level in the VCHPs. Lower condenser temperatures of VCHP 1 confirm the higher nitrogen mass than in VCHP 2 (0.188 g vs. 0.177 g).

	VCHP 1	VCHP 2
reservoir power [W]	0.5/0.6	0.5/0.6
reservoir temperature [K]	169/170	[not measured]
condenser top [K]	169/166	170/168
condenser middle [K]	170/167	173/169
condenser bottom [K]	176/176	175/175
evaporator [K]	177/178	177/177
connector plate [K]	178.5/178.5	

The stress test of the sVCHPs was postponed to the separate sVCHP optimisation because the cooling power of the radiator was too small. For the same reason it was not possible to do further stress tests at lower temperatures.

As a result of the camera and ring heat pipe stress test, the camera heat pipe was able to transport about 8 W, the ring heat pipe 35 W. Even if the heat pipes were able to transport that amount of power, the conductivity of the heat pipe saddles limited the performance and the CCD temperature was increasing permanently.

The result of the ring HP was already mentioned in section 3.4.2 while the result from the camera HP was gravity enhanced. Exact values of the maximum transport capability were found in a separate test, see section 3.4.1.

If major contamination on the CCDs occurred during the mission, it might be necessary to heat them up temporarily. One method would be to shut down the radiator completely. As it turned out this is not possible with heating up the sVCHP reservoirs. Despite high reservoir temperatures (150 K), the CCD temperature stabilized at 198 K after a short timescale, while the reservoir temperature was still rising. Only for the first 20–30 minutes the nitrogen front was able to block the complete condenser region.

This was proved by decreasing temperatures at the condensers as well as the radiator. But then about a fourth of the condenser length started transporting heat again. The partial pressure of the ethane was increasing because of the increasing temperature. The slope of the ethane vapour pressure is steeper than the linear pressure rise of the nitrogen, so the ethane pressure exceeded the nitrogen pressure at a certain point (refer to section 3.1.5). This explains the observation that after about half an hour the connector plate temperature was saturating; the heat pipe did have a non-zero heat transport capability by then.

For the shut-down of the radiator not being possible, we tried another method to heat up the CCDs. All power available was used to bring the ring and camera heat pipe to their limit. With about 45 W on the heat pipe system in total it was possible to reach more than 280 K at the CCD and this was not even the saturation temperature. But the main reason for these high temperatures was the transportation limit of the camera HP. After reducing the power at the CCD ceramics, the CCD temperature decreases despite of more than 30 W at the ring heat pipe. To have this possibility also during the mission, heaters with enough power to rise the radiator temperature have to be foreseen at the heat pipe system, more specifically at the connector plates

since this is the only available area. The required amount of power has to be examined in a future test campaign.

4.3.5 Adaption of the thermal model

Test data and predicted temperatures show deviations of a few degrees. To find the best fit of the thermal model, the conductive and radiative connectors were adapted until the calculated data were as close to the results as possible. In the following the most important results and lessons learned are listed.

The radiator temperature was extremely sensitive to any power input. Only a few watts are sufficient to change its temperature significantly. Therefore parasitics have to be reduced to a minimum.

The distance between the camera radiator and the thermal shroud radiator did have a great influence on the heat input from the thermal shroud. So even a slightly different distance in the model causes different results than during the test. The parasitic heat loads onto the heat pipe system have the same effect on the radiator temperature.

Measured radiator temperatures were lower than predicted. The properties of the thermal insulation on the backside of the radiator were not able to explain these deviations. The best fit for all cases simultaneously was the reducing of the assumed parasitic heat load onto the heat pipe system (including the connector plate) by a factor of two.

Both VCHPs were working quite differently. VCHP 2 had a more efficient heat transport with almost no measurable gradient over the condenser region in nominal operation. The heat transfer coefficient at the condenser of VCHP 2 increased as soon as power was applied onto the ring heat pipe and the CCD. In the non-operational modes the performance of both heat pipes was quite similar. An overview is given in table 4.7.

The value of the VCHP heat transfer coefficients at the evaporator and condenser had a large impact on the CCD temperature. Even small deviations caused significant changes. The difference between the two heat pipes could be explained by the smaller amount of gaseous nitrogen in VCHP 2 (0.177 g vs. 0.188 g at 293 K). 0.188 g seemed to be too much non-condensable gas; the ethane partial pressure at working temperature was not able to push the nitrogen into its reservoir. So even in full operational mode the condenser was partially blocked by the nitrogen.

Table 4.7: VCHP global heat transfer coefficients

	VCHP 1 [W K ⁻¹]	VCHP 2 [W K ⁻¹]
non-op. cold case	0.3	0.1
non-op. nominal case	0.4	0.6
non-op. hot case	0.4	0.8
op. cold case	5.6	6.9
op. nominal case	2.3	4.2
op. hot case	7.4	8.0

In table 4.8 the original test prediction is compared to the measured data. The third column contains the results from the overworked model, which is the best fit to the measured data (see figure 4.14).

Apparently, the conductive interfaces between heat pipes and attachment areas were more effective than assumed. The only exception was the attachment of the VCHPs to the connector plate. Figure 4.15 shows the corresponding thermal budget for the nominal case in thermal equilibrium. The complete test report can be found in Fürmetz (2011a).

Table 4.8: Comparison of prediction and data for the operational nominal case

	test prediction [K]	test data [K]	overworked model [K]
thermal shroud	288	283–290	288
camera platform	283	284	283
e-box interface	302	289	291
Cu-shielding	283	284	283
CCD	190.5	185.3	185.4
Al-casing	189.9	184.8	184.8
camera HP (evap/cond)	189.7/189.3	183.6/184.8	184.7/184.4
ring HP (evap/cond)	187.5/184.9	184.6/179.7	183.6/179.2
connector plate	183.3	179.0	178.5
VCHP1 (evap/cond)	179/177–180	176/172–176	177/173–177
VCHP2 (evap/cond)	179/177–180	106/174	106–175
radiator	172–178	172–173	170–175
reservoir radiator 1/2	164	165/162	165/163

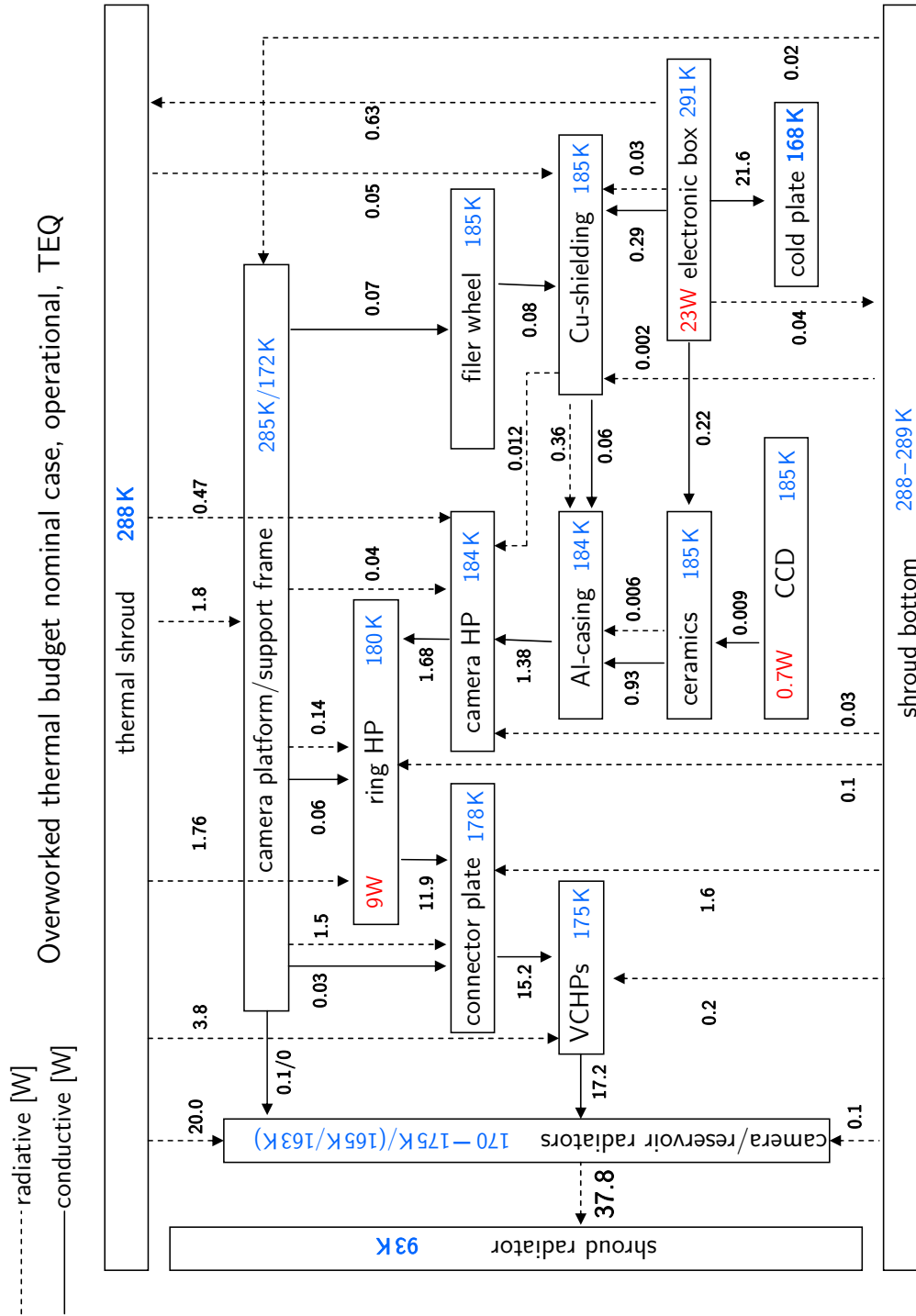


Figure 4.15: Thermal budget for the nominal operation

5 eROSITA thermal control system

For reliable predictions of the thermal behaviour of eROSITA and its submodels a thermal model of the complete telescope is necessary. Since all subsystems interact with each other and the heat exchange with the environment only happens via radiation, even small changes in couplings may cause major changes in the thermal equilibrium.

The thermal model of the eROSITA telescope consists of approximately 3800 nodes in total. Due to the hexagonal symmetry, the submodel concept is used. One complete single telescope, consisting of a mirror assembly, a contamination shield and a camera assembly, is modelled and calculated separately as shown in figure 5.1. The resulting thermal couplings are then implemented in the ESATAN code of the telescope structure seven times.

This saves calculation time¹ and still allows for a very detailed modelling. Critical parts as the camera modules and the mirror modules have a finer node grid than less crucial components as the telescope structure. So-called supernodes provide the connection between the submodels and the main model.

Nevertheless, the geometry of the thermal model is simplified with respect to the real telescope design. Most components are modelled only with their raw geometrical shape, capacity and surface properties, whereas thermally less important details such as complex cut-outs and noses are ignored. As long as these simplifications do not change the view factors and heat capacities significantly, this method saves modelling and computation time without distorting the results.

All radiative links between node pairs are calculated by the workbench as described in chapter C. Conductive couplings that are not coming out of the model automatically – for example screwed and glued connections – are inserted manually. Also complex connections such as the radiator attachments – in the radiative model represented by a single node – have to be modelled by serial connections of thermal resistances. The model of the camera cooling system was discussed in chapter 4, in the following

¹Most time-consuming is the calculation of the radiative exchange factors

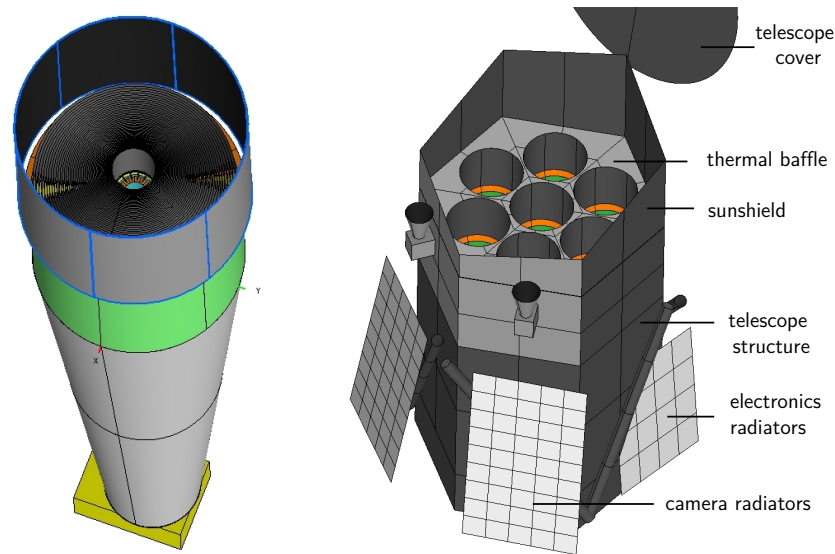


Figure 5.1: Submodel principle for the eROSITA thermal model: The detailed model of a single telescope (left) is implemented in the model of the telescope structure (right)

sections now the modelling of the remaining subsystems is described. The spacecraft and the ART telescope are both modelled as a single node with representative surface properties to simulate the environment and boundary conditions during the mission.

5.1 Multilayer insulation (MLI)

The MLI covers all surfaces with direct contact to deep space with except of the front side of the radiators. Sun radiation on the one side and cold deep space on the other pose extreme boundary conditions to the telescope. MLI materials are heat resistant, robust and with low outgassing values, which makes them predestined for space applications.

It is a multilayer envelope, consisting of several layers of aluminium coated polyimide (PI) and polyethylene terephthalate (PET) (see figure 5.2). Aluminium coating is an effective but cheap method to achieve a very low emissivity and thus reduce the radiative exchange between the layers. Each layer acts as a radiation shield and reduces the thermal throughput.



Figure 5.2: Multi-layer insulation lay-up (left: eROSITA MLI blankets; right: image credit to AerospaceEd.org)

To suppress conduction through a blanket, polyester nettings with a low thermal conductivity are used for separation of the layers. While the inner layout always looks very similar in MLI applications, except for the number of layers, the outer- and innermost layers have to fulfil certain thermal, electrostatic and mechanical requirements. With stacks of about typically 15–20 layers the heat transfer through a blanket can be reduced by more than two orders of magnitude as shown below. This ensures stable conditions with moderate temperatures inside the telescope structure.

The eROSITA MLI consists mainly of 6 μm PET layers with $\epsilon = 0.035$. Only the innermost layer has 25 μm for handling purposes. The outermost layer differs. Four different types of MLI lay-ups, described in table 5.1, are used to optimize the telescope temperatures (a detailed description may be found in Lindenmaier (2010)).

The optical values, more specifically the α/ϵ -ratio of the outermost layer, determine the equilibrium temperature on the inner side of the blanket by defining the initial amount of heat being absorbed. Blankets of lay-up 1 with $\alpha/\epsilon \approx 1$ in combination with Sun illumination result in a moderate equilibrium temperature on the inside. Those parts of the sun-shield facing only deep space have an outer surface with a very low emissivity to reduce heat losses.

Only 5 layers (lay-up no. 3, see table 5.1) prevents the telescope cover from cooling down by providing a larger solar heat input.

The camera radiators, which are partially illuminated by the Sun, do have a special

Table 5.1: eROSITA MLI lay-ups

lay-up	layers	outermost layer	α/ε	application area
1	20	160 DUN-MET AL/BLACK 'XC' polyimide film	0.93/0.84	telescope structure
2	20	aluminium coated (one side) polyimide	0.14/0.035	sunshield, CE radiators, thermal baffle
3	5	aluminium coated (one side) polyimide	0.14/0.035	telescope cover
4	20	silver coated (one side) FEP	0.09/0.47	rear side of camera radiators

kind of blanket (no. 4) with an optimized small α/ε -ratio. This provides the lowest possible radiator temperature due to solar and thermal radiation on its back side. One has to keep in mind that optical properties, especially the solar absorptivity, degrade during a mission. This has to be considered in the sensitivity trade-off. The only exception is the black Kapton because it already has a very high absorptivity from the beginning. A thermal concept with intrinsically high α - and ε -values does not have to deal with degradation due to decreasing of optical properties.

The MLI performance has a major input on the overall telescope temperature level. It cannot be tested before it is manufactured and mounted onto the telescope since the mounting procedure itself is partly responsible for the performance values. This requires a careful modelling and sensitivity analysis.

Each blanket is represented by one or more separate nodes on the outermost layer. Heat transfer through blankets happens in general via convection, conduction and radiation. Convection can be neglected for space applications due to pressures below 10^{-5} mbar (Glaser et al. 1967, pp. 55–56). The thermal links between this outermost layer and the structure beneath are taken into account by effective radiative (GR) and conductive (GL) couplings through the layers (Folkman et al. 1968). Therefore the resulting heat flux can be calculated as follows:

$$\dot{q}_{cond} = GL \cdot (T_{hot} - T_{cold}) \quad \dot{q}_{rad} = GR \cdot \sigma (T_{hot}^4 - T_{cold}^4) \quad (5.1)$$

T_{hot} and T_{cold} are the temperatures of the outermost and innermost layer. The order depends on the boundary conditions. If not announced otherwise, the arithmetic mean of both values is used for the overall MLI temperature. Despite a large number of very complex calculation methods for all kinds of irregularities, as done for example in Keller et al. (1974) or Stimpson et al. (1972), most thermal engineers use very simple modelling techniques. Often only one single value for the effective heat transport through a blanket is used, taken from test reports, without specifying the test conditions or the lay-up. But most MLI measurements were done with large, ideal blankets, not accounting for overlaps or other irregularities. Temperatures of the outer layer also have to be considered. Moreover, the lay-up – perforation, number of layers, surface coatings – has a great influence on the MLI performance. The value measured under ideal conditions can be taken as an upper performance limit, but it has to be ensured that a similar lay-up was used. For a realistic performance value test data from other projects are a good reference.

In the following section a simplified but reasonable model is developed for the eROSITA MLI which accounts for different boundary conditions and load cases.

For ideal blankets holds that $GL = 0$. GR can be interpreted as an effective emissivity times area with respect to the Stefan-Boltzmann law (equation (A.21)). For the calculation of the effective emissivity between the outermost and innermost layer and $(n - 2)$ layers in between with an emissivity ϵ on both sides applies the equation for parallel plates (figure 5.3). The effective heat flow through a MLI blanket with n layers due to radiation is reduced by the factor of $(n - 1)$ compared to two parallel plates (Schmidt 1961; Edelstein et al. 1979).

For 10 layers and $\epsilon = 0.035^2$, we determine a lower limit of $\epsilon_{eff} = 0.002$; for 20 layers $\epsilon_{eff} = 0.001$. Figure 5.4 shows the effective emissivity as a function of the number of layers for two different emissivities of the single layers. For thick blankets this value plays a less important role than for thin blankets.

Beyond 20 layers the increase of performance is only marginal with an increasing number of layers. This is why typical MLI blankets for space applications consist of 15–20 layers (with the exception of cryogenic experiments). Beyond that the performance

²typical value for aluminium coated layers

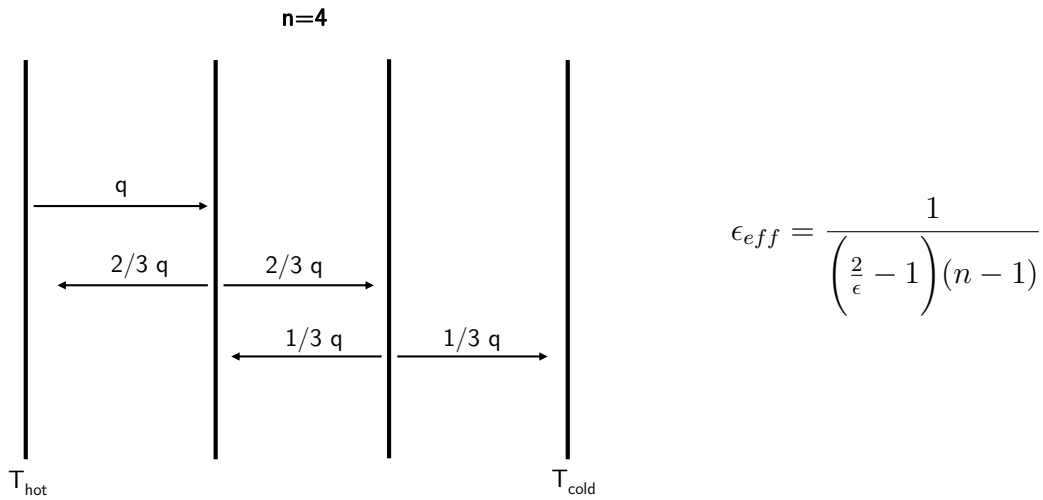


Figure 5.3: Influence of MLI layers

does not justify the additional costs and handling problems that come with such thick blankets.

Highly complex models were made for calculating the heat transfer through MLI blankets with different parameters for spacer conductivity, venting holes, stitching areas etc. as explained in Stimpson et al. (1972) or Keller et al. (1974). Even temperature dependent material properties were considered (derivation in appendix B of Cunningham et al. (1971)). Usually a much simpler approach can be made for thermal models. Assuming only radiative heat transport, which is a good approximation for almost ideal³ blankets (Edelstein et al. 1979, p. 9; Mayrhofer et al. 2009), the measured heat transfer coefficient (HTC) can be translated into an effective emissivity:

$$\epsilon_{eff} = \frac{HTC \cdot (T_{hot} - T_{cold})}{\sigma \cdot A (T_{hot}^4 - T_{cold}^4)} \quad (5.2)$$

In the same way a calculated effective emissivity can be translated into an HTC for comparison of theory and data.

In figure 5.5 calculated⁴ and measured values for HTCs are plotted against the average temperature between the outermost and innermost layers. Data are from comparable

³large, regular, not compressed

⁴with equation (5.2)

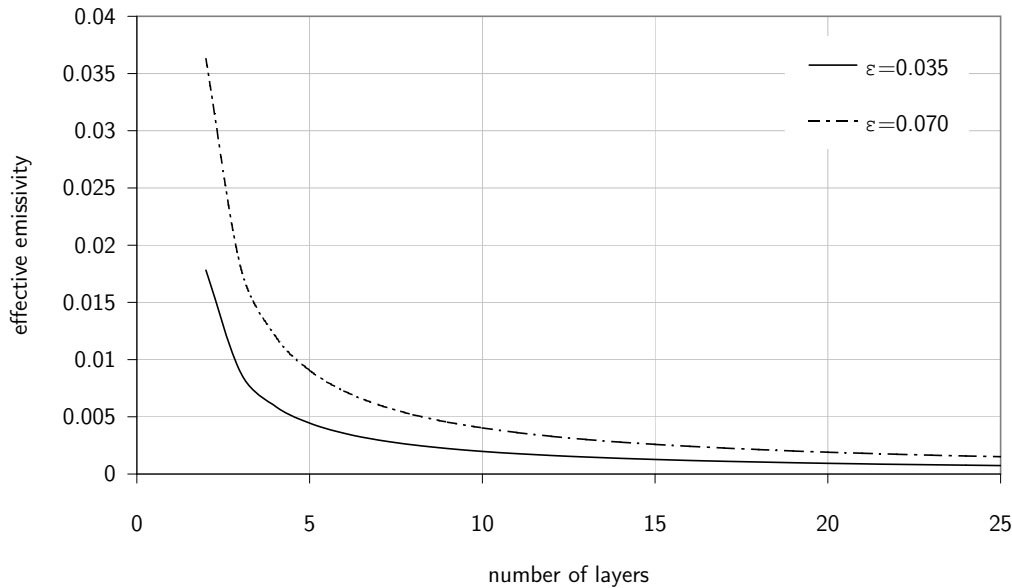


Figure 5.4: Effective emissivity as a function of number of layers for two different emissivity values of a single layer

ESTEC calorimeter measurements for 20 layers. While we have an almost perfect conformance of calculations and data for low average temperatures limit, deviations up to a factor of 3 appear for higher temperatures. The best fit is achieved with increased effective emissivity. The increasing deviations for low temperatures indicate a larger temperature dependence than T^4 which is confirmed by Cunnington et al. (1971). An increased effective conductivity is not able to reproduce the data. This only causes an even flatter slope.

By plotting the effective emissivity against the average temperature as shown in figure 5.6, it is obvious that a simple T^4 dependence is not capable of fully reproducing the data (Cunnington et al. 1971). Nevertheless, in the range between 220 K and 320 K it is a very good approximation.

The discrepancies to the calculated values, however, can be explained by an increased radiative heat flux due to perforation of the blankets. Depending on the fractional open area and the hole diameter, the heat flux can increase up to 30% for 1% perforated area and 1.2 mm holes (table 4–8 of Keller et al. 1974) or almost 80% for 2.5% of open area (Glaser et al. 1967, pp. 57–58).

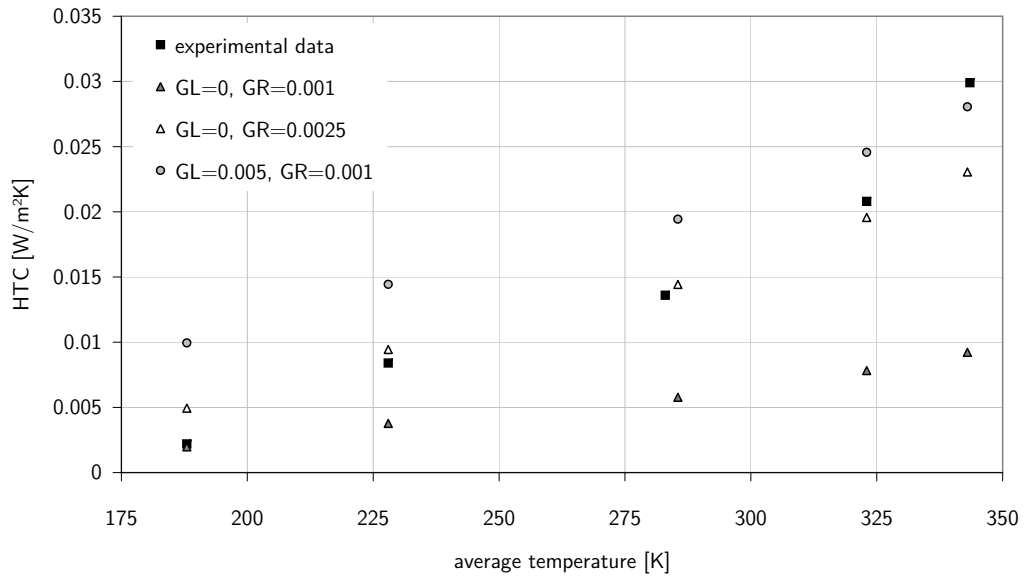


Figure 5.5: Fitting of measured heat transfer coefficients with different model parameters. The best fit is achieved with $GL = 0$ and $GR = 0.0025$. For $GL > 0$ the experimental data cannot be reproduced for low and medium temperatures.

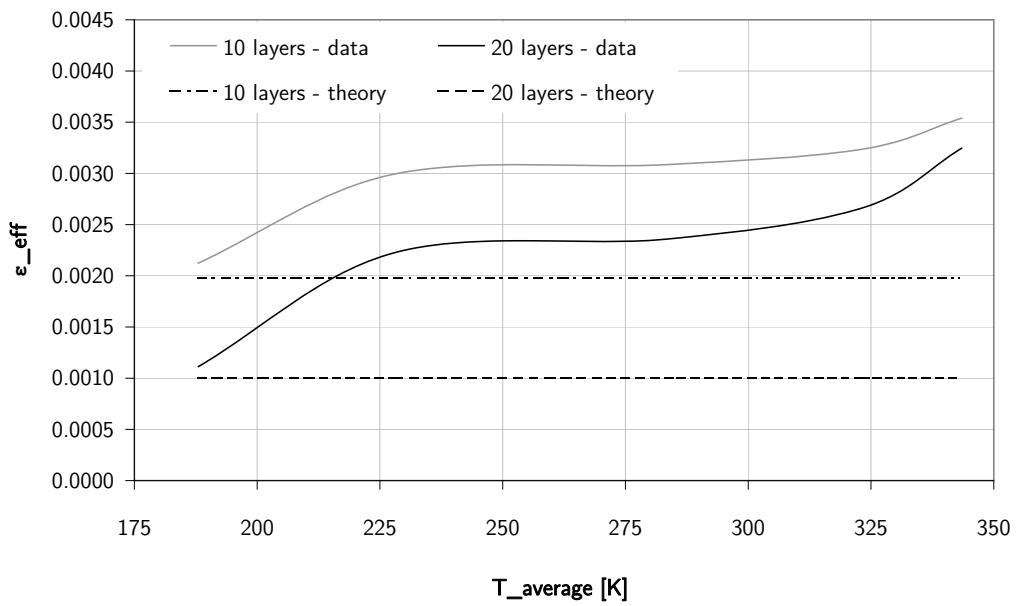


Figure 5.6: Effective emissivity of MLI as a function of average temperature

Also gas conduction due to outgassing effects can cause strong temperature dependencies. Above a pressure of $\approx 10^{-4}$ mbar, the HTC increases rapidly with pressure (Glaser et al. 1967, pp. 55–56).

If we increase the ideal effective emissivity until it fits the data, we get the result shown in figure 5.5. It is a reasonable approximation, even if the deviations for low temperatures indicate some minor weakness in the simple approach of solely radiation heat transfer as discussed earlier.

The resulting effective emissivity (equation (5.2)) for 10 and 20 layers is ≈ 0.0032 W/m²/K and ≈ 0.0025 W/m²/K respectively. This corresponds to past extensive NASA measurements (Keller et al. 1974), where it was also shown that for an 80-layer-blanket this value can be reduced down to 0.0004 W/m²/K – but only with substantial manufacturing efforts which are not feasible for most space telescopes.

To find the best approach for the eROSITA project, different experience values of former projects were used. The ESTEC data collection (Mayrhofer et al. 2009) contains applicable measurements of similar lay-ups, shown in figure 5.7. Under ideal conditions a value of less than $\epsilon_{eff} = 0.003$ can be achieved as here in the calorimeter, assuming no degradation (begin-of-life, BOL).

But for taking into account attachments, stitches, patches and overlaps as done in Stimpson et al. (1972) and Keller et al. (1974), degradation factors have to be implemented – between 2–5 for large and medium sized blankets (Mayrhofer et al. 2009) and up to 10 for small blankets with a high discontinuity density. This is verified by many data of actual spacecraft MLI performances as shown in figure 1 of Stimpson et al. (1972). Eventually this gives us an effective emissivity of $0.006 \leq \epsilon_{eff} \leq 0.03$ which agrees with a mean experience value of $\epsilon_{eff} = 0.01$ suggested by Edelstein et al. (1979). Additionally, the results for a seasoned⁵ blanket are shown where a degradation of ϵ_{eff} of a factor of 4–5 occurs. This represents a possible end-of-life (EOL) scenario, giving a good reference point for the sensitivity analysis. The 6-layer-blanket with double the effective emissivity applies to the cover blanket of eROSITA with 5 layers. For $T_{mean} \geq 320$ K, i.e. for blankets on the Sun side⁶, an additional factor of 1.5 is applied with respect to the nominal case (see figure 5.6 and figure 5.7).

A reasonable approach of effective emissivities, including values for sensitivity analysis which is done in section 5.4, is shown in table 5.2. These assumptions have to be verified during the solar simulation test of the qualification model (refer to chapter 7).

⁵by punching holes into the blanket

⁶ $T_{cold} = 290$ K, $T_{hot} = 390$ K

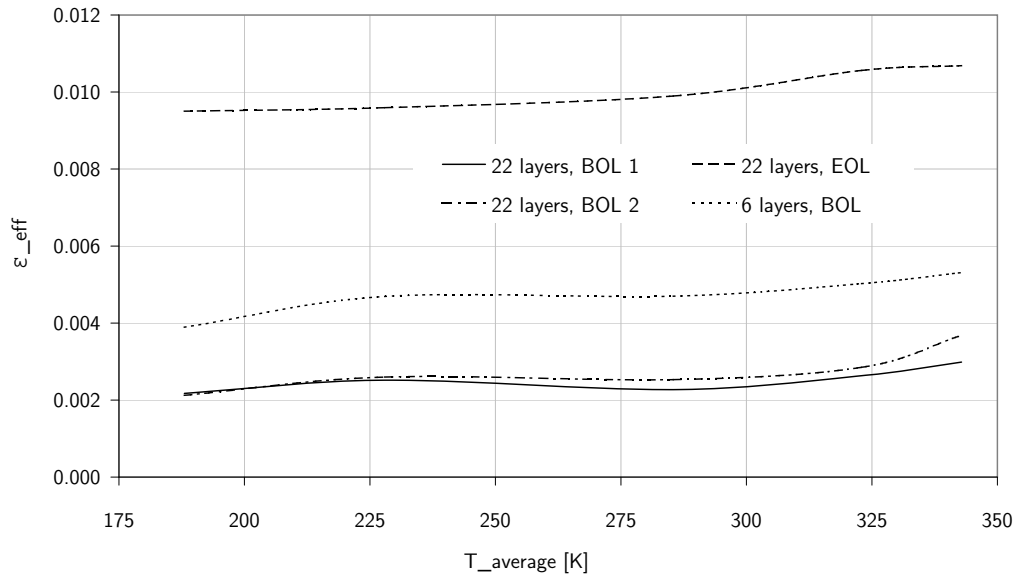


Figure 5.7: ESTEC measurements of lay-ups that are comparable to the *eROSITA* MLI. BOL 1 (ESTEC-notation: YCV/2248.BA), BOL 2 (YCV/2241.BA-Sun Side) and EOL with 22 layers (YCV/2241.BA-Anti Sun Side) are blankets similar to the *eROSITA* lay-up 1 while 6 layers are similar to lay-up 3 (YCV/1965.BA-Internal).

Table 5.2: Effective emissivity and conductance values for the *eROSITA* MLI thermal model. In case 1 only radiative heat transport (GR) is assumed while in case 2 an additional conductive contribution (GL) is considered. For small blankets always case 2 is assumed.

GR/GL	20 layers (Sun side)	20 layers (anti-Sun side)	5 layers (Sun side)
nominal case 1	0.015/0	0.01/0	0.02/0
nominal case 2	0.015/0.01	0.01/0.01	0.02/0.01
cold case 1	0.009/0	0.006/0	0.012/0
cold case 2	0.009/0.01	0.006/0.01	0.012/0.01
hot case 1	0.045/0	0.03/0	0.06/0
hot case 2	0.045/0.01	0.03/0.01	0.06/0.01

For small blankets and blankets with a lot of edges, conductivity through the layers cannot be neglected since a certain grade of compression hardly can be avoided during installation. Compressive loads on formerly ideal blankets have a significant impact on the heat flux as shown by Keller et al. (1974). Thus for small blankets always an additional conductivity of $GL = 0.01 \text{ W/m}^2\text{K}$ is assumed. In addition, this value is applied to all blankets in a separate sensitivity analysis. Most of the eROSITA MLI has a black outer layer, whose emissivity and absorptivity is almost 1 from the beginning. Therefore a performance degradation due to optical properties will not occur.

For comparison, the MLI performance of XMM-Newton is shown in figure 5.8, derived from data of the thermal balance test of the flight model (Stramaccioni et al. 2000). The performance is almost about a factor of 2 better than the assumptions for eROSITA. But one has to keep in mind that especially the upper module blankets are larger than those of eROSITA. Together with the almost identical lay-up⁷ this is a very good indication of the eROSITA MLI performance.

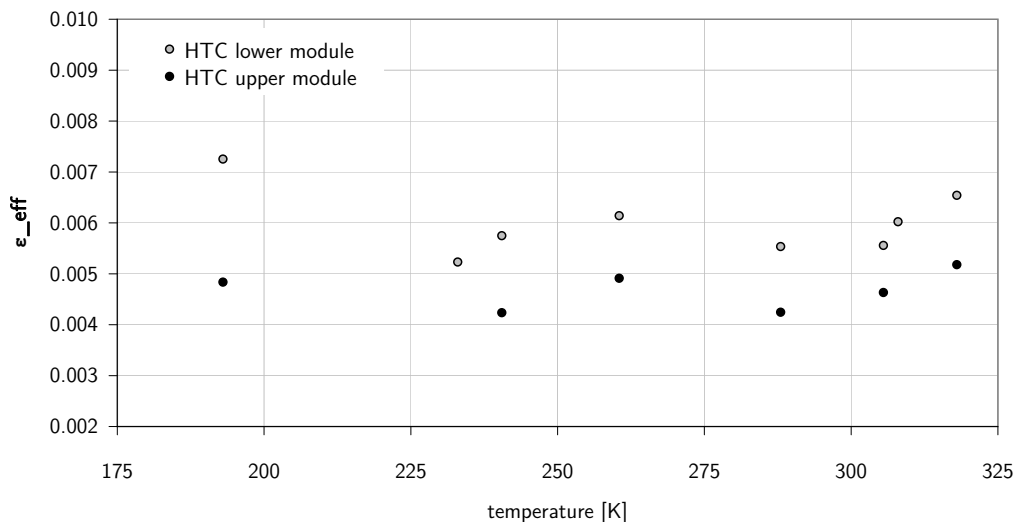


Figure 5.8: Effective emissivity of the XMM-Newton MLI, based on measurements of Stramaccioni et al. (2000)

⁷20 double-sided aluminised layers separated by Dacron nets plus carbon-filled Kapton 100 XC as outermost layer (Stramaccioni et al. 2000)

5.2 Mirror assembly

The main component of the mirror assembly is the mirror module. It consists of the mirror spider with 54 glued-in mirror shells. The X-ray baffle is attached to the mirror spider. Its purpose is to shadow photons which would hit the detector with a single reflection on the mirror⁸. It has an Invar spider and 54 shells with increasing height.

A thermal/optical baffle made of aluminium and a length of 36 cm reduces the field of view and therefore the thermal radiation into space. Furthermore it has saw tooth light traps with black coating on the inside. A trade-off was made to examine the influence of the baffle coating. There is no significant difference in the heat loss of the mirror module with respect to a black or an uncoated baffle. However, the thermal baffle temperature would benefit from a coating with low emissivity, which would in turn reduce the mirror heat loss. But this is not an option due to the required reduction of optical light.

The objective of the mirror thermal control is to achieve a uniform temperature distribution within a range of $20 \pm 2^\circ\text{C}$ at the mirror shells. Since the shells are integrated at that temperature, deviations would cause deformations due to thermal expansion (Gutruf 2009; Grzesik 2007). This again would result in a reduced angular resolution. Due to heat losses of the mirror shells, heating power has to be applied. The heating system consists of foil heaters that are glued on the mirror spiders, on each spoke as well as the outer rim (figure 5.10).

The power of the spoke heaters decreases from the outer rim to the inner rim. Due to the different shell sizes and the resulting different radiation heat losses, this power gradient is necessary to get a uniform temperature distribution over all shells.

Each heater has a nominal and redundant coil. Furthermore the heating circuit consists of two independent control circuits on every other spoke.

The heaters are not powered continuously but pulsed within intervals of a couple of seconds, depending on the exact power needed. All in all, approximately 10 W to 15 W per mirror module are required as shown in section 5.4 while the maximum possible heating power is 85 W. This provides a safety factor of more than 5.

The radiation model of the mirror assembly consists of all 54 mirror shells as well as the 54 X-ray baffle shells (figure 5.11).

⁸Reflection only at the hyperbola

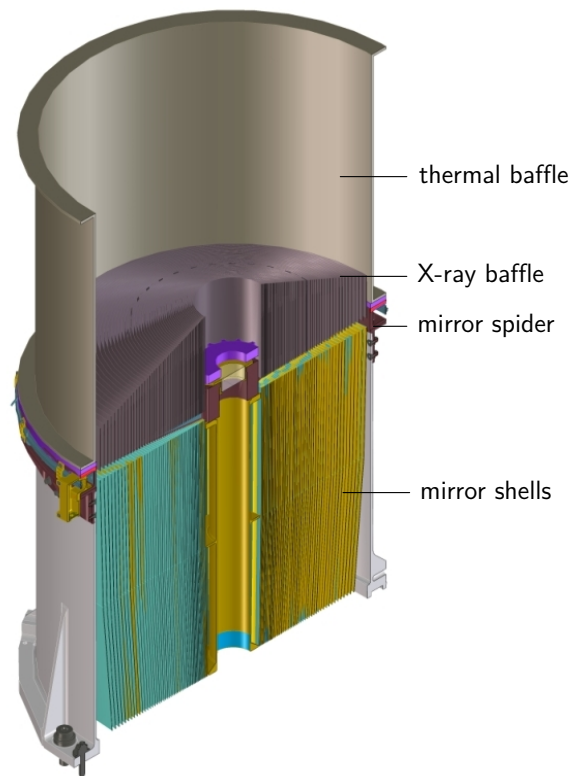


Figure 5.9: Design of the mirror assembly

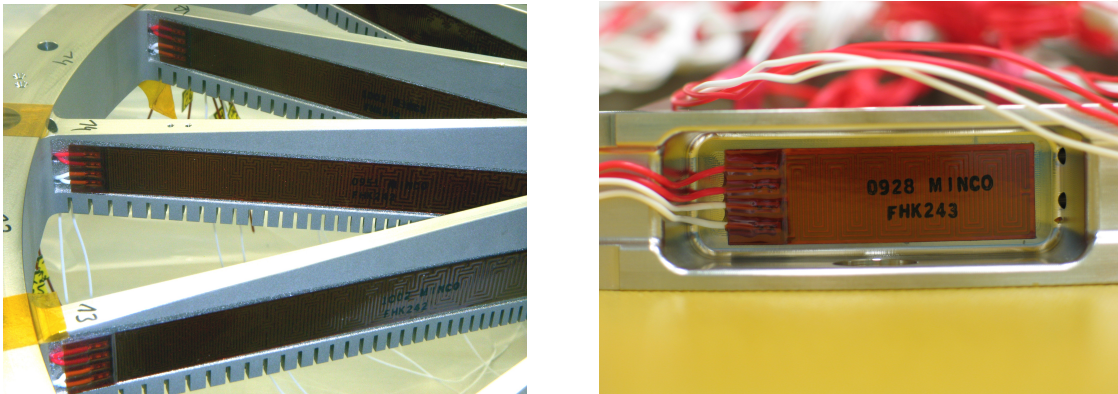


Figure 5.10: Heater positions at the mirror module spider spokes (left) and the spider outer rim (right)

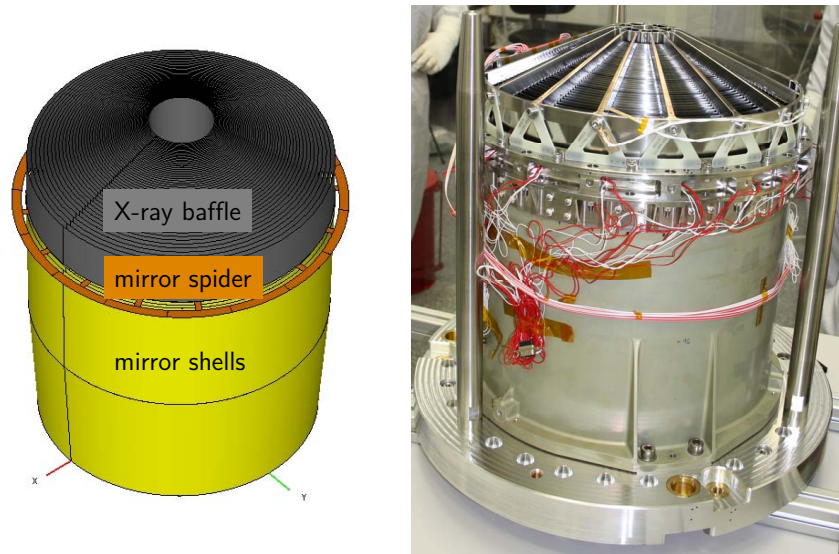


Figure 5.11: Thermal model of the mirror assembly (left) and the mirror demonstrator model (right)

Here the exact⁹ geometrical shape for the model shells is an important factor, especially for the calculation of the radiative exchange factors, since the rays coming from above are focused onto the CCDs and vice versa. Therefore, the heat input onto the cameras and the heat loss to space can be calculated very accurately, which is important for determining the final CCD temperature and the required mirror heating power. The mirror module apertures are the main source of undesired heat loss to space. The inner surface of the mirror shells is gold coated, while the outer surface is untreated electroformed nickel. The X-ray baffle shells, made of Invar, also do not have any surface treatment. All shell surfaces have a specular reflectivity (refer to appendix A.3). An overview of the thermally important parts and materials can be found in table 5.3.

Conductive couplings are generated automatically for the mirror and baffle spiders, while all other values have to be inserted manually – such as the interfaces between the X-ray baffle and the mirror module, the glued spider-shell-transitions, and the connection between the mirror spider and the baffle spider. This attention to detail guarantees a maximum model validity.

⁹Two truncated cones are used instead of hyperboloids and paraboloids, which is a good approximation for thermal aspects.

In figure 5.12 all conductive and radiative couplings of the mirror assembly are summarized and visualised in the thermal model. This model already contains results from the mirror assembly thermal balance test with the mirror demonstrator model (Fürmetz 2011d). The resulting temperature profile for the nominal operation is visualized in figure 5.13.

Table 5.3: Parts and materials of the mirror assembly

part	material	dimensions [mm]	ρ [kg/m ³]	λ [W/mK]	c_p [J/kg K]	ϵ (side 1/2)
MIS	AW-7075	$r = 187, h = 320,$ $d = 2$	2800	150	890	0.5/0.5
mirror spider	Inconel 600	$r_a = 187, r_i = 23$	8420	14.9	444	–
mirror shells	Nickel	$37 \leq r_{mean} \leq 175,$ $0.20 \leq d \leq 0.54,$ $h = 320$	8900	86	460	0.08/0.05
blocking shell	AW-5083	$r = 23, h = 320,$ $d = 1.5$	2660	120	895	0.5/0.5
X-ray baffle spider	Invar 36	$r_a = 187, r_i = 23$	8200	12.8	515	–
X-ray baffle shells	Invar 36	$38 \leq r_{mean} \leq 179,$ $d = 0.1$	8200	12.8	515	0.1/0.1
thermal baffle	Al6061 T6	$r = 205,$ $d = 1.5, h = 314$	2700	167	895	0.44/0.56* 0.97/0.89*

*chromic acid anodizing/MAP PU1 non-conductive black paint

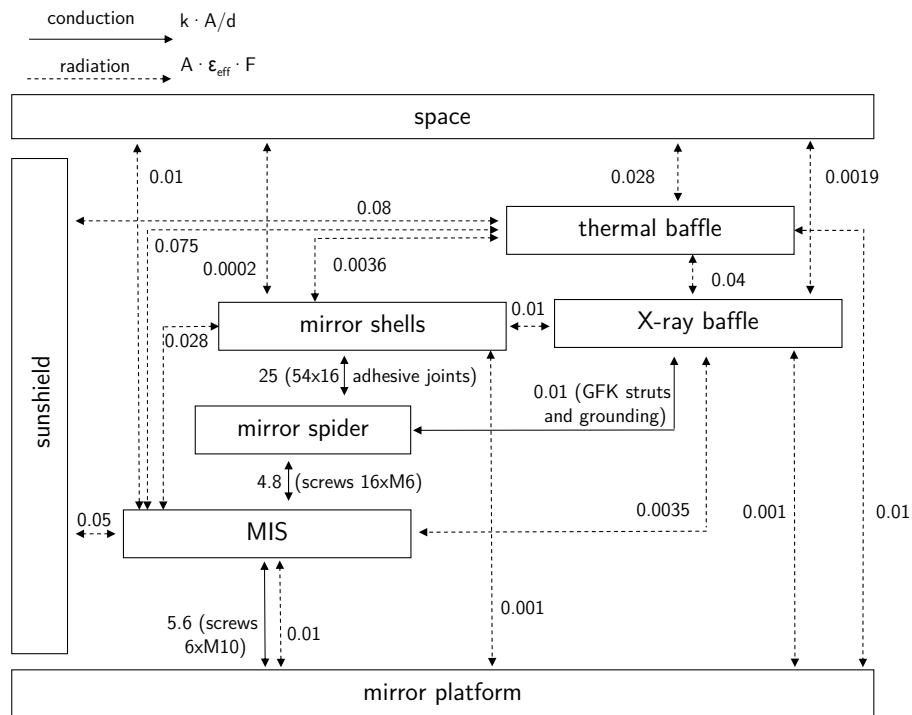


Figure 5.12: Thermal connectors of the mirror module

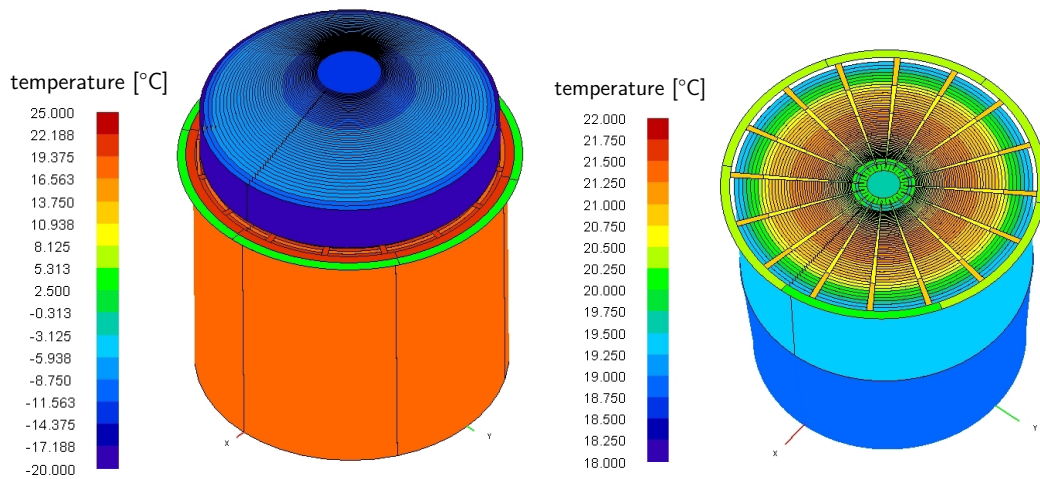


Figure 5.13: Mirror assembly (left) and mirror module temperature profile

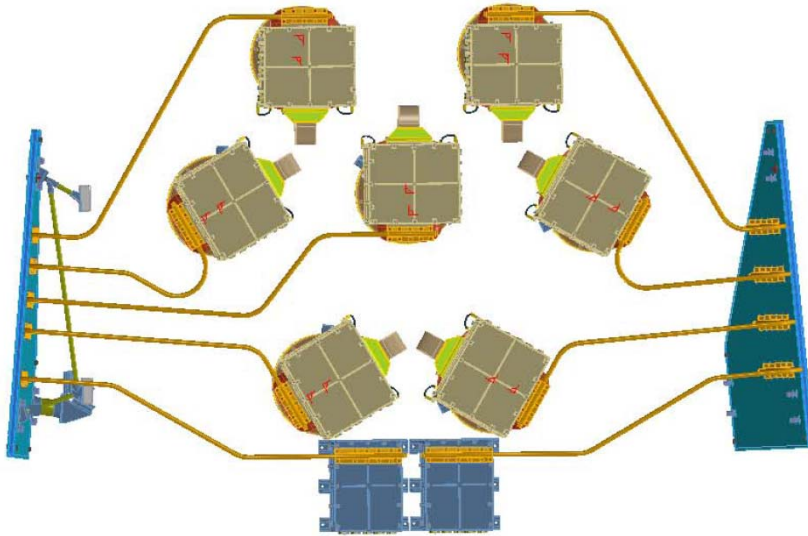


Figure 5.14: Design of the electronics cooling

5.3 Camera electronics

The cooling of the camera electronics (CE) and the interface controller (ITC) is very similar to the camera cooling system, only at higher temperatures. Waste heat load from the electronics is transported via heat pipes to two separate radiators, shown in figure 5.14. Each box has its own heat pipe and is connected to the evaporator, whereas the condenser is attached to one of the two radiators with 0.5 m^2 each.

The working fluid here is ammonia. At the working temperature of about 273 K , ammonia has a larger heat transport capability than ethane. The heat pipes have an outer diameter of 10 mm . Both radiators also have a sandwich structure and the front sides are covered with the same high emissivity white paint as the camera radiators. Radiative heat transport is much more effective than at low temperatures (refer to figure 2.3). So the total required radiator area only is about 1 m^2 , even if the electronics produces more than 200 W in total.

The heat of the electronic boxes is dissipated on printed circuit boards (PCBs). They are clamped to the bottom and top plate of the CEs and ITCs via wedge lock connections as already described in section 4.1.

Water heat pipes embedded in the casing's bottom (CE) and top plates (ITC) re-

spectively guarantee an optimum heat transport to the ammonia heat pipe interface (figure 5.15).

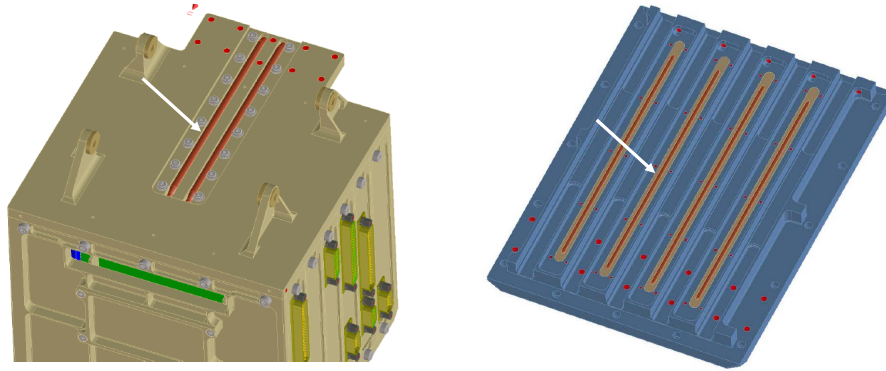


Figure 5.15: Embedded water heat pipes in CE (left) and ITC (right)

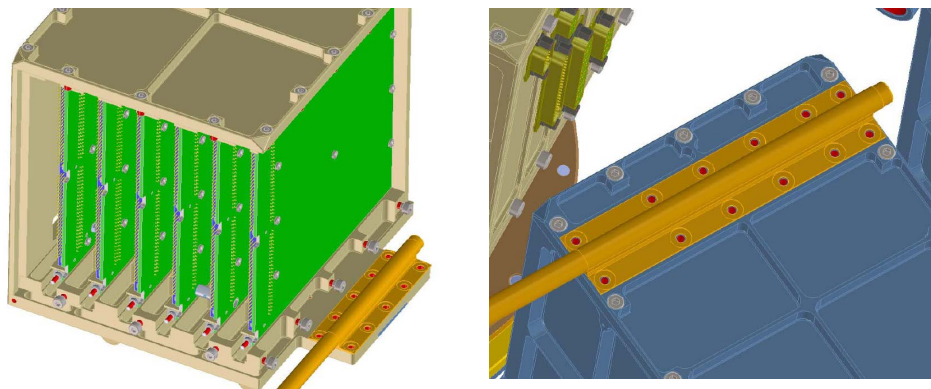


Figure 5.16: Heat pipe interfaces at CE (left) and ITC (right)

Alternative cooling concept

During an earlier phase of the project an alternative cooling concept for the camera electronics was considered. On the one hand 200 W are dissipated at the bottom of the telescope, and on the other hand the mirror modules have to be powered with almost 100 W. This almost suggests to use the wasted heat load for mirror thermal control.

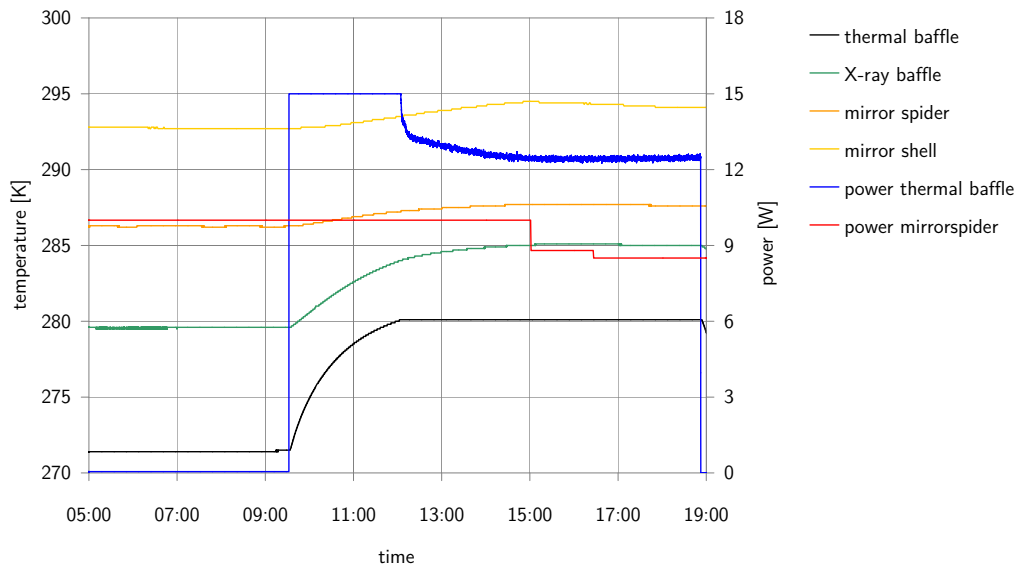


Figure 5.17: Influence of the thermal baffle temperature on the mirror thermal control system. The combination of a black inner surface (to prevent stray light) with a high emissivity and a thermally isolated attachment causes low temperatures. For demonstration, the thermal baffle temperature was increased from 271.5 K to 280 K. The necessary heating power to keep the mirrors at 293 K was reduced from 10 W to 8.5 W (figure 5.17).

Apart from the aperture looking to deep space, the cold thermal baffle cylinders are the main reason for the large heat loss of the mirror modules. The dependence of the required heating power from the baffle temperature is significant as verified in the thermal balance test of the mirror assembly (see figure 5.17). The colder the thermal baffles, the more heating power is required.

Thus we wanted to heat up the thermal baffles by using them as radiator area for the electronics. Due to the large distance common heat pipes were not suitable. Not only the length itself would limit the maximum heat transfer, but also the parasitic heat losses of the necessary mounting to the telescope structure, not speaking of the mounting procedure itself. So we went for loop heat pipes (LHP). In contrast to common heat pipes the liquid and vapour phase are separated and the tubes are capillaries with only few millimetres in diameter. The evaporator has an outlet for vapour and an inlet for liquid, which forces the flow into one specific direction. The advantages of LHPs are a high heat transport capability over large distances, flexibility, low mass

and a high tolerance regarding to tilt against gravity. An overview over the working principle may be found in Maydanik (2005). In addition, LHPs are thermal diodes and as soon as no power is applied to the evaporator, the conductivity approaches zero. This would prevent a cooling of the electronics beyond the minimum temperature without any additional efforts.

In our *Green Satellite Concept* a LHP evaporator is mounted on each of the nine electronics casings. The LHP condensers are attached to the thermal baffle as shown in figure 5.18.

Despite the great advantages, the first breadboard tests showed the weaknesses of the considered miniLHP. The temperature difference between evaporator and condenser was rather high in the first place due to a maximum global heat conductance of only about 1 W K^{-1} . Moreover, only if the power was applied very close to the evaporator, the cooling was effective and the nominal heat transfer value was reached. This value was highly temperature dependent and the less power reaches the evaporator, the larger was the gradient. As a result the applied power determined the gradient and a lower condenser temperature did not result in a lower evaporator temperature automatically.

A test set-up with a LHP and a structural-thermal model of the camera electronics showed PCB temperatures up to 350 K. Even improvements like a better decoupling from the proton shielding and a higher thermal coupling between casing and LHP interface did not produce satisfying results. Other LHP types would have been more promising due to a larger power transport capability and smaller gradients, but this would have meant to make a new design. Furthermore, handling issues and mounting problems, together with a very tight schedule, let us drop this concept and chose a conventional cooling concept instead – with constant conductance heat pipes and two radiators as described above.

5.4 Predictions for the eROSITA thermal control system performance

After implementing the results of all pre-tests into the main model, the different load cases with transient and steady state solutions are examined.

This last step in thermal analysis procedure now uses the theoretical background and

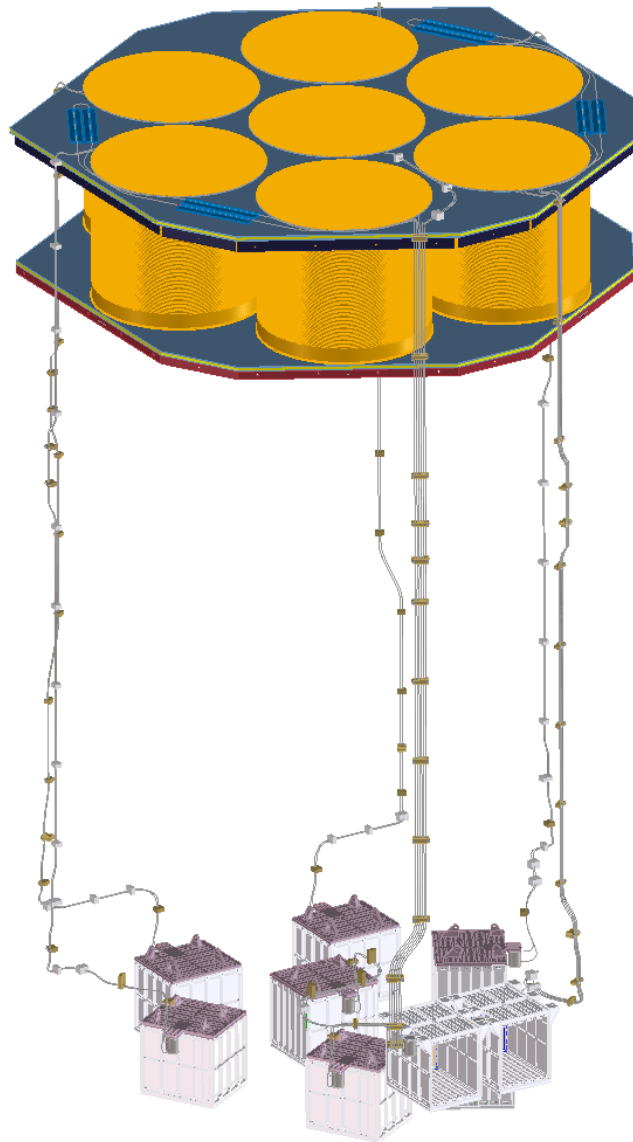


Figure 5.18: Loop Heat Pipe concept for electronics cooling

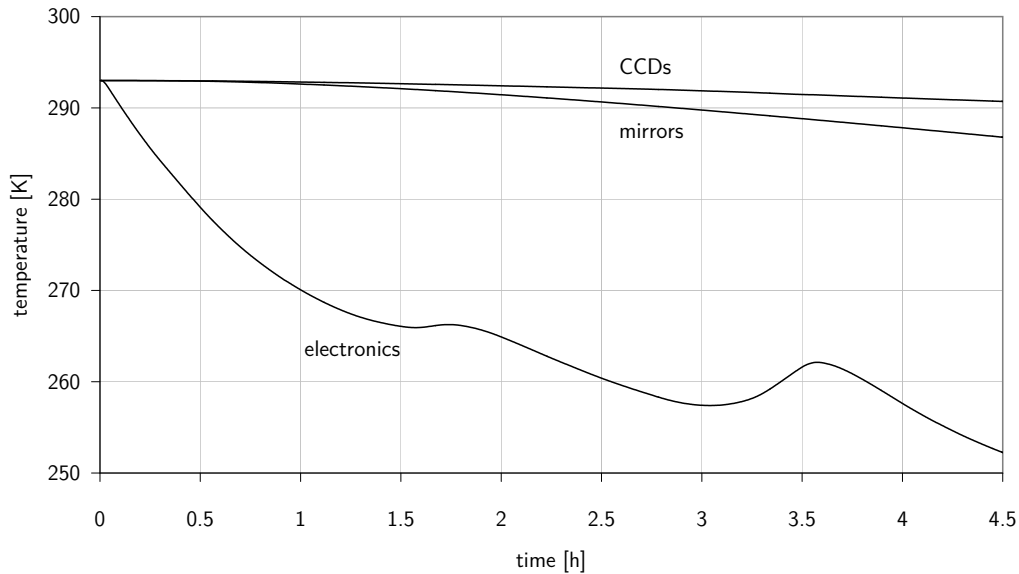


Figure 5.19: Cooling curve after launch

the test results collected so far to prepare a thermal model for an accurate prediction of the thermal performance of the complete telescope.

With the transient analysis it is possible for example to determine the cooling after launch and to examine the influence of temperature fluctuations and changing power inputs. The steady state analysis gives the equilibrium conditions. Results are presented in the following.

First, the cooling behaviour of the satellite after launch is examined. After one revolution in a Low-Earth-Orbit with a height of 200 km, the spacecraft is lifted into an eccentric parking orbit with an apogee of 3000 km. Subsequently, it starts its journey to the Lagrange Point 2 (refer to section 6.1). About one hour after the last course correction, power from the solar panels is available. Until then, solar panels are in hinged position, no power is applied. As long as the satellite is orbiting the Earth, a significant amount of thermal radiation from the Earth and albedo decelerates the cooling (see figure 5.19). In this scenario, all critical parts stay above their minimum required temperatures, until the thermal control system is powered.

In table 5.4 the reference values for the nominal operational case and the survival case, mentioned in section 1.3, are summarized. The temperatures of the spacecraft and the ART-telescope are assumed to be constant with 273 K and 293 K respectively, space

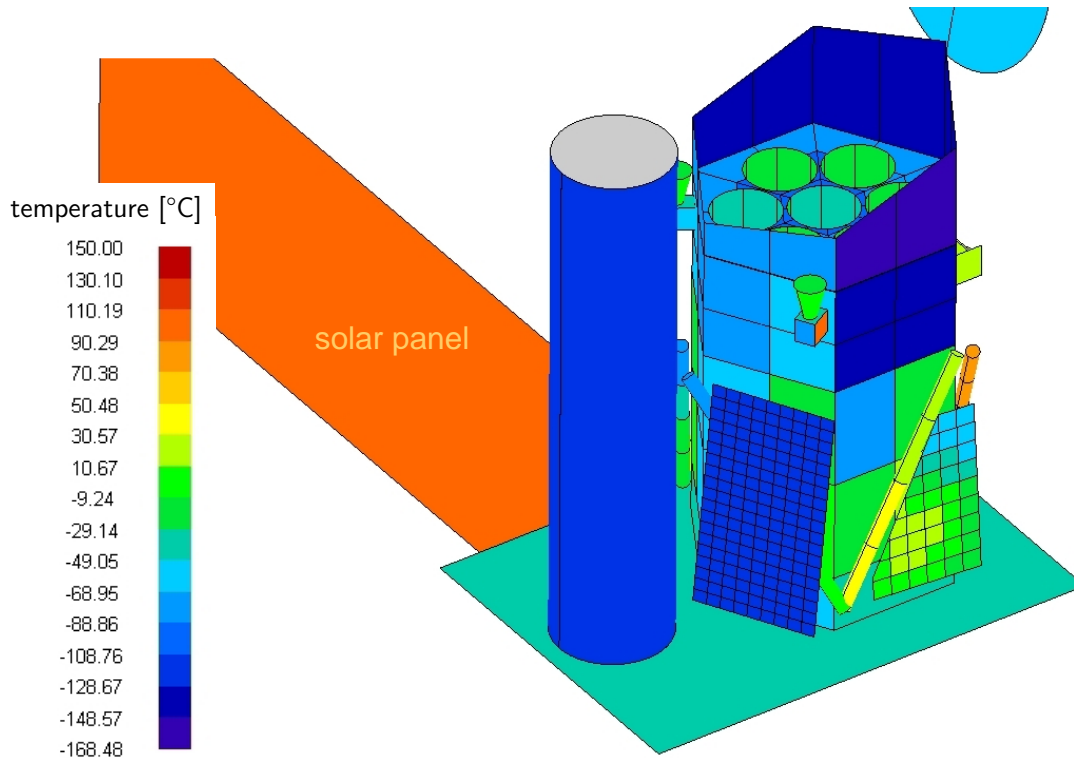


Figure 5.20: Surface temperatures in nominal operation

temperature is 3 K. An overview over the complete satellite surface temperatures is given in figure 5.20.

As discussed in section 5.1, the properties of the MLI have a large influence on the final temperature level. In table 5.5 different MLI values and their impact on the telescope temperatures are compared; the corresponding load cases are also defined in section 5.1.

With a sufficient and well-balanced amount of heating power at the mirror spiders, all shells stay within the required limit between 291 K and 295 K and the temperature gradient is not larger than 2 K. However, the absolute value depends on the boundary conditions as well as on the position of the mirror module within the telescope. At the side pointing towards the Sun the heat input is larger and thus the temperature of the mirror platform is higher than on the anti-Sun side. This reduces the heat

Table 5.4: Comparison of reference values for the nominal operational case and the survival case

	nominal case	survival case
heating power mirrors [W]	78	65
power CAMEX [W]	7×0.75	7×0
power camera electronics [W]	7×26	$7 \times 10^*$
power ITC [W]	1×26	1×26
sunshield [K]	260 – 292	248 – 283
thermal baffle [K]	236 – 276	214 – 265
X-ray baffle [K]	252 – 271	239 – 256
mirror shells [K]	291 – 295	274 – 278
mirror platform [K]	280 – 293	265 – 275
optical bench [K]	287 – 296	266 – 278
camera platform [K]	286 – 296	260 – 270
proton shielding [K]	286 – 296	259 – 268
CCDs [K]	181	168
camera radiators [K]	151 – 165	147 – 159
camera electronics [K]	293 – 309	255 – 276
electronic radiators [K]	231 – 296	215 – 255

*survival heaters

Table 5.5: Sensitivity analysis of the influence of MLI properties. For definition of the separate cases refer to table 5.2.

	nominal case 1/2	cold case 1/2	hot case 1/2
heating power mirrors [W]	78/79	81/82	68/68
power CAMEX [W]	7×0.75	7×0.75	7×0.75
power CE [W]	7×26	7×26	7×26
power ITC [W]	26	26	26
sunshield [K]	260 – 292/ 254 – 292	248 – 290/ 249 – 290	250 – 302/ 248 – 302
thermal baffle [K]	236 – 276	236 – 273	236 – 282
X-ray baffle [K]	252 – 271	252 – 271	252 – 273
mirror shells [K]	291 – 295	291 – 295	291 – 295
mirror platform [K]	281 – 293/ 280 – 293	281 – 290/ 280 – 291	281 – 303
optical bench [K]	287 – 296/ 286 – 297	286 – 293	287 – 311
camera platform [K]	286 – 296	285 – 295	292 – 301
proton shieldings [K]	286 – 296	285 – 295	292 – 301
CCDs [°C]	181/183	179/181	190/191
camera radiators [K]	151 – 165/ 153 – 166	149 – 162/ 151 – 164	161 – 173/ 161 – 175
camera electronics [K]	193 – 309	192 – 309	197 – 311
electronic radiators [K]	131 – 296	130 – 296	135 – 298

losses towards the mounting and therefore saves heating power. The temperature of the central mirror module for the nominal operation is shown in figure 5.13.

The most critical point is the camera radiator temperature. It directly influences the CCD temperature, so it has to be as low as possible. As it follows from table 5.5, the MLI on the backside plays an important role in the thermal control. Any irregularities of the blankets have to be avoided to suppress conduction through the blankets. In addition, all kinds of parasitics onto the cooling chain have to be reduced to a minimum.

6 Orbit scenarios

In the early stages of the eROSITA project a Low Earth Orbit (LEO) with about 600 km altitude was foreseen for the operation of Spektrum Röntgen Gamma (SRG) (Fürmetz et al. 2008). In the autumn of 2008 this was changed to an orbit at the Lagrange point 2 (L_2) of the Sun-Earth-system due to technical reasons of the spacecraft.

6.1 The Lagrange point 2

The Lagrange points are the five stationary solutions of the circular restricted three-body problem, where the sum of the gravitational forces of two co-orbiting massive bodies on a third (much more lighter) body exactly provides the centripetal force to rotate with them. Looking at the Sun-Earth-system, an ideal spot for space telescopes is the Lagrange point 2 (L_2) (see figure 6.1). It lies on the line defined by the Sun and the Earth, in anti-Sun direction. So the spacecraft keeps pace with Earth as orbiting the Sun. The distance to the Earth is 1.5×10^6 km, which is one percent of the Sun-Earth distance of 150×10^6 km.

As described in Fürmetz et al. (2010), advantages of the larger distance to the Earth are much more stable thermal conditions and no observing constraints by the Earth. Neither line-of-sight obstructions nor disturbances by radiation belts will limit the observations. The background radiation, however, is much higher, which implicates that the electronics have to be designed for larger radiation exposure. Since it is a saddle point of the effective potential and therefore dynamically unstable with an e-folding time of ≈ 23 days, it is necessary to make regular course corrections.

The orbit of SRG around L_2 will be an ellipse with a semi-major axis of 1×10^6 km (alternatively a smaller one of 3×10^5 km, depending on the launch scenario – see below) and a semi-minor axis of 2.5×10^5 km. The normal to the orbital plane will be tilted about 35° with respect to the ecliptic which will lead to an effective semi-minor

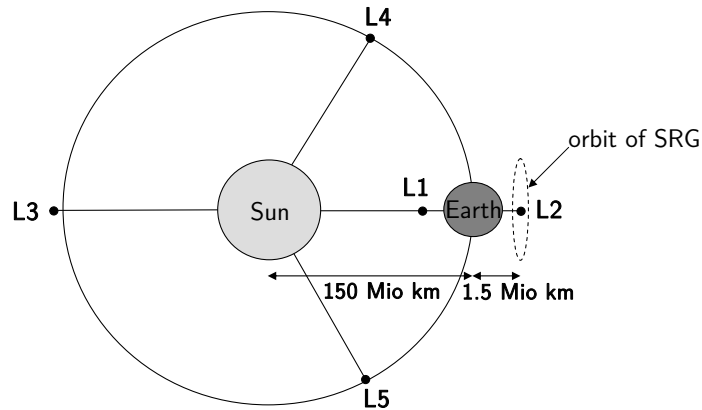


Figure 6.1: Operation of SRG at L2

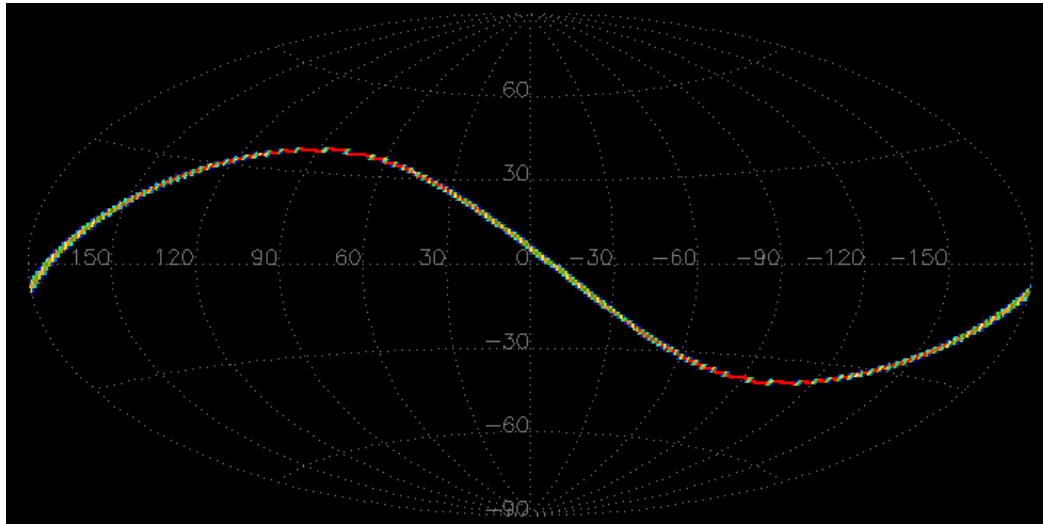
axis of $2.5 \times 10^5 \text{ km} \cdot \cos 35^\circ \approx 2.05 \times 10^5 \text{ km}$. The final value of the semi-major axis depends on the launch manoeuvre. With a challenging lunar swing-by it would be possible to reach the smaller orbit. The final trajectory effects the possible pointing scenarios as described in the next section.

6.2 Spacecraft pointing

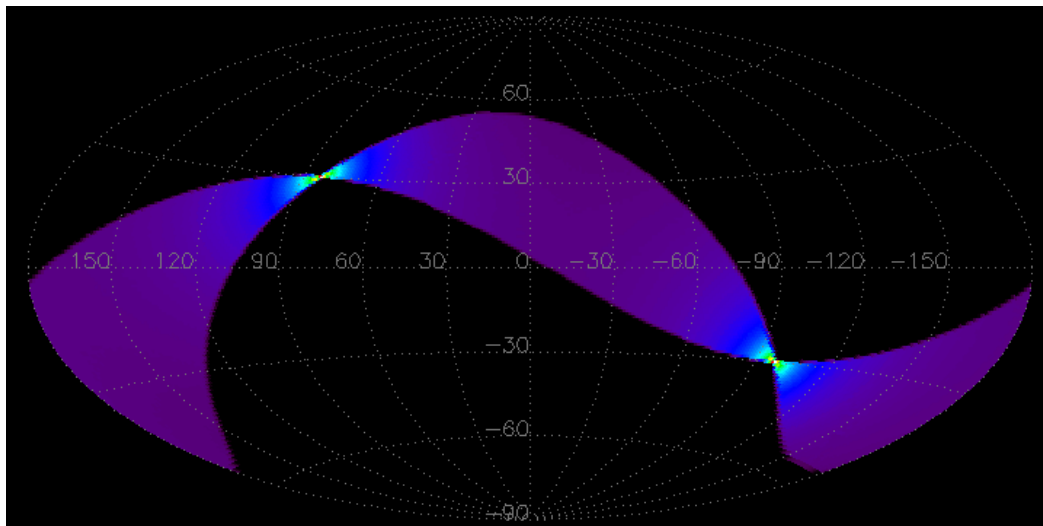
During the 4 years of all-sky survey, the satellite will spin around its scan axis, which is defined in the satellite coordinate system. The scan axis is perpendicular towards the viewing direction of the telescope. It is supposed either to point towards the Earth or the Sun, depending on constraints of the spacecraft. On the one hand, the deviation of the solar panels from the Sun direction must not exceed 30° to ensure power supply. On the other hand, the cone angle of the radio complex for data transmission is only 2° . In case of Sun pointing this would require a constant tracking but would have scientific advantages as described in section 6.3.

One revolution of the telescope around the scan axis takes about 4 h to 6 h and covers a great circle of the sky with a width of 0.81 deg^2 , the field of view of eROSITA. With the superimposed orbit around the Sun, these great circles gradually cover the complete sky within half a year (refer to figure 6.3).

The third motion is because of the orbital period around L_2 of 180 days. For Earth pointing, this causes noticeable irregularities in the smooth distribution of the great



(a) One day



(b) 50 days

Figure 6.2: Exposure footprint of great circles due to spacecraft spinning in galactic coordinates. The scan axis points towards the Sun.

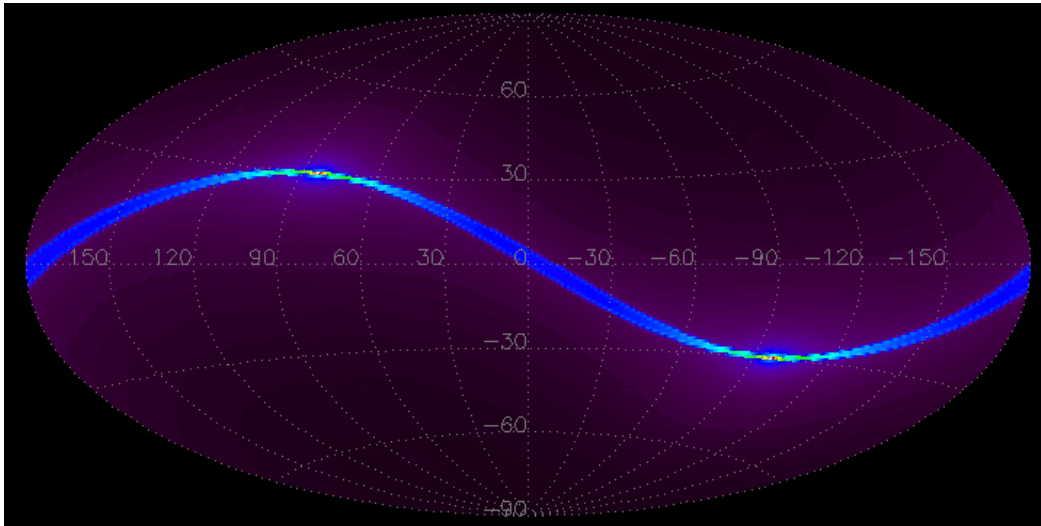
circles, because the maximum tilt angle of the scan axis is about 11° . Since the revolution time is almost exactly half a year, undesired effects due to superposition with the Earth's revolution around the Sun had to be ruled out.

The movement in the ecliptic only creates a belt of irregular exposure, which is not of a certain scientific interest (figure 6.3(a)). But more important, the superposition of spacecraft motion and Earth revolution does not have undesired effects. In contrast, the movement perpendicular towards the ecliptic expands the otherwise singularity-like points of largest exposure, where all the great circles overlap – the scan poles (figure 6.3(b)). This smearing of the pole region is appreciated for getting deep fields with rather high exposure since they are of a much higher value for science than singularities at the scan poles. Deep surveys are necessary for very faint sources such as active galaxies and galaxy clusters with large redshifts. But only if the semi-major axis of the orbit around L_2 is small enough, an Earth pointing of the scan axis is possible. This solution is also preferred because of a very small communication antenna cone angle of only 2° . Otherwise the antenna has to be re-adjusted continuously. For Sun pointing this effect is much smaller and can be neglected for exposure calculations because of the large distance to the Sun (150×10^6 km) and the resulting negligible angle variation.

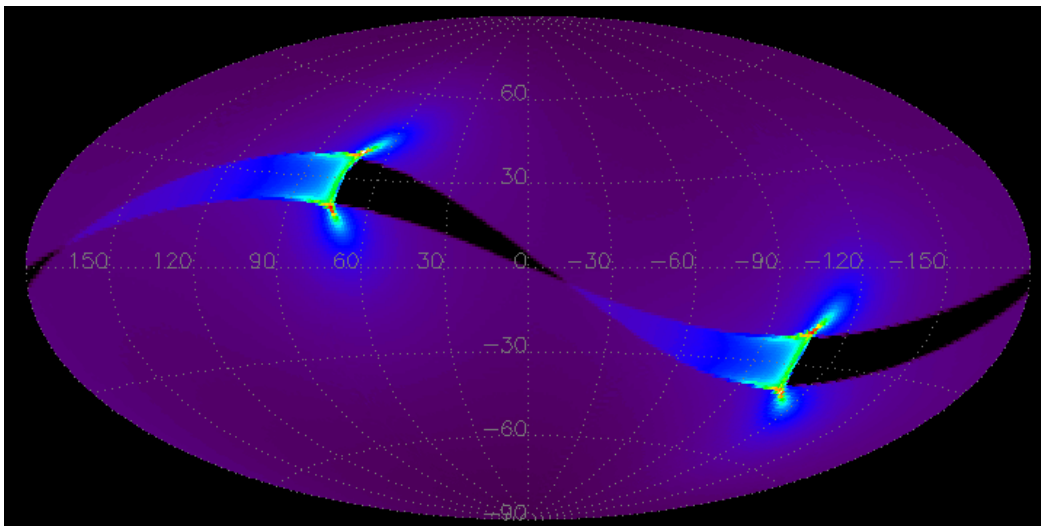
6.3 Exposure

The exposure describes the time (in seconds) eROSITA is looking at certain areas in the sky. With the exposure being proportional to the number of photons, it is an important means for the mission characteristics. Summing up the exposure for the whole sky and the complete mission duration, we get the exposure map.

For a possible eROSITA scenario with a semi-major axis of the orbit around L_2 of 3×10^5 km and a semi-minor axis of 2.05×10^5 km this results in areas of increased exposure with a few hundred square degrees as can be seen in figure 6.4(a). They are located around the ecliptic poles and grow with the semi-minor axis of the orbit. In case of the scan axis pointing towards the Sun, the effect of the orbit motion is marginal as described above. The consequences are sharp exposure maxima at the ecliptic poles (see figure 6.4(b)). To still enlarge this area and to achieve a similar result as with Earth pointing of the scan axis, it is currently considered to alter the exact pointing direction of the scan axis periodically during a revolution around L_2 .

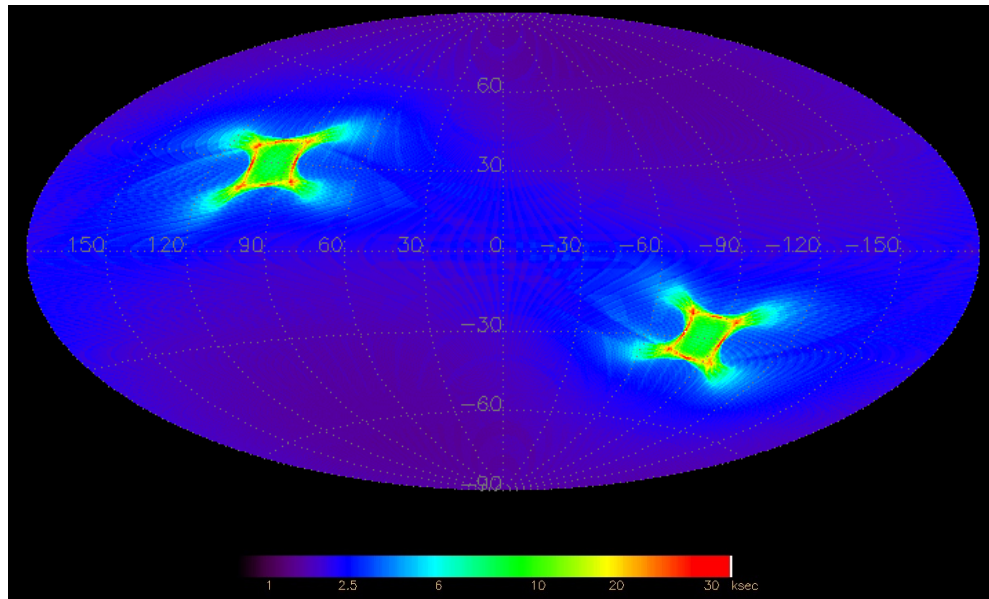


(a) Movement of the scan axis within the ecliptic

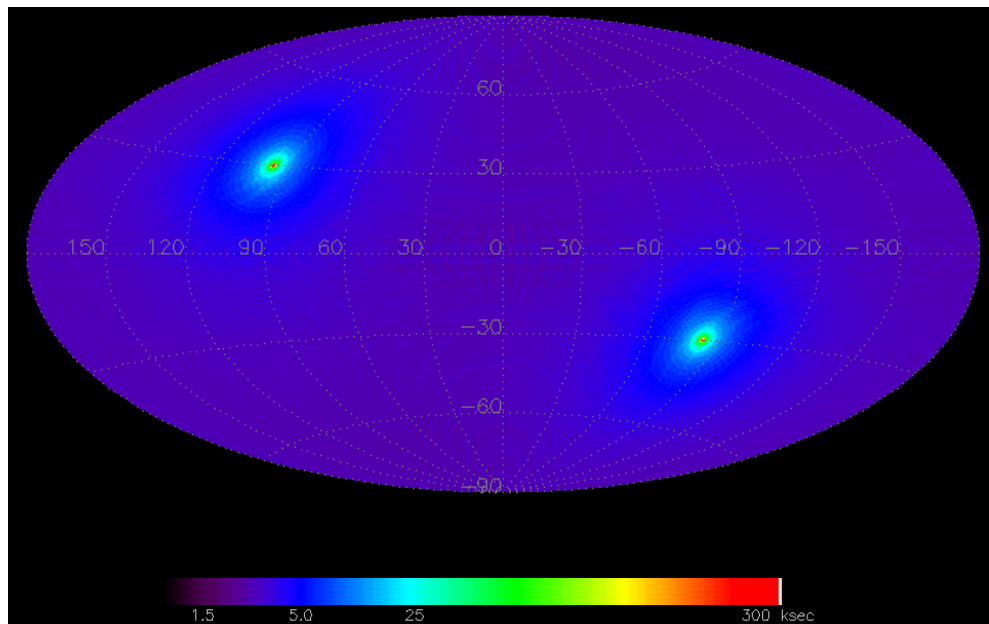


(b) Movement of the scan axis perpendicular to the ecliptic

Figure 6.3: Influence of orbital movements in the ecliptic and perpendicular to the ecliptic in galactic coordinates. The scan axis points towards the Earth, scan duration is 180 days.



(a) Exposure with Earth pointing of scan axis



(b) Exposure with Sun pointing of scan axis

Figure 6.4: Complete exposure maps for the eROSITA mission in galactic coordinates: 4 years of all-sky survey, 180 days for one revolution around L2, 4 hours for one revolution around the scan axis. The field of view is 0.81 deg^2 and an efficiency of 80% is assumed for the survey which is a conservative estimation based on former missions. Mean radii of the orbit around L2 are 300 000 km in the ecliptic and 205 000 km perpendicular.

6.4 The Low Earth Orbit

As mentioned above, Spektrum-Röntgen-Gamma was supposed to be operated in a Low Earth Orbit (LEO) with a height of approximately 600 km in an earlier phase of the mission. Apart from some other advantages and disadvantages, high parasitic heat loads due to thermal radiation from the Earth and albedo would have risen the temperature level of the satellite. Especially the radiators would have been affected. An elaborated examination of the thermal boundary conditions and their influence on the radiator temperatures are done in Fürmetz (2007).

This concept only works if both radiators point in opposite directions and at least one radiator is exposed to deep space while the other is irradiated by the Sun and the Earth. As a consequence, one radiator has to provide the complete cooling power and the connection to the cameras has to be switchable. This is realized by variable conductance heat pipes. The nitrogen reservoirs are powered as long as the radiator temperature is above the average temperature during an orbit. To suppress large temperature deviations, a latent cold storage is foreseen between the radiators and the cameras. This results even without parasitics onto the cooling chain in a CCD temperature not lower than 185 K, see figure 6.5.

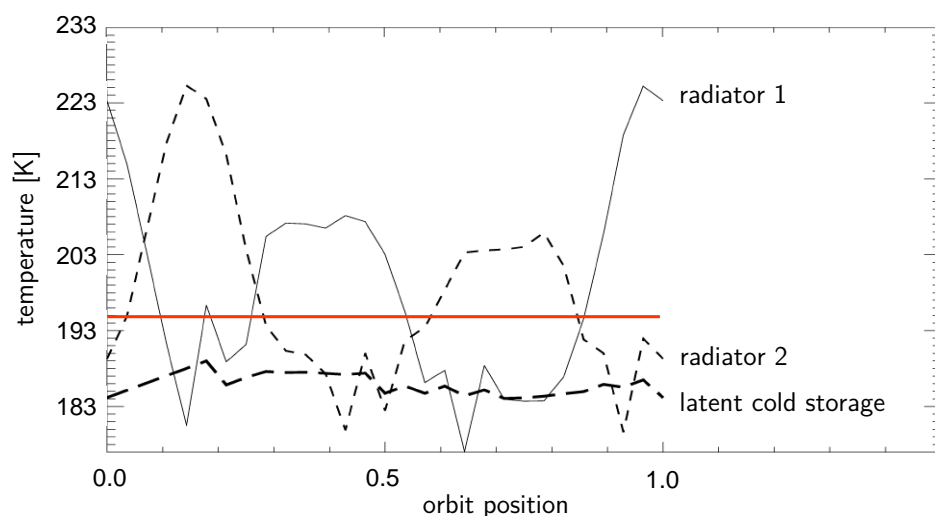


Figure 6.5: Theoretical radiator temperatures in the Low Earth Orbit, image taken from Fürmetz (2007). Both radiators – on opposite sides of the telescope – are connected to a latent cold storage as thermal capacity.

7 Summary and outlook

In the course of this work an innovative cooling system for the cameras of the X-ray telescope eROSITA has been developed, manufactured and tested.

Camera thermal control

The complex design with the sevenfold symmetry of the eROSITA telescope requires an innovative concept of the camera cooling system. Large distances in combination with a very low operating temperature between 173 K and 183 K make it difficult to benefit from existing projects. Extreme temperatures with the Sun on the one side and the cold space on the other provide extreme boundary conditions. All in all three different low-temperature ethane heat pipes are used to transport the heat from the cameras to two radiators outside the telescope structure. Due to the radiator's special surface paint a very high emissivity for an effective thermal radiation emission is achieved.

Heat pipes

All three different kinds of low-temperature ethane heat pipes were developed and optimised in the course of this work. Altogether, they make the cooling chain for the eROSITA CCD cameras, beginning with small camera heat pipes, connected to each CCD module. These heat pipes are bent in three dimensions due to limited space and testing purposes, because ethane heat pipes are very sensitive to tilt and cannot work against gravity. Two ring heat pipes are collecting the heat of all seven cameras and are conducting it to two exchange points. Each of these points is connected to one camera radiator with special variable conductance heat pipes. A special challenge was the requirement that the CCDs must not be cooled after launch, to avoid condensation of compounds – outgassed by satellite materials – on the CCDs. So the sVCHPs can be switched on after a certain period in space by telecommand with the help of an

electric solenoid latching valve. This valve separates the working fluid from the heat pipe tube in the first weeks of the mission. Furthermore, these heat pipes provide a sensitive means of temperature control by adjusting the length where condensation of the working fluid takes place. This is accomplished by increasing or decreasing the range of the condenser that is filled with non-condensable gas. Only a small amount of electrical power is needed to heat the reservoir of the non-condensable gas to expand the diffusion barrier further in the condenser range and so to control the cooling capacity of the VCHP. Since this reservoir with the electric heater is thermally decoupled from the main radiator, no additional power is fed into the cooling chain.

A lot of tests were made to characterize and optimise the heat pipes. During a drop tower experiment the liquid velocity was determined, and also the functionality under zero gravity was proven. Afterwards, in several thermal balance test of all three heat pipe types, maximum heat transport capabilities and heat transfer coefficients were determined and correlated with the underlying theory. Further thermal vacuum tests were made to optimise the heat pipe performance. This included the ideal amount of working fluid and non-condensable gas inside the variable conductance heat pipes.

Thermal analysis

A thermal model of the complete telescope was used to examine and predict the thermal behaviour of the subsystems. Step by step this model was improved by the results of the different thermal tests. The most complex set-up so far verified one branch of the cooling system. It consisted of one radiator, two variable conductance heat pipes, one ring heat pipe and a structural-thermal model of the camera assembly, including a camera heat pipe. Prior assumptions of heat transfer coefficients and optical properties were confirmed and improved respectively.

Apart from the camera cooling system the other subsystems were modelled and tested as well; for example, the thermal control system of the mirror module and the camera electronics.

Multi-layer insulation as a very effective, passive means of temperature control covers most of the outer surface of the telescope. Only the apertures and the radiators are left open. The exact properties of the insulation have a wide influence on the final telescope temperature level. Since the final performance is significantly influenced by overlaps, edges and gaps, the integration itself determines the properties of the insulation. Therefore it cannot be tested separately. Experimental results will not be

available before the solar simulation test with the complete telescope, including the flight multi-layer insulation (see below). Thus, the thermal modelling has to consider values from former experiments and missions, in combination with a detailed modelling and an uncertainty analysis.

Orbit scenarios

In an earlier phase of the mission, after the change from a low Earth orbit to an orbit around the Lagrange point 2 (L2), the impact on the mission had to be estimated. Apart from a much higher radiation background, the complete mission scenario needed to be changed. It is no longer necessary to avoid the Earth. Only the solar panels and the communication antenna are limiting the orientation of the satellite. Since the orbit around L2 has a duration of approximately 180 days, an undesired superposition with the Earth's revolution around the Sun had to be eliminated. The influences of spacecraft movements within and perpendicular to the ecliptic were separated and classified as uncritical.

Additionally, the telescope's attitude of possible orbit scenarios was used to generate exposure maps. These maps show the distribution of the telescope's observation time for the whole mission over the complete sky. They are an important means for the mission planning and vice versa, since the scan procedure may be – to some degree – adjusted to the scientific requirements.

Manufacturing of flight hardware

In the near future, the flight models of all heat pipes have to be completed and tested extensively. Further tests and long-term measurements of leak rates and heat transport capabilities have to be made. The performance of the camera heat pipes strongly depends on the ethane filling level. Therefore, each heat pipe has to undergo extensive tests and is only chosen for flight if it shows the required performance. The ring heat pipes have to run through further measurements of heat transport capabilities over a wider temperature range. For the variable conductance heat pipes, the optimum mass of non-condensable gas strongly depends on the radiator temperature. So we have to wait for the solar simulation test (see below) to confirm the theoretical predictions and adjust the nitrogen amount if necessary.

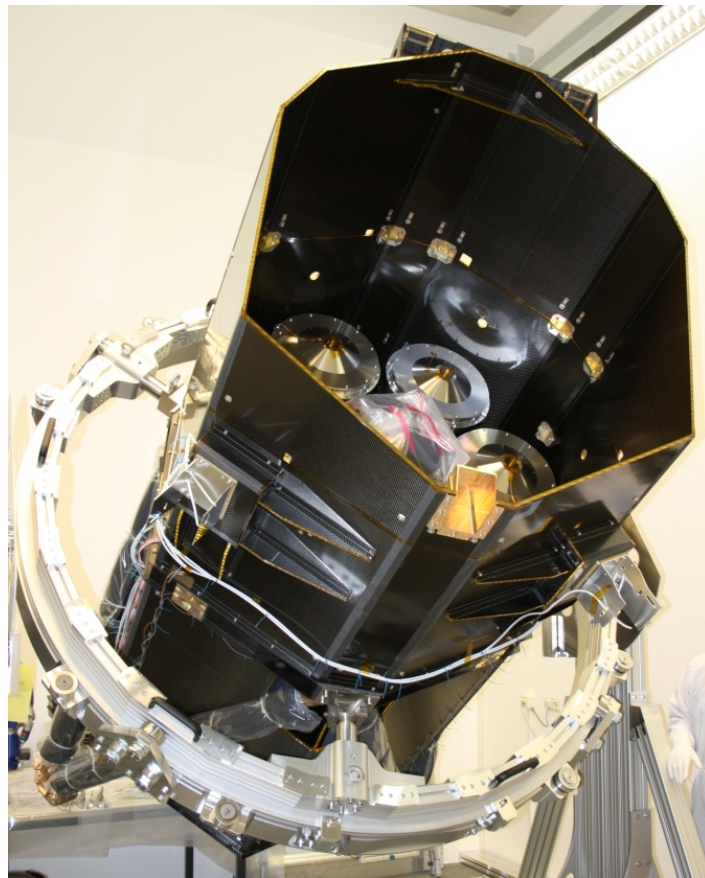


Figure 7.1: Assembly of the eROSITA qualification model

Solar simulation test

A solar simulation test of the telescope qualification model with the flight structure, the flight-like cooling system and mass dummies for mirror modules and camera assemblies is in preparation. All components have representative thermal properties. This test is absolutely necessary to verify and improve the thermal model by narrowing down uncertainties in equilibrium temperatures and transient behaviour. In figure 7.1 the current status of the assembly is shown. About 200 temperature sensors, distributed over the whole structure and all subsystems, will monitor the relevant temperatures during the test. This allows for a reliable prediction of the thermal behaviour during the mission.

A Heat transport

We have to distinguish between three different main types of heat transport: (1) conduction, (2) convection and (3) radiation. Conduction is bound to the existence of matter and heat is only transferred between adjacent particles. For convection, material particles remove the heat by their motion. This kind of heat transport only takes place in streaming fluids and therefore is mostly not relevant for space telescopes. The only exceptions are for example built-in gas systems for detector purging or heat pipes (chapter 3). Radiation finally describes the heat exchange by means of electromagnetic waves and is highly relevant since it is the only means the telescope may exchange heat with its environment.

A.1 From Fourier's law to the heat equation – conductive heat transport

In the first section we deal with heat conduction. Heat transport via conduction (as well as convection) is the result of temperature gradients which connect the heat flux to the temperature field. Heat itself may be interpreted as kinetic energy of the involved molecules. We will deduce the heat equation, also called the Fourier equation, and give an overview over the possible solutions.

In his famous book *Théorie analytique de la Chaleur*, J. Fourier stated the empirical law that also bears his name (Fourier 1822). It postulates that the heat flux \vec{q} with $[\vec{q}] = \text{W m}^{-2}$ is proportional to the negative temperature gradient:

$$\vec{q} = -k\nabla T \tag{A.1}$$

where the k is the thermal conductivity of the material and generally also is temperature dependent.

Since T and q are independent variables, we have to use the conservation of energy to eliminate the heat flux q and to solve the equation for T (Gröber et al. 1963; Lienhard 2003).

The change in internal energy of a three-dimensional isotropic homogeneous volume dV is composed of the amount of energy created (or consumed) inside the volume, minus the energy conducted out of the system:

$$\delta Q = \delta Q_{created} - \delta Q_{out} \quad (\text{A.2})$$

The left side of this equation can be described by the first law of thermodynamics (Fließbach 2010). It is the combination of the change in internal energy and work done by the system (which we will neglect in the remainder of the derivation by assuming an incompressible medium):

$$\delta Q = dU + \delta W \stackrel{\delta W=0}{=} dU$$

Assuming a medium with constant density ρ and specific heat capacity c , dU can be calculated as follows:

$$dU = \delta Q = \rho \cdot c \cdot \frac{\partial T}{\partial t} dV dt$$

To replace the right side of equation (A.2), we first have to find an expression for the created heat inside dV . The internal heat source could be of various nature and is denoted as q_i :

$$\delta Q_{created} = q_i dV dt$$

Finally the outgoing heat through the surface dS of our volume dV is the result of an integration of the temperature gradient over dS :

$$\begin{aligned} \delta Q &= -k \cdot dt \cdot \vec{\nabla} T \cdot \vec{dS} \\ &= dt \nabla(-k \nabla T) dV \\ &= -k \cdot dt \nabla^2 T dV \end{aligned}$$

In the second step we used the divergence theorem, also known as *Gauss theorem* and in the third step we assumed k as a constant.

With inserting our results in equation (A.2), we finally get the heat equation:

$$\begin{aligned} \rho c \cdot \frac{\partial T}{\partial t} dV dt &= q_i dV dt + k \cdot dt \nabla^2 T dV \\ \frac{\partial T}{\partial t} &= a \nabla^2 T + \frac{1}{c\rho} q_i \end{aligned} \quad (\text{A.3})$$

$a = \frac{k}{c\rho}$ often is called the thermal diffusivity. The heat equation is a parabolic linear partial differential equation (PDE) and describes the temperature variation within a homogeneous and isotropic medium in a certain area over time (Friedman 2008). It is a special case of the general diffusion equation.

A special case of the heat equation is the one-dimensional equation without internal heat sources (Cannon et al. 2008):

$$c\rho \frac{\partial T}{\partial t} = -k \cdot \frac{\partial^2 T}{\partial x^2} \quad (\text{A.4})$$

Without time dependence, this results in elliptical PDEs – namely Poisson's equation and Laplace's equation – which simply can be integrated twice. Many analytical solved examples may be found for instance in Grigull et al. (1979).

One approach for getting particular solutions of the transient equation is the separation of variables, where the temperature field is assumed to be the product of a temporal and a spatial function:

$$T(x, t) = \varphi(t) \cdot \psi(x) \quad (\text{A.5})$$

Possible solutions can be obtained with the Euler function and sinus/cosinus as demonstrated in Lienhard (2003, p.146 f.) and Gröber et al. (1963, p.25 ff.). The general solution may be written as a linear combination:

$$T(x, t) = \left(C \cdot \sin(\alpha x) + D \cdot \cos(\alpha x) \right) \exp(-\alpha at) \quad (\text{A.6})$$

Another method is the formulation of the fundamental solution, also known as heat kernel (Grigull et al. 1979, p.62 ff.):

$$\Phi(x, t) = \frac{C}{\sqrt{t}} \cdot \exp\left(-\frac{x^2}{4at}\right), \quad C = \text{const.} \quad (\text{A.7})$$

The general solution then is obtained with a (spatial) convolution. To calculate the resulting temperature distribution of a medium, we need initial (temporal) and boundary (spatial) conditions to fit into the particular solutions. Usually this is the initial temperature distribution and certain constraints at the surface. A distinction is drawn between different kinds of boundary conditions (b.c.) as done in Gröber et al. (1963, pp. 11–12):

- Dirichlet condition or b.c. of the first kind: The temperature distribution at the surface is specified
- Neumann condition or b.c. of the second kind: The heat flux through the surface is specified
- B.c. of the third kind: The heat flux through the surface is proportional to the temperature difference between the surface and the environment; environmental temperature and heat transfer coefficient are specified

For most complex applications, approximation procedures are reasonable and necessary. Numerical approaches are shown in chapter B.

Up to now, we treated material properties such as density, specific heat and especially the thermal conductivity as constant. For small temperature ranges and certain materials this might be a good approximation, but in general those values are temperature dependent.

For metals for example the thermal conductivity is caused mostly by electron movement – the phonon part can be neglected as a first approximation (Sommerfeld et al. 1967). The electron’s movement is limited by scattering on phonons (resistance r_p) and lattice defects (resistance r_d) and for low temperatures we get the following correlation (Grigull et al. 1979, p. 7):

$$k \approx k_e = \frac{1}{r_p + r_d} = \frac{1}{\alpha T^2 + \beta/T} \quad (\text{A.8})$$

As it is shown in figure (2.2) in Lienhard (2003), this may cause significant changes in the thermal conductivity. This is also true for liquids and gases, although the underlying physics is different. Strong temperature dependencies have to be taken into

account in thermal calculations and thermal models, especially if the conductivity is important for desired temperature ranges and gradients. For eROSITA in particular mostly aluminium alloys are used for thermal critical components. The less pure the metal, the larger is the influence of the second term r_d in equation (A.8) and therefore the smoother is the conductivity curve.

A.2 Convection

Convection is the heat transfer between a surface and a streaming fluid. If the flow is caused by a pressure difference, we have forced convection. If it originates from gravity or density differences, we have natural (or free) convection. The amount of exchanged heat Q can be calculated with

$$Q = h \cdot A(T_s - T_f) \quad (\text{A.9})$$

with the convection coefficient h , the surface area A and temperatures of the surface T_s and the fluid far away from the surface T_f . h depends on the corresponding fluids and their temperatures. Since convection is not an issue in space, we only have to deal with it for the heat pipes of the cooling system. In chapter 3 basic principles of fluid dynamics, such as liquid and vapour flow inside a tube, pressure loss due to friction and flow limitations will be introduced.

A.3 Radiative heat exchange

In contrast to conductive and convective heat transport, radiative heat exchange is not bound to matter and not caused by a temperature gradient. Moreover, thermal radiation energy at a certain place is independent of the temperature of the local medium. The term "exchange" indicates that heat is not only transferred towards lower temperatures. Due to thermal motion of its atoms and molecules, each body with an absolute temperature greater than zero emits photons with the energy $e = h\nu$ ¹ and therefore electromagnetic waves, depending on its temperature and material properties. The transversal waves are propagating linearly and are reconverted to thermal energy as soon as being absorbed by another body.

¹with h the Planck constant and ν the frequency

Thermal radiation is defined as a certain part of the electromagnetic spectrum with wavelengths approximately between $0.1\ \mu\text{m}$ and $1000\ \mu\text{m}$. This classification is more or less arbitrary, because a body can radiate also beyond these boundaries, especially at very high and low temperatures.

The interaction of thermal radiation with matter takes place between an emitter on the one hand and a receiver on the other hand. Hence it is described by emissivity ϵ , reflectivity ρ , absorptivity α and transmissivity τ with the relation $\rho + \alpha + \tau = 1$. As we will see later, $\epsilon = \alpha$ under certain circumstances, also known as Kirchhoff's law. Apart from the wavelength dependency, the heat exchange can also rely on the direction, polarisation and even coherence of the radiation.

Especially the spatial distribution in addition to the wavelength dependency plays an important role in heat exchange problems. So we distinguish between directional and hemispherical, as well as spectral and total quantities. While directional spectral quantities are of great importance for theoretical considerations, for practical applications at least one integration (over the complete half space or all wavelengths) is done.

Starting with the **emission of thermal radiation**, we assume that the radiation leaving the body originates completely from its surface ($\approx 1\ \mu\text{m}$). Photons from deeper layers are absorbed immediately by adjacent molecules. Therefore we can speak of radiation *surfaces*.

The *radiant exitance* from a surface element dA is defined as the radiant flux² $d\Phi$ per surface element dA , which is a hemispherical total quantity:

$$M(T) = \frac{d\Phi}{dA}, \quad [M] = \frac{\text{W}}{\text{m}^2} \quad (\text{A.10})$$

M mainly depends on the surface temperature. By adding a wavelength dependence, we get the *spectral radiant exitance* M_λ . To obtain the total emitted radiant flux, we have to integrate over the emitting surface and over all wavelengths if applicable.

For taking into account non-uniform emitting characteristics, we introduce the *spectral radiance* L_λ as significant distribution function. This directional and spectral quantity describes the spatial distribution and wavelength dependency of the emitted energy:

²radiant energy per unit time, $[\Phi]=\text{W}$

$$L_\lambda(\lambda, \beta, \varphi, T) = \frac{d^3\Phi}{\cos\beta d\Omega d\lambda dA}, \quad [L_\lambda] = \frac{\text{W}}{\text{sr } \mu\text{m m}^2} \quad (\text{A.11})$$

with β the polar angle, φ the azimuth angle and $d\Omega = \sin\beta d\beta d\varphi$ the solid angle. $\cos\beta dA$ describes the projection of the emitting surface normal to the direction of emission.

If $L_\lambda(\lambda, \beta, \varphi, T)$ is independent of β and φ – which is a reasonable approach for many applications – we have a diffuse emitter with the radiant flux $d^2\Phi'$ being emitted into the solid angle $d\Omega$ (in contrast to the hemispherical quantity $d\Phi$):

$$d^2\Phi' = L(T)\cos\beta d\Omega dA \quad (\text{A.12})$$

$$L(T) = \int_{\lambda=0}^{\infty} L_\lambda(\lambda, T) d\lambda \quad (\text{A.13})$$

With defining the power per unit solid angle, the *radiant intensity* I , we can show the polar angle dependence of I which is also known as **Lambert's cosine law** for diffuse – or Lambertian – emitters:

$$I(\beta, \varphi, T) = \frac{d^2\Phi'}{dA d\Omega}, \quad [I] = \frac{\text{W}}{\text{sr m}^2} \quad (\text{A.14})$$

$$d^2\Phi' = I(\beta, \varphi, T) d\Omega dA \stackrel{(\text{A.12})}{=} L(T)\cos\beta d\Omega dA \quad (\text{A.15})$$

$$\Rightarrow I(\beta, T) = L(T)\cos\beta = I_n(T)\cos\beta \quad (\text{A.16})$$

$I_n(T)$ is the radiant intensity in direction of the surface normal ($\beta = 0$).

The spectral and total radiant exitance result in simple correlations to the corresponding isotropic radiance:

$$M_\lambda(\lambda, T) = L_\lambda(\lambda, T) \int_{d\Omega} \cos\beta d\Omega \quad (\text{A.17})$$

$$= L_\lambda(\lambda, T) \int_{\varphi=0}^{2\pi} \int_{\beta=0}^{\frac{\pi}{2}} \cos\beta \sin\beta d\beta d\varphi \quad (\text{A.18})$$

$$= \pi \cdot L_\lambda(\lambda, T) \quad (\text{A.19})$$

and similarly

$$M(T) = \pi \cdot L(T) \quad (\text{A.20})$$

The perfect thermal radiator is the *black body*. It absorbs the complete energy that reaches it, independent of wavelength or direction. Therefore $\alpha = 1$ and $\rho = \tau = 0$. It can be realized experimentally by a large enclosure with a small hole in the wall. The total thermal emission of a black body in thermal equilibrium is diffuse and determined only by its temperature, and is described by the Stefan-Boltzmann law:

$$M_b = \sigma T^4 \quad (\text{A.21})$$

with the Stefan-Boltzmann constant $\sigma = 5.67 \times 10^{-8} \text{ W/m}^2/\text{K}^4$. Found experimentally by J. Stefan in 1879 (Stefan 1879) and derived from classical electromagnetic theory by L. Boltzmann in 1884 (Boltzmann 1884), it describes the maximum power that can be emitted from a unit surface. Otherwise the second law of thermodynamics would be violated as shown in chapter 2 of Howell et al. (2010).

A few years later in 1900, Max Planck derived the spectral distribution of the emissive power for radiation in vacuum on the basis of quantum mechanics and showed that σ only consists of natural constants (Planck 1901):

$$M_{\lambda,b}(\lambda, T) = \pi L_{\lambda,b}(\lambda, T) = \frac{2\pi hc^2}{\lambda^5} \frac{1}{e^{\frac{hc}{\lambda kT}} - 1} \quad (\text{A.22})$$

Integration over λ then results in the Stefan-Boltzmann law with $\sigma = \frac{2\pi^5 k_B^4}{15h^3 c^2}$.

In figure A.1 the spectral radiant exitance resulting of Planck's law is plotted for different black body temperatures.

Each black body with a given temperature emits a unique energy distribution in wavelength. The wavelength of the maximum emission then is characteristic for that temperature and decreases with increasing temperature. It obeys a relation first found by W. Wien (Wien 1894), hence named Wien's displacement law:

$$\lambda_{max} = 2897.8 \mu\text{m K}^{-1} \quad (\text{A.23})$$

It also can be derived analytically by differentiating Planck's law.

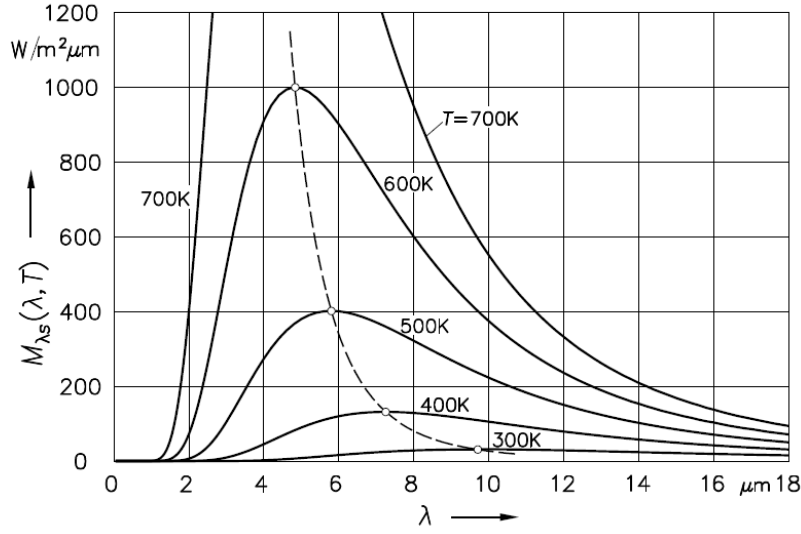


Figure A.1: Spectral radiant exitance for different black body temperatures, taken from Baehr et al. (2004)

Approximate forms of Planck's distribution are known as Wien's formula for small wavelengths ($e^{\frac{hc_0}{\lambda kT}} \gg 1$) and Rayleigh-Jeans formula for large wavelengths ($e^{\frac{hc_0}{\lambda kT}} \ll 1$) (Howell et al. 2010).

Non-black bodies emit less radiation than a black body, defined by the emissivity ϵ . The directional spectral and the hemispherical total emissivity $\epsilon(T)$ for example are

$$\epsilon'_\lambda(\lambda, \beta, \varphi, T) = \frac{L_\lambda(\lambda, \beta, \varphi, T)}{L_{\lambda,b}(\lambda, T)} \quad (\text{A.24})$$

$$\epsilon(T) = \frac{M(T)}{\sigma T^4} \quad (\text{A.25})$$

For other definitions of ϵ , refer to table A.1.

The next important step towards heat exchange is the absorption of radiation. Since the absorptivity of a material is not only a property of the absorbing material but depends also on the spectral distribution at the source of the incident energy, we have to make further assumptions. The **irradiance** E of a surface dA is determined by the corresponding radiant flux incidence Φ_i :

$$E = \frac{d\Phi_i}{dA} \quad (\text{A.26})$$

Φ_i depends on the *spectral irradiance* E_λ , counterpart of the spectral radiant exitance, which on its part is a function of the *spectral irradiance density* K_λ , the equivalent of the spectral radiance L_λ :

$$d^2\Phi_i = E_\lambda(\lambda)d\lambda dA \quad (\text{A.27})$$

$$E_\lambda(\lambda) = \int_{d\Omega} K_\lambda(\lambda, \beta, \varphi)d\Omega \quad (\text{A.28})$$

As mentioned before, K_λ is not a material property of the irradiated surface in contrast to L_λ . As noted in Baehr et al. (2004, p. 603), $K_\lambda(\lambda, \beta, \varphi) = L_\lambda(\lambda, \beta^*, \varphi^*, T^*)$ if the intermediate medium does not absorb, emit or scatter radiation from the source with temperature T^* . In particular this yields $K_\lambda = L_{\lambda,b}(\lambda^*, T)$ for the angle-independent black-body radiation.

For the **absorption of radiation** we can formulate similar coefficients as for the emissivities, as the *directional spectral absorptivity* α'_λ :

$$\alpha'_\lambda(\lambda, \beta, \varphi, T) = \frac{d^3\Phi_{i,abs}}{d^3\Phi_i} \quad (\text{A.29})$$

with $d^3\Phi_i$ from equation (A.27). Again, integration over the wavelength or solid angle

Table A.1: Definition of different emissivities

Emissivity	Definition	Description
$\epsilon'_\lambda(\lambda, \beta, \varphi, T)$	$\frac{L_\lambda(\lambda, \beta, \varphi, T)}{L_{\lambda,b}(\lambda, T)}$	directional spectral emissivity
$\epsilon_\lambda(\lambda, T)$	$\frac{M_\lambda(\lambda, T)}{M_{\lambda,b}(\lambda, T)} = \frac{\pi}{\sigma T^4} L(\beta, \varphi, T)$	hemispherical spectral emissivity
$\epsilon'(\beta, \varphi, T)$	$\frac{L(\beta, \varphi, T)}{L_b(T)}$	directional total emissivity
$\epsilon(T)$	$\frac{M(T)}{M_b(T)} = \frac{M(T)}{\sigma T^4}$	hemispherical total emissivity

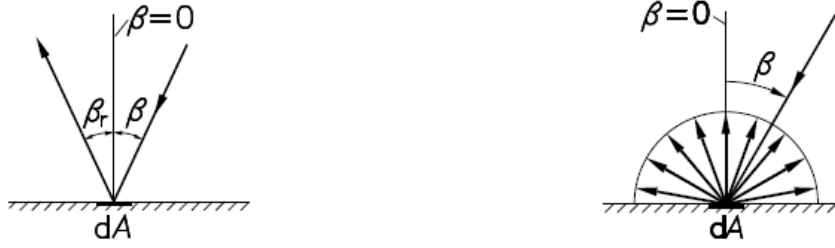


Figure A.2: Specular (left) and diffuse (right) reflectivity, taken from Baehr et al. (2004)

results in expressions for directional/hemispherical and spectral/total absorptivities while the basic definition is the same for all absorptivity coefficients (refer to table A.1).

As an analogue we can define different kinds of reflectivities $\rho = \frac{d^3\Phi_{i,ref}}{d^3\Phi_i}$. Although this is more complex due to the bidirectional character of reflection. A comprehensive treatise with wave and emergent angles was done by Howell et al. (2010). Two simple limiting cases are specular and diffuse reflecting surface, see figure A.2.

Between the directional spectral emissivity and absorptivity of a material exists the following connection, known as **Kirchhoff's law**:

$$\epsilon'_\lambda(\lambda, \beta, \varphi, T) = \alpha'_\lambda(\lambda, \beta, \varphi, T) \quad (\text{A.30})$$

This is valid for all different kinds of materials since α'_λ is a material property, but impossible to be measured exactly in reality. For a diffuse emitter without any angular dependence Kirchhoff's law becomes

$$\epsilon_\lambda(\lambda, T) = \alpha_\lambda(\lambda, T) \quad (\text{A.31})$$

and for additionally grey bodies this is further simplified to

$$\epsilon(T) = \alpha(T) \quad (\text{A.32})$$

The grey-body approximation is accurate as long as ϵ does not vary strongly with wavelength or if the temperatures of the involved bodies are rather similar. As a consequence, separate absorptivity values for the visible (solar radiation) and infrared (thermal radiation) wavelength should be used in thermal models. Different values

for solar absorptivity and thermal emissivity are utilized for example in energy-saving window panes or white radiator paints.

Not taking into account bidirectional reflections and assuming an opaque medium, we also can express the reflectivity in terms of emissivity:

$$\rho'_\lambda(\lambda, \beta, \varphi, T) = 1 - \alpha'_\lambda(\lambda, \beta, \varphi, T) = 1 - \epsilon'_\lambda(\lambda, \beta, \varphi, T) \quad (\text{A.33})$$

Since it is not possible to measure exactly the directional spectral emissivity for all angles and wavelengths for a material, we have to make use of theoretical considerations. With the classical electromagnetic theory, we can make predictions of total radiative properties on the basis of easier accessible quantities as demonstrated in Howell et al. (2010). Depending mostly on the specific electrical resistance, it is common to differentiate by dielectrics and metals. For dielectrics³, the spectral emissivity in direction of the surface normal $\epsilon'_{\lambda,n}$ ($\beta = 0$) can be computed from the complex refractive index $\tilde{n} = n - ik$. It depends on the permeability μ_r and permittivity γ_r (Baehr et al. 2004, p. 636):

$$\epsilon'_{\lambda,n} = \frac{4n}{(n+1)^2}, \quad n = \sqrt{\mu_r \gamma_r} \quad (\text{A.34})$$

Wavelength dependency can be neglected and dielectrics treated as grey bodies with good approximation. Thus the total hemispherical emissivity can be determined by $\frac{\epsilon}{\epsilon'_n} \approx \frac{\epsilon_\lambda(n)}{\epsilon'_{\lambda,n}}$. Due to the fact that the validity of Lambert's cosine law is given for a large range of the polar angles ($\beta < 70^\circ$, see figure A.3), this ratio can be set to ≈ 1 for dielectric media as demonstrated in Baehr et al. (2004, section 5.3.3.1).

Metals in contrast cannot be treated as diffuse emitters and do have much smaller emissivities with exception of large polar angles, see figure A.4. Thus also the ratio of total to normal emissivity differs and can take values up to ≈ 1.3 (Baehr et al. 2004, table 5.6):

$$\epsilon'_{\lambda,n}(n, k) = \frac{4n}{(n+1)^2 + k^2} \quad n = k = \sqrt{\frac{c_0 \mu_0 \lambda}{4\pi r_e}} \quad (\text{A.35})$$

with the specific electrical resistance r_e .

³electrical resistance $R \rightarrow \infty$

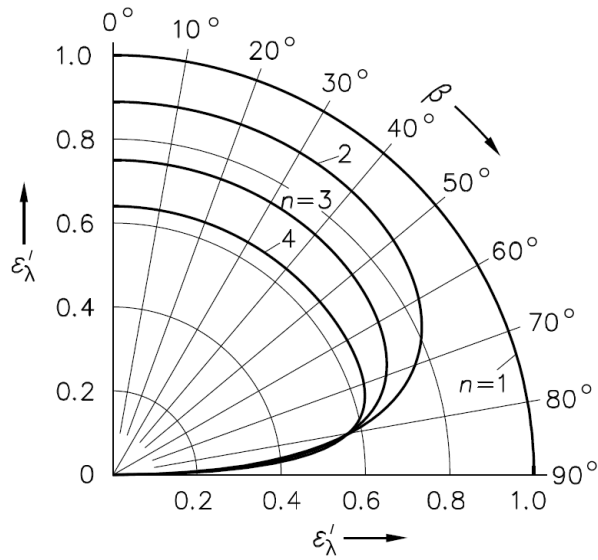


Figure A.3: Directional spectral emissivity of dielectrics, taken from Baehr et al. (2004), confirmed by measurements of Schmidt et al. (1935)

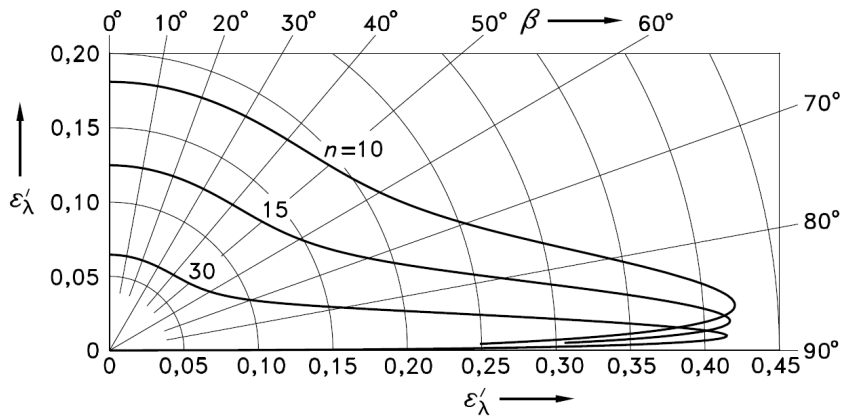


Figure A.4: Directional spectral emissivity of metals, taken from Baehr et al. (2004), confirmed by measurements of Schmidt et al. (1935)

Passivated⁴ surfaces on the other hand do fall in the category of Lambertian sources which simplifies the thermal modelling of eROSITA. The only important exception are the high-reflective mirror and X-ray baffle shells which have specular properties also for thermal radiation.

Besides all the material dependent properties for calculating the effective heat transfer between two bodies, the geometric constellation is a significant factor we have to include in our considerations. For black bodies, it is the only correction needed of the Stefan-Boltzmann law. As already mentioned in the beginning, thermal radiation between two bodies with temperature T_1 and T_2 is always mutual and only the sign of the net heat flux takes into account different temperature values.

The so-called transfer factor \mathcal{F}_{12} defines the ratio of radiation being emitted by surface A_1 and absorbed by surface A_2 . It depends on the emissivity and absorptivity values of both surfaces as well as their shape, distance and orientation. The pure geometrical information is contained in the view factor F_{12} – the fraction of the field of view of surface 1 being occupied by surface 2 – and can be calculated with the following integral:

$$\begin{aligned} F_{12} &= \frac{\Phi_{12}}{\Phi_1} = \frac{L_1 \int_{A_1} \int_{A_2} \frac{\cos\beta_1 \cos\beta_2}{r^2} dA_1 dA_2}{\pi L_1 A_1} \\ &= \frac{1}{\pi A_1} \int_{A_1} \int_{A_2} \frac{\cos\beta_1 \cos\beta_2}{r^2} dA_1 dA_2 \end{aligned} \quad (\text{A.36})$$

with $\Phi_{12} = L_1 \cos\beta_1 dA_1 d\Omega_2$ being the net radiation flux from A_1 to A_2 and $\Phi_1 = \pi L_1 A_1$ the total flux leaving A_1 (with equation (A.10), A.12 and (A.20)). As shown in figure A.5, the solid angle $d\Omega_2 = \frac{\cos\beta_2 dA_2}{r^2}$ on his part depends on the distance and orientation of the two surfaces.

In Lienhard (2003), a large collection of analytically determined view factors can be found. In practice, for complex configurations numerical methods as the Monte-Carlo ray tracing (see chapter B) provide a powerful method to calculate any geometry.

⁴to avoid oxidation

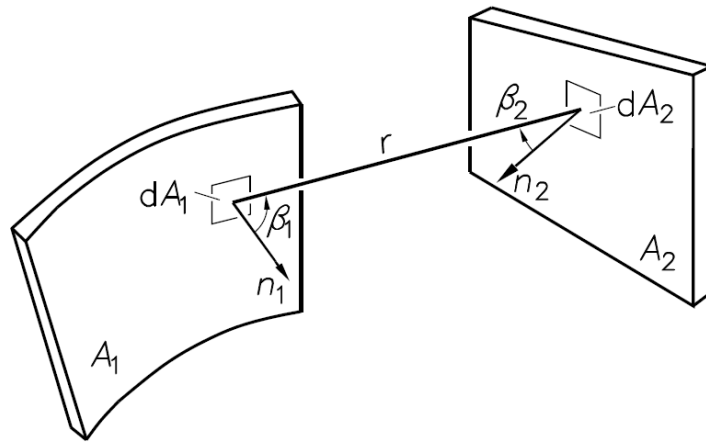


Figure A.5: Calculation of view factors, taken from Baehr et al. (2004)

B Computational methods for solving differential equations

The solutions of mathematical thermal models either are steady state or transient, depending on the particular problem. Often a problem begins as transient and ends in a steady state thermal equilibrium. If $\frac{\partial y}{\partial t} = 0$, we have a steady state case and the parabolic PDE becomes an elliptic PDE. Otherwise we get the general time dependent heat equation:

steady state:

$$0 = \alpha \nabla^2 y \quad (\text{B.1})$$

transient:

$$\frac{\partial y}{\partial t} = \alpha \nabla^2 y \quad (\text{B.2})$$

To find solutions for both types of equations we have to find a way to express the second spatial derivative. A common approximation is the central discretisation, resulting of the forward and backwards Taylor expansion:

$$y_{n+1} = y_n + \left(\frac{\partial y}{\partial x} \right)_n \Delta x + \left(\frac{\partial^2 y}{\partial x^2} \right)_n \frac{\Delta x^2}{2} + O(\Delta x^3)$$

$$y_{n-1} = y_n - \left(\frac{\partial y}{\partial x} \right)_n \Delta x + \left(\frac{\partial^2 y}{\partial x^2} \right)_n \frac{\Delta x^2}{2} - O(\Delta x^3)$$

By summing these equations, we get the following approximation:

$$y_{n+1} + y_{n-1} = 2y_n + \nabla^2 y \cdot \Delta x^2 + O(\Delta x^4)$$

$$\nabla^2 y \approx \frac{y_{n+1} - 2y_n + y_{n-1}}{\Delta x^2} \quad (\text{B.3})$$

For transient analysis we additionally need a time expansion. Starting with the initial value problem

$$\frac{\partial y}{\partial t} = f\left(t, x, y, \frac{\partial y}{\partial x}\right), \quad y(x, t_0) = y_0 \quad (\text{B.4})$$

we have to integrate over the corresponding time interval:

$$\int_t^{t+\Delta t} \frac{\partial y}{\partial t} dt = \int_t^{t+\Delta t} f\left(t, x, y, \frac{\partial y}{\partial x}\right) dt$$

$$y(t + \Delta t) = y(t) + \int_t^{t+\Delta t} f\left(t, x, y, \frac{\partial y}{\partial x}\right) dt \quad (\text{B.5})$$

This equation cannot be solved straight forward due to the fact that $y(t + \Delta t)$ needs to be given for the integration. Therefore some kind of approximation method is necessary. The quality of those methods can be determined by the order of corresponding terms to the formal Taylor expansion:

$$y(t + \Delta t) = y(t) + \int_t^{t+\Delta t} \sum_{i=0}^{\infty} \frac{(\Delta t)^i}{i!} \left(\frac{d^i}{dt^i} f \right)_t dt$$

$$= y(t) + \sum_{i=1}^{\infty} \frac{(\Delta t)^i}{i!} \left(\frac{d^{i-1}}{dt^{i-1}} f \right)_t dt \quad (\text{B.6})$$

$$= y(t) + \Delta t \cdot f_t + \frac{(\Delta t)^2}{2} \left(\frac{\partial f}{\partial t} \right)_t + \dots$$

The most basic method for solving time dependent differential equations is the explicit – since $y(t + \Delta t)$ can be calculated directly – forward Euler method (Thomas 1995):

$$y(t + \Delta t) \approx y(t) + \Delta t \cdot f(t, y(t)) \quad (\text{B.7})$$

This method is a first order approximation, since only the linear term corresponds to the formal Taylor expansion at time t (equation (B.6)). This makes it less accurate than higher-order methods and complicated for stiff equations¹ and large time steps.

Of the same order but more stable is the implicit backward Euler method (Ascher et al. 1998), where

$$y(t + \Delta t) \approx y(t) + \Delta t \cdot f(t + \Delta t, y(t + \Delta t)) \quad (\text{B.8})$$

Implicit methods lead to an equation system to be solved since $y(t + \Delta t)$ occurs on both sides of the equation. This has the advantage of more stable solutions, but at the expense of solving time.

¹The solution is very unstable unless extremely small step sizes are used (Lambert 1991; Aiken 1985)

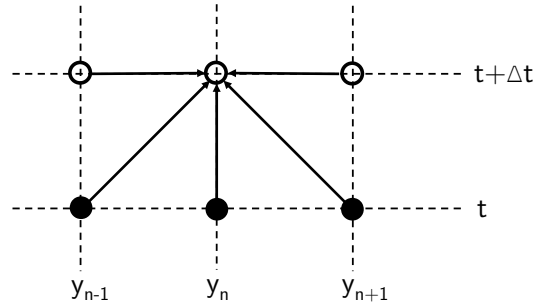


Figure B.1: Node scheme for the Crank-Nicolson method

Advancements of the Euler methods like the Crank-Nicolson method are more accurate and predestined for spacecraft thermal problems (Krishnaprakas 1998). Also implicit in time, they take the arithmetic average of the forward and backwards Euler method (Crank et al. 1996). A scheme of the involved nodes and time steps is shown in figure B.1.

$$y(t + \Delta t) \approx y(t) + \frac{\Delta t}{2} \left(f(t, y(t)) + f(t + \Delta t, y(t + \Delta t)) \right) \quad (\text{B.9})$$

Together with equation (B.3) this leads to the second-order approximation:

$$y(t + \Delta t) \approx y(t) + \frac{\alpha \Delta t}{2 \Delta x^2} \left(y_{n+1}(t + \Delta t) - 2y_n(t + \Delta t) + y_{n-1}(t + \Delta t) + y_{n+1}(t) - 2y(t) + y_{n-1}(t) \right) \quad (\text{B.10})$$

Using the approximation of the Laplace operator (B.3) and the time expansion (B.10), if applicable, we get one or more systems of ordinary differential equations (ODEs) out of the heat equation. ODEs then can be solved by standard techniques as Gaussian eliminations and its derivatives like the tridiagonal matrix algorithm, successive point iterations, full matrix inversions or conjugate gradient iterative methods (Conte et al. 1972).

C Thermal software

All thermal calculations were made with the ESATAN Thermal Modelling suite (TMS)¹. This software package allows for obtaining solutions of the lumped parameter model. It contains a graphic user interface for geometric and orbital modelling, determination of heat transfer coefficients, solving routines and result post processing.

With ESATAN, conductive, convective and radiative heat transfer can be calculated. Three-dimensional shapes are used for determination of radiative couplings. Each surface is attributed to certain optical properties as the solar absorption coefficient α and the thermal emission coefficient ϵ . The surfaces are divided into one or more thermal nodes, depending on the desired accuracy. Besides the surface properties, especially the view factor F_{ij} between two nodes is essential for calculating the corresponding heat exchange. It describes which proportion of the rays leaving node i is reaching node j . View factors can be calculated analytically with equation (A.36), but this is only reasonable for simple geometries:

$$F_{ij} = \frac{1}{\pi A_i} \int_{A_i} \int_{A_j} \frac{\cos \beta_{ij} \cdot \cos \beta_{ji}}{r^2} dA_i dA_j \quad (\text{C.1})$$

with r the distance and β the angle between dA_i and dA_j . With the radiative coupling

$$GR = \epsilon_i \alpha_j A_i F_{ij} \quad (\text{C.2})$$

the heat exchange due to radiation can be determined:

$$q_{ij} = \sigma \cdot GR \cdot (T_i^4 - T_j^4) \quad (\text{C.3})$$

For complex models computational methods are recommended. The ESATAN-TMS uses Monte-Carlo-Raytracing (Glassner 1989). Every node emits several thousand of

¹distributed by ITP Engines UK

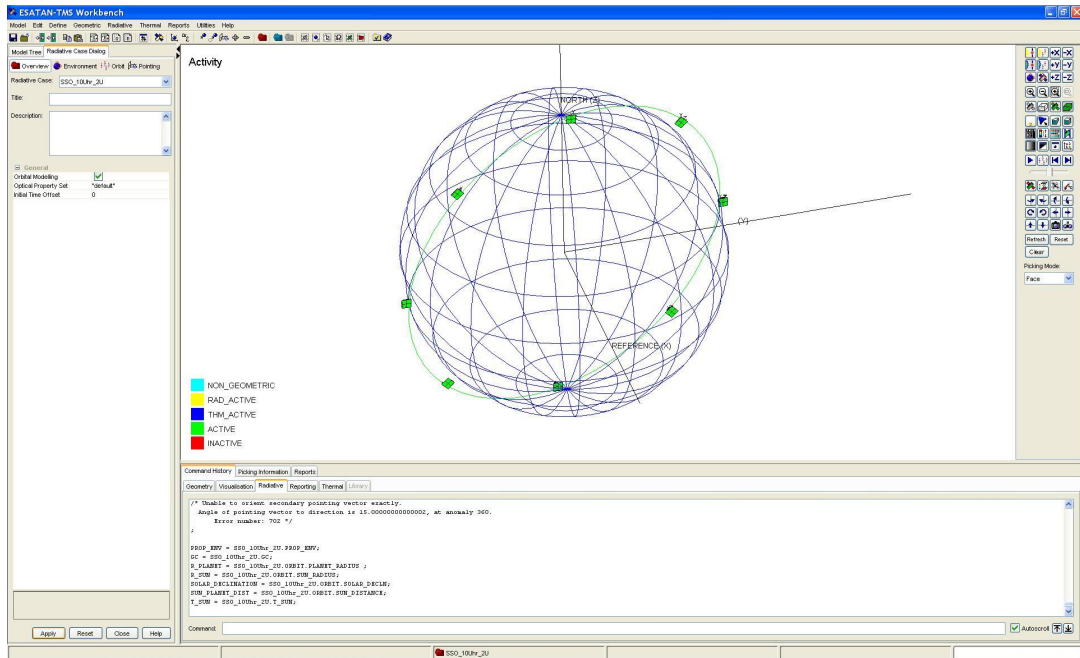


Figure C.1: ESATAN-TMS workbench

rays which are reflected until they are finally absorbed. This results in view factors and therefore in radiative couplings between node i and node j (ITP Engines UK Ltd. 2010).

During this step also solar radiation and albedo can be taken into account. The orbital modelling is either Sun or Earth centred and provides the opportunity to include spacecraft rotation and movements, such as solar panels.

Afterwards, the conductive links (GL) have to be determined. Some are created automatically in the workbench if one single shell is divided into several nodes, but all others have to be defined manually. Every kind of mechanical contact has to be considered, regardless whether it is screwed, glued or clamped. For the first approach mostly empirical values are used. Step by step they are exchanged by measured data if available. Convective coefficients and fluids can be modelled as well, but they do not apply for the eROSITA telescope. Conductive heat transfer between node i and node j is calculated as follows:

$$q_{ij} = GL \cdot (T_i - T_j) \quad (\text{C.4})$$

Now all thermal nodes are linked by radiative and conductive exchange coefficients. Initial and boundary temperatures can be defined as well as heat loads. With MORTRAN code², the ESATAN software allows to write loops, conditional events and control sequences as in any other programming language (see figure C.2).

Different solving routines are available for the resulting differential equations. Steady state solutions for equilibrium temperatures as well as transient solutions for cooling or heating processes are possible. For every node used in the thermal model, and therefore for every temperature, one equation is required.

In the simplest steady state case with only conductive interfaces, the net heat flow is $\frac{dT}{dt} = 0$ and the resulting system of linear equations could be solved by standard matrix techniques. If we assume a model with three adjacent nodes 1, 2 and 3 and the conductive couplings k_{21} and k_{23} , the equation for the balance heat flow of node 2 is as follows:

$$C_2 \frac{dT_2}{dt} = 0 = k_{21}(T_1 - T_2) + k_{23}(T_3 - T_2) \quad (\text{C.5})$$

The general system of equations contains also radiative couplings r_{ij} and internal heat sources Q_i . In the transient case the heat flow is not negligible:

$$C_i \frac{dT_i}{dt} = \sum_{i \neq j} r_{ij}(T_j^4 - T_i^4) + k_{ij}(T_j - T_i) + QI_i \quad (\text{C.6})$$

where C_i is the heat capacity of node i .

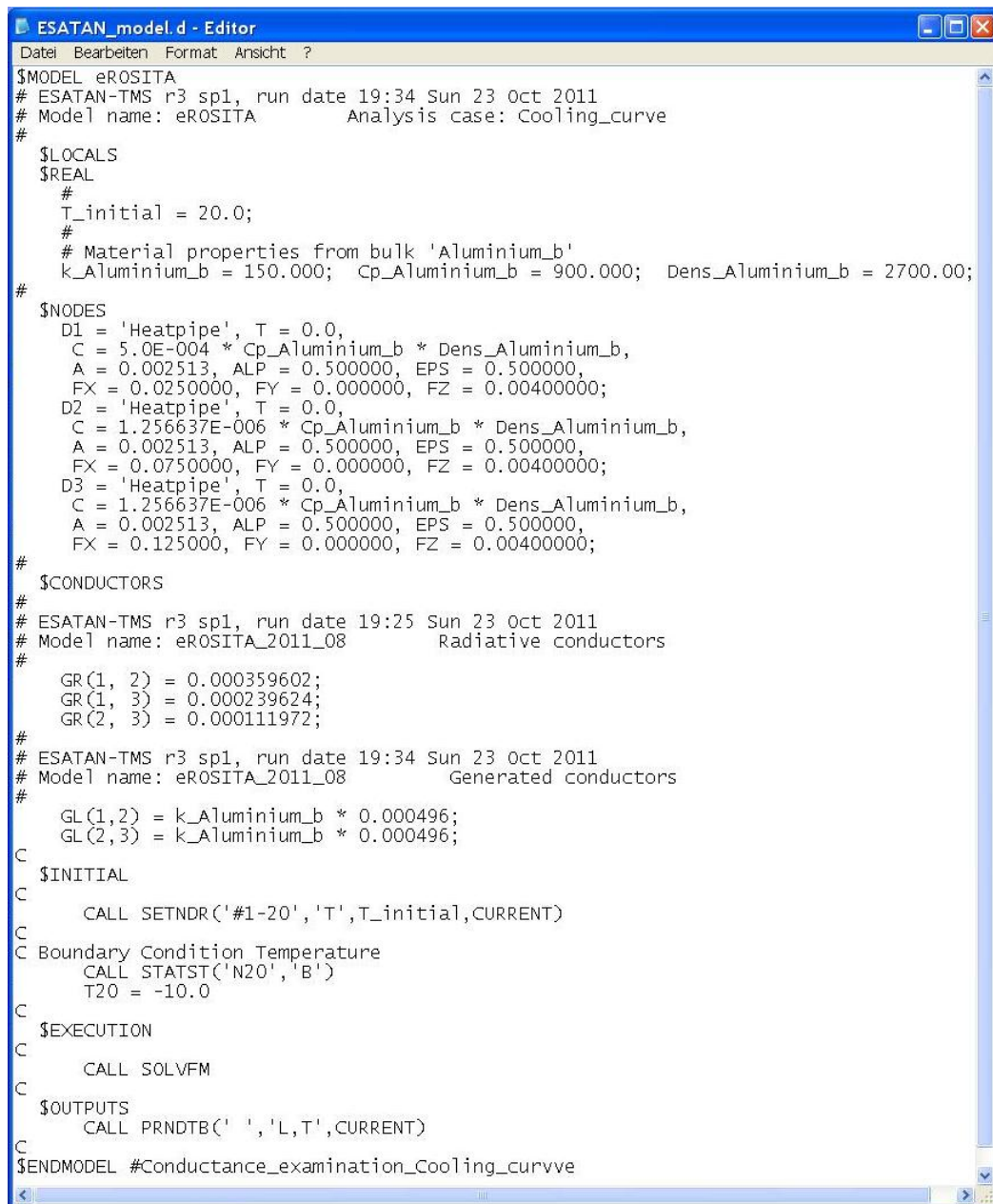
This corresponds to the first order finite differential approximation of the heat equation (A.1):

$$\frac{\partial T}{\partial t} - \alpha \nabla^2 T = 0 \quad (\text{C.7})$$

with $\nabla^2 = \frac{\partial^2}{\partial x^2} + \frac{\partial^2}{\partial y^2}$, $\alpha = \frac{\lambda}{\rho c}$, λ the thermal conductivity of the material, ρ the density and c the specific heat.

This connection is shown with help of a two-dimensional rectangular irregular grid (ITP Engines UK Ltd. 2010).

²extended FORTRAN 77



```
ESATAN_model.d - Editor
Datei Bearbeiten Format Ansicht ?
$MODEL eROSITA
# ESATAN-TMS r3 sp1, run date 19:34 Sun 23 Oct 2011
# Model name: eROSITA Analysis case: Cooling_curve
#
$LOCALS
$REAL
#
T_initial = 20.0;
#
# Material properties from bulk 'Aluminium_b'
k_Aluminium_b = 150.000; Cp_Aluminium_b = 900.000; Dens_Aluminium_b = 2700.00;
#
$NODES
D1 = 'Heatpipe', T = 0.0,
C = 5.0E-004 * Cp_Aluminium_b * Dens_Aluminium_b,
A = 0.002513, ALP = 0.500000, EPS = 0.500000,
FX = 0.0250000, FY = 0.000000, FZ = 0.00400000;
D2 = 'Heatpipe', T = 0.0,
C = 1.256637E-006 * Cp_Aluminium_b * Dens_Aluminium_b,
A = 0.002513, ALP = 0.500000, EPS = 0.500000,
FX = 0.0750000, FY = 0.000000, FZ = 0.00400000;
D3 = 'Heatpipe', T = 0.0,
C = 1.256637E-006 * Cp_Aluminium_b * Dens_Aluminium_b,
A = 0.002513, ALP = 0.500000, EPS = 0.500000,
FX = 0.125000, FY = 0.000000, FZ = 0.00400000;
#
$CONDUCTORS
#
# ESATAN-TMS r3 sp1, run date 19:25 Sun 23 Oct 2011
# Model name: eROSITA_2011_08 Radiative conductors
#
GR(1, 2) = 0.000359602;
GR(1, 3) = 0.000239624;
GR(2, 3) = 0.000111972;
#
# ESATAN-TMS r3 sp1, run date 19:34 Sun 23 Oct 2011
# Model name: eROSITA_2011_08 Generated conductors
#
GL(1,2) = k_Aluminium_b * 0.000496;
GL(2,3) = k_Aluminium_b * 0.000496;
C
$INITIAL
C
CALL SETNDR('#1-20','T',T_initial,CURRENT)
C
C Boundary Condition Temperature
CALL STATST('N20','B')
T20 = -10.0
C
$EXECUTION
C
CALL SOLVFM
C
$OUTPUTS
CALL PRNDB(' ', 'L,T',CURRENT)
C
$ENDMODEL #Conductance_examination_Cooling_curve
```

Figure C.2: Example of an ESATAN model

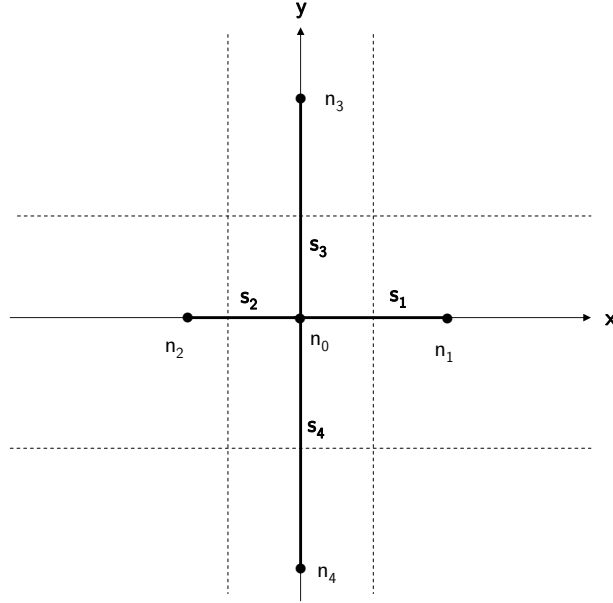


Figure C.3: Grid with thermal nodes of various distances

Assuming a node grid as shown in figure C.3, the temperature of the node n_0 in the origin can be evaluated as follows by using Taylor series for the adjacent nodes:

$$T_1 = T_0 + \frac{\partial T}{\partial x} s_1 + \frac{\partial^2 T}{\partial x^2} \frac{s_1^2}{2} + \frac{\partial^3 T}{\partial x^3} \frac{s_1^3}{6} + O(s_1^4) \quad (\text{C.8})$$

$$T_2 = T_0 + \frac{\partial T}{\partial x} s_2 + \frac{\partial^2 T}{\partial x^2} \frac{s_2^2}{2} + \frac{\partial^3 T}{\partial x^3} \frac{s_2^3}{6} + O(s_2^4) \quad (\text{C.9})$$

$$T_3 = T_0 + \frac{\partial T}{\partial x} s_3 + \frac{\partial^2 T}{\partial x^2} \frac{s_3^2}{2} + \frac{\partial^3 T}{\partial x^3} \frac{s_3^3}{6} + O(s_3^4) \quad (\text{C.10})$$

$$T_4 = T_0 + \frac{\partial T}{\partial x} s_4 + \frac{\partial^2 T}{\partial x^2} \frac{s_4^2}{2} + \frac{\partial^3 T}{\partial x^3} \frac{s_4^3}{6} + O(s_4^4) \quad (\text{C.11})$$

By solving equations (C.9) and (C.11) for $\frac{\partial^2 T}{\partial x^2}$ and $\frac{\partial^2 T}{\partial y^2}$ respectively, dropping terms in $\frac{\partial^3 T}{\partial x^3}$ and higher, we get:

$$\frac{\partial^2 T}{\partial x^2} = \frac{2(T_1 - T_0)}{s_1(s_1 + s_3)} + \frac{2(T_3 - T_0)}{s_3(s_1 + s_3)} \quad (\text{C.12})$$

$$\frac{\partial^2 T}{\partial y^2} = \frac{2(T_2 - T_0)}{s_2(s_2 + s_4)} + \frac{2(T_4 - T_0)}{s_4(s_2 + s_4)} \quad (\text{C.13})$$

Transferring that to the heat equation at position 0, this gives us an approximation for the temperature variation in node n_0 :

$$\left. \frac{\partial T}{\partial t} \right|_{n_0} = \alpha \nabla^2 T \Big|_{n_0} \quad (\text{C.14})$$

$$\frac{dT_0}{dt} \approx 2\alpha \left[\frac{T_1 - T_0}{s_1(s_1 + s_3)} + \frac{T_2 - T_0}{s_2(s_2 + s_4)} + \frac{T_3 - T_0}{s_3(s_1 + s_3)} + \frac{T_4 - T_0}{s_4(s_2 + s_4)} \right] \quad (\text{C.15})$$

With the interpretation of each node as a cell with a certain volume V_i , defined by half the distance to the surrounding nodes, and a heat capacity $C_0 = \rho \cdot V_0 \cdot c$, this leads to the (conductive) lumped parameter heat balance equation (C.6):

$$\frac{dT_0}{dt} \approx \frac{1}{C_0} \sum_{i=0}^4 k_{0i}(T_i - T_0) \quad (\text{C.16})$$

with $k_i = \lambda d \frac{s_2 + s_4}{2s_i}$ for $i \in \{1, 3\}$ and $k_i = \lambda d \frac{s_1 + s_3}{2s_i}$ for $i \in \{2, 4\}$

The last equation has to be applied to every node in the thermal model. For steady state solutions with $\frac{dT_0}{dt} = 0$, this results in a tridiagonal system of equations which can be solved by standard techniques as the Thomas algorithm. For transient solutions time also has to be discretised with a differential quotient and solved for time steps Δt :

$$\frac{dT_0}{dt} \approx \frac{T_0(t + \Delta t) - T_0(t)}{\Delta t} \quad (\text{C.17})$$

$$T_0(t + \Delta t) \approx T_0(t) + \Delta t \cdot \frac{dT_0}{dt} \quad (\text{C.18})$$

$$\approx T_0(t) + \Delta t \cdot \frac{1}{C_0} \sum_{i=0}^4 k_{0i}(T_i - T_0) \quad (\text{C.19})$$

This corresponds to the Crank-Nicolson method of time expansion as shown in equation (B.10).

For regular grids ($s_1 = s_2 = s_3 = s_4$) terms in third order cancel, for irregular grids this is only a second order approximation.

Several solution routines come with the software package. Steady-state solvers use successive point iteration, full matrix inversion or conjugate gradient iterative methods (Kirtley et al. 2011); transient solvers use either the explicit forward differencing method or the implicit forward-backward Crank-Nicolson-method as described in chapter B. Solving routines based on this method are more accurate and numerically stable, even if using larger step sizes (Thomas 1995), and need less computation time (Krishnaprakas 1998).

Bibliography

- Aiken, R. C. (1985). *Stiff computation*. Oxford University Press.
- Ascher, U. and L. Petzold (1998). *Computer Methods for Ordinary Differential Equations and Differential-Algebraic Equations*. Philadelphia: Society for Industrial and Applied Mathematics.
- B&K Engineering (1979). *Advanced thermal control flight experiment (ATFE) – Final report*. Tech. rep. CR-152305. NASA.
- Baehr, H. D. und K. Stephan (2004). *Wärme- und Stoffübertragung*. Gabler Wissenschaftsverlage.
- Batchelor, G. K. (2000). *An introduction to fluid dynamics*. Vol. 2. Cambridge University Press.
- Bienert, W. and P. J. Brennan (1971). “Feedback controlled variable conductance heat pipes”. In: *6th Thermophysics Conference*. 71-421. AIAA.
- Bobco, R. P. (1987). “Variable Conductance Heat Pipes: A First Order Model”. In: *Journal of Thermophysics and Heat Transfer* 1, pp. 35–42.
- Boltzmann, L. (1884). „Ableitung des Stefan’schen Gesetzes, betreffend die Abhängigkeit der Wärmestrahlung von der Temperatur aus der electromagnetischen Lichttheorie“. In: *Annalen der Physik* 258.6, S. 291–294.
- Brennan, P. J. (1970). *Study to evaluate the feasibility of a feedback controlled variable conductance heat pipe*. Tech. rep. CR-73475. NASA.
- Brennan, P. J. and E. J. Krociczek (1979). *Heat pipe design handbook*. B & K Engineering, Inc.
- Busse, C. A. (1967). “Pressure Drop in the Vapour Phase of Long Heat Pipes”. In: *Thermionic Conversion Specialist Conference*. IEEE, pp. 391–398.
- Cannon, J. R. and F. E. Browder (2008). *The One-Dimensional Heat Equation*. Encyclopedia of Mathematics and its Applications Series. Cambridge University Press.

- Chi, S. W. (1976). *Heat pipe theory and practice: A sourcebook*. Hemisphere Pub. Corp.
- Cleveland, P. E., M. T. Buchko, R. A. Stavely, et al. (2003). “Thermal Vacuum Test Performance of the Hubble Space Telescope (HST) Wide Field Camera 3 (WFC3) Variable Conductance Heat Pipe Assembly”. In: *33rd International Conference on Environmental Systems*. 2003-01-2459. SAE International.
- Conte, S. D. and C. D. Boor (1972). *Elementary numerical analysis: An algorithmic approach*. 3rd ed. International series in pure and applied mathematics. McGraw-Hill.
- Crank, J. and P. Nicolson (1996). “A practical method for numerical evaluation of solutions of partial differential equations of the heat-conduction type”. In: *Advances in Computational Mathematics* 6 (1), pp. 207–226.
- Cunnington, G. R., C. W. Keller, and G. A. Bell (1971). *Interim Report Thermal Performance of Multi-layer Insulations*. Tech. rep. NASA CR-72605. Lockheed Missiles and Space Center.
- Delil, A. and J. Van Der Vooren (1981). “Uniaxial Model for Gas-Loaded Variable Conductance Heat Pipe Performance in the Inertial Flow Regime”. In: *Proceedings of the 4th International Heat Pipe Conference*.
- Edelstein, F., W. Harwelf, R. Haslett, et al. (1979). “Insulation Design & Fabrication”. In: *Shuttle Payload Thermal Control*. Vol. 2. Grumman Aerospace Corporation.
- Edwards, D. K. and B. D. Marcus (1972). “Heat and Mass Transfer in the Vicinity of the Vapor-Gas Front in a Gas-Loaded Heat Pipe”. In: *International Journal of Heat and Mass Transfer* 94, pp. 155–162.
- FABmbH, ZARM, ed. (2011). *ZARM Drop Tower Bremen User Manual*.
- Faghri, A. (1995). *Heat pipe science and technology*. Mechanical Engineering. Taylor & Francis.
- Faghri, A. and C. Harley (1994). “Transient Lumped Heat Pipe Analyses”. In: *Heat Recovery Systems & CHP* 14 (4), pp. 351–363.
- Fixsen, D. J. (2009). “The Temperature of the Cosmic Microwave Background”. In: *Astrophysical Journal* 707, pp. 916–920.
- Fließbach, T. (2010). *Statistische Physik: Lehrbuch Zur Theoretischen Physik IV*. Fließbach, Torsten: Lehrbuch zur theoretischen Physik. Spektrum Akademischer Verlag.

- Folkman, N. R. and T. G. Lee (1968). “Thermodynamic design fundamentals of high-performance insulation”. In: *Journal of Spacecraft and Rockets* 5.8, pp. 954–959.
- Fourier, Jean Baptiste Joseph (1822). *Théorie analytique de la chaleur*. English translation by A. Freeman, Cambridge 1878. Chez Firmin Didot, père et fils.
- Friedman, A. (2008). *Partial Differential Equations of Parabolic Type*. Dover Books on Mathematics. Dover Publications.
- Friedrich, P. (2009). “Telescope Error Budget Analysis”. eROSITA document server, eRO-MPE-TN-13-01-2.
- Friedrich, P., P. Predehl, N. Meidinger, et al. (2005). “Results from a contamination experiment on the ISS”. In: *Proceedings of SPIE*. Vol. 5900. SPIE, pp. 172–183.
- Friedrich, P., H. Bräuninger, B. Budau, et al. (2008). “Design and development of the eROSITA X-ray mirrors”. In: *Proceedings of SPIE*. Vol. 7011. SPIE, 70112T-1.
- Fürmetz, M. (2007). „Entwicklung eines Kühlkonzepts für das Röntgenteleskop eROSITA“. Diplomarbeit. Technische Universität München.
- (2011a). “Camera assembly STM thermal balance and thermal cycling test”. eROSITA document server, eRO-MPE-RP-30-02-2.
 - (2011b). “Camera electronics STM thermal balance test”. eROSITA document server, eRO-MPE-RP-35-02-1.
 - (2011c). “Camera head STM thermal balance test”. eROSITA document server, eRO-MPE-RP-31-03.
 - (2011d). “Mirror assembly thermal balance test”. eROSITA document server, eRO-MPE-RP-44-02.
- Fürmetz, M., E. Pfeffermann, P. Predehl, et al. (2008). “The cooling concept of the X-ray telescope eROSITA”. In: *Proceedings of SPIE*. Vol. 7011. SPIE, 70113Y-1.
- Fürmetz, M., J. Eder, P. Predehl, et al. (2010). “Operation of the X-ray telescope eROSITA”. In: *Proceedings of SPIE*. Vol. 7732. SPIE, 77323K-1.
- Funke, M., R. Kleinrahm, and W. Wagner (2002). “Measurement and correlation of the (p , ρ , T) relation of ethane II. Saturated-liquid and saturated-vapour densities and vapour pressures along the entire coexistence curve”. In: *The Journal of Chemical Thermodynamics* 34 (12), pp. 2017–2039.
- Glaser, P. E., I. A. Black, R. S. Lindstrom, et al. (1967). *Thermal Insulation Systems – A Survey*. Tech. rep. SP-5027. NASA.

- Glassner, A. S. (1989). *An introduction to Ray tracing*. Academic Press.
- Gröber, H., S. Erk und U. Grigull (1963). *Wärmeübertragung*. 3. Aufl. Springer-Verlag.
- Grigull, U. und H. Sandner (1979). *Wärmeleitung*. Springer-Verlag.
- Grover, G. M., T. P. Cotter, and G. F. Erickson (1964). “Structures of very high thermal conductivity”. In: *Journal of Applied Physics* 35 (6), pp. 1190–1191.
- Grzesik, A. (2007). “Structural Analysis”. eROSITA document server, eRO-KTM-AN-40-01-2.
- Gutruf, S. (2009). “Optical Analysis”. eROSITA document server, eRO-MPE-AN-40-02-2.
- Haiman, Z., S. Allen, N. Bahcall, et al. (2005). *An X-ray Galaxy Cluster Survey for Investigations of Dark Energy*. arXiv:astro-ph/0507013v1.
- Harley, C. (1993). “Transient Analyses of Noncondensable-Gas-Buffered Two-Phase Heat Transfer Devices”. MA thesis. Dayton, Ohio 45435: Wright State University.
- Harley, C. and A. Faghri (1972). “Transient Two-Dimensional Gas-Loaded Heat Pipe Analysis”. In: *ASME Journal of Heat Transfer* 116.3.
- Hermann, E., H. Koch und H. Kreeb (1976). *Handbuch der Rillenwärmerohre*. Forschungsbericht des Bundesministerium für Forschung und Technologie 76-0017. English translation available, NASA TM-77700. Zentralstelle für Luft- und Raumfahrt-dokumentation und -information.
- Howell, J.R., R. Siegel, and M.P. Mengüç (2010). *Thermal radiation heat transfer*. CRC Press.
- Hufschmidt, W., E. Burck, G. Dicola, et al. (1975). *The Shearing Effect of Vapour Flow on Laminar Liquid Flow in Capillaries of Heat Pipes*. Tech. rep. TT-F-16601. NASA.
- ITP Engines UK Ltd., ed. (2010). *ESATAN-TMS Thermal Engineering Manual*.
- Ivanovsky, M. N., V. P. Sorokin, and I. V. Yagodkin (1982). *The Physical Principles of Heat Pipes*. Clarendon Press, Oxford, England, UK.
- Karam, R. D. (1998). *Satellite Thermal Control for System Engineers*. Progress in astronautics and aeronautics. AIAA.
- Kays, W. M. and M. E. Crawford (1993). *Convective Heat and Mass Transfer*. McGraw-Hill Science/Engineering/Math.

- Keller, C. W., G. R. Cunnington, and A. P. Glassford (1974). *Thermal Performance of Multi-layer Insulations*. Tech. rep. NASA CR-134477. Lockheed Missiles and Space Center.
- Kemme, J. E. (1967). “High Performance Heat Pipes”. In: *Thermionic Conversion Specialist Conference*. IEEE, pp. 355–358.
- (1976). “2nd International Heat Pipe Conference”. In: *Thermionic Conversion Specialist Conference*. ESA Scientific & Technical Information Branch, pp. 11–22.
- Kim, A. (2012). “Optimization of variable conductance heat pipes for the eROSITA telescope”. in preparation. MA thesis. Technische Universität München.
- Kirtley, C. and H. Brouquet (2011). “ESATAN Thermal Modelling Suite”. In: *24th European Workshop on Thermal and ECLS Software*. ESA/ESTEC/TEC-MTV, pp. 111–133.
- Kobel, M. and K. Jentung (2003). “Thermal vacuum testing of SWIFT XRT ethane heat pipes”. In: *1st International Energy Conversion Engineering Conference*. 20040012810. AIAA.
- Krishnaprakas, C. K. (1998). “A comparison of ODE solution methods for spacecraft thermal problems”. In: *Heat transfer engineering* 19.3, pp. 103–109.
- Lambert, J. D. (1991). *Numerical Methods for Ordinary Differential Systems: The Initial Value Problem*. Wiley.
- Lemmon, E. W., M. O. McLinden, and D. G. Friend (2012). “NIST Chemistry WebBook, NIST Standard Reference Database”. In: 69. Gaithersburg MD, 20899: P. J. Lindstrom and W. G. Mallard. Chap. Thermophysical Properties of Fluid Systems. URL: <http://webbook.nist.gov>.
- Levy, E. K. (1968). “Theoretical investigation of heat pipes operating at low vapor pressures”. In: *Journal of Engineering for Industry* 90, pp. 547–552.
- Lienhard, J. H. (2003). *A heat transfer textbook*. Phlogiston Press.
- Lindenmaier, Peter (2010). *eROSITA MLI Design Description*. Tech. rep. eMLI-HPS-TN-010. HPS GmbH.
- Marcus, B. D. (1972). *Theory and Design of Variable Conductance Heat Pipes*. Tech. rep. CR-2018. NASA.
- Marcus, B. D. and G. L. Fleischman (1970). “Steady State and Transient Performance of Hot Reservoir Gas-Controlled Heat Pipes”. In: *ASME 70-HT/SpT-11*.

- Maydanik, Yu. F. (2005). “Loop Heat Pipes”. In: *Applied Thermal Engineering*, pp. 635–657.
- Mayrhofer, R., I. Eberhart, C. Laa, et al. (2009). *ESTEC Calorimeter: Thirty-five Years of Measurements*. Tech. rep. 2009-01-2412. SAE International.
- McIntosh, R., C. McCreight, and P. J. Brennan (1993). *Long duration exposure facility (LDEF) low temperature Heat Pipe Experiment Package (HEPP) flight results*. Tech. rep. 93N29701.
- Meidinger, N. (2009). “eROSITA CCD radiation protection”. eROSITA document server, eRO-MPE-TN-32-01-2.
- Meidinger, N., R. Andritschke, J. Elbs, et al. (2008). “eROSITA camera design and first performance measurements with CCDs”. In: *Proceedings of SPIE*. Vol. 7011. SPIE, 70110J-1.
- Meidinger, N., R. Andritschke, W. Assman, et al. (2010). “CCD Detector Development for the eROSITA Space Telescope”. In: *Nuclear Science Symposium Conference Record*. IEEE.
- Muehlegger, M. L. (2010). “Simulated Observations of Galaxy Clusters for Current and Future X-ray Surveys”. PhD thesis. Technische Universität München.
- Peeples, M. E. and L. D. Calhoun (1977). “Fabrication and comparative performance of three variable conductance heat pipe concepts”. In: *ASME 77-ENAS-42*.
- Planck, M. (1901). „Ueber das Gesetz der Energieverteilung im Normalspectrum“. In: *Annalen der Physik* 309.3, S. 553–563.
- Predehl, P. (1999). “ABRIXAS: scientific goal and mission concept”. In: *Proceedings of SPIE*. Vol. 3765. SPIE, pp. 172–183.
- Predehl, P., P. Friedrich, and G. Hasinger (2003). “ROSITA: scientific goal and mission concept”. In: *Proceedings of SPIE*. Vol. 4851. SPIE, pp. 314–323.
- Predehl, P., R. Andritschke, H. Böhringer, et al. (2010). “eROSITA on SRG”. In: *Proceedings of SPIE*. Vol. 7732. SPIE, 77320U.
- Rayleigh, Lord (1892). “On the influence of obstacles arranged in rectangular order upon the properties of a medium”. In: *Philosophical Magazine* XXXIV, pp. 481–502.
- Reiprich, T. H. and H. Böhringer (2002). “The Mass Function of an X-Ray Flux-Limited Sample of Galaxy Clusters”. In: *The Astrophysical Journal* 567 (2). arXiv:astro-ph/0111285v1, pp. 716–740.

- Rybkin, B. I., Yu. Yu. Sergeev, E. M. Sidorenko, et al. (1979). "Investigation of the coolant edge wetting angle for mesh heat pipe wicks". In: *Journal of engineering physics and thermophysics* 36 (4), pp. 408–413.
- Schmidt, Dr. F. (1961). *Thermische Isolation*. Techn. Ber. Verein deutscher Ingenieure.
- Schmidt, E. und E. Eckert (1935). „Über die Richtungsverteilung der Wärmestrahlung von Oberflächen“. In: *Forschung im Ingenieurwesen* 6, S. 175–183.
- Shukla, K. N. (1972). "Transient Response of a Gas-Controlled Heat Pipe". In: *AIAA Journal* 19 (8), pp. 1063–1070.
- Sommerfeld, A. und H. Bethe (1967). *Elektronentheorie der Metalle*. Springer Verlag.
- Springel, V., S. D. M. White, A. Jenkins, et al. (2005). "Simulating the Joint Evolution of Quasars, Galaxies and their Large-scale Distribution". In: *Nature*.
- Stefan, Josef (1879). „Über die Beziehung zwischen der Wärmestrahlung und der Temperatur“. In: *Sitzungsberichte der mathematisch-naturwissenschaftlichen Classe der kaiserlichen Akademie der Wissenschaften* 79 (2), S. 391–428.
- Stimpson, L. D. and W. Jaworksi (1972). "Effects on overlaps, stitches and patches on multilayer insulation". In: *7th Thermophysics Conference*. 72–285. AIAA.
- Stramaccioni, D., T. Faust, and J. Hinger (2000). "XMM-Newton Thermal Design and In-orbit Performance". In: *30th International Conference on Environmental Systems*. 2000-01-2372. SAE International.
- Suman, B. (2009). "Microgrooved Heat Pipe". In: *Advances in Heat Transfer* 41.
- Sze, S. M. (2007). *Physics of Semiconductor Devices*. John Wiley & Sons.
- Thomas, J. W. (1995). *Numerical Partial Differential Equations*. Berlin: Springer.
- Wanous, D. J., B. D. Marcus, and J. P. Kirkpatrick (1975). "A variable conductance heat pipe flight experiment: Performance in space". In: *10th Thermophysics Conference*. 75-725. AIAA.
- Wien, W. (1894). „Temperatur und Entropie der Strahlung“. In: *Annalen der Physik* 288 (5), S. 132–165.
- Wright, P. E. (1970). *ICICLE Feasibility Study*. Tech. rep. 70N34012.